PACIFIC EARTHQUAKE ENGINEERING
RESEARCH CENTER

Experimental and Analytical Study of the Seismic Performance of Retaining Structures

Linda Al Atik

and

Nicholas Sitar

University of California, Berkeley

PEER 2008/104
MARCH 2009

Experimental and Analytical Study of the Seismic Performance of Retaining Structures

Linda Al Atik and Nicholas Sitar
Department of Civil and Environmental Engineering
University of California, Berkeley

PEER Report 2008/104
Pacific Earthquake Engineering Research Center
College of Engineering
University of California, Berkeley

October 2008

ABSTRACT

Recent changes in codes and improved understanding of strong ground motions have led to increased demands in the seismic design of retaining structures. Correspondingly, the dynamic loads computed using currently available design procedures significantly exceed loads used in the design of most of the existing retaining structures, suggesting that they may have been significantly underdesigned. Field evidence from recent major earthquakes fails to show any significant problems with the performance of retaining structures designed for static earth pressures only. In view of this, an experimental and analytical study of seismic earth pressures on cantilever retaining structures was performed to address the apparent discrepancy between theory and actual performance.

Two sets of dynamic centrifuge model experiments were performed to evaluate the magnitude and distribution of seismically induced lateral earth pressures on retaining structures and to study the seismic response of retaining wall–backfill systems. Two U-shaped cantilever retaining structures, one flexible and one stiff, were used in each experiment to model prototype structures representative of retaining-wall designs currently under consideration by the Bay Area Rapid Transit (BART) and the Valley Transportation Authority (VTA). Dry medium-dense sand at 61% and 72% relative density was used as backfill. The results obtained from the centrifuge experiments were used to develop and calibrate a two-dimensional (2-D) nonlinear finite element (FE) model built on the OpenSees platform. The finite element model was used to further study the seismic response of retaining wall–backfill systems and to evaluate the ability of numerical modeling in capturing the essential features of the seismic response observed in the centrifuge experiments.

In general, the magnitude of the observed seismic earth pressures depends on the magnitude and intensity of shaking, the density of the backfill soil, and the flexibility of the retaining walls. Specifically, the results of the centrifuge experiments show that the maximum dynamic earth pressures increase with depth and can be reasonably approximated by a triangular distribution analogous to that used to represent static earth pressures. Hence the current practice and assumption that the resultant of the dynamic earth pressures acts at 0.6–0.7H is not consistent with the experimental results. A similar conclusion was reached by Nakamura (2006) based on centrifuge experiments on gravity walls. An important contribution to the overall dynamic moment acting on the wall is the mass of the wall itself. The data from the centrifuge

experiments suggest that this contribution can be substantial. Moreover, the dynamic earth pressures and inertial forces do not act simultaneously. The experimental results show that when the inertial force is at its local maximum, the overall dynamic moment acting on the wall reaches its local maximum as well, while the dynamic earth pressure increment is at its local minimum or is around zero. This observation contradicts the Mononobe-Okabe hypothetical assumptions and suggests that designing retaining walls for maximum dynamic earth pressure increment and maximum wall inertia is overly conservative. The relationship between the seismic earth pressure increment coefficient (ΔK_{AE}) at the time of maximum overall wall moment and peak ground acceleration obtained from the centrifuge experiments suggests that seismic earth pressures can be neglected at accelerations below 0.4 g. This is consistent with the observations and analyses performed by Clough and Fragaszy (1977) and Fragaszy and Clough (1980), who concluded that conventionally designed cantilever walls with granular backfill could be expected to resist seismic loads at accelerations up to 0.5 g. The finite element model results using nonlinear soil model parameters are in good agreement with centrifuge results and are consistent with the observed trends. The results of finite element modeling with denser soil parameters showed that the seismic earth pressures decreased on the order of 23–30%, suggesting that seismic earth pressures may not be a significant issue in good soil conditions. This aspect of the problem requires further experimental and analytical evaluation.

ACKNOWLEDGMENTS

This work made use of the Earthquake Engineering Research Centers Shared Facilities supported by the National Science Foundation, under award number EEC-9701568 through the Pacific Earthquake Engineering Research (PEER) Center. Any opinions, findings, and conclusions or recommendations expressed in this material are those of the authors and do not necessarily reflect those of the National Science Foundation.

This research was supported by the San Francisco Bay Area Rapid Transit (BART), the Santa Clara Valley Transportation Authority (VTA), and the Pacific Earthquake Engineering Research Center (PEER).

The authors gratefully acknowledge the support and technical input provided by Mr. Ed Matsuda and Dr. Jose Vallenas at BART, and Mr. James Chai at VTA. The authors also received much valuable input from Mr. John Egan at GeoMatrix, Mr. Tom Boardman at Kleinfelder, Dr. Marshall Lew at MACTEC, and Prof. Jonathan Bray at UC Berkeley. Prof. Bruce Kutter, Dr. Dan Wilson, and all the staff at the Center for Geotechnical Modeling at the University of California, Davis, provided much support and valuable input during the experimental phase of this study. Dr. Gang Wang and Dr. Zaohui Yang also provided valuable input in the analytical phase of this study.

CONTENTS

LIST OF FIGURES

LIST OF TABLES

1 Introduction

The problem of retaining soil is one of the oldest in geotechnical engineering, and some of the earliest and most fundamental principles of soil mechanics were developed to allow for rational design of earth retaining structures. Earth retaining structures take many different forms supporting slopes, bridge abutments, quay walls, and excavations. As such, they are frequently key elements of ports and harbors, transportation systems, lifelines, and other constructed facilities. Therefore, their design for static and seismic loading has always been an important subject in geotechnical engineering.

Lateral earth pressures are those imparted by soils onto vertical or near-vertical supporting structures. The solution of lateral static earth pressure problems was among the first applications of the scientific method to the design of structures. Two of the pioneers in this effort were Coulomb and Rankine. Although many others have since made significant contributions to our knowledge of static earth pressures, the work of these two scientists was so fundamental that it still forms the basis for earth pressure calculations today. The magnitude of earth pressures is largely related to the allowed movement of the retaining structure. Minimum (active) and maximum (passive) earth pressures occur when the retaining structure is allowed to move away from and into the soil, respectively. At-rest earth pressures fall in between these two extremes and occur when the retaining system is not allowed to move.

Coulomb (1776) first studied the problem of lateral static earth pressures on retaining structures. He used force equilibrium to determine the magnitude of the soil thrust acting on the wall for the minimum active and maximum passive conditions. Since the problem is indeterminate, a number of potential failure surfaces must be analyzed to identify the critical failure surface. Rankine (1857) developed a much simpler procedure for computing minimum active and maximum passive static earth pressures. By making assumptions about the stress conditions and the strength envelope of the soil behind the wall, Rankine was able to render the lateral earth pressure problem determinate and directly compute the static earth pressures acting

on retaining structures. The work of Rankine and Coulomb forms the basis of static earth pressure analyses, and their design procedures for static lateral loading on retaining structures are well developed and accepted.

The evaluation of seismically induced lateral earth pressures on retaining structures, however, represents a much more challenging problem. Permanent deformations of retaining structures occurred in many historical earthquakes. In some cases, these deformations were negligibly small, while in others they caused significant damage. With the occurrence of large-magnitude earthquakes that caused significant damage to different types of engineering structures, designing earth retaining systems for seismic loading became a necessity, and understanding the seismic behavior of the backfill–retaining structure system became essential.

The dynamic response of even the simplest type of retaining wall is a complex soil-structure-interaction problem. Wall movements and dynamic earth pressures depend on the response of the soil underlying the wall, the response of the backfill, the inertial and flexural response of the wall itself, and the nature of the input motions. The problem of seismically induced lateral earth pressures on retaining structures and basement walls has received significant attention from researchers over the years. The pioneering work was performed in Japan following the Great Kwanto Earthquake of 1923 by Okabe (1926) and Mononobe and Matsuo (1929). The method proposed by these authors and currently known as the Mononobe-Okabe (M-O) method is based on Coulomb's theory of static earth pressures. The M-O method was originally developed for gravity walls retaining cohesionless backfill materials and is today, with its derivatives, the most commonly used approach to determine seismically induced lateral earth pressures. Later studies provided design methods mostly based on analytical solutions or experimental programs.

While many theoretical, experimental and analytical studies have been conducted on the subject of seismic earth pressures in the last eighty years, to date, there seems to be no general agreement on a seismic design method for retaining structures or whether seismic provisions should be applied at all (see Chapter 2). Given the importance of the seismically induced lateral earth pressures problem in the design of retaining structures in seismically active areas, an experimental and analytical study was undertaken aimed at improving our understanding of seismically induced lateral earth pressures on U-shaped cantilever walls retaining medium-dense sand deposits. This study started with an extensive literature review of previous analytical, numerical, and experimental work related to dynamic earth pressures. The results of this

literature review and a review of the available case histories of retaining structures under seismic loading are presented in Chapter 2 of this report.

The experimental phase of this study consisted of performing a series of two dynamic centrifuge experiments to measure the magnitude and distribution of seismic earth pressures on U-shaped cantilever retaining structures. The centrifuge models were extensively instrumented with accelerometers, air hammers, bender elements, strain gages, force-sensing bolts, pressure sensors, and displacement transducers in order to study the behavior of walls and backfills under earthquake loading. A detailed description of the experimental design and setup is presented in Chapter 3. The results of the two centrifuge experiments are presented in terms of acceleration, displacement, moment, and pressure responses in Chapter 4.

After performing the dynamic centrifuge experiments and analyzing the experimental results and observations, a two-dimensional (2-D) nonlinear finite element (FE) model was developed on the OpenSees platform to study the behavior of retaining walls and backfill under seismic loading. The 2-D FE model was calibrated against the recorded data and observations from the two centrifuge experiments. Through comparison between the computed and centrifuge-recorded responses, the FE model was evaluated for its ability to capture the essential features and soil-structure interaction of the retaining wall–backfill system during earthquakes. A detailed description of the development and calibration of the FE model is presented in Chapter 5. The calibrated finite element was used to predict earth pressures for retaining wall–backfill scenarios of interest. The results of these predictions are also presented in Chapter 5. Conclusions and design recommendations are presented in Chapter 6.

2 Literature Review

Since the pioneering work of Mononobe and Matsuo (1929) and analytical work of Okabe (1926), researchers have developed a variety of analytical and numerical models to predict the dynamic behavior of retaining walls, and have performed various types of experiments to study the mechanisms behind the development of seismic earth pressures on retaining structures. The different approaches available for studying dynamic earth pressures can be divided into analytical, numerical, and experimental methods. While a vast amount of literature exists on the topic of seismically induced lateral earth pressures, this chapter summarizes previous research performed highlighting selected works of relevance to this study.

2.1 ANALYTICAL METHODS

As suggested by Stadler (1996), analytical solutions for the dynamic earth pressures problem can be divided into three broad categories depending on the magnitude of the anticipated wall deflection. These categories include rigid-plastic, elastic, and elasto-plastic methods. Relatively large wall deflections are usually assumed for rigid-plastic methods, while very small deflections are assumed for elastic methods. Elasto-plastic methods, appropriate for moderate wall deflections, are usually developed using finite element analysis and are therefore presented under the numerical methods section of this chapter. It is important to note that analytical seismic earth pressures methods are usually based on idealized assumptions and simplifications that do not necessarily represent the real retaining structures–backfill seismic behavior. Therefore, such methods often result in overconservative estimates of dynamic earth pressures.

2.1.1 Rigid-Plastic Methods

Rigid-plastic methods, which generally assume large wall deflections, are either force based or displacement based. The most commonly used force-based rigid-plastic methods are the M-O and Seed and Whitman (1970) methods. Displacement methods are generally based on the Newmark (1965) or modified Newmark sliding block.

The Mononobe-Okabe Method and Its Derivatives

The M-O method developed by Okabe (1926) and Mononobe and Matsuo (1929) is the earliest and the most widely used method for estimating the magnitude of seismic forces acting on a retaining wall. The M-O method is an extension of Coulomb's static earth pressure theory to include the inertial forces due to the horizontal and vertical backfill accelerations. The M-O force diagram is presented in Figure 2.1.

The M-O method was developed for dry cohesionless backfill retained by a gravity wall and is based on the following assumptions (Seed and Whitman 1970):

1. The wall yields sufficiently to produce minimum active pressure;
2. The soil is assumed to satisfy the Mohr-Coulomb failure criterion;
3. When the minimum active pressure is attained, a soil wedge behind the wall is at the point of incipient failure, and the maximum shear strength is mobilized along the potential sliding surface;
4. Failure in the backfill occurs along a plane surface inclined at some angle with respect to the horizontal backfill passing through the toe of the wall;
5. The soil wedge behaves as a rigid body, and accelerations are constant throughout the mass;
6. Equivalent static horizontal and vertical forces, $W.k_h$ and $W.k_v$, are applied at the center of gravity of the wedge represent the earthquake forces. Parameters K_h and K_v represent gravitational accelerations in the soil wedge.

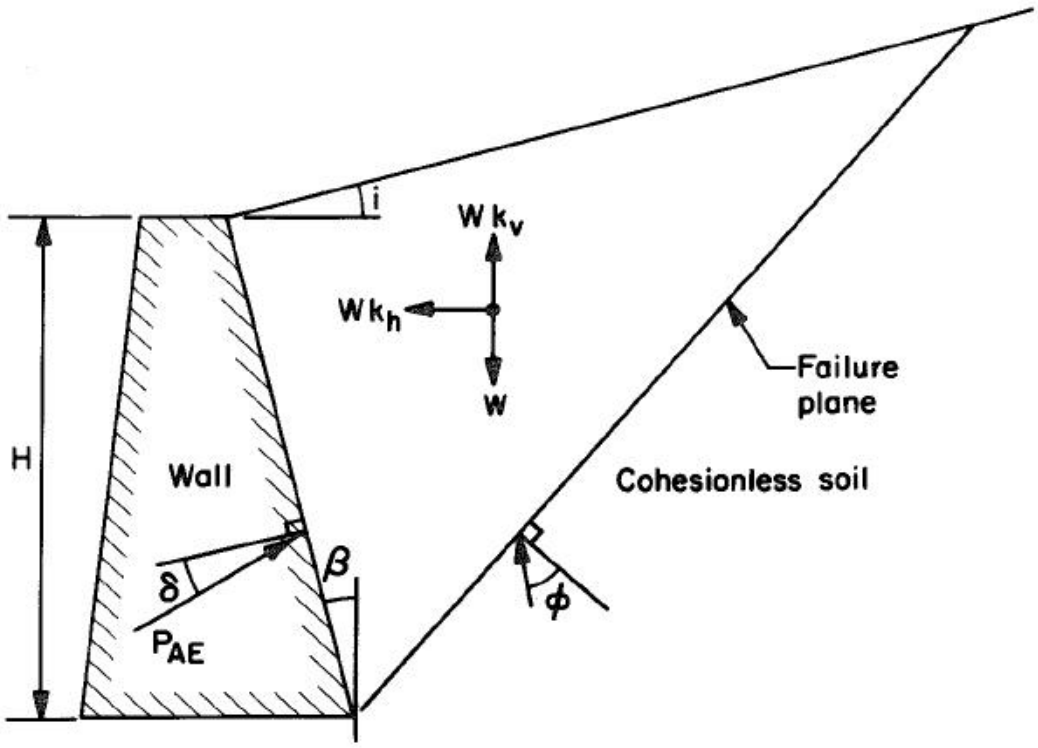

Fig. 2.1 Forces considered in Mononobe-Okabe analysis (Wood 1973).

Based on the M-O method, the active lateral thrust can be determined by the static equilibrium of the soil wedge shown in Figure 2.1. The maximum dynamic active thrust per unit width of the wall, P_{AE}, is determined by optimizing the angle of the failure plane to the horizontal plane, and is given by:

$$P_{AE} = \frac{1}{2} \cdot \gamma \cdot H^2 \cdot (1 - k_v) \cdot K_{AE} \tag{2.1}$$

where, $$K_{AE} = \frac{\cos^2(\varphi - \theta - \beta)}{\cos\theta . \cos^2\beta . \cos(\delta + \beta + \theta) . \left[1 + \sqrt{\frac{\sin(\varphi + \delta) . \sin(\varphi - \theta - i)}{\cos(\delta + \beta + \theta) . \cos(i - \beta)}}\right]^2} \tag{2.2}$$

P_{AE} = Maximum dynamic active force per unit width of the wall;

K_{AE} = Total lateral earth pressure coefficient;

γ = unit weight of the soil;

H = height of the wall;

Φ = angle of internal friction of the soil;

δ = angle of wall friction;

i = slope of ground surface behind the wall;

β = slope of the wall relative to the vertical;

$$\theta = \tan^{-1}\left(\frac{k_h}{1-k_v}\right)$$

k_h = horizontal wedge acceleration divided by g; and

k_v = vertical wedge acceleration divided by g.

The M-O method gives the total active thrust acting on the wall but does not explicitly give the point of application of the thrust or the dynamic earth pressure distribution. The point of application of the M-O active thrust is assumed to be at H/3 above the base of the wall.

Seed and Whitman (1970) performed a parametric study to evaluate the effects of changing the angle of wall friction, the friction angle of the soil, the backfill slope and the vertical acceleration on the magnitude of dynamic earth pressures. They observed that the maximum total earth pressure acting on a retaining wall can be divided into two components: the initial static pressure and the dynamic increment due to the base motion. Seed and Whitman (1970) suggested that the static, dynamic increment, and total lateral earth pressure coefficients can be related as: $K_{AE} = K_A + \Delta K_{AE,}$ where the dynamic earth pressure increment coefficient $\Delta K_{AE} \approx ¾\ k_h$ for the case of a vertical wall, the horizontal backfill slope, and a friction angle of 35°. After reviewing the results of experimental work based on small, 1-g, shaking table experiments, Seed and Whitman (1970) suggested that the point of application of the dynamic increment thrust should be between one half to two thirds the wall height above its base. Moreover, the authors observed that the peak ground acceleration occurs for an instant and does not have sufficient duration to cause significant wall movements. Therefore, they recommended using a reduced ground acceleration of about 85% of the peak value in the seismic design of retaining walls. Finally, Seed and Whitman (1970) concluded that "many walls adequately designed for static earth pressures will automatically have the capacity to withstand earthquake ground motions of substantial magnitudes and in many cases, special seismic earth pressure provisions may not be needed."

Displacement-based methods are generally developed for gravity retaining walls and are mostly based on the Newmark (1965) and modified Newmark sliding block model. The concept of displacement-based methods involves calculating an acceleration coefficient value based on the amount of permissible displacement of the wall. This reduced acceleration coefficient is then used with the M-O method to determine the dynamic thrust. Wall inertial effects are usually

accounted for in displacement-based methods. Richards and Elms (1979) observed that inertial forces on gravity retaining walls can be significant and concluded that the M-O method provides adequate estimates of seismic earth pressures provided that wall inertial effects are properly accounted for. Other examples of such methods are Zarrabi (1979), and Jacobson (1980).

2.1.2 Elastic Methods

Elastic methods are generally applied in the design of basement walls that usually experience very small displacements and can be considered as "truely" rigid walls. The underlying assumption is that the relative soil-structure movement generates soil stresses in the elastic range. Elastic methods are usually based on elastic wave solutions and result in the upper-bound dynamic earth pressures estimates. The Wood (1973) method is the most widely used under this category. Other work in this area includes Matsuo and Ohara (1960), Tajimi (1973), and Scott (1973).

The Wood (1973) method is based on linear elastic theory and on idealized representations of the wall-soil systems. Wood (1973) performed an extensive study on the behavior of rigid retaining walls subject to earthquake loading and provided chart solutions for the cases of arbitrary horizontal forcing of the rigid boundaries and a uniform horizontal body force. The Wood (1973) method predicts a total dynamic thrust approximately equal to $\gamma H2A$ acting at 0.58H above the base of the wall. Figure 2.2 presents Wood's formulation for the case of a uniform horizontal body force.

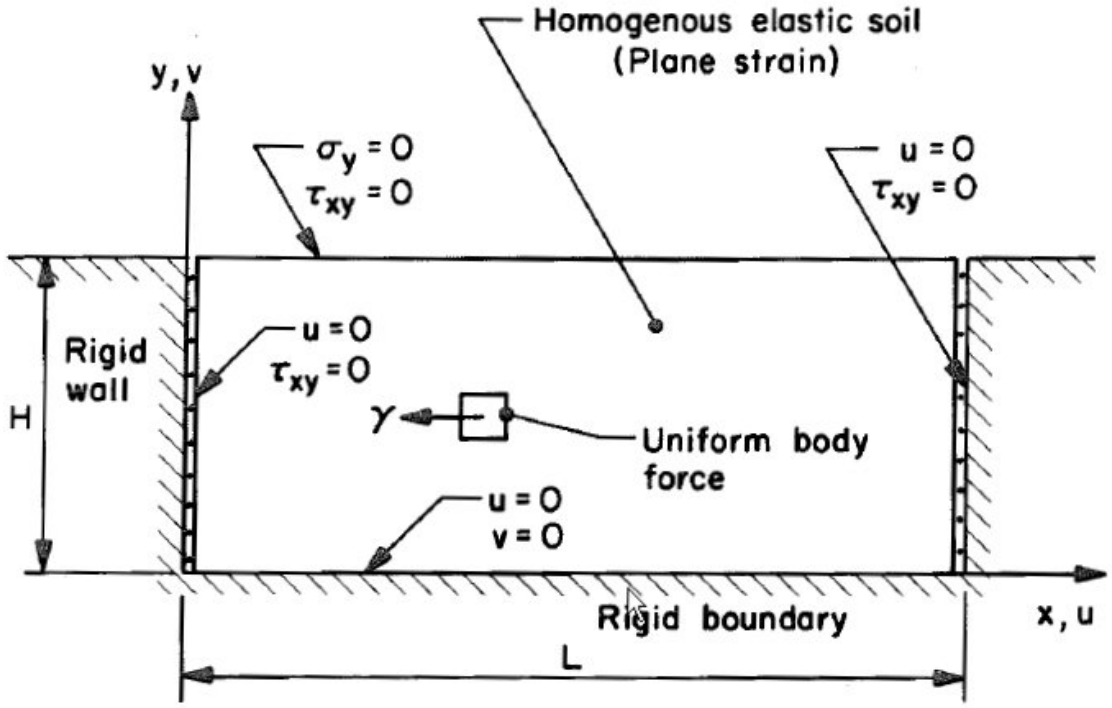

Fig. 2.2 Wood (1973) rigid problem.

2.2 NUMERICAL METHODS

Numerical modeling efforts have been applied to verify the seismic design methods in practice and to provide new insights into the problem. Various assumptions have been made and several numerical codes have been applied (PLAXIS, FLAC, SASSI…) to solve the problem. While elaborate finite element techniques and constitutive models are available in the literature to obtain the soil pressure for design, simple methods for quick prediction of the maximum soil pressure are rare. Moreover, while some of the numerical studies reproduced experimental data quite successfully, independent predictions of the performance of retaining walls are not available. Hence, the predictive capability of the various approaches is not clear. Selected research in the numerical methods area is presented in this section.

As mentioned by Stadler (1996), Clough and Duncan (1971) were among the first researchers to apply finite elements methods for studying the static behavior of retaining walls that included the interface effects between the structure and the surrounding soil. Wood (1973) modeled a rigid retaining wall–soil system using linear plane-strain conditions and compared the results with analytical calculations for rigid walls and found good agreement. Aggour and Brown

(1973) conducted 2-D plane-strain analyses on a 20-ft-tall cantilever retaining wall to study the effects of wall flexibility and backfill length and shape on the dynamic earth pressure distribution. They concluded that greater wall flexibility reduces the total dynamic moments acting on the retaining structure and that the shape of the backfill has a considerable effect on the frequencies of the system.

Siddharthan and Maragakis (1989) conducted finite element analyses to model the dynamic behavior of a flexible retaining wall supporting dry cohesionless soil. They used an incrementally elastic approach to model soil nonlinear hysteretic behavior and validated their model by comparing its results to recorded responses from a dynamic centrifuge experiment. Siddharthan and Maragakis (1989) concluded that higher bending moments and lower wall deflections occur for stiffer retaining walls supporting looser sandy backfills. Steedman and Zeng (1990) proposed a pseudo-dynamic model for seismic earth pressures taking into account dynamic amplification and phase shifting, and validated their model with results from a centrifuge experiment. They concluded that the dynamic active thrust acts at a point above one third the height of the wall above its base. Veletsos and Younan (1997) modeled flexible retaining walls supporting a uniform linear viscoelastic soil medium and observed that forces acting on flexible walls are much lower than those acting on rigid ones.

Green et al. (2003) performed a series of nonlinear dynamic response analyses of a cantilever retaining wall–soil system using the FLAC modeling tool, and concluded that at very low levels of acceleration, the seismic earth pressures were in agreement with the M-O predictions. As accelerations increased, seismic earth pressures were larger than those predicted by the M-O method. Gazetas et al. (2004) performed a series of finite element analyses on several types of flexible retaining systems subject to short-duration, moderately strong excitations. They observed that "as the degree of realism in the analysis increases, we can explain the frequently observed satisfactory performance of retaining systems during strong seismic shaking."

To investigate the characteristics of the lateral seismic soil pressure on building walls, Ostadan (2005) performed a series of soil-structure-interaction analyses using SASSI. Using the concept of a single degree-of-freedom, Ostadan (2005) proposed a simplified method to predict maximum seismic soil pressures for building walls resting on firm foundation material. This proposed method resulted in dynamic earth pressure profiles comparable to or larger than the Wood (1973) solution, with the maximum earth pressure occurring at the top of the wall.

2.3 EXPERIMENTAL METHODS

Experimental studies of seismically induced lateral earth pressures on retaining structures started in 1929 by Mononobe and Matsuo after the Great Kwanto Earthquake of 1923. To verify the analytical method of calculation of dynamic earth pressures developed by Okabe (1926), Mononobe and Matsuo (1929) carried out experiments on dry relatively loose sand in a rigid 1-g shaking table container in order to measure dynamic earth pressures on retaining walls. The Mononobe and Matsuo (1929) experimental configuration is presented in Figure 2.3. The experiments consisted of river bed sand boxes with two vertical doors hinged at their base and hydraulic pressure gages at their top to measure the horizontal pressure exerted on the walls. The modeled walls were of 4 and 6 ft height. The sand boxes were set on rollers and horizontal simple harmonic motion was imparted by means of a winch driven by an electric motor.

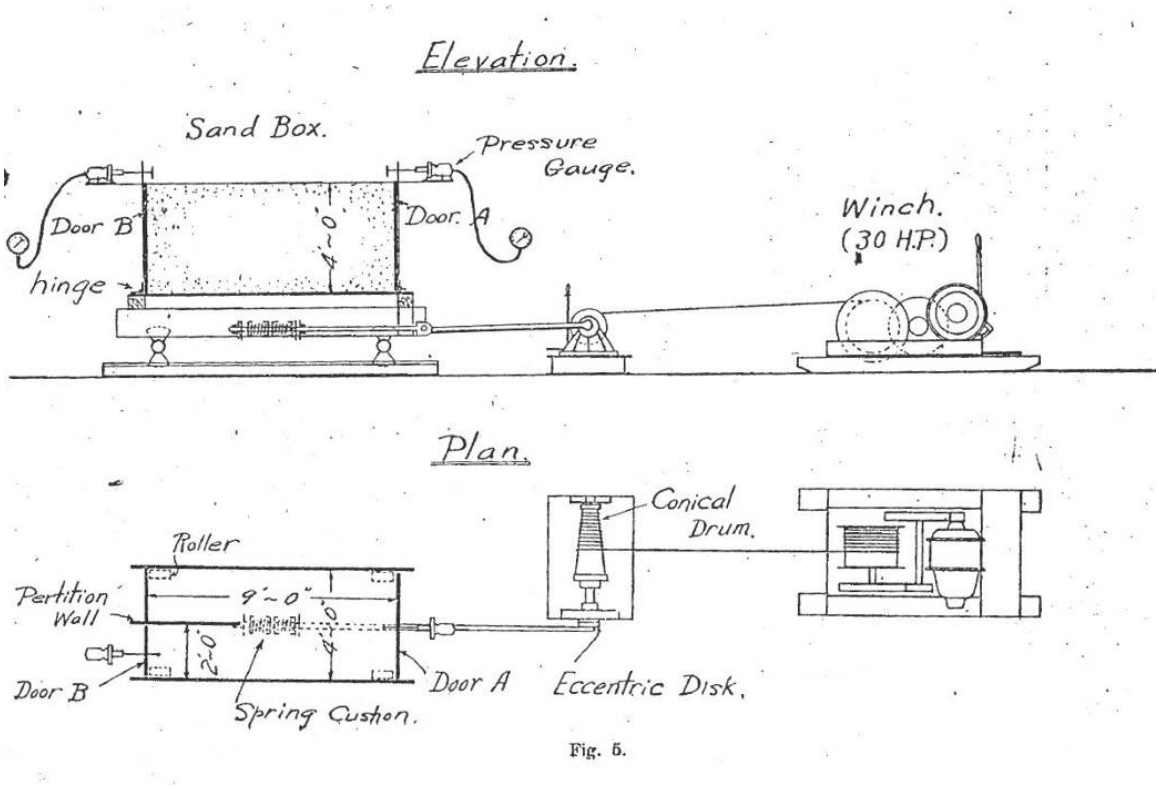

Fig. 2.3 Setup of Mononobe and Matsuo (1929) experiments.

Mononobe and Mastuo (1929) obtained experimental results consistent with the Okabe (1926) principle and their proposed seismic earth pressure theory, presented in Section 2.1.1 became known as the M-O method. While these experiments were very meticulous and pioneering in their scope, they cannot be simply scaled to taller structures. More importantly, the observed amplification of ground motion and the observed increase in earth pressure upward is a direct result of the physical layout of the geometry of the shaking table box and the properties of the sand. In that sense, Mononobe and Matsuo's results are correct for the given geometry and material, and are directly applicable to walls up to 6 ft in height with relatively loose granular backfill but are limited to such scenarios.

The results from various later experimental programs aimed at determining dynamic earth pressures on retaining walls have been reported in the literature. The majority of these experimental studies were performed on 1-g shaking tables. Similarly to the Mononobe and Matsuo (1929) experiments, the accuracy and usefulness of these 1-g shaking table experiments are limited due to the inability to replicate in-situ soil stress conditions especially for granular backfills. The results from the 1-g shaking table experiments were published in the literature by Matsuo (1941), Ishii et al. (1960), Matsuo and Ohara (1960), Sherif et al. (1982), Bolton and Steedman (1982), Sherif and Fang (1984), Steedman (1984), Bolton and Steedman (1985), and Ishibashi and Fang (1987). As expected, the results of such experiments generally suggested that the M-O method predicts reasonably well the total resultant thrust but that the point of application of the resultant thrust should be higher than one third the height of the wall above its base.

Dynamic centrifuge tests on model retaining walls with dry and saturated cohesionless backfills have been performed by Ortiz (1983), Bolton and Steedman (1985), Zeng (1990), Steedman and Zeng (1991), Stadler (1996), and Dewoolkar et al. (2001). The majority of these dynamic centrifuge experiments used sinusoidal input motions and pressure cells to measure earth pressures on the walls. Ortiz et al. (1983) performed a series of dynamic centrifuge experiments on cantilever retaining walls with dry medium-dense sand backfill and observed a broad agreement between the maximum measured forces and the M-O predictions. Ortiz et al. (1983) commented that the maximum dynamic force acted at about one third the height of the wall above its base. The importance of inertial effects was not considered.

Bolton and Steedman conducted dynamic centrifuge experiments on concrete (1982) and aluminum (1985) cantilever retaining walls supporting dry cohesionless backfill, and their results

generally supported the M-O method. Steedman (1984) performed centrifuge experiments on cantilever retaining walls with dry dense sand backfill and measured dynamic forces in agreement with the values predicted by the M-O method, but suggested that the point of application should be located at midheight of the wall. Based on the Zeng (1990) dynamic centrifuge experiments, Steedman and Zeng (1990) suggested that the dynamic amplification or attenuation of input motion through the soil and that phase shifting are important factors in the determination of the magnitude and the distribution of dynamic earth pressures.

Stadler (1996) performed 14 dynamic centrifuge experiments on cantilever retaining walls with dry medium-dense sand backfill and observed that the total dynamic lateral earth pressure profile is triangular with depth but that the incremental dynamic lateral earth pressure profile ranges between triangular and rectangular. Moreover, Stadler (1996) suggested that using reduced acceleration coefficients of 20–70% of the original magnitude with the M-O method provides good agreement with the measured forces.

Nakamura (2006) performed a series of dynamic centrifuge experiments to study the seismic behavior of gravity retaining walls and investigate the accuracy of the M-O assumptions. His study presented invaluable insights into the seismic behavior of the gravity wall–backfill system. The configuration of the Nakamura (2006) centrifuge model is presented in Figure 2.4.

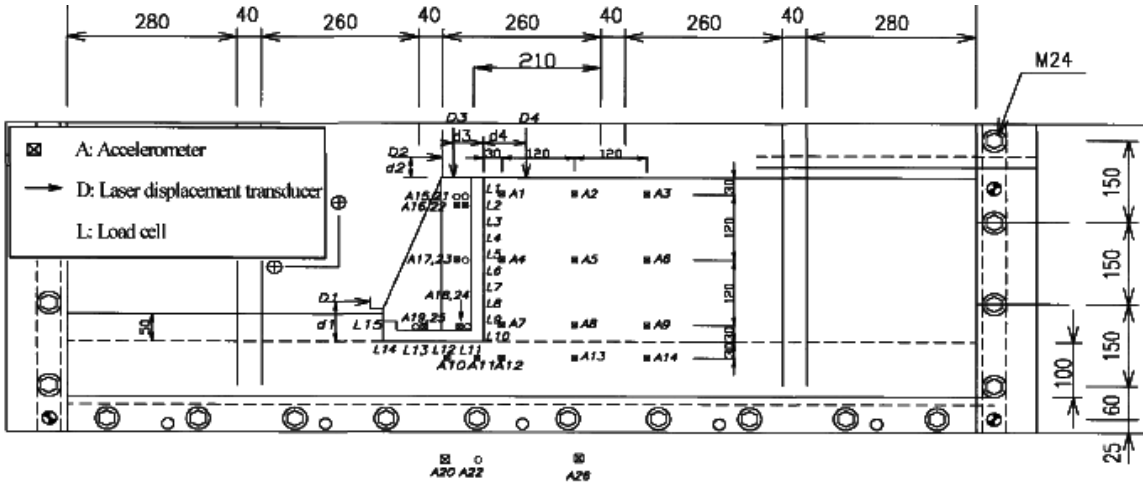

Fig. 2.4 Nakamura (2006) centrifuge model, horizontal shaking direction (in mm).

Nakamura (2006) studied the displacement, acceleration, and earth pressures responses in order to understand the seismic behavior of the wall/backfill system. His conclusions can be summarized as follows:

1. Contrary to the M-O rigid wedge assumption, the part of the backfill that follows the displacement of the retaining wall deforms plastically while sliding down;
2. While the M-O theory assumes that no phase difference occurs between the motion of the retaining wall and backfill, Nakamura (2006) experimentally observed that the acceleration is transmitted instantaneously through the retaining wall and then transmitted into the backfill; and
3. The M-O theory assumes that seismic earth pressures increase when the inertial force acts in the active direction on the wall/backfill system. In reality, dynamic earth pressures and inertial forces are not in phase. The dynamic earth pressure increment is around zero when the inertial force is at its maximum.

2.4 FIELD PERFORMANCE

Limited information is available on the field performance of retaining structures in recent major earthquakes due to the lack of well-documented retaining structures failures in non-liquefiable backfills. As discussed in Gazetas et al. (2004), the performance of retaining structures and basement walls during earthquakes greatly depends on the presence of liquefaction-prone loose cohensionless backfills. Case histories from recent major earthquakes (such as San Fernando (1971), Loma Prieta (1989), Northridge (1994), Kobe (1995), Chi-Chi (1999), Kocaeli (1999) and Athens (1999)) show that retaining structures supporting loose saturated liquefiable cohesionless soils are quite vulnerable to strong seismic shaking. On the other hand, flexible retaining walls supporting dry cohesionless sands or saturated clayey soils have performed particularly well during earthquakes. It is important to note that some of these retaining walls were not designed for seismic loading and that others were designed for base accelerations not more than 20% of the peak accelerations that they actually experienced during the earthquake. Selected case histories describing the behavior of retaining structures with non-liquefiable backfills are presented in this section.

Clough and Fragaszy (1977) investigated the seismic performance of open channel floodway structures in the Greater Los Angeles area during the 1971 San Fernando earthquake.

The floodway structures studied consisted of open U-shaped channels with wall tops set flush to the ground surface as shown in Figure 2.5. The backfill soil consisted of dry medium-dense sand with an estimated friction angle of 35°. The structures were designed for a conventional Rankine static triangular earth pressure distribution, and no seismic provisions were applied in the design. The cantilever walls were damaged during the earthquake, with the typical mode of failure as shown in Figure 2.5.

Clough and Fragaszy (1977) performed pseudo-static analyses and shear-wave propagation studies, and concluded that "conventional factors of safety used in design of retaining structures for static loadings provide a substantial strength reserve to resist seismic loadings. Peak accelerations of up to 0.5 g were sustained by the floodways with no damage even though no seismic loads were explicitly considered in the design." The relationship between wall damage and ground acceleration obtained by Clough and Fragaszy (1977) is shown in Figure 2.6. After performing M-O analyses and while applying the resulting dynamic force at two thirds the height of the wall above its base, they observed that M-O type analysis used with an effective acceleration of 0.7 g adequately predicted the failure loads. While they considered the moment capacity of the walls in their analyses, they did not specifically address the inertia of the walls themselves.

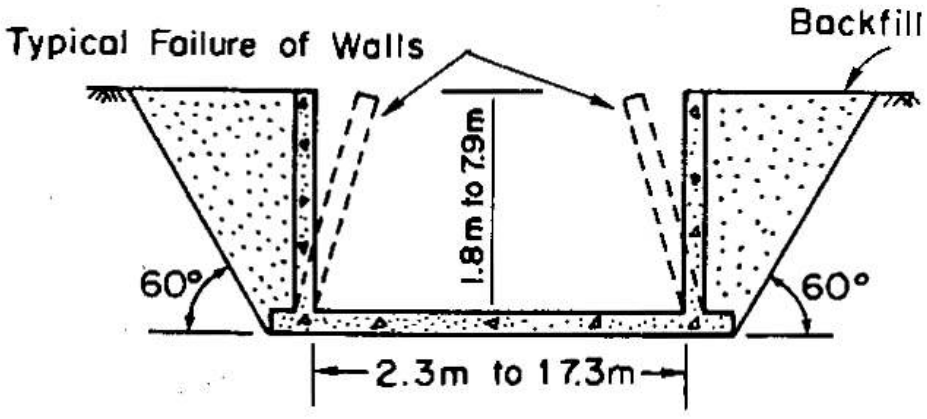

Fig. 2.3 Section through open channel floodway and typical mode of failure due to earthquake shaking (from Clough and Fragaszy 1977).

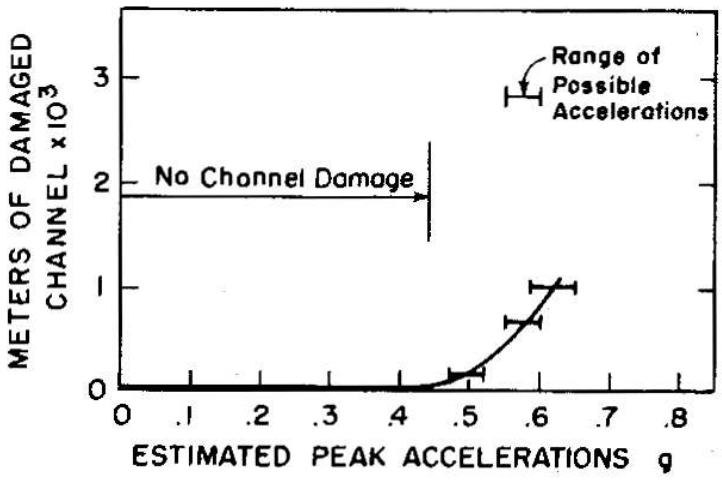

Fig. 2.4 Relationship between channel damage and peak accelerations (from Clough and Fragaszy 1977).

Successful field measurements of seismic lateral earth pressures on the embedded walls of the Lotung, Taiwan, quarter-scale reactor containment structure during several moderate earthquakes were reported by Chang et al. (1990). The authors reported that measured seismic earth pressures were similar to or lower than estimates calculated by the M-O method.

During the 1994 magnitude 6.7 Northridge earthquake, numerous "temporary" anchored walls were subjected to acceleration levels in excess of 0.2 g and in some cases as large as 0.6 g. Lew et al. (1995) described four such prestressed-anchored piled walls in the Greater Los Angeles area with excavation depths of 15–25 m and supporting relatively stiff soils. The authors reported that the measured deflections of these walls did not exceed 1 cm and that no significant damage was observed.

During the 1995 magnitude 7 Kobe, Japan, earthquake, a wide variety of retaining structures, mostly located along railway lines, were put to the test. Gravity-type retaining walls such as masonry, unreinforced concrete and leaning type were heavily damaged. On the other hand, reinforced concrete walls experienced only limited damage. Koseki et al. (1998) presented preliminary evaluations of the internal and external stability of several damaged retaining walls during the Kobe earthquake. The aim of their study was to improve the current design procedures that are mostly based on the M-O theory. Koseki et al. (1998) concluded that a horizontal acceleration coefficient based on a reduced value of the measured peak horizontal acceleration (60–100% of peak ground acceleration) is appropriate for use with the M-O method.

During the 1999 magnitude 7.6 Chi-Chi, Taiwan, earthquake, flexible reinforced-concrete walls and reinforced-soil retaining walls performed relatively well. Ling et al. (2001) studied cases of modular-block geosynthetic-reinforced soil retaining walls and reinforced slopes failures during the Chi-Chi earthquake. They attributed part of these failures to the topography and geotechnical conditions in Taiwan, whereby many walls are located along slopes and mountains and are constructed with obvious lack of professional design.

Gazetas et al. (2004) reported that during the 1999 magnitude 5.9 Athens earthquake several metro stations were being constructed. Although the retaining structure of the Kerameikos metro station was not designed for seismic shaking, it was able to withstand nearly 0.5 g of peak ground acceleration during the earthquake with no visible damage. Maximum wall displacements were estimated to have been on the order of a few centimeters. Overall, these case histories show that retaining structures perform quite well under seismic loading even if they were not specifically designed to handle dynamic loads.

3 Experimental Method

3.1 OVERVIEW OF DYNAMIC GEOTECHNICAL TESTING

Soil behavior is governed to a large extent by the existing stress state. In order for a centrifuge test model to represent actual prototype conditions, the stresses at homologous points in the model and the prototype should be the same. Thus, the basic principle behind centrifuge testing in geotechnical engineering is to create a stress field in the model that simulates prototype conditions. This allows the investigation of phenomena that otherwise would be possible only on full-scale prototypes.

The centrifuge arm consists of a model bucket at one end, where the model container sits. The weight of the model container is offset by adjustable counterweights at the other end of the arm. The model container containing the test specimen sits on the arm with its long dimension, which is parallel to the direction of shaking, horizontal until the arm starts to spin. As centrifugal acceleration increases, the bucket holding the model container rotates about 90˚ outward and upward. When the target centrifugal acceleration is reached, shaking is applied to the model container along its long, now vertical, dimension.

3.1.1 Scaling Relationships

In centrifuge testing, if a reduced-scale model with dimensions 1/N of the prototype is subject to a gravitational acceleration during spinning that is N times the acceleration of gravity, the soil in the model will have the same strength, stiffness, stress, and strain as the prototype. Based on centrifuge scaling laws, the time period of shaking and displacements are scaled by a factor of 1/N during centrifuge testing, while accelerations are scaled by a factor of N (Kutter 1995). Thorough discussions of centrifuge scaling laws are given by Scott (1998) and Kutter (1995). A

complete listing of the scaling relationships relevant to centrifuge model testing is presented in Table 3.1.

Table 3.1 Centrifuge scaling relationships.

Parameter	Model Dimension/Prototype Dimension
Length, L	1/N
Area, A	$1/N^2$
Volume, V	$1/N^3$
Mass, m	$1/N^3$
Density, ρ	1
Force, F	$1/N^2$
Moment, M	$1/N^3$
Stress, σ	1
Strain, ε	1
Strain Rate	N
Acceleration, Gravity	N
Acceleration, Dynamic	N
Time, Dynamic	1/N
Frequency	N

Particle size effects are important in centrifuge modeling and should be properly accounted for. Particle size cannot simply be scaled according to the scaling relationship for volume. According to Kutter (1995), interparticle contact forces and particle deformations depend on stress and absolute particle size. For models involving foundation elements, a significant number of contacts between the soil and the structure's foundation is required to minimize particle effects. For the 0.14-mm-diameter sand particles used in the centrifuge experiments described herein, a minimum foundation width of 4.2 mm is required. This requirement is easily satisfied with the use of 327.7-mm-diameter mat foundations used in the experiments.

3.1.2 Advantages of Centrifuge Modeling

Dynamic centrifuge testing has become an invaluable tool to understanding geotechnical earthquake engineering problems that otherwise would have been very hard to study. Advantages

of dynamic centrifuge modeling have been discussed by many researchers such as Kutter (1995) and Dobry and Liu (1994). These advantages are summarized as:

- Use of small-scale models to accurately simulate prototypes with realistic soil stress states and depths;
- Repeatability of results for like models;
- Direct observation of modes of failures and deformations;
- Efficient and cost-effective solution compared to full-scale testing;
- Ability to apply earthquake motions with a wide range of magnitudes and frequency contents; and
- Evaluation of empirical methods and validation of numerical modeling techniques.

3.1.3 Limitations of Centrifuge Modeling

While centrifuge model experiments have many advantages over other experimental approaches, there are also inherent limitations (Hausler 2002):

- Slight nonlinear stress distribution due to the increasing radius of rotation with depth of the model, which results in a small variation in the g level and hence the scaling factors with depth;
- Container side-wall interacts with the neighboring soil. This effect was minimized in the performed centrifuge experiments by using a flexible shear beam container. This type of container is designed such that its natural frequency is much less than the initial natural frequency of the soil (Kutter 1995);
- The container bottom, which is the source of input motion imparted to the soil, represents a rather unnatural and very rigid geologic transition; and
- Experimental errors that can be exacerbated through adherence to the scaling relationships.

3.2 UC DAVIS CENTRIFUGE, SHAKING TABLE, AND MODEL CONTAINER

Two centrifuge experiments were performed on the dynamic centrifuge at the Center for Geotechnical Modeling (CGM) at the University of California, Davis. The centrifuge has a radius of 9.1 m, a maximum payload of 4,500 kg, and an available bucket area of 4 m^2. The

centrifuge capacity in terms of the maximum acceleration multiplied by the maximum payload is 240 g-ton. The shaking table has a maximum payload mass of 2,700 kg and a maximum centrifugal acceleration of 75 g. Additional technical specifications for the centrifuge and shaking table are available in the literature (Kutter et al. 1994; Kutter 1995).

The two models were constructed in a rectangular flexible shear beam container known as FSB2 with internal dimensions of 1.65 m long x 0.79 m wide x approximately 0.58 m deep. The bottom of the container is coated with grains of coarse sand and is uneven. The container consists of a series of stacked aluminum rings separated by neoprene rubber, as shown in Figure 3.1. The flexible model container is mounted on a servo-hydraulic shaking table. The shaker actuators are controlled by a conventional closed-loop feedback control system and have the capacity of producing between 14 and 30 g shaking accelerations at frequencies up to 200 Hz. The maximum absolute shaking velocity is about 1 m/sec and the stroke is 2.5 cm peak to peak.

Fig. 3.1 Model container FSB2.

To minimize boundary effects, the container is designed such that its natural frequency is less than the initial natural frequency of the soil (Kutter 1995). The centrifugal acceleration used in the two experiments was 36 g. All results are presented in terms of prototype units unless otherwise stated.

3.3 MODEL TEST CONFIGURATIONS

The first centrifuge experiment, LAA01, was performed on a two-layer sand model. The model configuration is shown in Figures 3.2 and 3.3 in model scale units in profile and plan views, respectively. In prototype scale, the LAA01 model consists of two retaining wall structures, stiff and flexible, of approximately 6 m height spanning the width of the container. The structures were designed to have the stiffness, mass, and natural frequency of typical reinforced concrete structures. They sit on approximately 12.5 m of dry medium-dense sand (Dr = 73%) and the backfill soil consists of dry medium-dense sand (Dr = 61%). Both structures have stiff mat foundations.

The second centrifuge experiment, LAA02, was performed on a uniform-density sand model. The model configuration is shown in Figures 3.4 and 3.5 in model scale units in profile and plan views, respectively. The LAA02 model consists of the same stiff and flexible retaining wall structures that were used in LAA01. The structures sit on approximately 12.5 m of dry medium-dense sand (Dr = 72%) and support a dry medium-dense sand backfill (Dr = 72%).

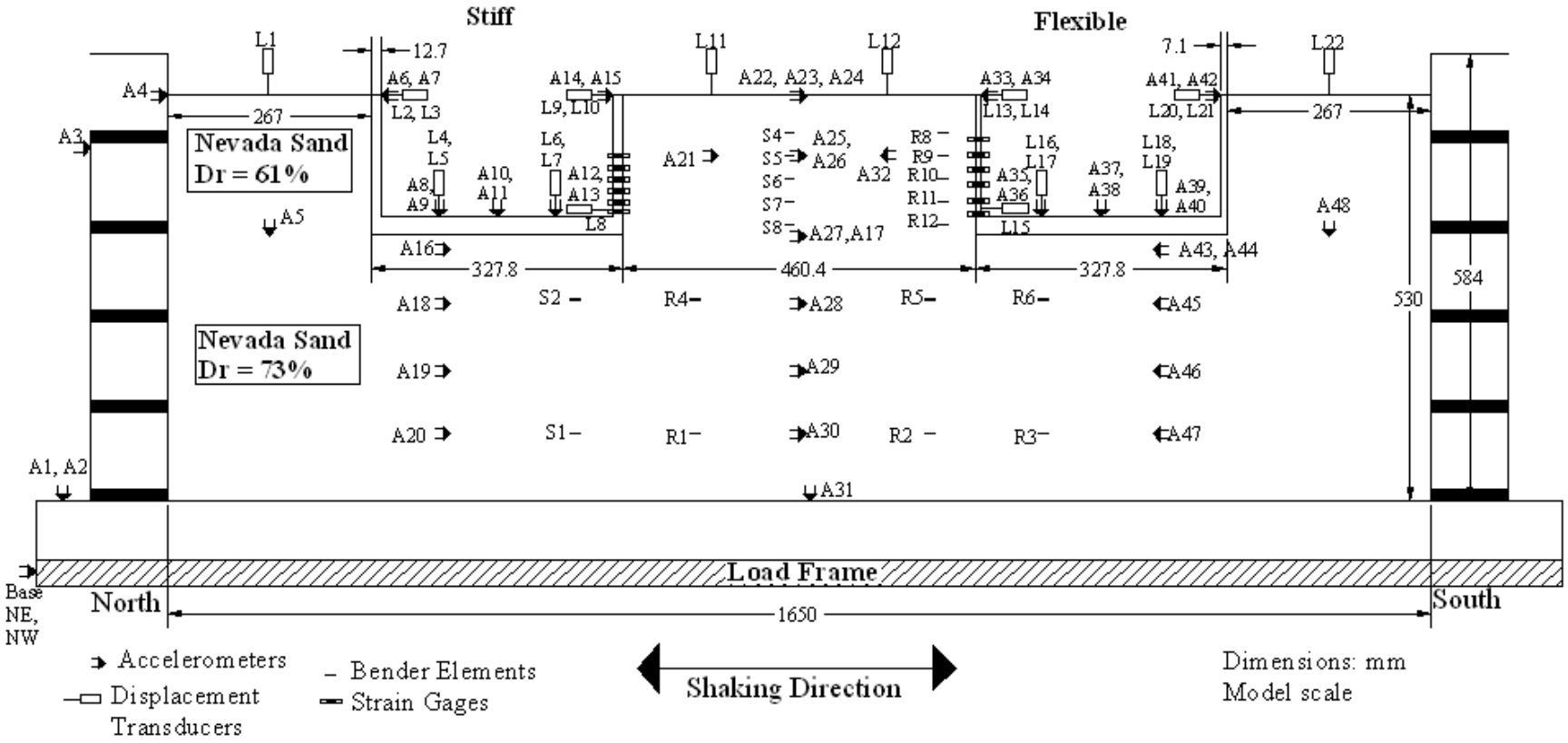

Fig. 3.2 LAA01 model configuration, profile view.

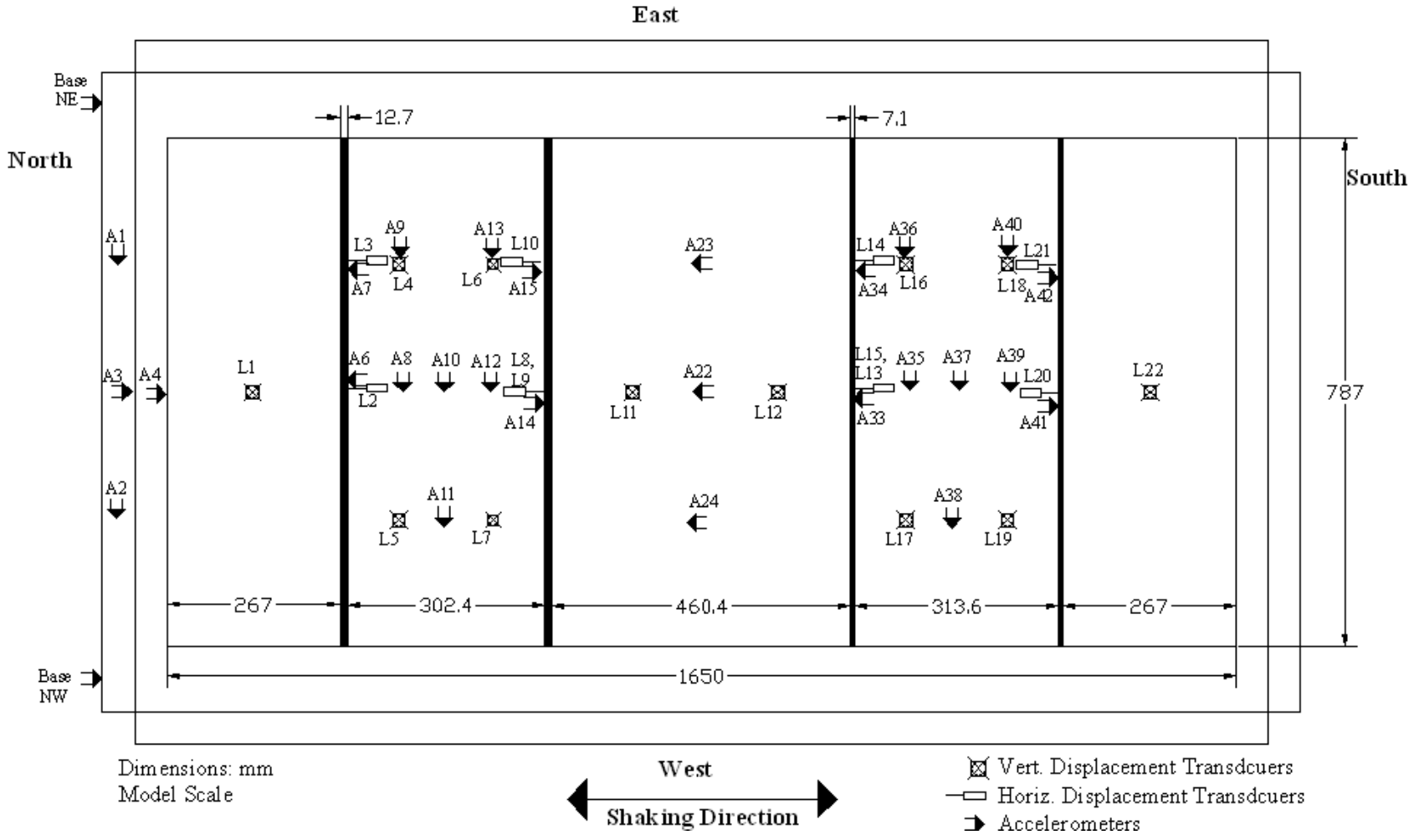

Fig. 3.3 LAA01 model configuration, plan view.

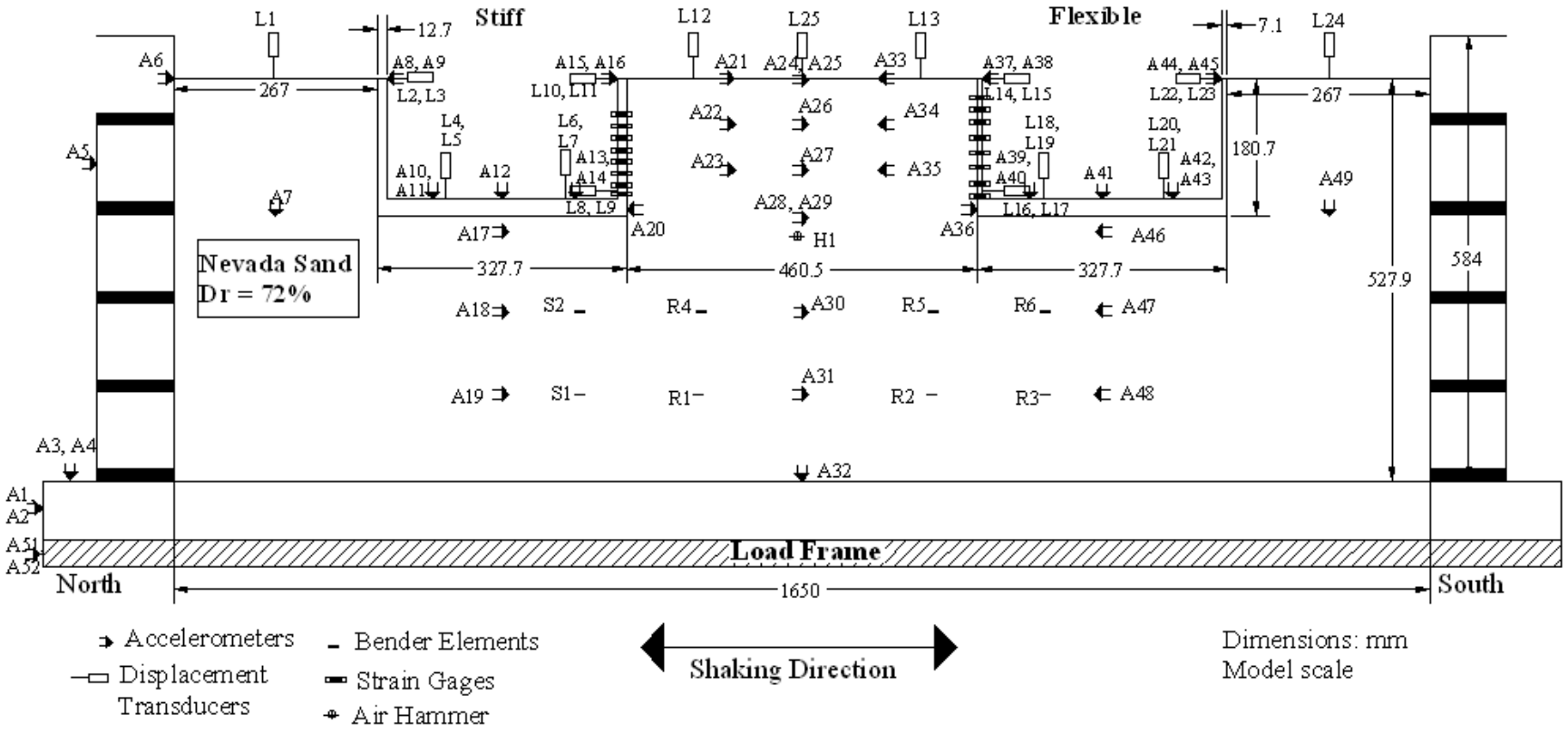

Fig. 3.4 LAA02 model configuration, profile view.

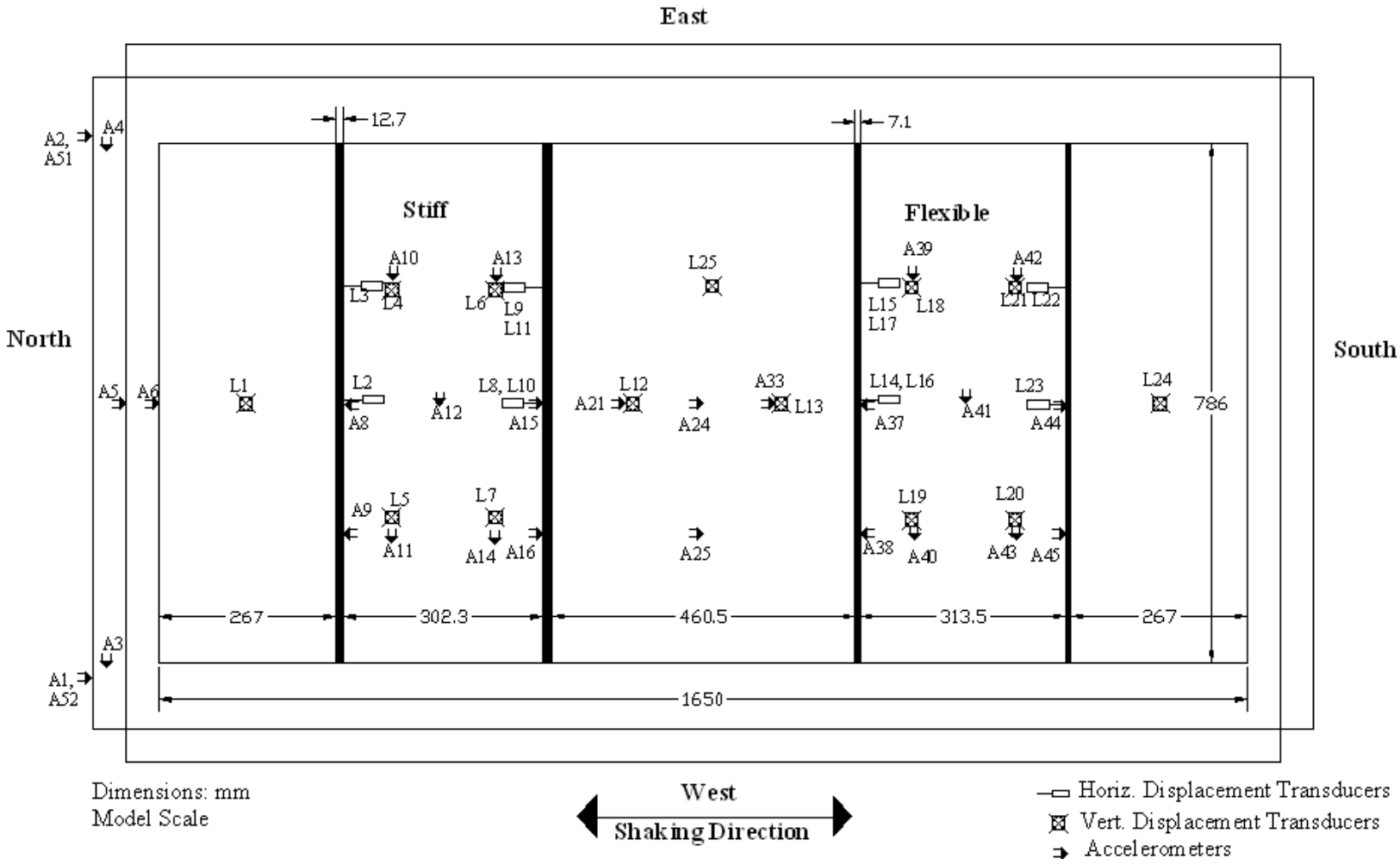

Fig. 3.5 LAA02 model configuration, plan view.

3.4 SOIL PROPERTIES

The sand used in the two centrifuge models was fine uniform angular Nevada sand. It has a mean grain size of 0.14–0.17 mm, a uniformity coefficient of 1.67, a specific gravity of 2.67, and less than 5% fines (Kammerer et al. 2000). Mechanical grain size analyses of Nevada sand are shown in Figure 3.6. Minimum and maximum dry density tests have been performed on several batches of Nevada sand and have been reported in the literature as summarized in Table 3.2. Slight variations in the results can be attributed to the inherent changes in the different sand batches delivered to the CGM facility and to the different testing methods used (ASTM versus Japanese standards). The minimum and maximum dry densities determined at the University of California, Davis, in January 2007 using the Japanese standard methods, yielded 14.50 and 17.49 kN/m3, respectively. These minimum and maximum dry density values were used in this study. The initial friction angle value for the backfill Nevada sand is estimated to be 33° for LAA01 and 35° for LAA02 (Arulmoli et al. 1992).

Table 3.2 Nevada sand properties.

Source	Gs	e_{min}	e_{max}	γ_d,min (KN/m^3)	γ_d,max (KN/m^3)
Arulmoli et al. (1991)	2.67	0.511	0.887	13.87	17.33
Woodward Clyde (1997)	-	-	-	13.97	16.75
Kammerer et al. (2000)	2.67	0.533	0.8875	13.87	17.09
UC Davis - Seiji Kano (2007)	2.65	0.486	0.793	14.50	17.49

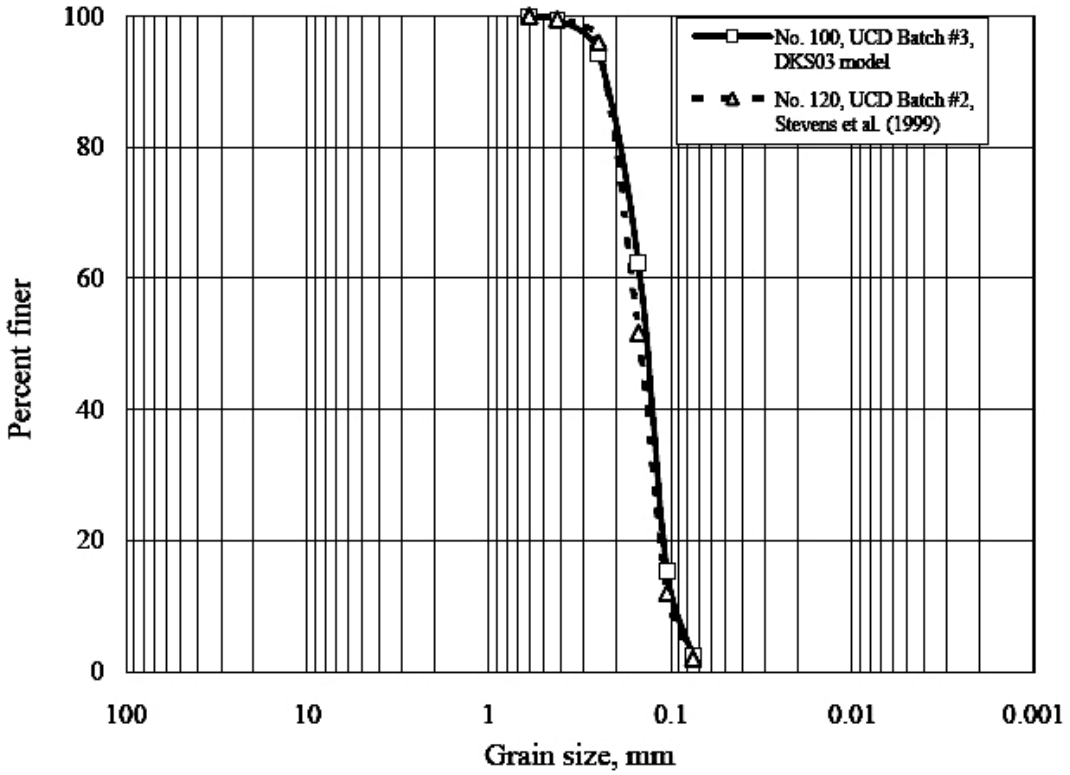

Fig. 3.6 Grain size distribution for Nevada sand (from Stevens 1999).

3.5 STRUCTURES' PROPERTIES

The model stiff and flexible U-shaped cantilever retaining structures were constructed of T6061 aluminum plate. The Young's modulus and Poisson's ratio for this grade of aluminum are 10,000 ksi and 0.32, respectively. Each structure was constructed of three plates in a tunnel-like configuration, a base plate and two wall plates. The walls were bolted to the plates using five force-sensing bolts on the south and north walls of the stiff and flexible structures, respectively, and five regular 5/16-in. aluminum bolts on the rest of the walls. Washers were placed between the bolts and the walls. The stiff and flexible structures spanned the width of the container.

Both stiff and flexible aluminum structures were designed to represent typical reinforced concrete U-shaped cantilever retaining structures. The thickness of the model walls was determined by matching the stiffness of the reinforced concrete prototypes. The stiffness of the reinforced concrete prototypes was calculated using the effective moment of inertia of the

concrete sections rather than the gross moment of inertia ($I_g = \frac{b \cdot h^3}{12}$). The effective moment of inertia takes into account the cracking of the concrete sections. The mass of the reinforced concrete prototypes was also matched by adding small lead pieces to the model structures, without significantly impacting their stiffness. Drawings of the stiff and flexible structures are shown in Figure 3.7 and 3.8, respectively, in model scale. The dimensions of the prototype aluminum structures and their properties are presented in Table 3.3.

Table 3.3 Prototype aluminum structures, dimensions and properties.

	Stiff	**Flexible**
Stem Height (ft)	18.6	18.6
Stem Thickness (ft)	1.5	0.84
Stem Stiffness (lb-in.^{2} per ft width)	5.92E+10	1.04E+10
Base Width (ft)	35.64	36.96
Base Thickness (ft)	2.7	2.7
Base Stiffness (lb-in.^{2} per ft width)	3.45E+11	3.45E+11
Estimated Natural Period (sec)	0.11	0.24

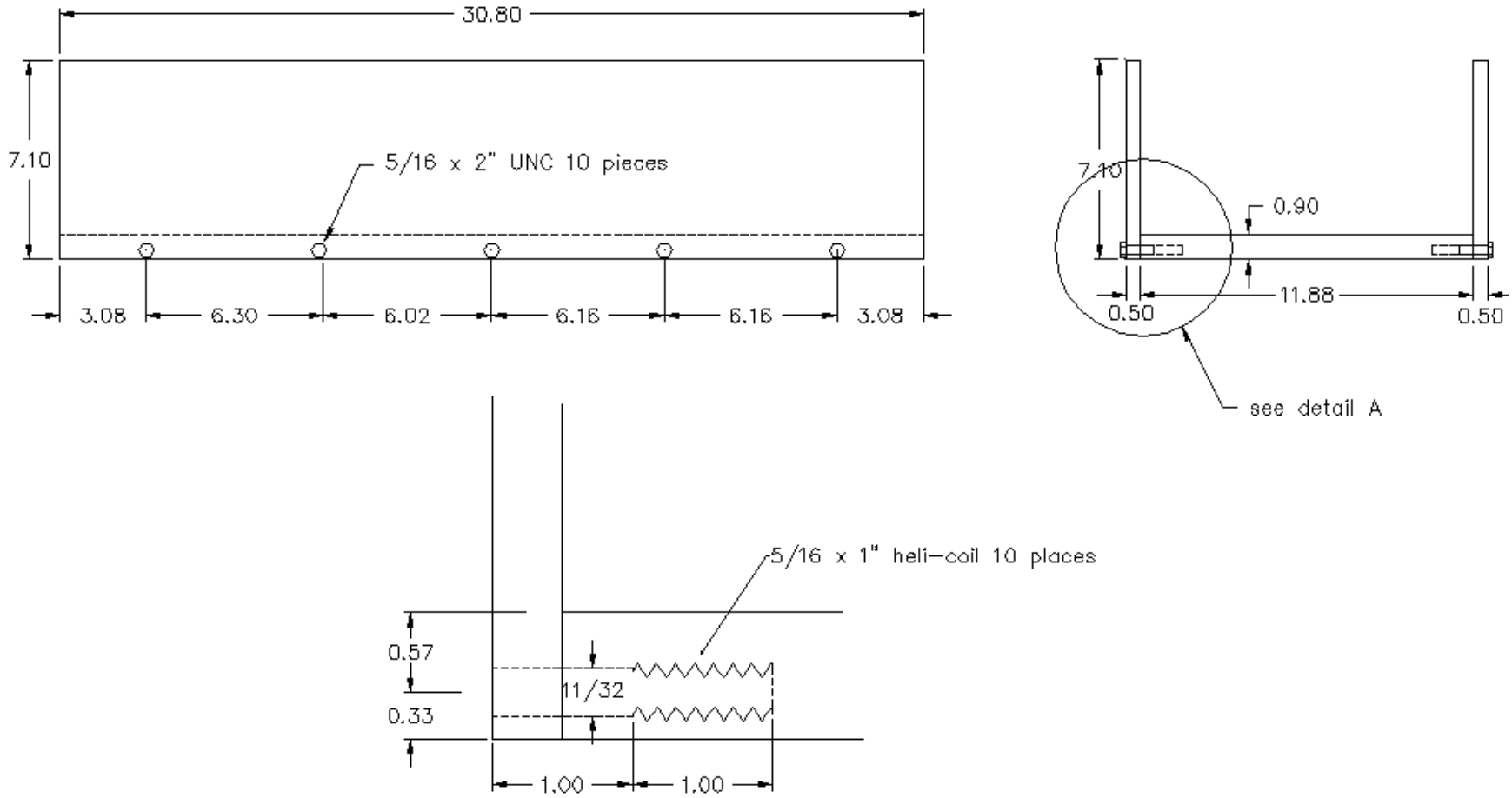

Fig. 3.7 Stiff model structure configuration (in., model scale).

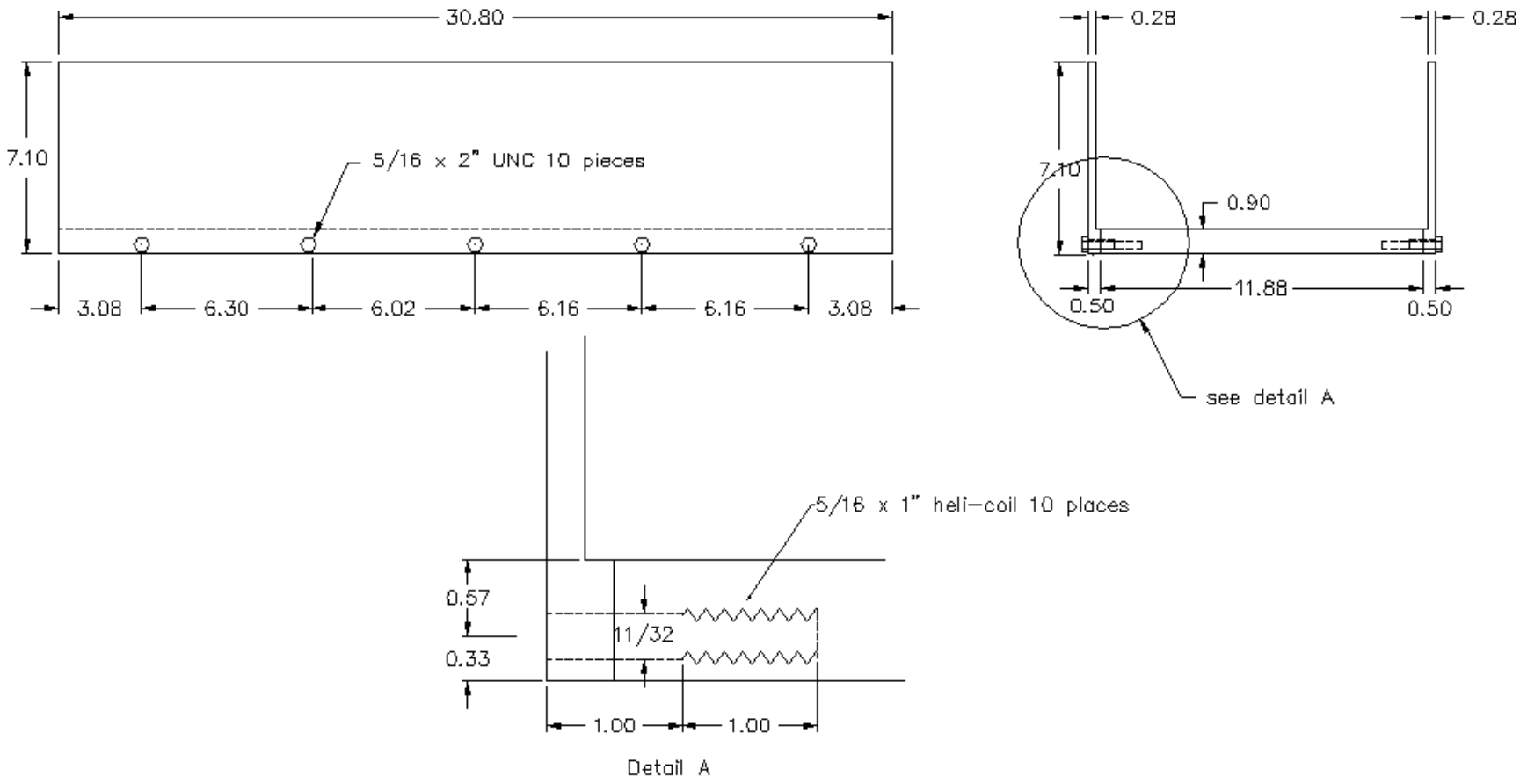

Fig. 3.8 Flexible model structure configuration (in., model scale).

3.6 MODEL CONSTRUCTION

The sand was placed using dry pluviation in different layers underneath and behind the structures. The height of each layer corresponds to a horizontal array of instruments, as shown in Figures 3.2 and 3.4. The soil density was produced by calibrating the drop height, mesh opening, and speed of drop for the pluviator. The optimal settings were determined prior to model construction through several successive pluviation trials using a constant volume container. After placement of each layer, the sand surface was smoothed with a vacuum and instruments were placed at their specific positions.

The sequence of the model construction consisted of first placing the sand underneath the structures in several lifts. The stiff and flexible structures were then placed at their appropriate locations. Finally, the backfill sand was placed behind the walls in several layers. Industrial grease was placed between the structures' walls and the container to provide a frictionless boundary and prevent sand from passing through. Lead was added to the structures in small pieces of 1 in. and 2 in. each in order to match the masses of the reinforced concrete structures. Photographs of the model under construction and on the centrifuge arm are shown in Figures 3.9–3.12.

Fig. 3.9 Pluviation of sand inside model container.

Fig. 3.10 Leveling sand surface with a vacuum.

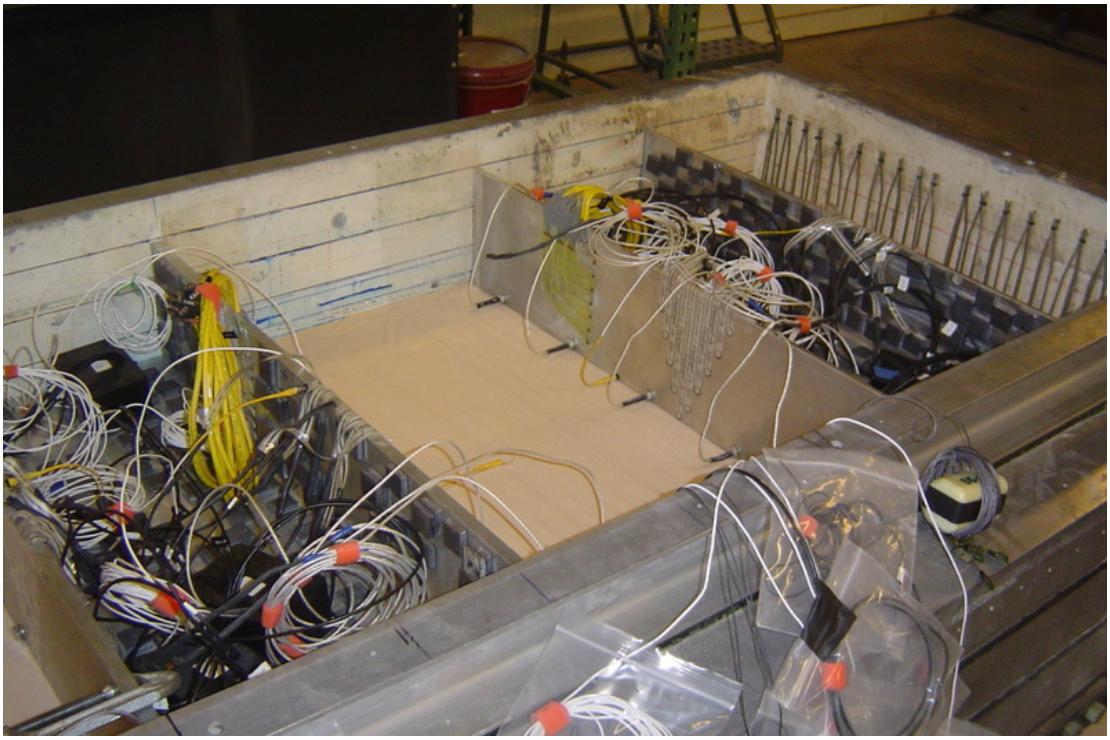

Fig. 3.11 Model under construction.

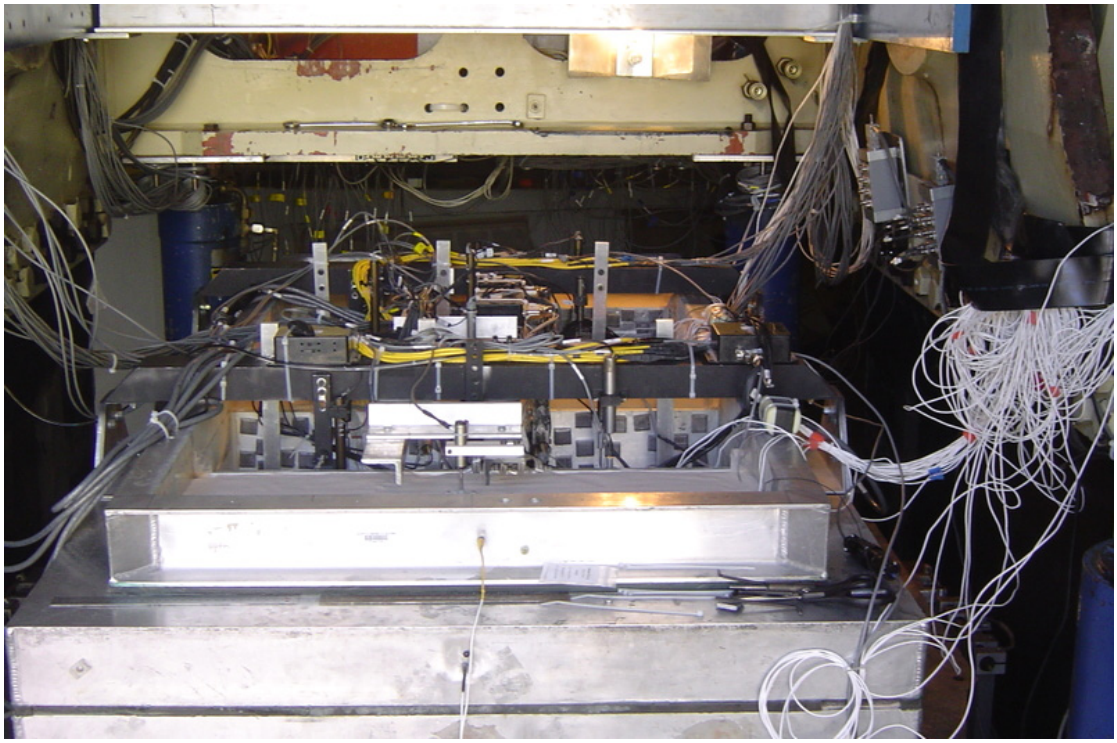

Fig. 3.12 Model on centrifuge arm.

3.7 INSTRUMENTATION AND MEASUREMENTS

The LAA01 and LAA02 models were densely instrumented in order to collect accurate and reliable measurements of accelerations, displacements, shear-wave velocities, strains, bending moments and earth pressures. Horizontal and vertical accelerations in the soil and on the structures were measured using miniature ICP accelerometers manufactured by PCB Piezotronics with 50–100 g maximum outputs and MEMS (Micro-Electro-Mechanical Systems) wireless accelerometers with 100 and 200 g maximum outputs. Soil settlement and the structures' deflections and settlement were measured at different locations using a combination of spring-loaded LVDTs with 1 and 2 in. range, manufactured by Omega Engineering, and Duncan 600 series linear potentiometers with 1, 2, and 4 in. range. Shear-wave velocities in the soil underneath and behind the structures were measured using piezo-ceramic bender elements and mini-shear air hammers. The locations of accelerometers, bender elements, air hammers, and displacement transducers are shown in Figures 3.2–3.5.

Accurate measurement of lateral earth pressure distribution was the major goal of this study. In the past, lateral stress measurements in laboratory experiments were usually made using pressure cells. Unfortunately, such measurements are not considered reliable because cell/soil reaction is a function of the relative stiffness of the cell with respect to the soil and arching effects caused by the disturbance of the stress field by the presence of the cell (Dewoolkar et al. 2001). Therefore, in order to avoid these problems in the experiments performed in this study, three different sets of instruments were used. The lateral earth pressures were directly measured in the two centrifuge experiments using flexible tactile pressure type A201-1 Flexiforce sensors, manufactured by Tekscan. The sensors consist of an ultra-thin (about 0.008 in. thick) and flexible printed circuit with a circular active sensing area of 0.375 in. diameter at the end of the sensor. These sensors can be used to measure static and dynamic forces and are thin enough to enable non-intrusive measurement. As shown in Figure 3.13, the sensing area consists of silver conductive material separated by semi-conductive ink, wherein the resistance is inversely proportional to the applied force. The Flexiforce sensors were spray-glued to the aluminum walls and then connected to the excitation circuit board recommended by Tekscan and assembled at the CGM facility at UC Davis. More specifications and performance characteristics of the Flexiforce sensors can be found in the Flexiforce sensors user manual (Tekscan 2007).

Fig. 3.13 Flexiforce A201-1 sensor.

Lateral earth pressures were also back-calculated based on the bending moments measured by the Wheatstone full bridge strain gages mounted on the model walls. The strain gages used in the experiments were of type J2A-13-S181H-350, manufactured by the Vishay Measurements Group, and directly measure the strain on the walls. Finally, direct measurements of the total bending moments at the bases of the walls were made using 5/16 by 2 in. long aluminum force-sensing bolts at the wall-foundation joints manufactured by Strainsert. The locations of the strain gages, Flexiforce sensors, and force-sensing bolts on the stiff and flexible walls for experiments LAA01 and LAA02 are shown in Figures 3.14–3.22.

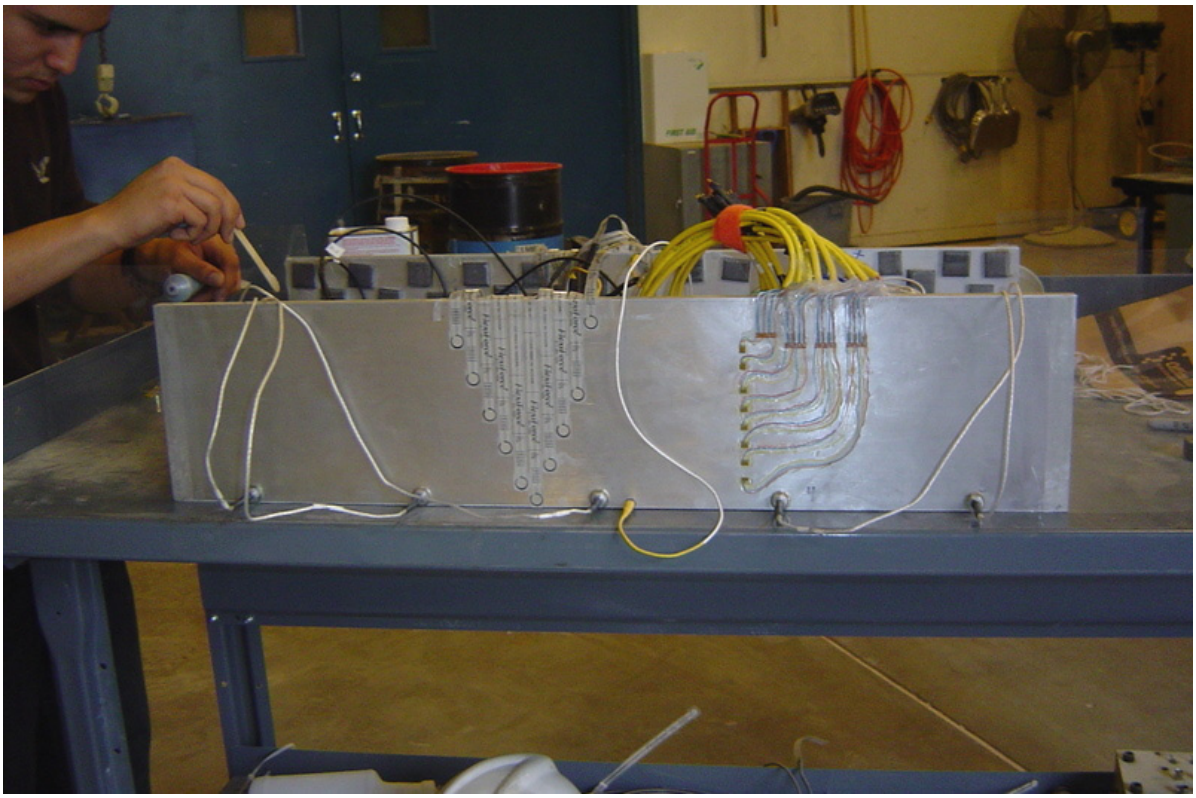

Fig. 3.14 Flexiforce, strain gages, and force-sensing bolts on south stiff wall during LAA02.

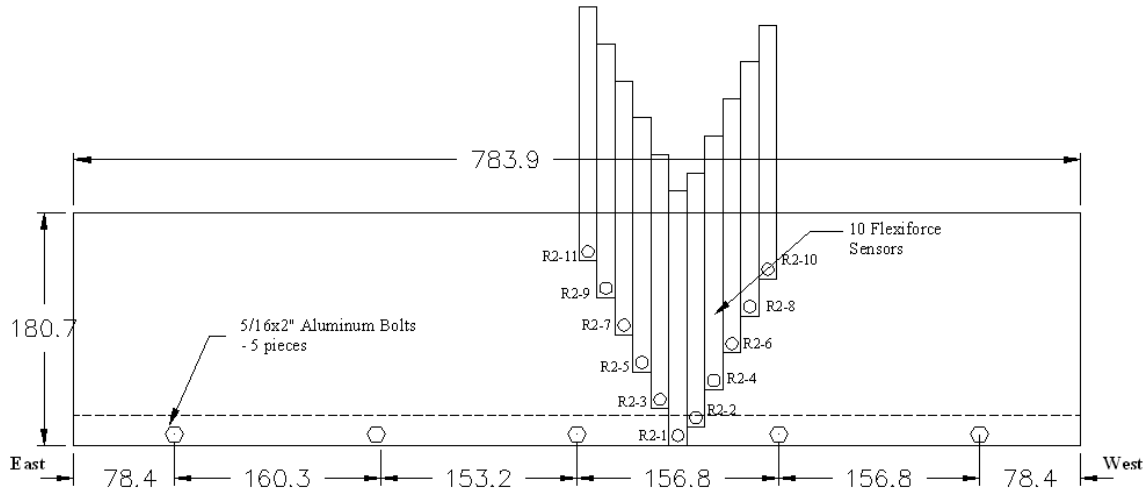

Fig. 3.15 Flexiforce layout on north stiff wall for LAA01 (mm, model scale).

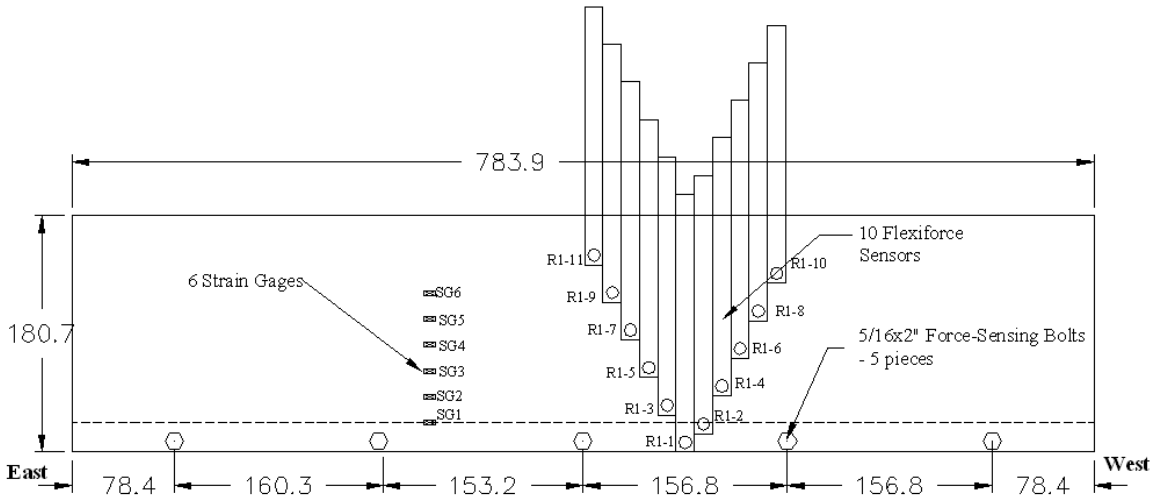

Fig. 3.16 Flexiforce, strain gages, and force-sensing bolts layout on south stiff wall for LAA01 (mm, model scale).

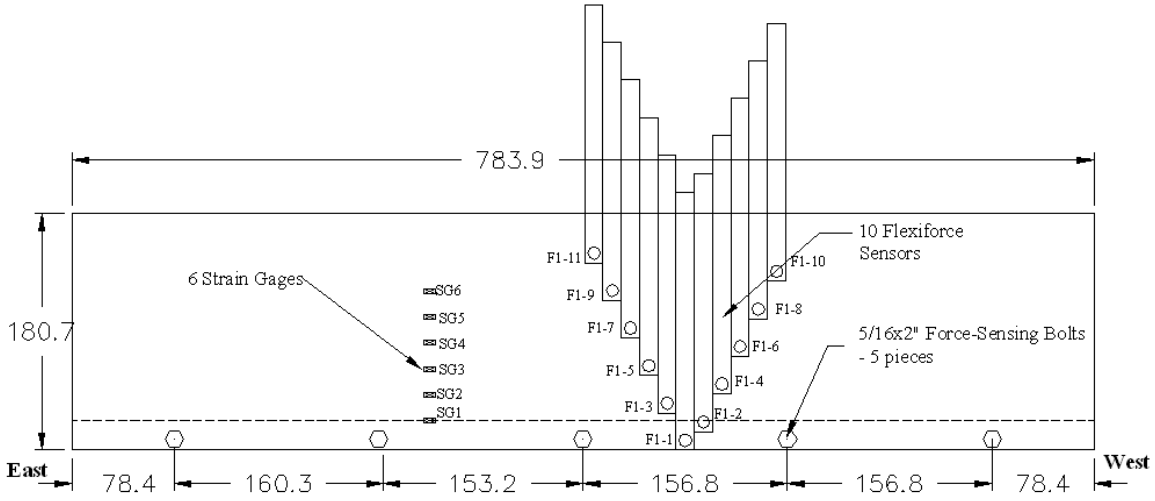

Fig. 3.17 Flexiforce, strain gages, and force-sensing bolts layout on north flexible wall for LAA01 (mm, model scale).

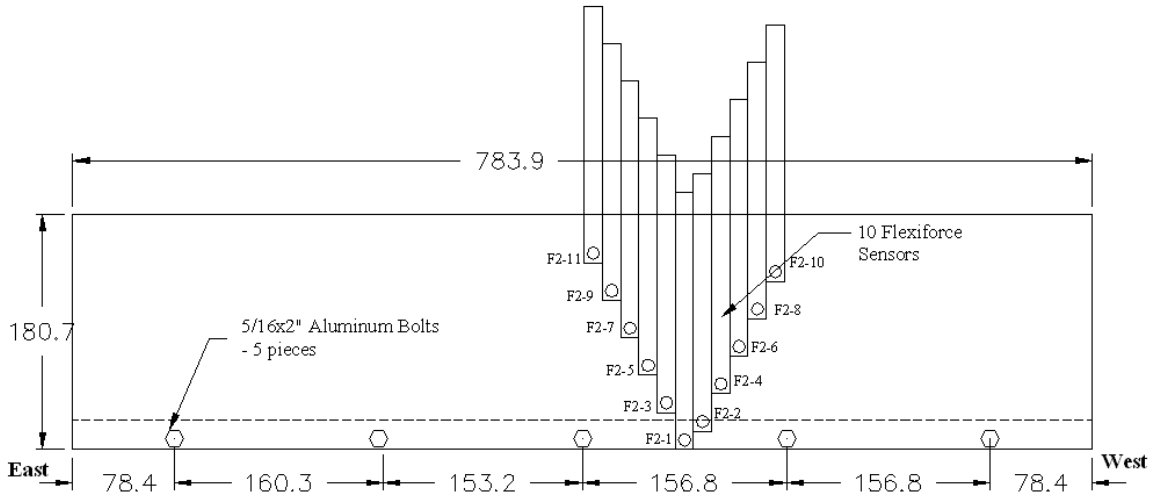

Fig. 3.18 Flexiforce layout on south flexible wall for LAA01 (mm, model scale).

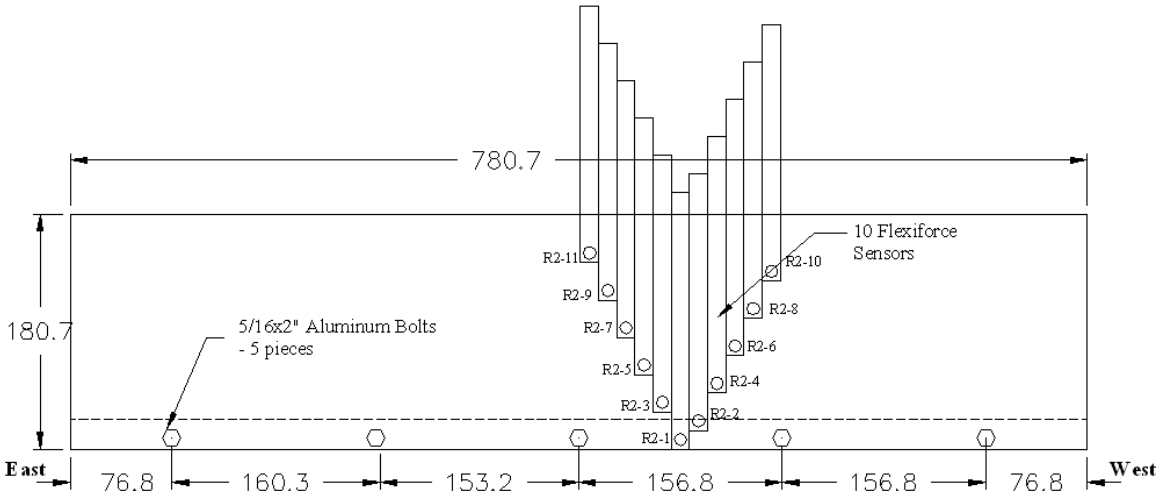

Fig. 3.19 Flexiforce layout on north stiff wall for LAA02 (mm, model scale).

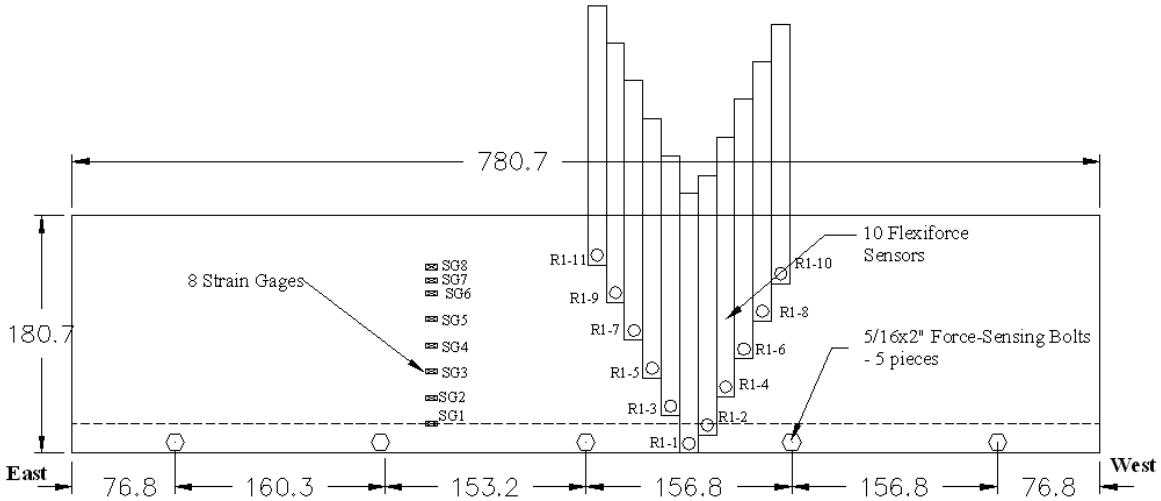

Fig. 3.20 Flexiforce, strain gages, and force-sensing bolts on south stiff wall for LAA02 (mm, model scale).

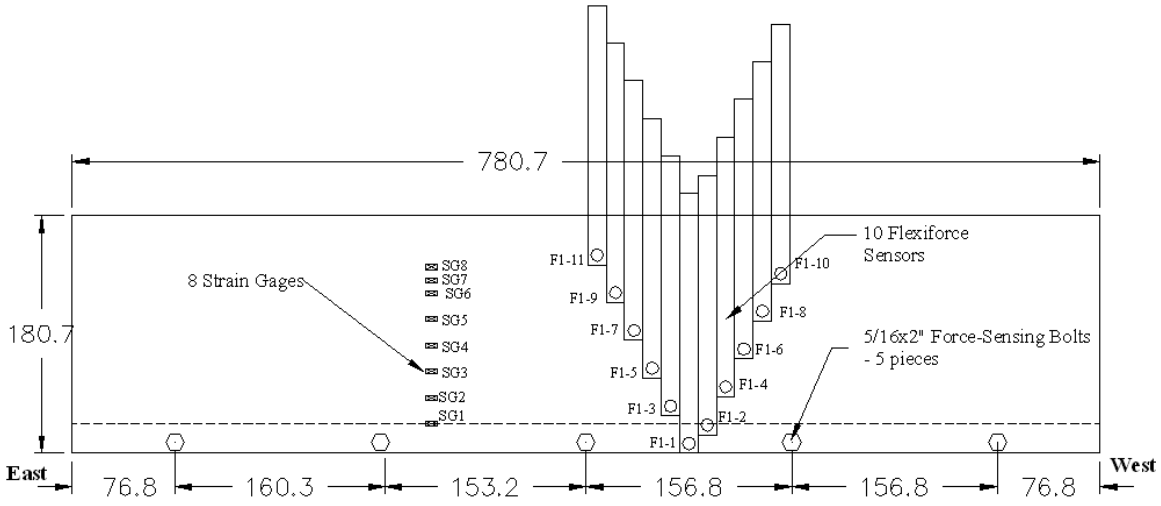

Fig. 3.21 Flexiforce, strain gages, and force-sensing bolts on north flexible wall for LAA02 (mm, model scale).

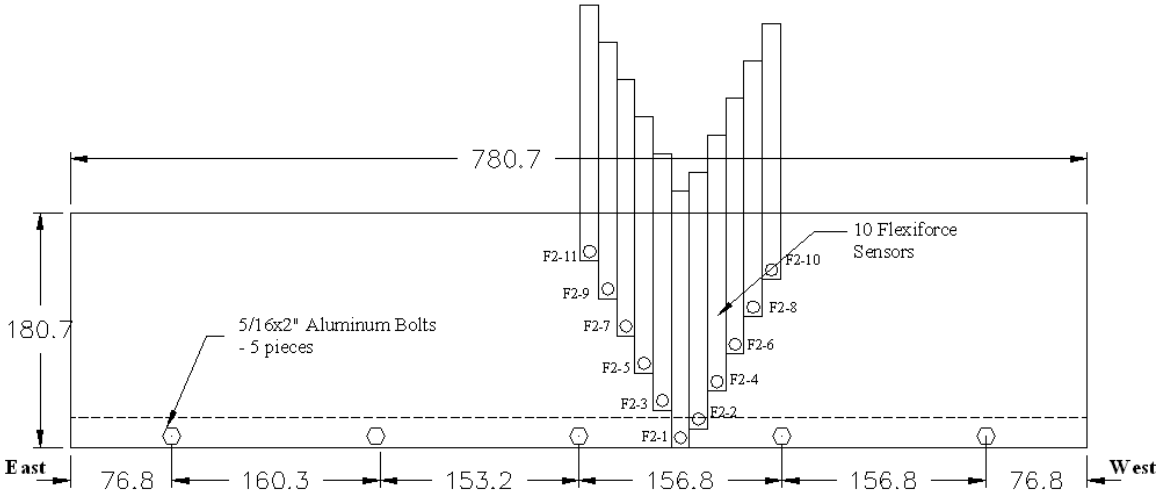

Fig. 3.22 Flexiforce layout on south flexible wall for LAA02 (mm, model scale).

3.8 CALIBRATION

Calibration factors are used to convert the recorded voltage output of the instruments into engineering data units. Linear potentiometers, LVDTs, and strain gages were manually calibrated specifically for these tests and compared to the manufacturer's specifications. The accelerometers were rated using the manufacturer's provided instrument sensitivities. Special

calibration techniques had to be developed for the force-sensing bolts and Flexiforce sensors, used for the first time at the CGM facility at UC Davis. Figure 3.23 shows the calibration of the force-sensing bolts and strain gages. A known uniform load was applied at the top of the wall, the response from the load sensing bolts and strain gages was recorded and calibration factors were obtained.

The Flexiforce sensors, being very sensitive to testing conditions, were calibrated under conditions similar to those expected during the experiment. Four sensors were mounted to the base plate of a small container filled with Nevada sand. A known pressure was applied to the container, and the Flexiforce responses were recorded. Calibration factors were thus obtained for individual sensors.

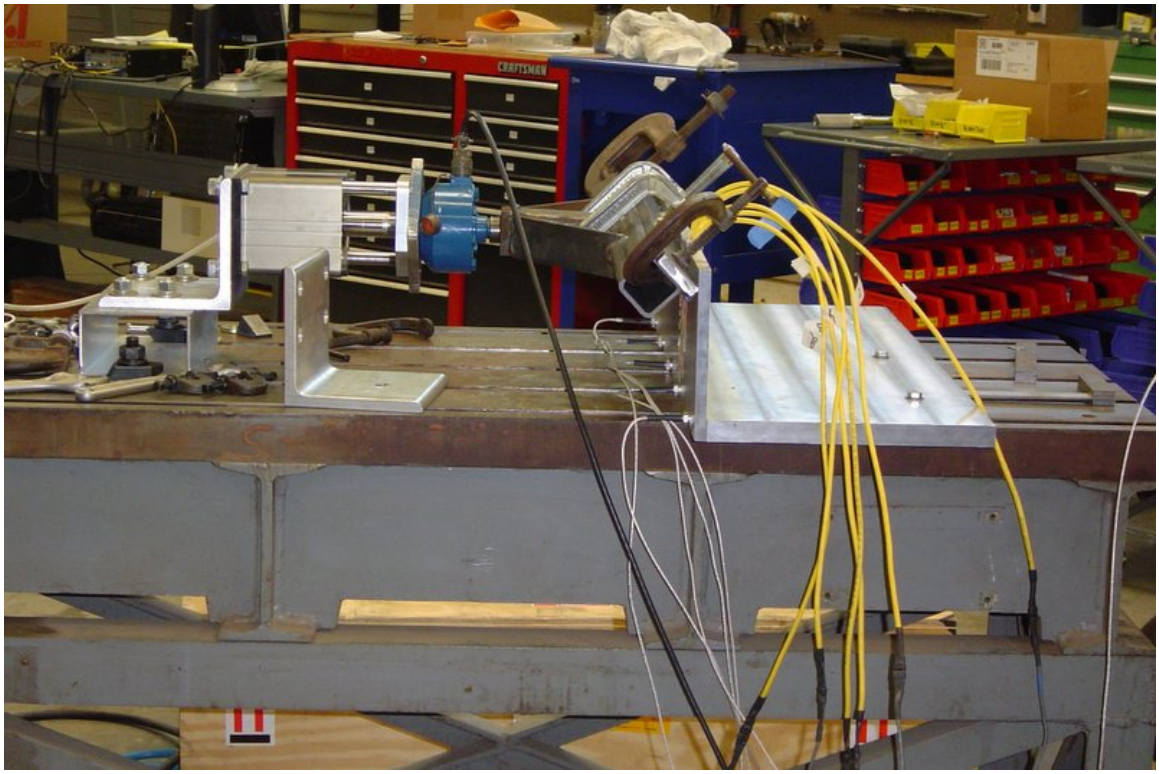

Fig. 3.23 Calibration of force-sensing bolts and strain gages.

3.9 DATA ACQUISITION

The data acquisition infrastructure at the CGM facility consists of several parallel systems that can be operated in combination or independently, and allows researchers to record data during all stages of model construction and testing. ICP accelerometers, displacement transducers, strain gages, force-sensing bolts, and Flexiforce sensors were routed through different amplifiers for signal conditioning to the main data acquisition system (RESDAQ-Main). Appropriate gain levels were set at the different amplifier channels to ensure good signal quality for the various sensors. RESDAQ-Main allows fast data sampling at a model scale rate of 4096 Hz during simulated seismic events. Slow data sampling at a rate of 1 Hz in model scale is used during spin up, spin down and between shaking events. Very fast data sampling at a frequency of 50,000 Hz is used when measuring shear-wave velocities. A wireless sensor manager data acquisition system (WIDAQ) is used to sample data from the MEMS accelerometers at a model scale sampling frequency of 2048 Hz during seismic events. RESDAQ-AUX is used to acquire data from the bender elements for shear-wave-velocity measurements.

The raw data in voltage obtained from the two experiments was converted to prototype scale engineering units by multiplying by the appropriate instrument calibration factors and adjusting for instruments gains. Details of the data acquisition systems are available at the CGM website (http://nees.ucdavis.edu).

3.10 SHAKING EVENTS

Five shaking events were applied to the LAA01 model in flight at 36 g centrifugal acceleration. The shaking was applied parallel to the long sides of the model container and orthogonal to the model structures. The shaking events consisted of a step wave, a ground motion recorded at the Santa Cruz station during the Loma Prieta 1989 earthquake and applied three times to the model, and a ground motion recorded at 83 m depth at Port Island during the 1995 Kobe earthquake. Step waves are usually applied at the beginning of a shaking series in order to test the instruments and the data acquisition system. The shaking events for LAA01 along with their prototype base peak accelerations are shown in Table 3.4.

Table 3.4 Shaking sequence for LAA01.

Shaking Event	Input Peak Acceleration (g)
Step Wave	0.06
Loma Prieta 1	-
Loma Prieta 2	0.43
Kobe	0.90
Loma Prieta 3	0.43

Fifteen shaking events were applied to the LAA02 model in flight at 36 g centrifugal acceleration. The shaking events consisted of step waves, ground motions recorded at the Santa Cruz (SC) station and the Saratoga West Valley College (WVC) stations during the Loma Prieta 1989 earthquake, ground motions recorded at 83 m depth at the Port Island (PI) and Takatori (TAK) stations during the 1995 Kobe earthquake, and ground motions recorded at the Yarmica (YPT) station during the Kocaeli, Turkey, 1999 earthquake.

Since the Kobe-TAK, Loma Prieta-WVC, and Kocaeli-YPT ground motions were used for the first time at the centrifuge facility at UC Davis, these ground motions had to be applied several times in order to scale the centrifuge input record as close as possible to the peak accelerations and frequency contents of the original records. The Kobe-PI ground motion was applied a second time to the model due to a power supply failure. The shaking events for LAA02 along with their prototype base peak accelerations are shown in Table 3.5. Input ground motions for experiments LAA01 and LAA02 should reasonably reproduce the range of frequencies present in the recorded earthquake motions. However, travel limitations of the shaking table limit the low-frequency content of the input motions and, therefore, affect the overall spectra of the motions. This is especially true for the Kobe-TAK, Loma Prieta-WVC, and Kocaeli-YPT shaking events that were applied for the first time at the CGM facility at UC Davis. Comparison examples of four recorded earthquake motions and their response spectra to the corresponding input motions applied to the models are shown in Figures 3.24–3.27.

Table 3.5 Shaking sequence for LAA02.

Shaking Event	Input Peak Acceleration (g)
Step Wave-1	0.05
Loma Prieta-SC-1	0.66
Kobe-PI-1	0.79
Step Wave-2	0.05
Kobe-PI-2	0.80
Loma Prieta-SC-2	0.49
Kocaeli-YPT060-1	0.04
Kocaeli-YPT060-2	0.15
Kocaeli-YPT060-3	0.24
Kocaeli-YPT330-1	0.10
Kocaeli-YPT330-2	0.27
Kobe-TAK090-1	0.74
Kobe-TAK090-2	0.87
Loma Prieta-WVC270-1	0.23
Kocaeli-YPT330-3	0.22

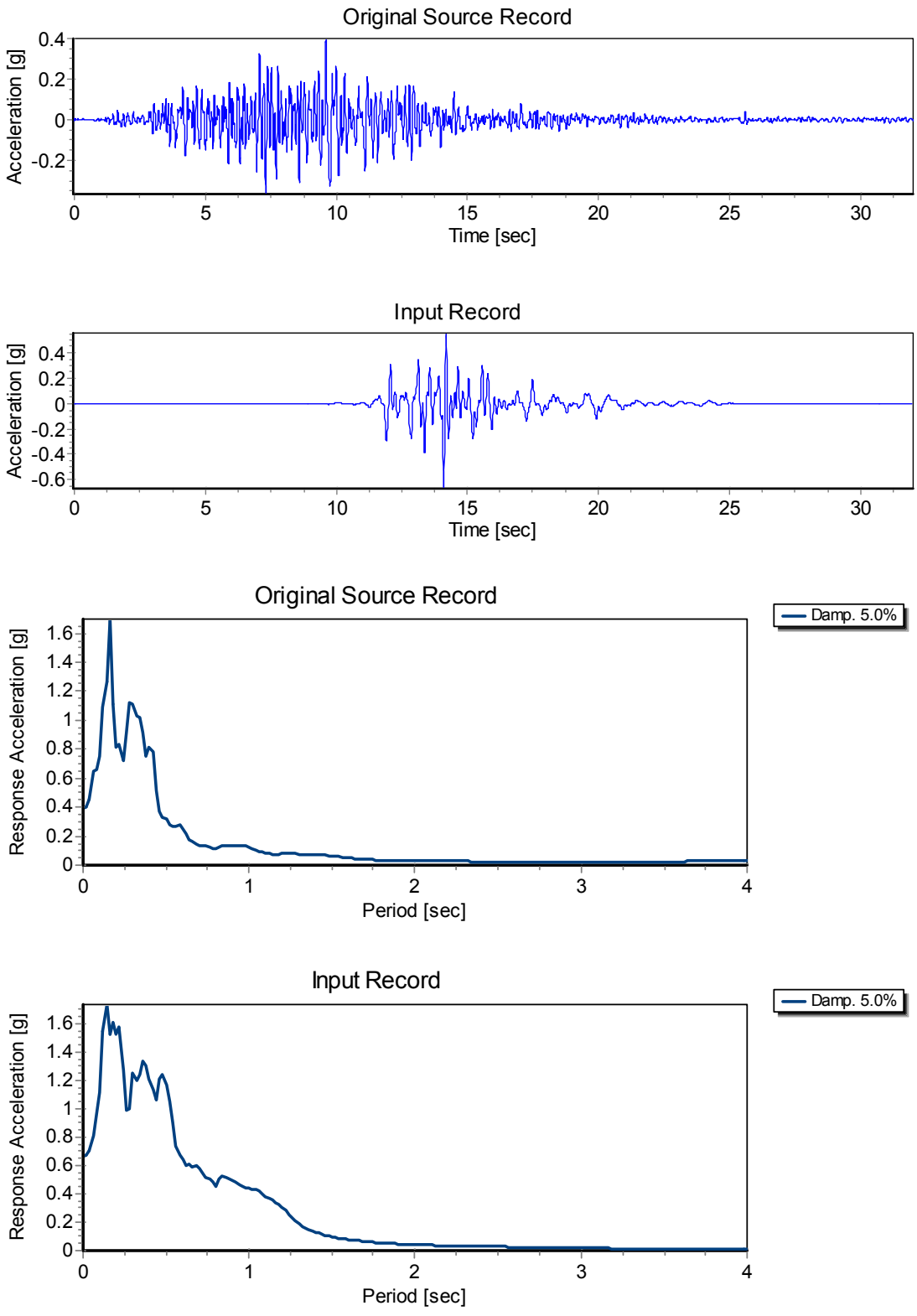

Fig. 3.24 Comparison of original Loma Prieta-SC 090 source record to input Loma Prieta-SC-1, LAA02 record and response spectra.

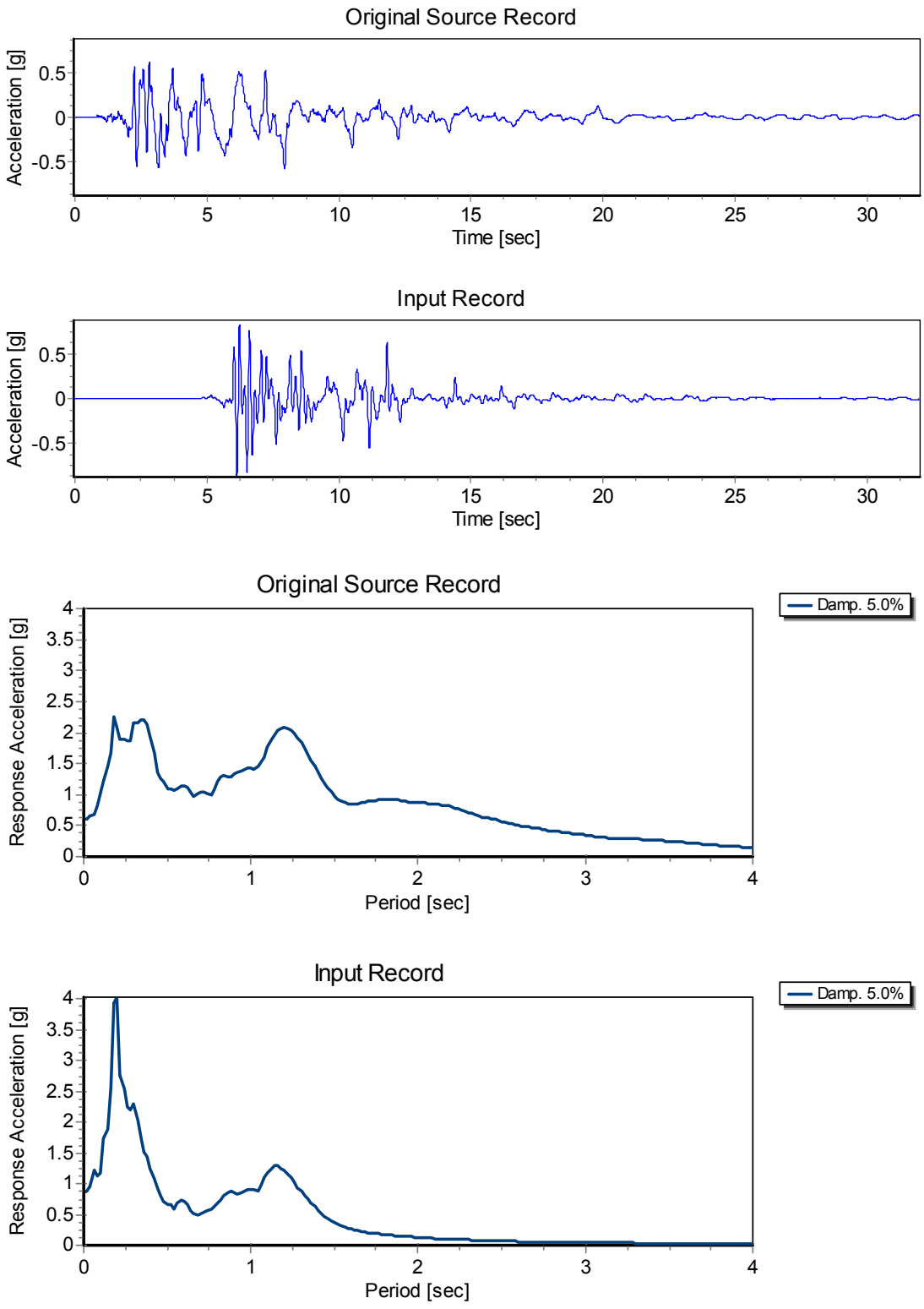

Fig. 3.25 Comparison of original Kobe-TAK090 source record to input Kobe-TAK090-2, LAA02 record and response spectra.

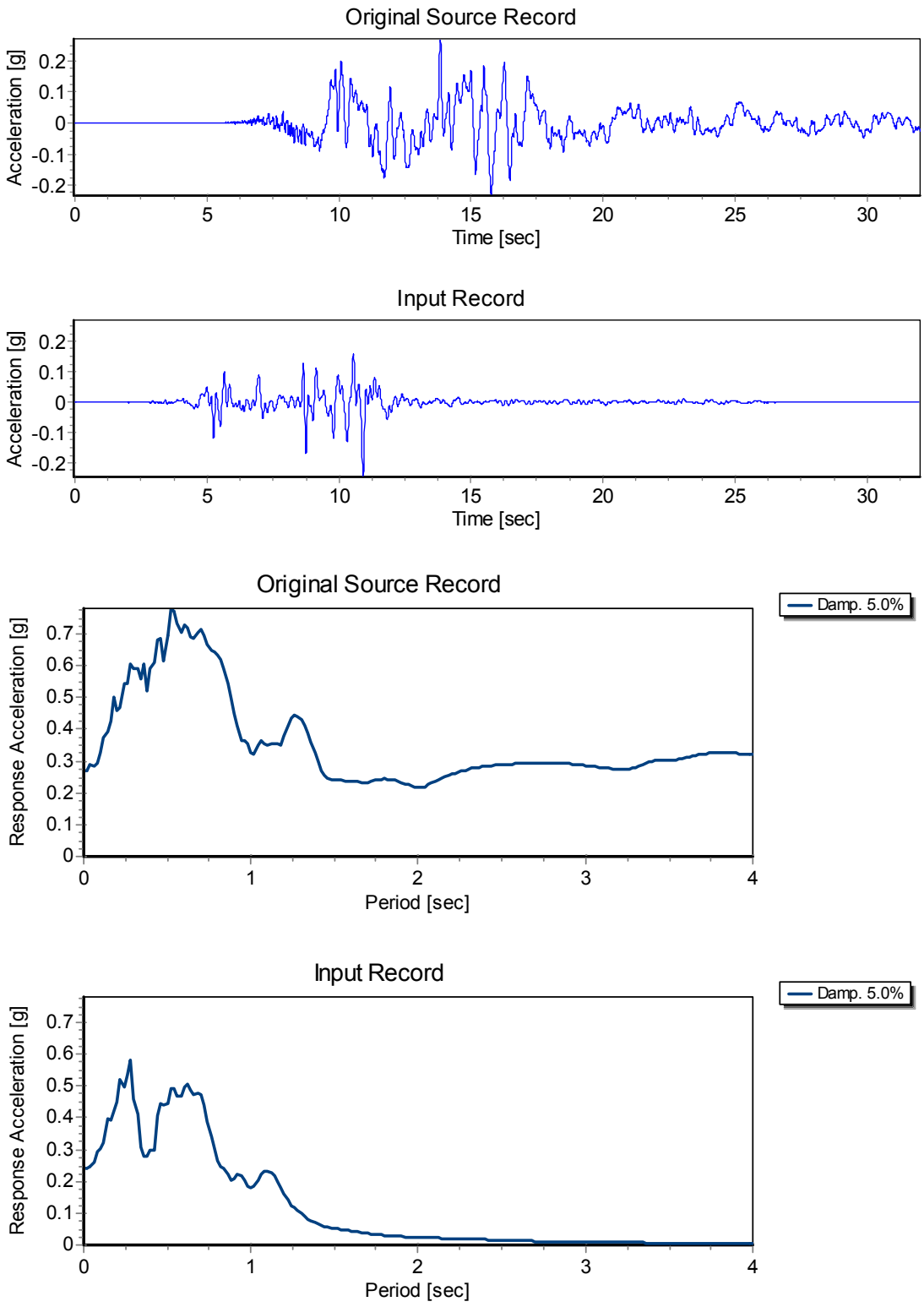

Fig. 3.26 Comparison of original Kocaeli-YPT060 source record to input Kocaeli-YPT060-3, LAA02 record and response spectra.

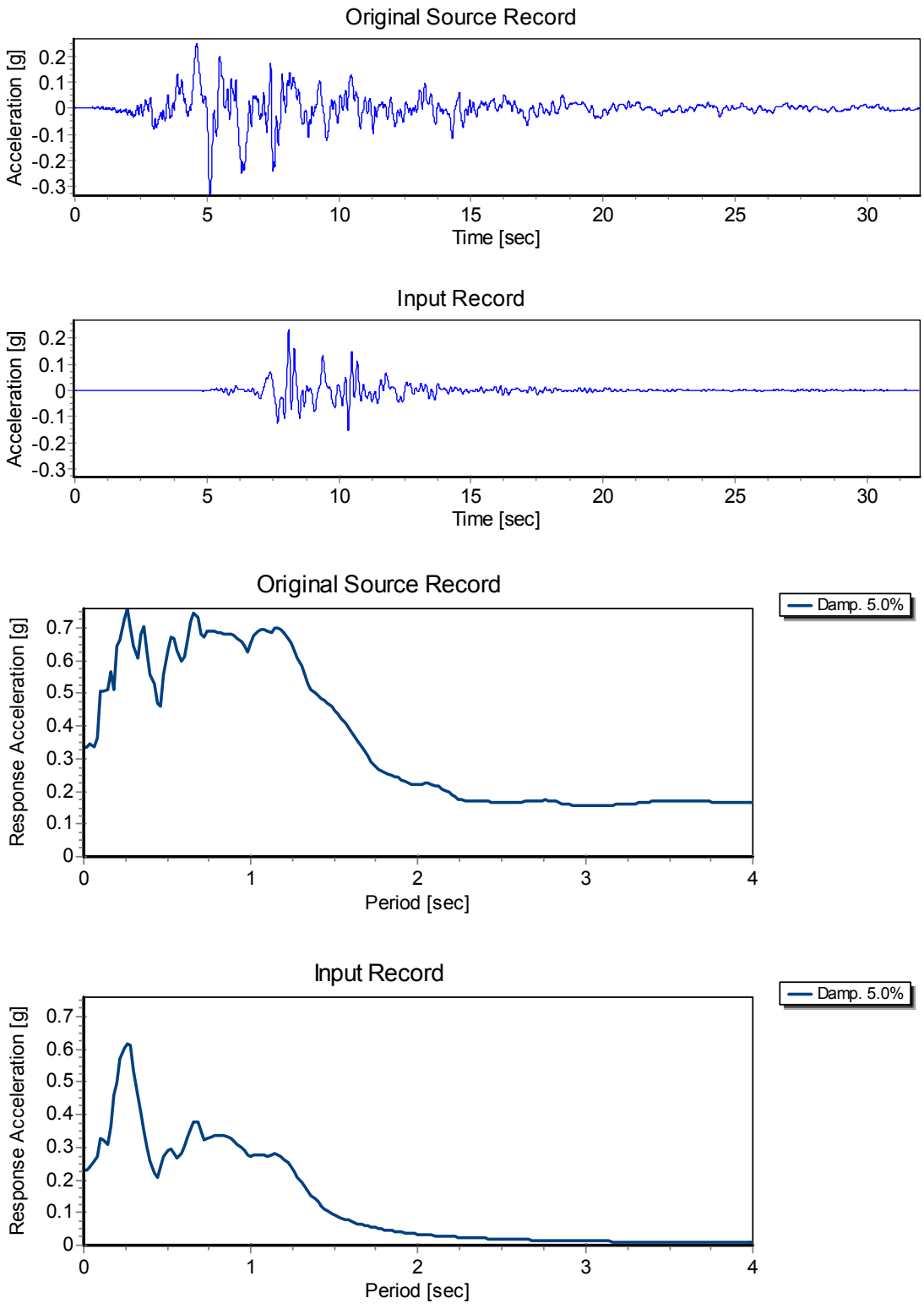

Fig. 3.27 Comparison of original Loma Prieta-WVC 270 source record to input Loma Prieta-WVC270-1, LAA02 record and response spectra.

3.11 KNOWN LIMITATIONS AND PROBLEMS

3.11.1 Overview

The main problems and limitations encountered during centrifuge experiment LAA01 are the following:

- During the first Loma Prieta shaking event, wired accelerometers were not set at the appropriate gain, and accelerations were recorded only by wireless accelerometers for this event. As a result of this problem, the Loma Prieta shaking event was applied a second time to the model.
- Accelerometer A12 failed during the experiment.
- SG1 on the flexible wall failed during the experiment.
- One force-sensing bolt on the north flexible wall failed at the beginning of the experiment. The moment carried by this bolt was estimated based on observations of the load distribution at the base of this wall using the calibration data.
- Data obtained from the bender elements located behind the retaining wall structures were very noisy, and shear-wave velocities of the backfill soil could not be interpreted for LAA01.

The main problems and limitations encountered during centrifuge experiment LAA02 are the following:

- A power supply failure was encountered during Kobe-PI-1 and as a result, the corresponding displacement, strain gage, and force-sensing bolt time series were very noisy. The Kobe-PI event preceded by a step wave was applied a second time to the model.
- Since the Kobe-TAK, Loma Prieta-WVC, and Kocaeli-YPT ground motions were used for the first time at the CGM facility at UC Davis, the original records had to be filtered before being applied to the shaking table. Unfortunately, the filtered input motions generally had significantly different peak accelerations and frequency contents than the source motions.
- Accelerometers A28 and A31 failed during the experiment.
- SG8 on the stiff wall and SG6 and SG2 on the flexible wall failed during the experiment.
- A data acquisition problem was encountered on one force-sensing bolt channel on the north flexible wall during the Step Wave-1, Loma Prieta-SC-1, and Kobe-PI-1 shaking

events. The moment carried by this bolt during these shaking events was estimated based on the calibration data.

- One force-sensing bolt on the south stiff wall gave noisy moment time series during all events. The moment carried by this bolt was estimated based on the calibration data.
- Bender elements data were not collected after Loma Prieta-SC-1, Kobe-PI-1, and Step Wave-2 due to technical problems.
- Air hammer data were not collected before Step Wave-1 and after Kobe-PI-1, Step Wave-2, Loma Prieta-SC-2, and Kocaeli-YPT330-2 due to technical problems.

During both centrifuge experiments, the dynamic displacements of the structures and the soil could not be measured accurately by the displacement transducers due to excessive vibration of the displacement transducers rack during dynamic shaking. Data recorded by the displacement transducers were mainly used to obtain the net soil settlement and wall movements after shaking. The dynamic displacements were interpreted by double integrating the acceleration time series.

3.11.2 Flexiforce Sensor Performance

Based on Tekscan (2005), the Flexiforce sensors are sensitive to loading conditions and their general performance characteristics are presented in Table 3.6. The sensors are sensitive to increases in temperature combined with high loads and are susceptible to linearity, repeatability, hysteresis, and drift errors. Exercising or conditioning the sensors before calibration and testing is highly recommended by Tekscan in order to achieve accurate results and lessen the effects of drift and hysteresis. During both centrifuge experiments LAA01 and LAA02, the Flexiforce sensors experienced static drift, and the original calibration factors developed for these sensors during LAA01 could not be applied to the results due to insufficient sensor conditioning. In order to interpret the Flexiforce voltage records, the static earth pressures recorded before each shaking event were matched to the corresponding static earth pressures interpreted from the strain gages for both experiments. New calibration factors were back-calculated for LAA01 based on the static pressures interpreted from strain gage readings. These new calibration factors were applied to interpret the total dynamic earth pressures recorded by the Flexiforce sensors for LAA01.

While the Flexiforce sensors used in experiment LAA02 were carefully conditioned and calibrated to lessen performance errors, testing did not happen immediately after conditioning and calibration, as recommended by Tekscan (2005), due to technical problems. Rather, it took

place more than a week after sensors calibration and conditioning, and sensor performance was possibly affected. While static drift experienced by the sensors was corrected for as mentioned previously, the performance of the Flexiforce sensors in experiment LAA02 was investigated by comparing their recorded static earth pressures profiles after shaking to the ones interpreted from the strain gage data. Figure 3.28 presents a comparison of the static earth pressures recorded by the Flexiforce sensors and interpreted from the strain gage measurement after the Kobe-PI-2 and Kocaeli-YPT060-2 shaking events. Static earth pressure comparison figures done after the rest of the shaking events of experiment LAA02 are presented in Figures A1–A5.

Table 3.6 Flexiforce sensor performance characteristics (source: Tekscan 2005).

Sensor Properties	Model A201
Operating Range	15°F (-9°C) to 140°F (60°C)
Linearity (Error)	<+/- 5%
Repeatability	<+/- 2.5% of full scale (conditioned sensor, 80% force applied)
Hysteresis	<4.5% of full scale (conditioned sensor, 80% force applied)
Drift	<3% per logarithmic time scale (constant load of 90% sensor rating)
Temperature Sensitivity	Output variance up to 0.2% per degree F (approximately 0.36% per degree C). For loads>10 lbs., operating temperature can be increased to 165°F (74°C)

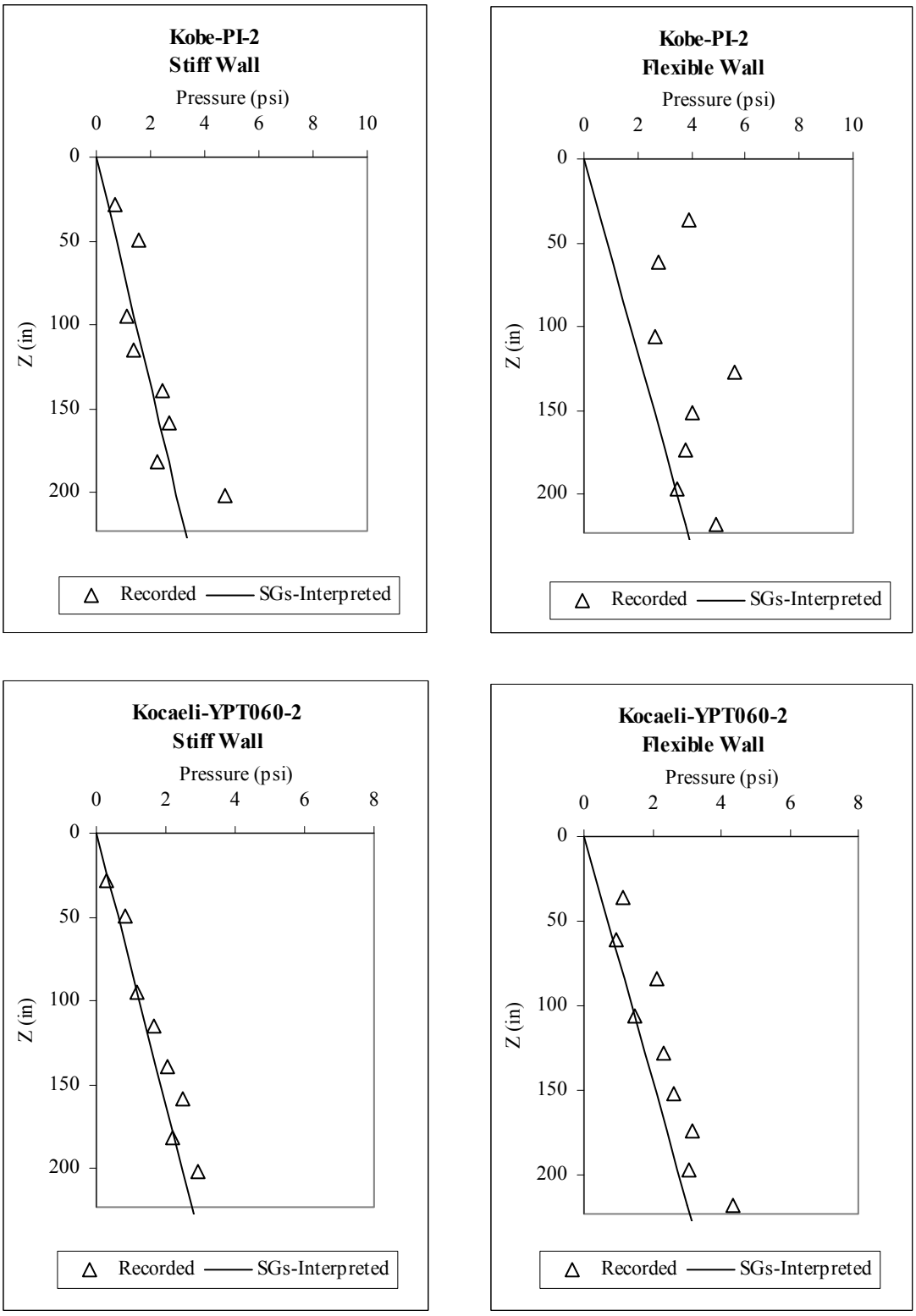

Fig. 3.28 Comparison of static earth pressure profiles recorded by Flexiforce sensors and interpreted from strain gage measurements on south stiff and north flexible walls after Kobe-PI-2 and Kocaeli-YPT060-2.

Figures 3.28 and A.1–A.5 show that static earth pressure profiles measured by the Flexiforce sensors and interpreted from the strain gage data are generally in agreement on the stiff wall after most of the shaking events. Differences are observed for some shaking events, especially Kobe, on the flexible wall. The procedure presented in this section helped finding and eliminating the individual sensors that consistently showed disagreement with the static earth pressures after shaking interpreted from the strain gage data. Overall, the performance of the Flexiforce sensors is considered acceptable though not highly accurate.

4 Experimental Results

4.1 DATA REDUCTION METHODOLOGY

The initial step in processing the instrument data recorded using the high-speed data acquisition system involved filtering to reduce noise and conversion to engineering units. The data were then further processed to interpret various responses of interest. This section describes the methodology used in analyzing the recorded data and in interpreting the different wall and soil backfill responses.

4.1.1 Acceleration

Acceleration time series were collected during both series of centrifuge experiments at the accelerometer locations shown in Figures 3.2–3.3 and Figures 3.4–3.5 for LAA01 and LAA02, respectively. All recorded acceleration time series were corrected such that horizontal accelerations are positive toward the north end of the model container and vertical accelerations are positive upward regardless of the orientation of the instruments themselves. Acceleration time series were filtered using a third-order Butterworth low-pass filter with prototype scale corner frequency of 25 Hz for noise reduction, as well as a third-order Butterworth high-pass filter with a prototype scale corner frequency of 0.3 Hz to remove the long-period drift that would appear in the records after integration to velocity and again to displacement. The disadvantage of such filtering is that any apparent permanent offset of the instrument is also removed. Acceleration time series recorded at the northeast and northwest ends of the load frame were averaged to obtain the input ground motion.

4.1.2 Displacement

Displacement time series measured by the linear potentiometers and the LVDTs were zeroed before shaking by removing the average of the first 50 data points from the records. They were also filtered with a first-order Butterworth low pass filter with a prototype scale corner frequency of 10 Hz for noise reduction.

4.1.3 Shear-Wave Velocity

Bender element arrays were used to measure shear-wave velocities in experiment LAA01 after each shaking event in the soil behind and underneath the retaining structures at the locations shown in Figure 3.2. Measured peak arrival times at the receiver bender elements were used to calculate shear-wave velocity. In experiment LAA02, shear-wave velocities in the soil underneath the retaining structures were measured using bender elements. Shear-wave velocities in the backfill soil were determined using a mini air hammer as a wave source and a vertical array of accelerometers as detectors, as shown in Figure 3.5. Signals detected at accelerometers A24, A26, and A27 were sampled at a model scale sampling frequency of 50,000 Hz. Shear-wave velocity was computed based on the peak arrivals in the time domain.

4.1.4 Bending Moment

Force-sensing bolts and strain gages were used in both series of centrifuge experiments to measure the moments on the south stiff and north flexible walls. Data recorded by the force-sensing bolts located at the wall-base connection of each wall were summed and converted into moments using calibration factors derived from direct load tests (see Section 3.8). These moment time series were filtered using a third-order low-pass Butterworth filter with a prototype scale corner frequency of 25 Hz for noise reduction. Data recorded by the strain gages on the walls were converted into strains using the strain gage calibration factors. Strain time series at each strain gage location were converted into stress and then into moment time series using the elastic bending theory for beams. The strain time series were filtered using a first-order low-pass Butterworth filter with a prototype scale corner frequency of 25 Hz for noise reduction.

The moments recorded by the force-sensing bolts and interpreted from strain gage measurements include contributions from static earth pressures, dynamic earth pressures, and

wall inertial moments. In order to evaluate the contribution of these different components to the moment, the following terminology is adapted throughout this report:

- Total wall moment refers to moment on the wall due to static earth pressure, the dynamic earth pressure increment, and wall inertial force;
- Total earth pressure moment refers to the moment due to static earth pressure and the dynamic earth pressure increment;
- Dynamic wall moment refers to moment due to the dynamic earth pressure increment and wall inertial force; and
- Dynamic earth pressure moment refers to moment due to dynamic earth pressure increment.

The dynamic wall moments (due to dynamic earth pressure increment and wall inertia) were interpreted by applying a moving average filter to the total wall moment time series. The moving average filter determines the static trend for each moment time series; deducing this trend from the corresponding total wall moment time series results in a dynamic wall moment time series.

Five force-sensing bolts and six strain gages were used to instrument the south stiff and north flexible walls in experiment LAA01, as shown in Figures 3.16 and 3.17, respectively. The total wall moment distributions along the height of the walls were interpreted from the strain gage measurements. For the stiff wall, six total dynamic wall moment profiles were computed for each shaking event; each moment profile corresponding to the time at which the maximum moment occurred at one of the strain gage locations and plotting the moments recorded at the other strain gages at the same time. For the flexible wall, applying the same procedure, five moment profiles were plotted for each shaking event instead of six, since the strain gage SG1 was damaged. The moment profiles for the same shaking event on each wall were very similar, with the envelope consistently occurring at the time the maximum moment was recorded at SG1 for the stiff wall and SG2 for the flexible walls. Therefore, all maximum total wall moment profiles and all maximum dynamic wall moment profiles for experiment LAA01 presented in this chapter correspond to the times at which the maximum moments occurred at SG1 and SG2 for the stiff and the flexible walls, respectively.

In experiment LAA02, the south stiff and north flexible walls were instrumented with five force-sensing bolts and eight strain gages each, as shown in Figures 3.20 and 3.21, respectively. The same procedure outlined above for experiment LAA01 was used to obtain the

maximum total wall moment and dynamic wall moment profiles. Therefore, all maximum total wall moment profiles and all maximum dynamic wall moment profiles for LAA02 correspond to the times at which the maximum moments occurred at SG1 for the stiff and flexible walls, respectively. The moment time series obtained during the Kocaeli-YPT060-1 and Kocaeli-YPT330-1 of centrifuge experiment LAA02 are not presented in this chapter due to the insignificant magnitude of shaking. It should also be noted that the moment time series obtained from SG1 on the stiff wall during LAA02 were consistently less than those obtained from other strain gages on the same wall, which suggests that SG1 results might not be accurate.

4.1.5 Wall Inertia

Strain gages and force-sensing bolts used in both series of centrifuge experiments recorded total wall moments resulting from wall inertia and earth pressures acting on the walls. The Flexiforce sensors measured only total earth pressures. In centrifuge experiment LAA02, accelerometers were placed at the top and the bases of the south stiff and north flexible walls. Records obtained from these accelerometers were used to estimate wall inertial forces and moments.

The inertial force at each time instant t and at any location on the wall can be estimated by:

$$f_I(z,t) = -m(z) \cdot A^t(z,t) \tag{4.1}$$

where z = depth from the top of the wall, z = L corresponds to the base of the wall,

$f_I(z, t)$ = inertial force at instant t and location z on the wall,

$m(z)$ = mass of the wall per unit height,

$A^t(z, t)$ = total acceleration at depth z and time t on the wall.

The total acceleration at any point on the wall can be estimated by:

$$A^t(z,t) = \psi(z) \cdot [A_{top}(t) - A_{base}(t)] + A_{base}(t) \tag{4.2}$$

where $\psi(z)$ = acceleration shape function,

$A_{top}(t)$ = acceleration recorded at the top of the wall,

$A_{base}(t)$ = acceleration recorded at the base of the wall.

A cantilever beam can deflect in an infinite variety of shapes, and for exact analysis, it must be treated as an infinite-degree-of-freedom system possessing an infinite number of natural modes of vibration (Chopra 2007). In this study, it is assumed that the stiff and flexible retaining

walls deflect at all times according to the first vibration mode (also known as the fundamental vibration mode) and a single shape function $\psi(z)$ was therefore used to approximate this vibration mode. The shape function $\psi(z)$ must satisfy the displacement boundary conditions for the cantilever wall. Having only three boundary conditions ($A^t(0, t) = A_{top}(t)$, $A^t(L, t) = A_{base}(t)$, $\psi'(L) = 0$), the following quadratic function was used to approximate the fundamental wall vibration mode:

$$\psi(z) = \frac{1}{L^2} \cdot z^2 - \frac{2}{L} \cdot z + 1 \tag{4.3}$$

The wall inertial force time series were estimated at any depth of the wall using Equations 4.1–4.3. The wall inertial moment time series were approximated by double integrating the inertial force profiles at all times. The wall inertial forces and moments were not estimated for LAA01, since only one accelerometer was placed at the tops of the south stiff and north flexible walls. One acceleration boundary condition on the wall is not sufficient to provide a reasonable estimate of the wall acceleration profile.

4.1.6 Lateral Earth Pressure

Ten Flexiforce sensors were mounted on all four walls to directly measure the seismically induced lateral earth pressures at the locations shown in Figures 3.15–3.18 for experiment LAA01 and Figures 3.19–3.22 for experiment LAA02. Time series recorded by the Flexiforce sensors were filtered using a first-order low-pass Butterworth filter with a prototype scale corner frequency of 22 Hz to reduce noise. The problems encountered with the Flexiforce sensors along with an evaluation of their performance were discussed in Section 3.11.2.

Total lateral earth pressure profiles (due to static and dynamic earth pressures) were plotted for each wall by choosing the time at which the maximum pressure occurred at the lowest Flexiforce sensor of each wall and then plotting the pressures at all other Flexiforce sensors at that same time. Total lateral earth pressure profiles were also interpreted from the total earth pressure moment profiles recorded by the strain gages and corrected to remove the wall inertial effects as discussed in Section 4.1.5.

4.2 ACCELERATION RESPONSE AND GROUND MOTION PARAMETERS

Tables 4.1 and 4.2 present the ground motion parameters for the different input shaking events for centrifuge experiments LAA01 and LAA02, respectively. These ground motion parameters include the peak ground acceleration (PGA), the Arias intensity (I_a), the predominant period (T_p), the mean period (T_m), and the bracketed duration (D). As shown in Table 4.1, the input PGA could not be measured for Loma Prieta-1 during experiment LAA01 because accelerometers were set at a large gain. D is the total time elapsed between the first and the last excursions of a level of acceleration of 5% of the PGA. T_p is the period at which the maximum spectral acceleration occurs in an acceleration response spectrum calculated at 5% damping. T_m is a better frequency content characterization parameter being estimated with equation $T_m = \frac{\sum C_i^2 / f_i}{\sum C_i^2}$, where C_i are the Fourier amplitudes, and f_i represent the discrete Fourier transform frequencies between 0.25–20 Hz (Rathje et al. 1998). The horizontal acceleration, the integrated velocity, the integrated displacement, the Arias intensity time series, and the acceleration response spectra at 5% damping are presented in Figures A.6–A.22 for the input ground motions applied during both experiments LAA01 and LAA02.

Table 4.1 Input ground motion parameters for different shaking events during LAA01.

Shaking Event	PGA (g)	I_a (m/sec)	T_p (sec)	T_m (sec)	D (sec)
Loma Prieta-1	-	1.19	0.34	0.53	27.06
Loma Prieta-2	0.43	1.22	0.30	0.52	23.46
Kobe	0.90	5.44	0.26	0.79	25.11
Loma Prieta-3	0.43	1.17	0.3	0.53	23.47

The acceleration time series obtained from the two sets of experiments, LAA01 and LAA02, were used to evaluate the amplification and de-amplification of the input ground motions, and to evaluate the magnitude of seismically induced forces. Tables 4.3 and 4.4 present the peak accelerations measured at the base of the container, at the top of the soil in the free field, and at the tops of the south stiff and north flexible walls during different shaking events. Figure 4.1 is a plot of the peak accelerations measured at the base of the container versus those measured at the top of the soil in the free field, at the top of the south stiff wall, and at the top of the north flexible wall, during the different shaking events. A 45° line is displayed for reference.

Based on Tables 4.3 and 4.4 and Figure 4.1, the ground motions are consistently amplified at the tops of the walls, and the acceleration at the top of the soil crosses over the 45° line, indicating attenuation of the large-magnitude input shaking events.

Table 4.2 Input ground motion parameters for different shaking events during LAA02.

Shaking Event	PGA (g)	I_a (m/sec)	T_p (sec)	T_m (sec)	D (sec)
Loma Prieta-SC-1	0.66	1.97	0.14	0.39	9.51
Kobe-PI-1	0.79	5.68	0.36	0.77	25.13
Kobe-PI-2	0.80	6.07	0.36	0.77	18.23
Loma Prieta-SC-2	0.49	1.33	0.3	0.52	23.45
Kocaeli-YPT060-1	0.04	0.011	0.62	0.62	23.50
Kocaeli-YPT060-2	0.15	0.12	0.28	0.54	18.60
Kocaeli-YPT060-3	0.24	0.30	0.28	0.51	15.65
Kocaeli-YPT330-1	0.10	0.054	0.20	0.57	20.41
Kocaeli-YPT330-2	0.27	0.39	0.24	0.53	15.44
Kobe-TAK090-1	0.74	4.95	0.50	0.41	8.61
Kobe-TAK090-2	0.87	6.23	0.20	0.44	16.16
Loma Prieta-WVC270	0.23	0.28	0.26	0.56	12.05
Kocaeli-YPT330-3	0.22	0.36	0.24	0.56	19.70

Table 4.3 Peak accelerations measured at base of container, top of soil in free field, and tops of south stiff and north flexible walls during LAA01 shaking events.

	Peak Accelerations (g)			
	Input	Top of soil	Top of South Stiff Wall	Top of North Flexible Wall
Step Wave	0.06	0.11	0.15	0.12
Loma Prieta-1	-	-	-	-
Loma Prieta-2	0.43	0.48	0.78	0.96
Kobe	0.90	0.73	1.03	1.11
Loma Prieta-3	0.43	0.52	0.83	1.01

Table 4.4 Peak accelerations measured at base of container, top of soil in free field, and tops of south stiff and north flexible walls during LAA02 shaking events.

	Peak Accelerations (g)			
	Input	Top of soil	Top of South Stiff Wall	Top of North Flexible Wall
Step Wave-1	0.05	0.08	0.10	0.14
Loma Prieta-SC-1	0.66	0.44	0.71	0.85
Kobe-PI-1	0.79	0.67	0.89	1.38
Step Wave-2	0.05	0.10	0.11	0.11
Kobe-PI-2	0.80	0.76	0.96	1.44
Loma Prieta-SC-2	0.49	0.52	0.85	0.84
Kocaeli-YPT060-1	0.04	0.06	0.07	0.09
Kocaeli-YPT060-2	0.15	0.28	0.36	0.31
Kocaeli-YPT060-3	0.24	0.40	0.57	0.54
Kocaeli-YPT330-1	0.10	0.17	0.21	0.22
Kocaeli-YPT330-2	0.27	0.39	0.49	0.49
Kobe-TAK090-1	0.74	0.86	1.27	1.75
Kobe-TAK090-2	0.87	0.64	1.32	1.21
Loma Prieta-WVC270-1	0.23	0.31	0.38	0.43
Kocaeli-YPT330-3	0.22	0.36	0.40	0.40

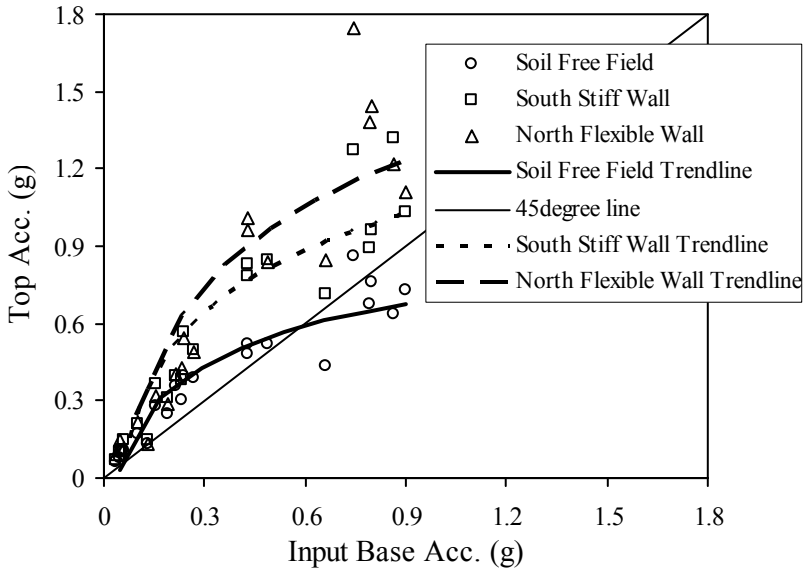

Fig. 4.1 Base motion amplification/de-amplification for soil, stiff, and flexible structures.

4.3 SOIL SETTLEMENT AND DENSIFICATION

Vertical soil deformation measurements were recorded at the soil surface and at the foundation level of each structure by linear potentiometers and LVDTs at the locations shown in Figures 3.2–3.3 and Figures 3.4–3.5 for LAA01 and LAA02, respectively. The static offsets measured by the displacement transducers were used to determine the settlement increment of the uniform density soil model after the different shaking events in experiment LAA02. In experiment LAA01, the settlement increment of the backfill soil as well as the soil underneath the structures (base soil) was determined for the two-layer model. Tables 4.5 and 4.6 show these settlement values along with the relative density (Dr) of the soil after each shaking event for LAA01 and LAA02, respectively. It is apparent that the maximum settlement occurred during the first Kobe event in both sets of experiments, LAA01 and LAA02, due to the large magnitude of shaking and the relatively low initial density of the sand.

Table 4.5 Soil settlement and relative density after different shaking events for LAA01.

	Base Soil		**Backfill**	
Shaking Event	***Settlement Increment (mm)***	***Dr (%)***	***Settlement Increment (mm)***	***Dr (%)***
Step Wave	0.36	74.4	0.50	61.7
Loma Prieta-1	31.64	75.6	22.75	63.5
Loma Prieta-2	17.85	76.4	2.37	63.7
Kobe	37.62	77.9	37.34	66.7
Loma Prieta-3	4.17	78.1	5.16	67.1

Table 4.6 Soil settlement and relative density after different shaking events for LAA02.

Shaking Event	*Settlement Increment (mm)*	*Dr (%)*
Step Wave-1	0.36	72.1
Loma Prieta-SC-1	52.62	73.9
Kobe-PI-1	98.51	77.0
Step Wave 2	0	77.0
Kobe-PI-2	56.07	78.8
Loma Prieta-SC-2	7.00	79.05
Kocaeli-YPT060-1	0	79.05
Kocaeli-YPT060-2	1.39	79.1
Kocaeli-YPT060-3	1.82	79.1
Kocaeli-YPT330-1	0	79.1
Kocaeli-YPT330-2	0.93	79.2
Kobe-TAK090-1	29.03	80.3
Kobe-TAK090-2	16.40	81.0
Loma Prieta-WVC270	0.31	81.0
Kocaeli-YPT330-3	0.07	81.0

4.4 SHEAR-WAVE VELOCITY

Table 4.7 presents the shear-wave velocities measured between the different shaking events of experiment LAA01 in the base soil along with the corresponding estimated fundamental natural periods. The fundamental natural period of the soil was estimated using the relationship: $T = \frac{4H}{V_s}$, where H is the height of the soil deposit and Vs is the corresponding shear-wave velocity. The data obtained from the bender elements located behind the retaining wall structures in experiment LAA01 were very noisy; hence shear-wave velocities for the backfill soil could not be measured directly. Shear-wave velocities were instead estimated by measuring the first arrival times to accelerometers A27 and A22, located at the base level of the structures and at the top of the backfill soil in the free field, respectively. The initial back-calculated backfill shear-wave velocity for LAA01 is on the order of 130 m/s. The shear-wave velocity estimated using the procedure outlined in Arulnathan et al. (2000) for measuring the shear-wave velocity of Nevada sand in model tests is in agreement with the back-calculated value. Therefore, the initial natural period of the backfill soil in experiment LAA01 is estimated to be around 0.2 sec. The shear-wave velocity of the backfill soil slightly increased after each shaking event due to the soil densification. However, this increase was not very significant.

Table 4.7 Shear-wave velocities and natural periods of base soil after different shaking events for LAA01.

	V_s (m/sec)	T (sec)
Initial	266	0.19
After Step Wave	221	0.23
After Loma Prieta-1	266	0.19
After Loma Prieta-2	280	0.18
After Kobe	271	0.19
After Loma Prieta-3	266	0.19

The shear-wave velocities measured between the different shaking events of experiment LAA02 and the corresponding natural periods in the base and the backfill soil are presented in Table 4.8. It should be noted that shear-wave velocity measurements were not collected in the base soil after Loma Prieta-SC-1, Kobe-PI-1, and Step Wave-2 and in the backfill soil before Step Wave-1, and after Kobe-PI-1, Step Wave-2, Loma Prieta-SC-2, Kocaeli-YPT060-2 and 3, and Kocaeli-YPT330-2 due to technical problems.

Table 4.8 Shear-wave velocities and natural periods of base and backfill soils after different shaking events for LAA02.

	Base Soil		Backfill Soil	
	V_s (m/sec)	T (sec)	V_s (m/sec)	T (sec)
Before Step Wave-1	260.74	0.19	-	-
After Step Wave-1	261.29	0.19	176.91	0.15
After Loma Prieta-SC-1	-	-	177.43	0.15
After Kobe-PI-1	-	-	-	-
After Step Wave-2	-	-	-	-
After Kobe-PI-2	261.68	0.19	188.61	0.14
After Loma Prieta-SC-2	264.03	0.19	202.16	0.13
After Kocaeli-YPT060-1	261.45	0.19	238.94	0.11
After Kocaeli-YPT060-2	265.55	0.19	-	-
After Kocaeli-YPT060-3	255.41	0.20	-	-
After Kocaeli-YPT330-1	256.75	0.19	188.61	0.14
After Kocaeli-YPT330-2	256.21	0.20	-	-
After Kobe-TAK090-1	267.12	0.19	191.78	0.14
After Kobe-TAK090-2	266.67	0.19	196.66	0.13
After Loma Prieta-WVC270-1	266.91	0.19	196.66	0.13
After Kocaeli-YPT330-3	267.12	0.19	233.30	0.11

Recall that the estimated natural periods of the stiff and flexible structures are 0.11 and 0.24 sec, respectively (Table 3.3). Thus the measured site periods of the backfill are close to the natural period of the stiff structure in experiment LAA02 and of the flexible structure in experiment LAA01. Similarly, the input motions have dominant periods ranging from 0.14 to 0.62 sec and mean periods ranging from 0.39 to 0.79 sec (Tables 4.1 and 4.2), which effectively span the range of periods expected to produce maximum response in the soil deposit and structures.

4.5 SEISMIC BEHAVIOR OF RETAINING WALL–BACKFILL SYSTEM

In this section, the seismic behavior of the backfill and retaining walls observed in the centrifuge experiments is analyzed through an evaluation of the acceleration and inertial responses of the backfill and the retaining walls.

4.5.1 Acceleration Response

Figure 4.2 presents the first few cycles of motion as recorded at the base of the model container (input acceleration), at the top of the soil in the free field, and at the tops of the south stiff and north flexible walls for the Kobe-PI-2 shaking event of experiment LAA02. Looking at the travel times for the first cycle of motion in the different acceleration records in Figure 4.2, it is noted that the first input peak arrival occurs at 7.831 sec, while the first peak arrivals at the top of soil and the tops of the stiff and flexible walls are 8.147, 8.112, and 8.112 sec, respectively. Therefore, the inertial force does not occur simultaneously in the backfill and the wall, and a phase difference is observed between the acceleration at the top of the soil and that at the top of the stiff or the flexible walls. It is clear that the retaining walls start to experience the inertial force and then the soil backfill follows. Moreover, the recorded accelerations in the soil backfill (A29, A27, A26, and A24) and at the bases and the tops of the walls show that the acceleration is not uniform in the backfill or on the walls.

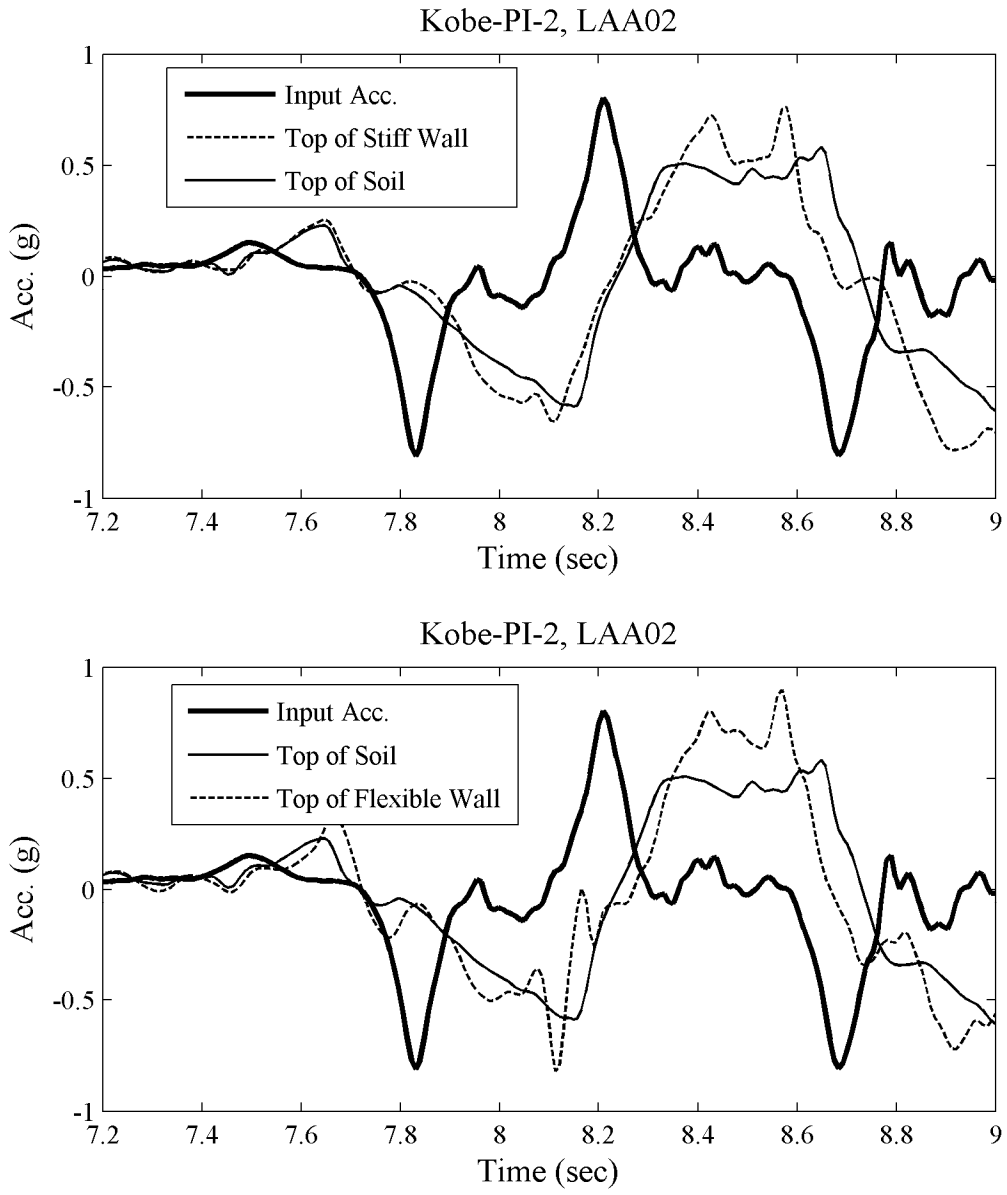

Fig. 4.2 First few acceleration cycles recorded at base of model container, top of soil in free field, and tops of south stiff and north flexible wall for Kobe-PI-2 of experiment LAA02.

4.5.2 Wall and Backfill Inertia

Figure 4.3 presents the sign convention for the positive accelerations, the moments measured by the strain gages, the force-sensing bolts, and the displacements for the south stiff and north flexible walls. The inertial force on the wall and the backfill is proportional to the negative recorded acceleration. Figure 4.3 shows that when the south stiff or the north flexible retaining

walls undergo negative accelerations, the inertial forces occur in the active direction for both walls. Pressure measurements recorded by the Flexiforce sensors are not polarized; readings increase in the positive direction for an increase in pressure regardless of the direction in which the pressure is applied.

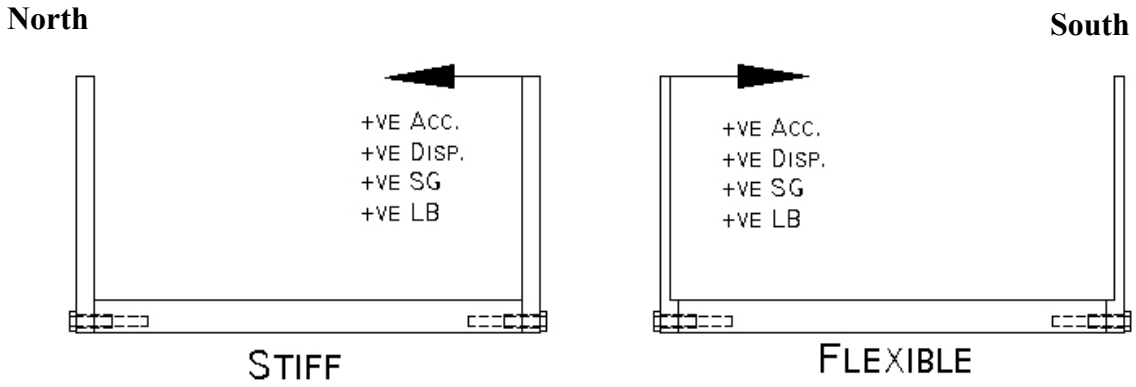

Fig. 4.3 Sign convention for positive accelerations, and moments and displacements, for south stiff and north flexible walls.

Figures 4.4 and 4.5 present the dynamic wall moments recorded by the force-sensing bolts and interpreted from SG1 measurements, the dynamic earth pressure increment recorded by one Flexiforce sensor, and the inertial force for the south stiff and north flexible walls, respectively, during the Loma Prieta-SC-1 shaking event of experiment LAA02. The dynamic wall moment time series include the dynamic earth pressure increment and wall inertial effects. For comparison purposes, the inertial force is computed by multiplying the negative value of the mass of each retaining wall by the acceleration recorded at its base. In Figures 4.4 and 4.5 the same ID is assigned to the dynamic wall moment, the dynamic earth pressure increment, and the inertial force corresponding to the same time. This helps in understanding the relation between the moment, the pressure, and the inertial force in time. Figure 4.5 presents a close-up of a few cycles of the dynamic wall moment and earth pressure increment time series recorded by one strain gage and one Flexiforce sensors on the stiff and flexible walls during Loma Prieta-SC-1. As shown in Figures 4.4–4.6, when the inertial force is at its local maximum, the dynamic wall moments reach their local maxima as well, but the dynamic earth pressure increments are at their local minima or around zero. On the other hand, when the dynamic earth pressure increment is at its local maximum, the inertial force and the dynamic wall moments reach their local minimum values or zero. The interpretation of this observation is that when the inertial force acts in the

active direction, the total earth pressure is equal to or less than the static earth pressure. The dynamic earth pressure increment is at its maximum when the inertial force is close to zero (static case) or when the inertial force acts in the passive direction.

These results show that when the retaining wall and the backfill are loaded in the active direction, the dynamic earth pressure increment is around its minimum or around zero. The likely explanation for such behavior is that the retaining wall and the backfill are not loaded by the inertial force simultaneously. As discussed in Section 4.5.1, a phase difference is generally observed in the acceleration response of the wall and that of the backfill which would reduce to a significant extent the earth pressure acting on the retaining wall. It should be noted that the maximum observed dynamic pressure and moment increments due to earth pressures generally occur in the passive direction. Finally, Figures 4.4–4.5 show that the dynamic wall moments, including wall inertial effects, behave in accordance with the inertial force acting on the wall and the backfill; they are at their maximum when the inertial force is maximum, and reach minimum at minimum inertial force.

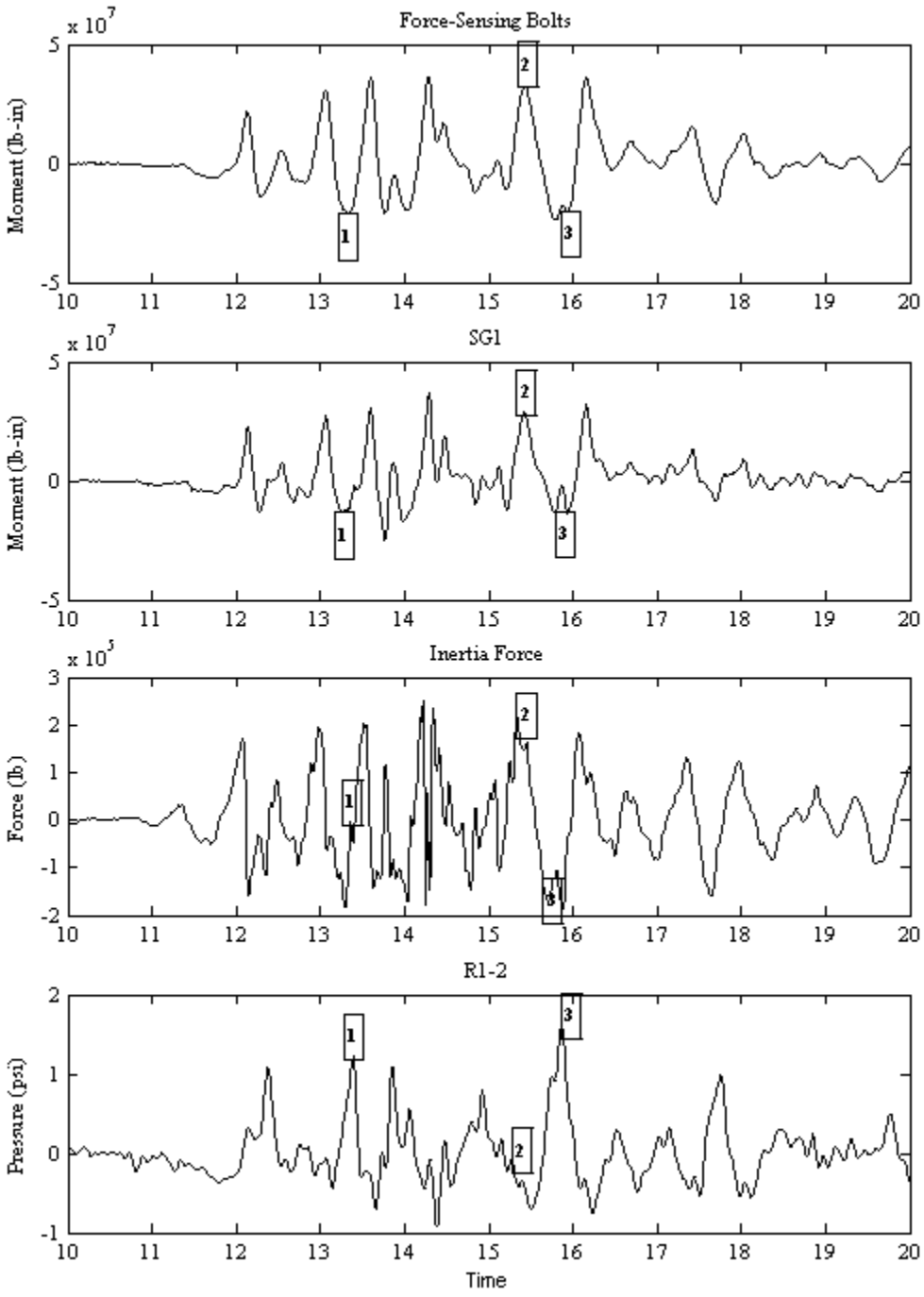

Fig. 4.4 Dynamic wall moments interpreted from SG1 and force-sensing bolt data, dynamic earth pressure increment interpreted from R1-2, and computed inertial force on south stiff wall during Loma Prieta-SC-1 in experiment LAA02.

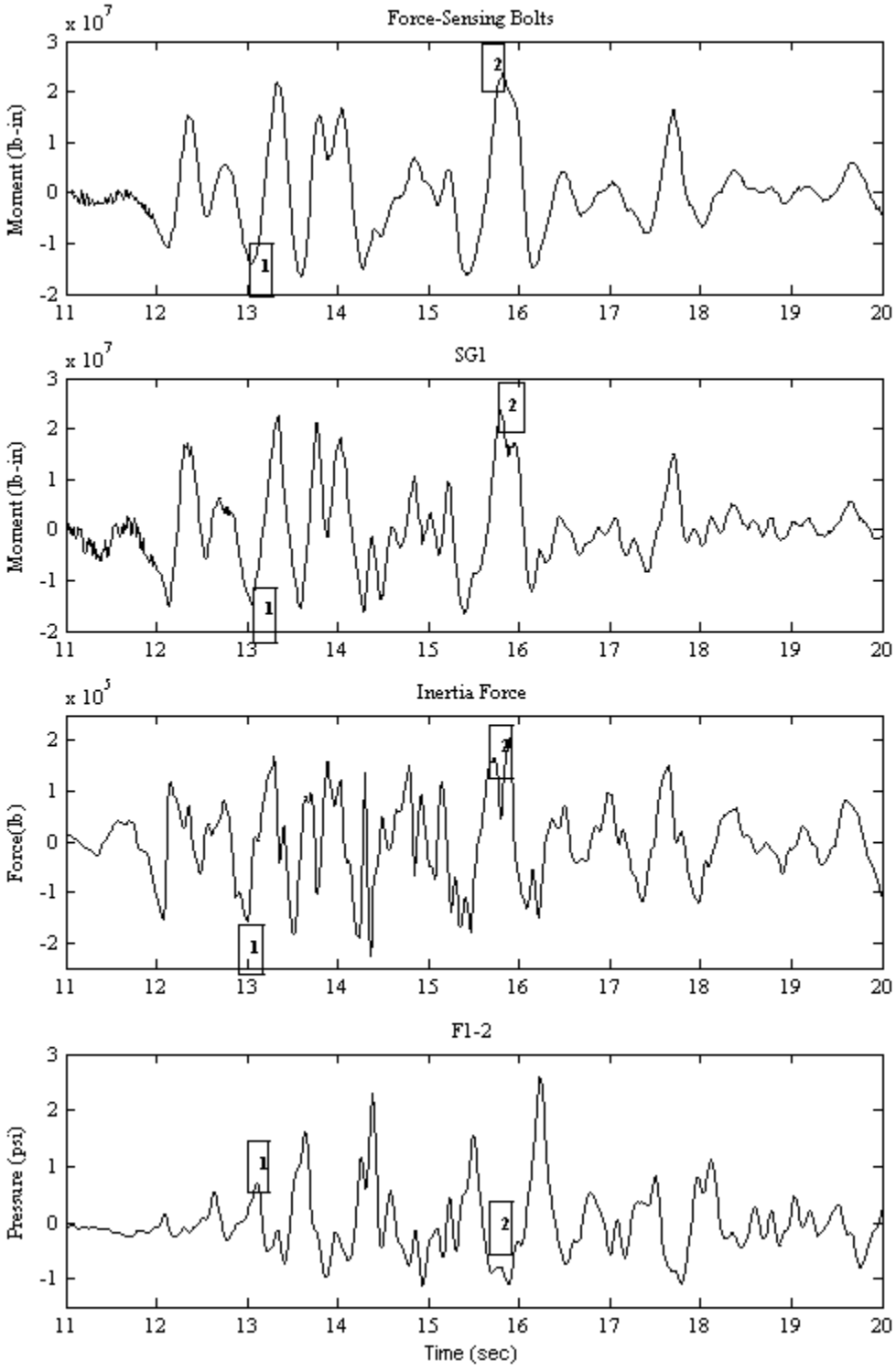

Fig. 4.5 Dynamic wall moments interpreted from SG1 and force-sensing bolt data, dynamic earth pressure increment interpreted from F1-2, and computed inertial force on north flexible wall during Loma Prieta-SC-1 in experiment LAA02.

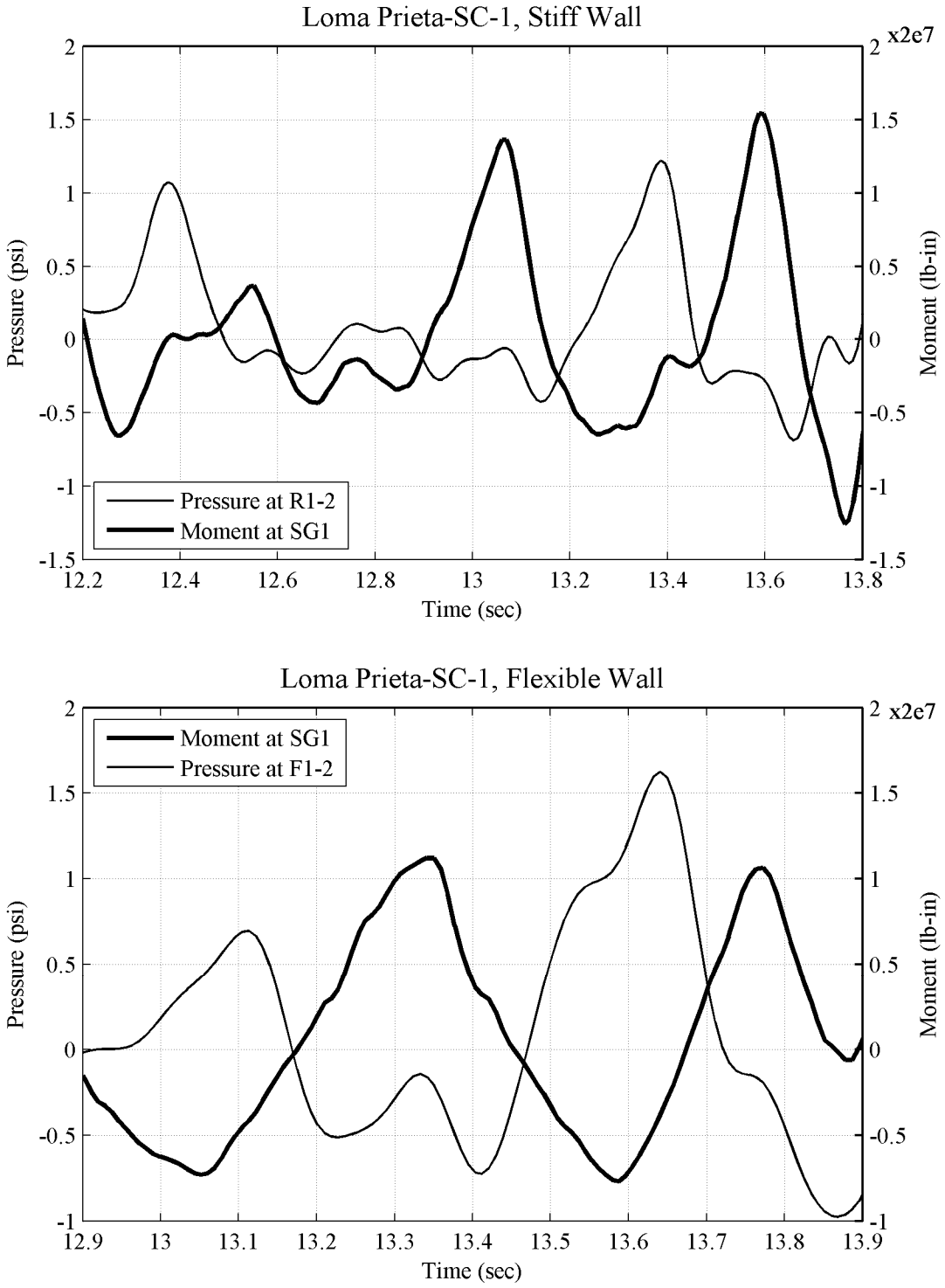

Fig. 4.6 Close-up view of dynamic wall moments and dynamic earth pressure increments interpreted from SG1 and R1-2 on south stiff wall, and SG1 and F1-2 on north flexible wall during Loma Prieta-SC-1 in experiment LAA02.

4.6 TOTAL LATERAL EARTH PRESSURES

Figure 4.7 presents an example of the maximum total lateral earth pressure profiles directly measured by the Flexiforce sensors on all stiff and flexible walls for Loma Prieta-1 and Loma Prieta-2 shaking events for LAA01. The maximum measured total lateral earth pressure profiles for the rest of the shaking events during centrifuge experiments LAA01 and LAA02 are presented in Figures A.23–A.29 and show similar characteristics to those observed in Figure 4.7. This figure shows that maximum total earth pressure profiles (static plus dynamic increment) monotonically increase with depth and can be approximated by linear trend lines. A consistent agreement between the total earth pressure profiles measured at the north and south walls of each structure is generally observed for experiments LAA01 and LAA02. This is an important observation in that it confirms that the models were not significantly influenced by the proximity to the container walls and that the motions of the container were reasonably symmetrical.

Figures 4.8–4.10 present the maximum total pressure distributions recorded by the Flexiforce sensors and interpreted from the strain gage measurements on the south stiff and north flexible walls during the different shaking events for experiments LAA01 and LAA02. In order to determine the maximum pressure profiles from the strain gage measurements, the maximum strain gage moment data were best fitted with cubic polynomials, as described in Section 4.1.4. The maximum total moments at the bases of the walls were extrapolated using the cubic polynomial fits, and the corresponding linear pressure profiles that generated these moments were back-calculated. The maximum total pressure profiles interpreted from the strain gage data were corrected to remove wall inertial effects for the shaking events in experiment LAA02, and therefore represent maximum total earth pressure profiles. For LAA01, the maximum total pressure distributions obtained from the strain gage measurements reflect the combined effects of total earth pressures and wall inertia. Data recorded by the Flexiforce sensors and interpreted from the strain gage measurements presented in Figures 4.8–4.10 were not necessarily recorded at the same time but present the maximum recorded profiles. The estimated static active pressures are also displayed in Figures 4.8–4.10 for reference.

As shown in Figure 4.8, the maximum pressure profiles measured by the Flexiforce sensors were not consistent with those interpreted from the strain gage measurements for centrifuge experiment LAA01. The Flexiforce sensors measured lower pressures than obtained from the strain gage measurements. This difference is mainly attributed to the fact that the

moments on the walls for the LAA01 shaking events include the wall inertial effects, while the direct earth pressure measurements include only the soil-wall interaction effects.

Figures 4.8–4.10 show a general agreement between the total earth pressure profiles measured by the Flexiforce sensors and those interpreted from the corrected strain gage measurements for all the shaking events in experiment LAA02 except for Kobe. The Flexiforce sensors generally measured lower pressures than those interpreted from the strain gage data for all Kobe shaking events. This observed difference can be attributed to the performance characteristics of the Flexiforce sensors discussed in Section 3.11.2 and to the fact that these sensors are sensitive to increase in temperature combined with high loads. While the Flexiforce sensors were carefully calibrated and conditioned for experiment LAA02 to lessen the performance errors, the large magnitude of shaking for Kobe induced high loads that possibly affected the performance of the sensors for these shaking events. Despite the problems encountered with the Flexiforce sensors, the maximum total earth pressure profiles measured by these sensors and presented in Figures 4.8–4.10 are generally considered acceptable except for large shaking events such as Kobe.

It should also be noted that other factors may have introduced slight errors to the total earth pressure profile plots interpreted from the strain gage measurements presented in Figures 4.8–4.10. Such factors include the assumed quadratic shape function for the wall inertial force profiles on the walls and the availability of only two acceleration records on each wall to estimate wall inertial effects. Inevitable numerical errors caused by curve-fitting the moment data and back-calculating the pressure profiles based on the resulting polynomial fits are also present in the pressure distributions interpreted from the strain gage measurements. Finally, it is important to note that total earth pressure profiles consistently increase monotonically downward in the manner that is typically observed and assumed under static conditions. This observation runs counter to the typical assumptions made in the current design methods and requires careful consideration in any future changes to the design methodology.

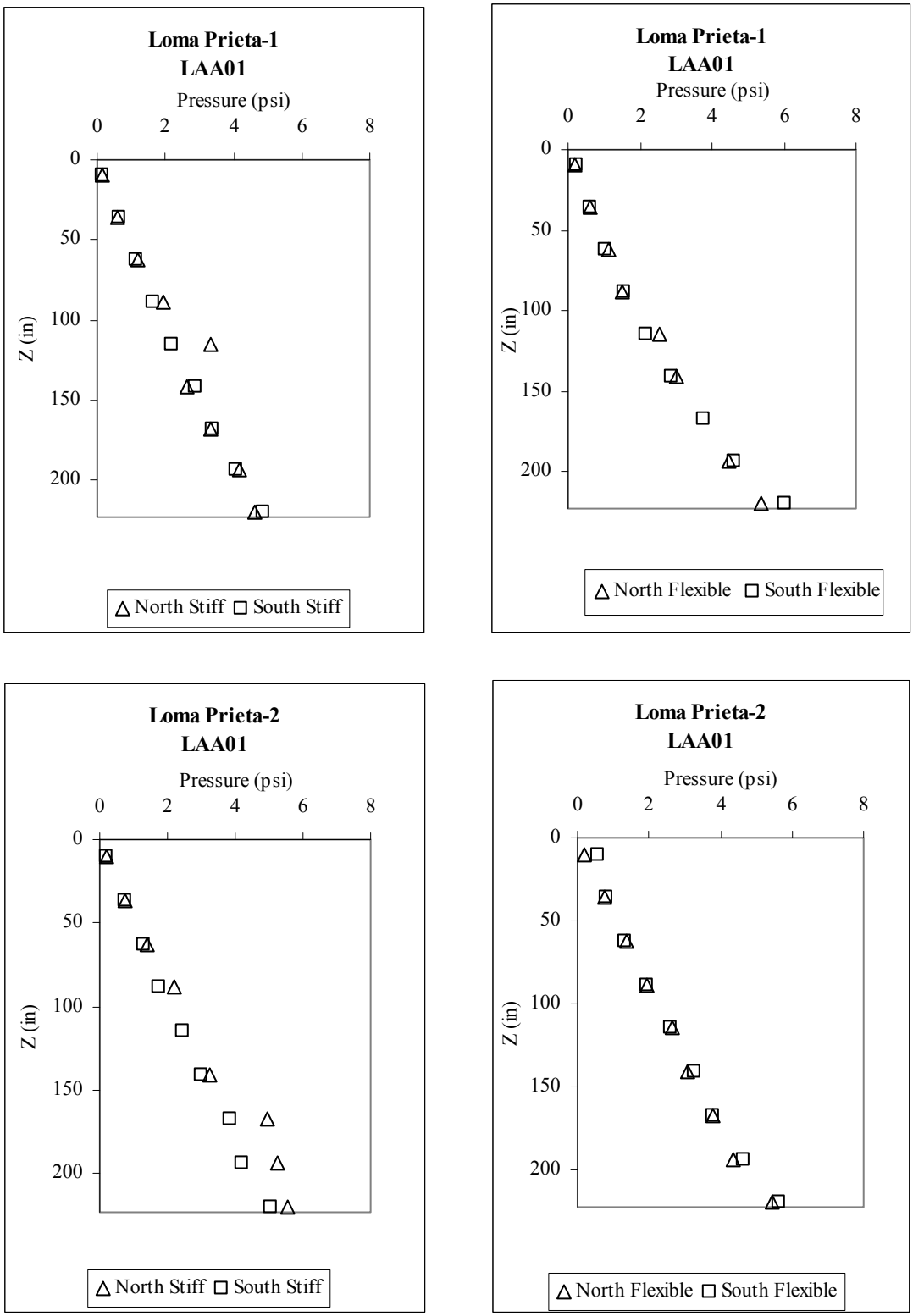

Fig. 4.7 Maximum total lateral earth pressure profiles measured by Flexiforce sensors on stiff and flexible walls during Loma Prieta-1 and 2 shaking events for LAA01.

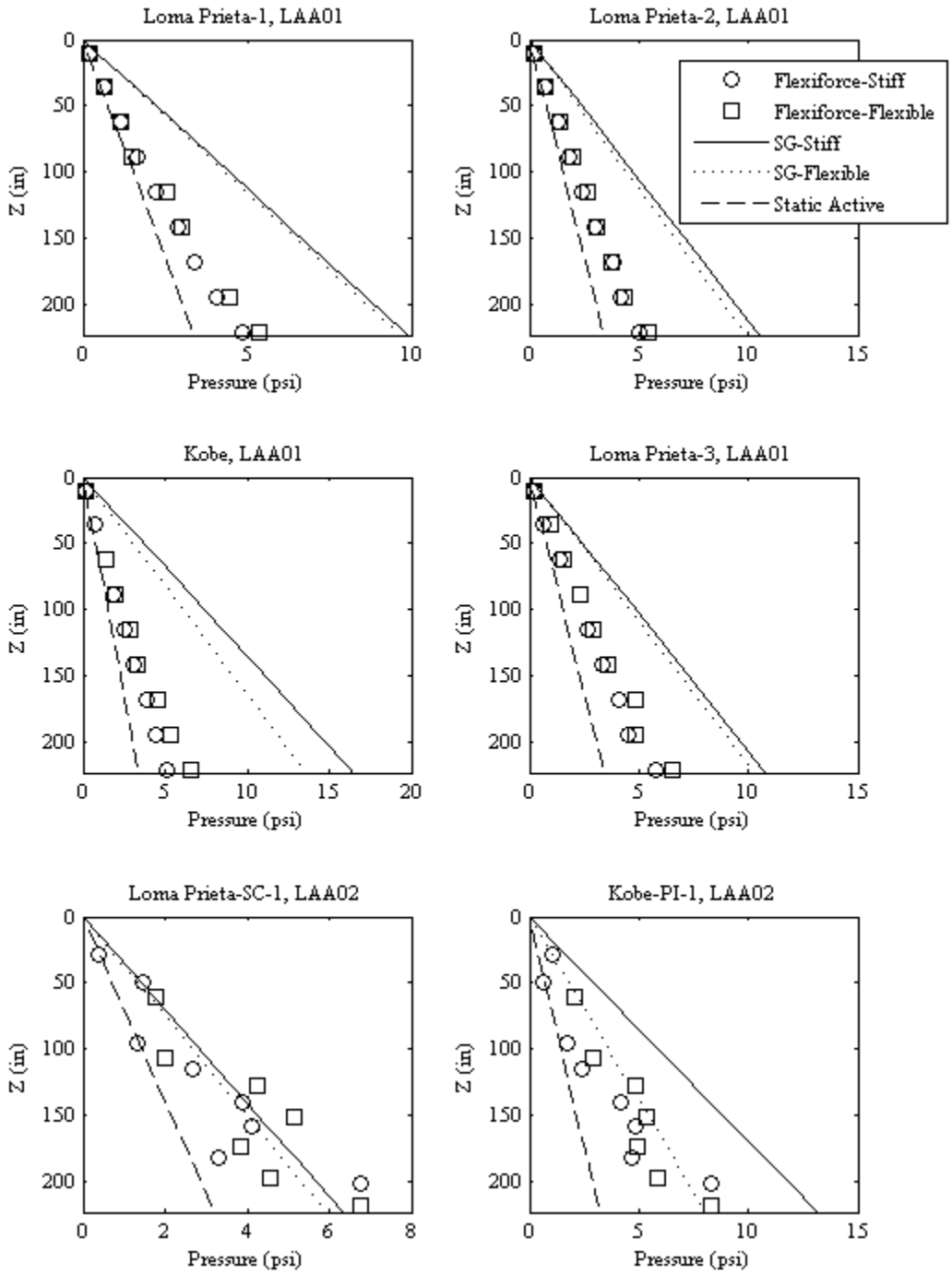

Fig. 4.8 Maximum total pressure distributions directly measured and interpreted from Flexiforce sensors and strain gage data, and estimated static active pressure profiles on south stiff and north flexible walls for all Loma Prieta and Kobe shaking events for LAA01 and for Loma Prieta-SC-1 and Kobe-PI-1 for LAA02.

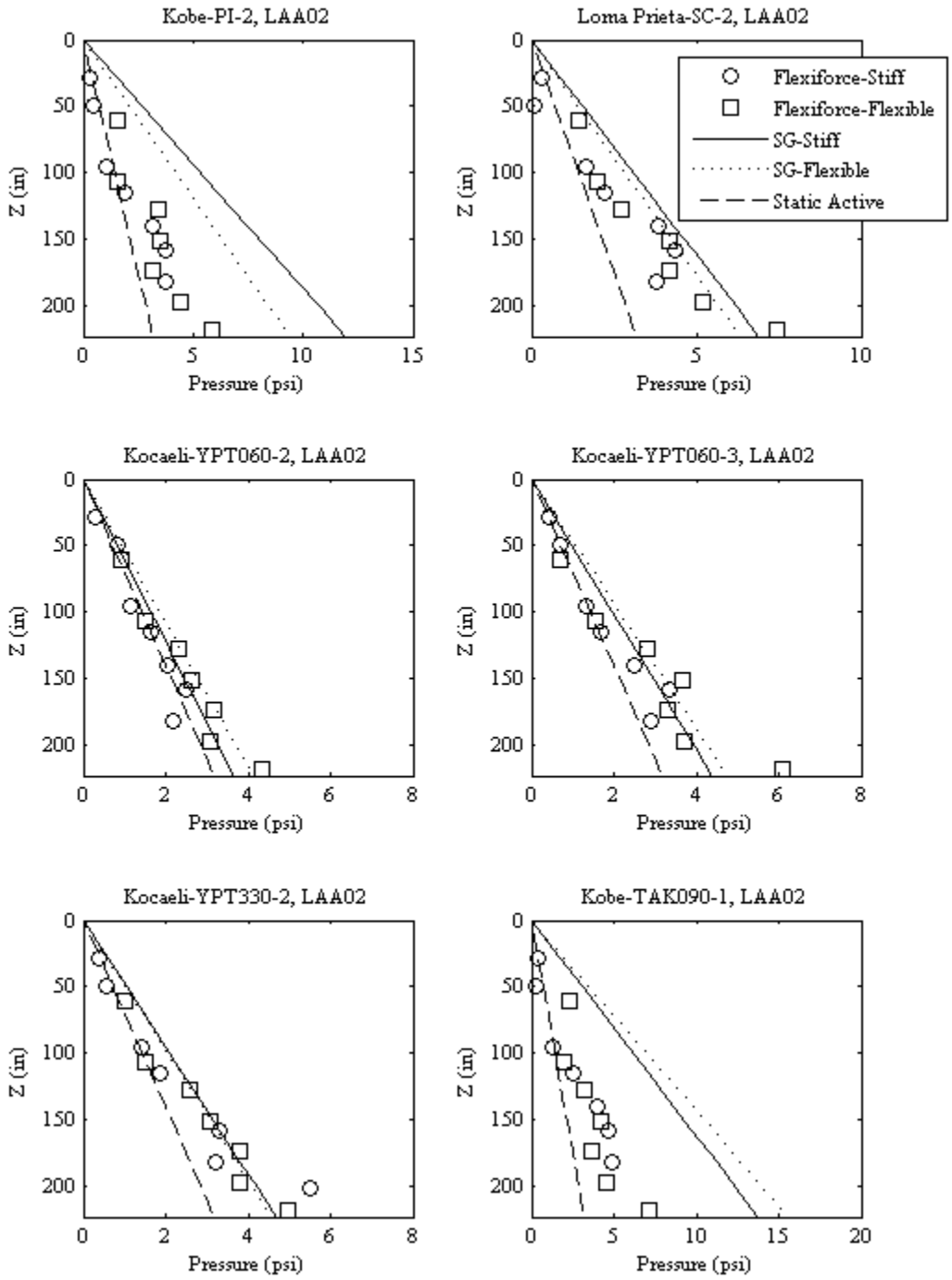

Fig. 4.9 Maximum total earth pressure distributions directly measured and interpreted from Flexiforce sensors and strain gage data, and estimated static active pressure profiles on south stiff and north flexible walls for Kobe-PI-2, Loma Prieta-SC-2, Kocaeli-YPT060-2 and 3, Kocaeli-YPT330-2 and Kobe-TAK090-1 for LAA02.

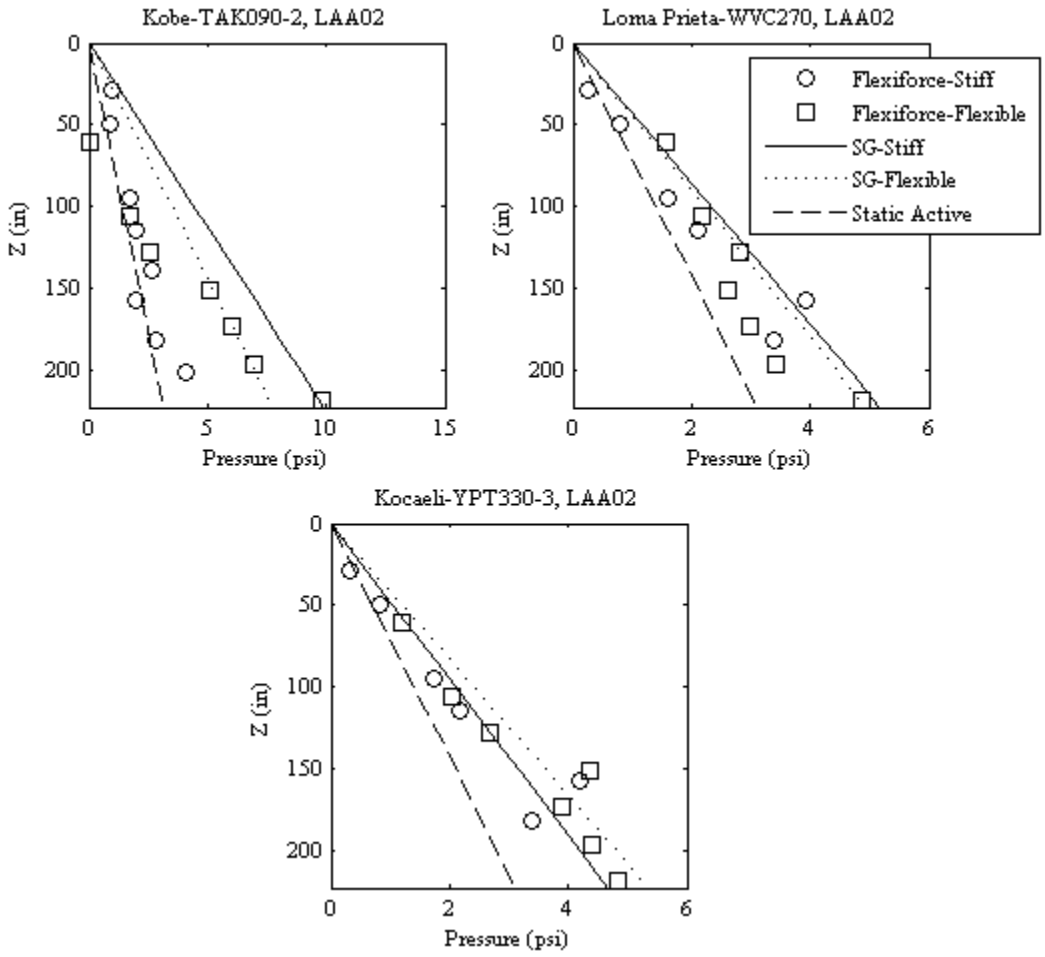

Fig. 4.10 Maximum total earth pressure distributions directly measured and interpreted from Flexiforce sensors and strain gage data, and estimated static active pressure profiles on south stiff and north flexible walls for Kobe-TAK090-2, Loma Prieta-WVC270, and Kocaeli-YPT330-3 for LAA02.

4.7 BENDING MOMENTS

4.7.1 Static Moments

Figures 4.11–4.15 present the static moment profiles measured by the strain gages on the south stiff and north flexible walls before shaking in both centrifuge experiments and between the successive shaking events. The static moments measured by the force-sensing bolts at the bases of the walls, as well as the static at-rest and static active moment estimates, are included in Figures 4.11–4.15 for comparison. The static at-rest and static active moments were estimated using a backfill initial friction angle of 33° in experiment LAA01 and 35° in experiment LAA02.

In experiment LAA02, the initial friction angle was assumed to increase gradually toward a final value of 36˚ to reflect the densification of the soil during each successive shaking event.

As shown in Figures 4.11–4.15, the moments measured by the force-sensing bolts at the bases of the stiff and flexible walls in experiment LAA01 are slightly higher than those interpreted from the strain gage measurements. The moments measured by the force-sensing bolts at the base of the flexible wall for LAA02 are consistently lower than those interpreted from the strain gage measurements. Overall, the results show that the initial moments measured on the stiff and flexible walls were less than predicted from active earth pressure, reflecting the interlocking grain fabric of the dry pluviated sand. Once subjected to shaking and the resulting compaction, the observed moments generally fell between the static at-rest and static active moment estimates reflecting the progressive compaction of the sand during the shaking events.

4.7.2 Total and Dynamic Moments

Figures 4.16–4.19 present the maximum total wall moment profiles interpreted from the strain gage measurements and directly measured by the force-sensing bolts on the south stiff and north flexible walls for the different shaking events in centrifuge experiments LAA01 and LAA02. Static active and static at-rest moment estimates at the bases of the walls are also included in the figures for reference. Recall that total wall moments are induced by static earth pressures, dynamic earth pressure increments and wall inertial forces. The magnitude of the contribution of the wall inertial forces to the total moment acting on the walls is discussed later in Section 4.7.3. Cubic polynomial curves generally provided the best least-squares fits for the moment data in Figures 4.16–4.19 with R-square generally greater than 0.98.

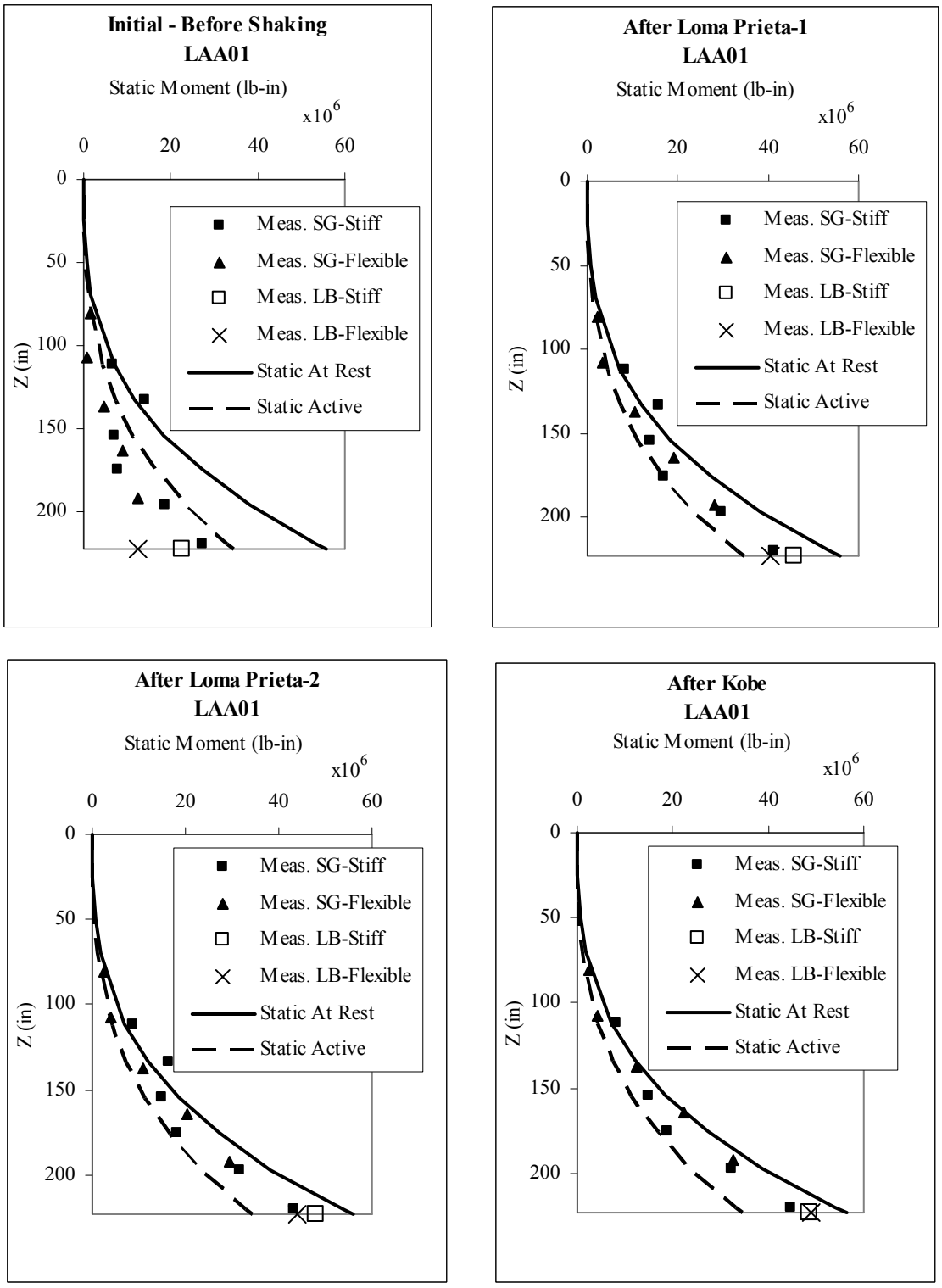

Fig. 4.11 Static moment profiles measured by strain gages and force-sensing bolts, and estimated using static at-rest and static active pressure distributions before shaking and after Loma Prieta-1, Loma Prieta-2, and Kobe for LAA01.

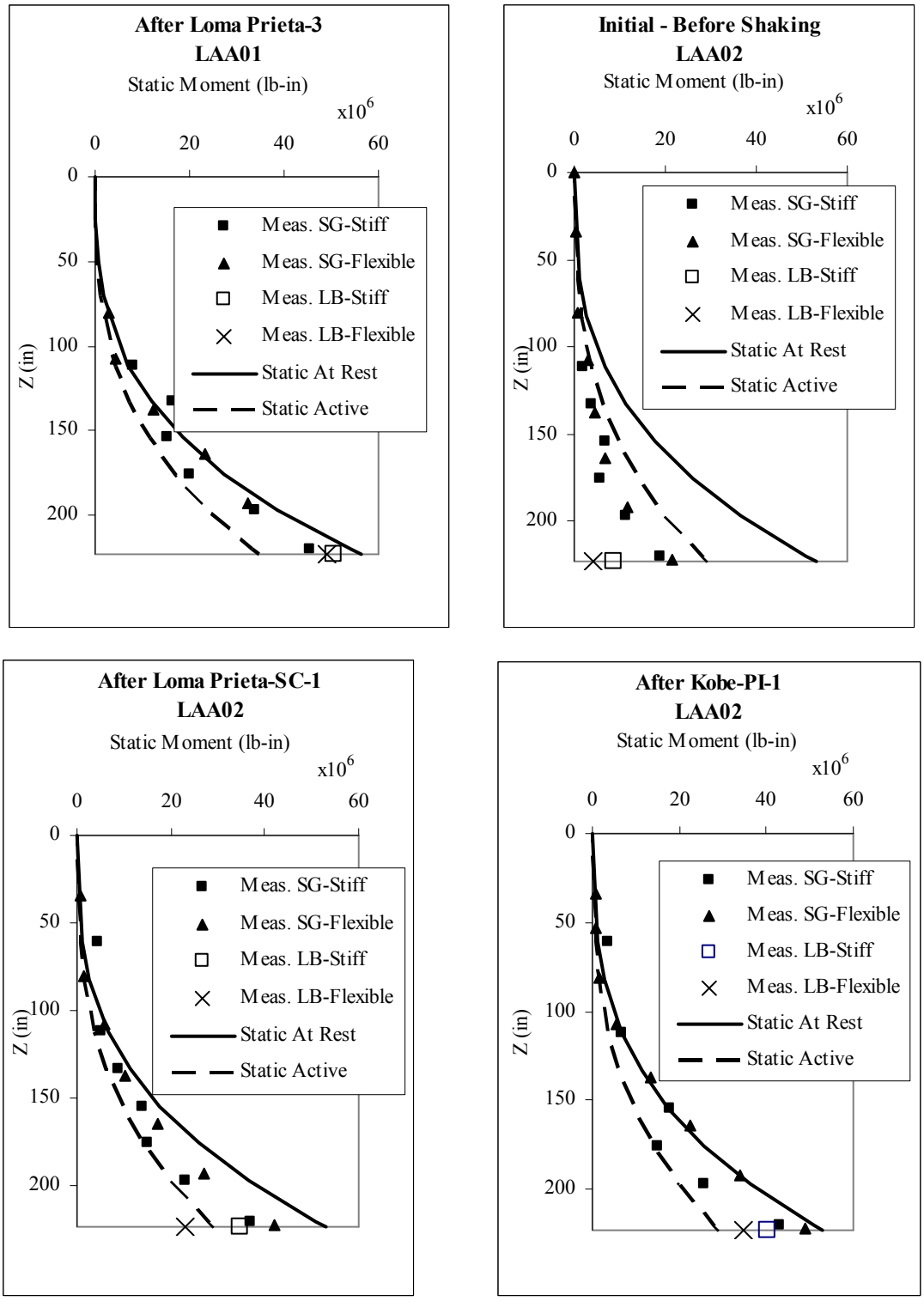

Fig. 4.12 Static moment profiles measured by strain gages and force-sensing bolts, and estimated using static at-rest and static active pressure distributions after Loma Prieta-3 for LAA01 and before shaking, after Loma Prieta-SC-1, and Kobe-PI-1 for LAA02.

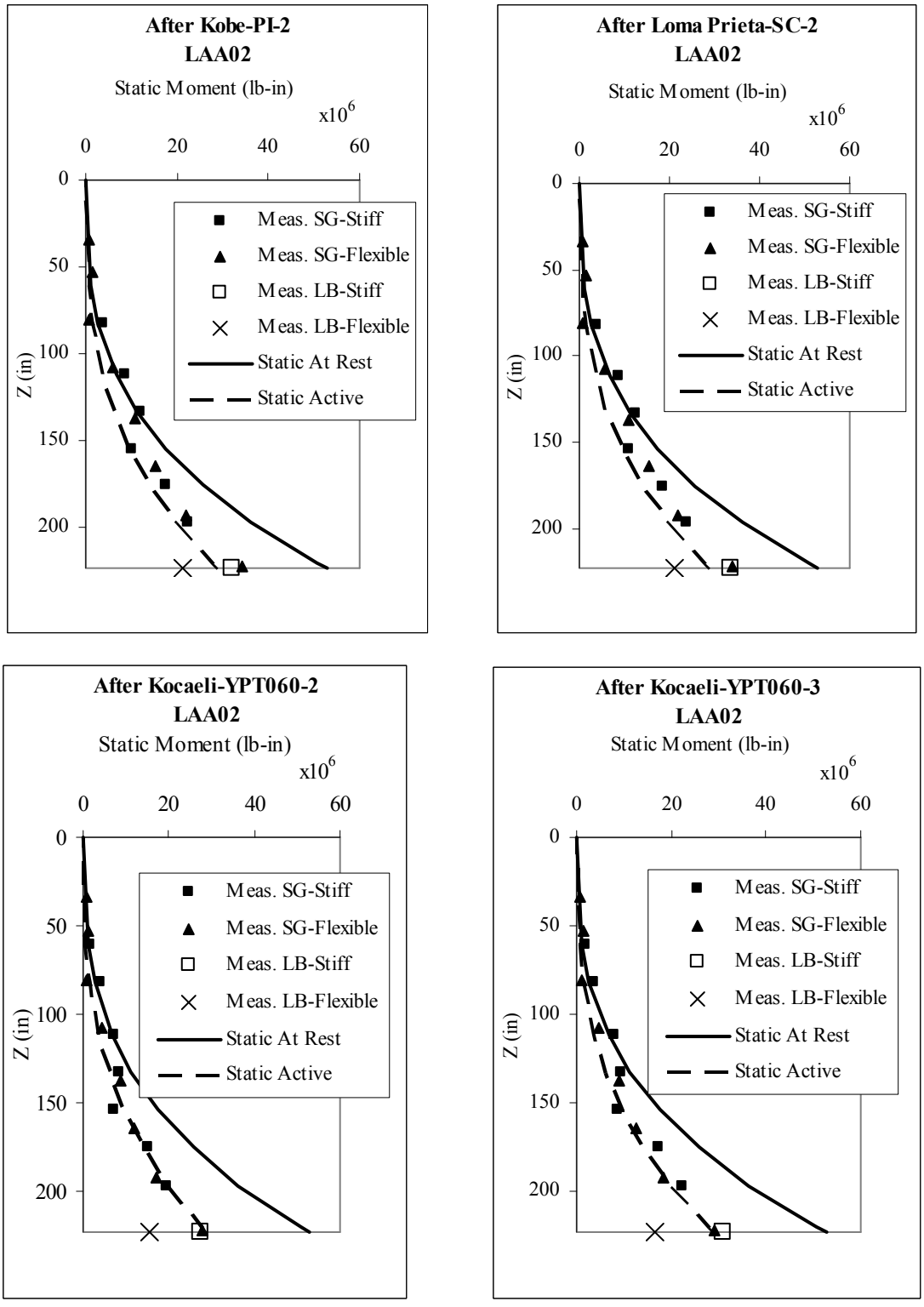

Fig. 4.13 Static moment profiles measured by strain gages and force-sensing bolts, and estimated using static at-rest and static active pressure distributions after Kobe-PI-2, Loma Prieta-SC-2, Kocaeli-YPT060-2, and Kocaeli-YPT060-3 for LAA02.

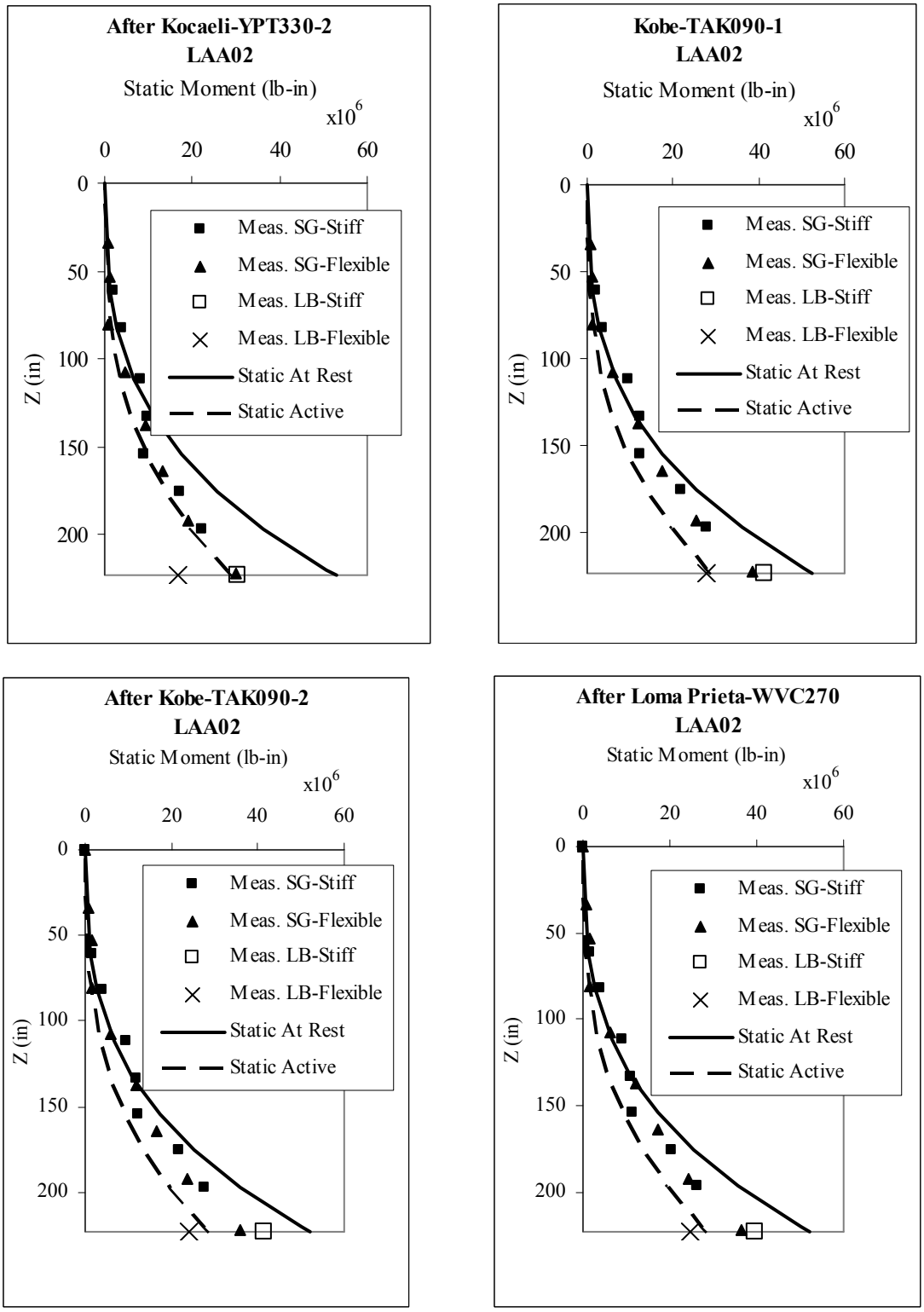

Fig. 4.14 Static moment profiles measured by strain gages and force-sensing bolts, and estimated using static at-rest and static active pressure distributions after Kocaeli-YPT330-2, Kobe-TAK090-1, Kobe-TAK090-2, and Loma Prieta-WVC270 for LAA02.

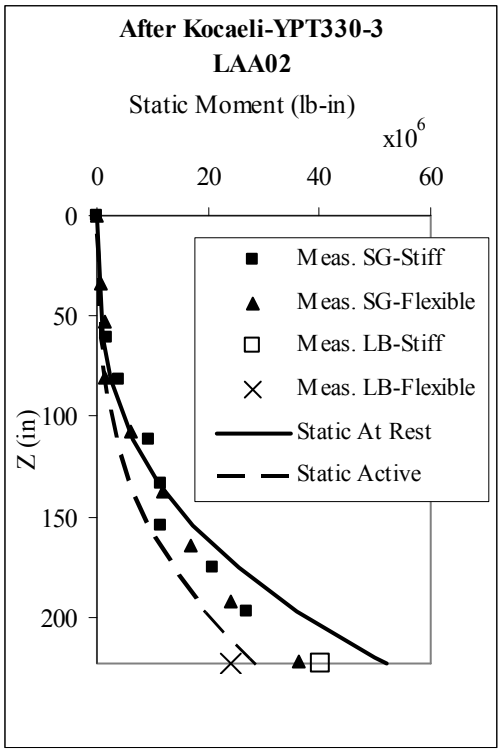

Fig. 4.15 Static moment profiles measured by strain gages and force-sensing bolts, and estimated using static at-rest and static active pressure distributions after Kocaeli-YPT330-3 for LAA02.

Figures 4.16–4.19 show that the moments measured by the force-sensing bolts at the base of the flexible wall in experiment LAA01 are consistently higher than those interpreted from the strain gage measurements. In experiment LAA02, the opposite trend is noted. The maximum total wall moments in both series of experiments, LAA01 and LAA02, occurs during the Kobe motions due to the large magnitude of shaking. Moment profiles measured on the stiff wall are generally larger than those recorded on the flexible wall. Moment profiles on both stiff and flexible walls are well represented by cubic polynomial fits.

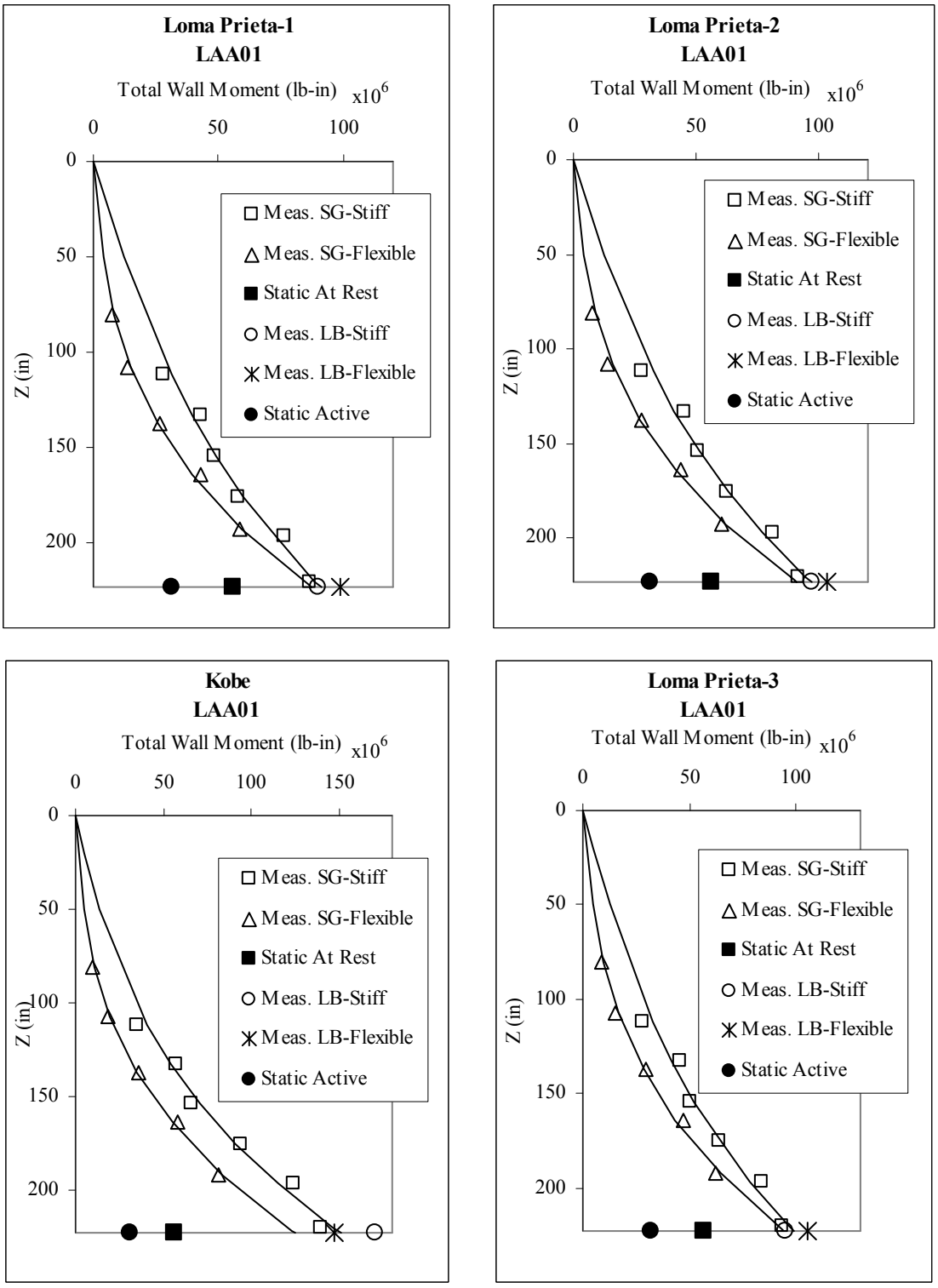

Fig. 4.16 Maximum total wall moment profiles measured by strain gages and force-sensing bolts, and static active and at-rest moment estimates on south stiff and north flexible walls for Loma Prieta-1, 2, and 3, and Kobe for LAA01.

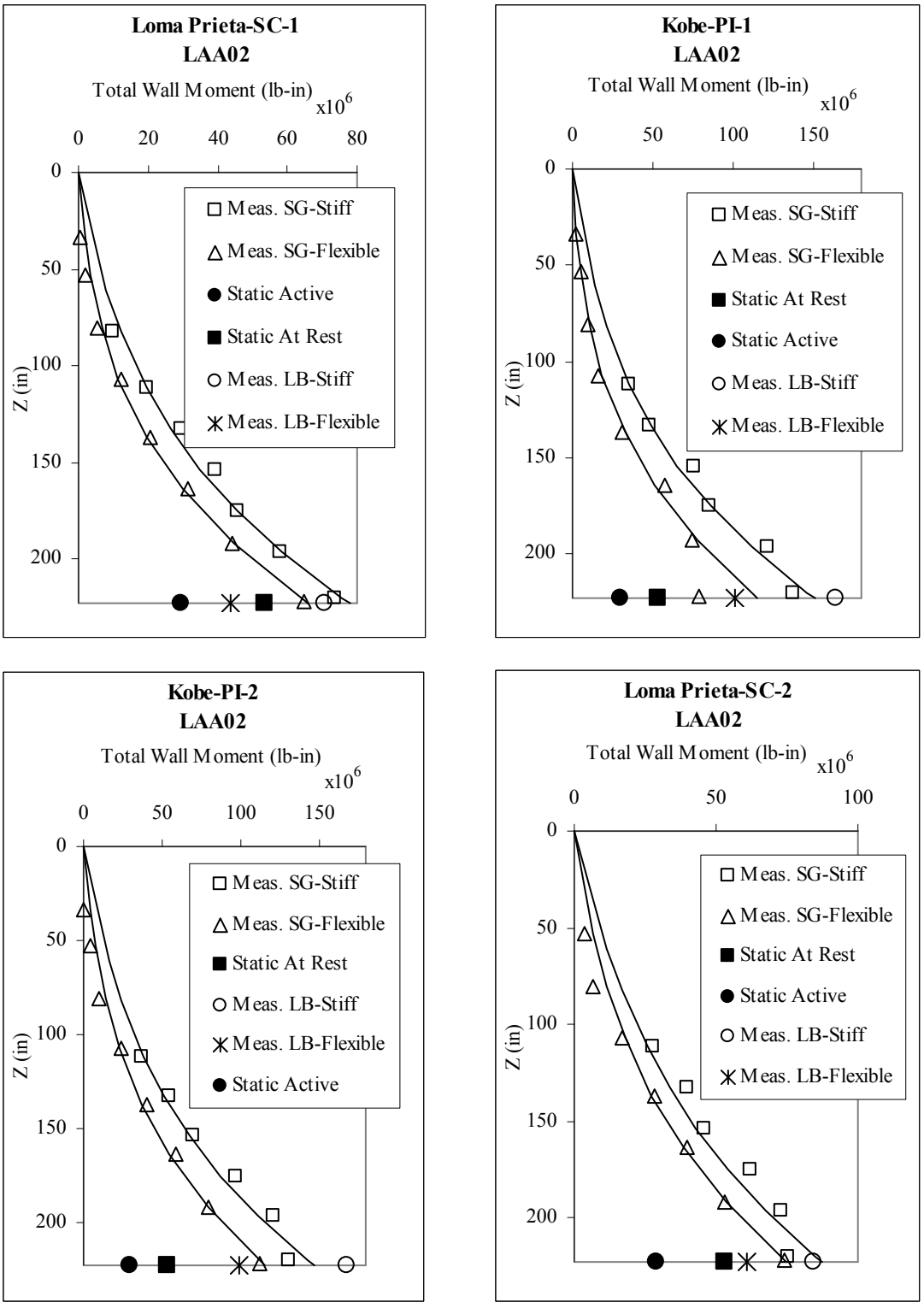

Fig. 4.17 Maximum total wall moment profiles measured by strain gages and force-sensing bolts, and static active and at-rest moment estimates on south stiff and north flexible walls for Loma Prieta-SC-1and 2 and Kobe-PI-1 and 2 for LAA02.

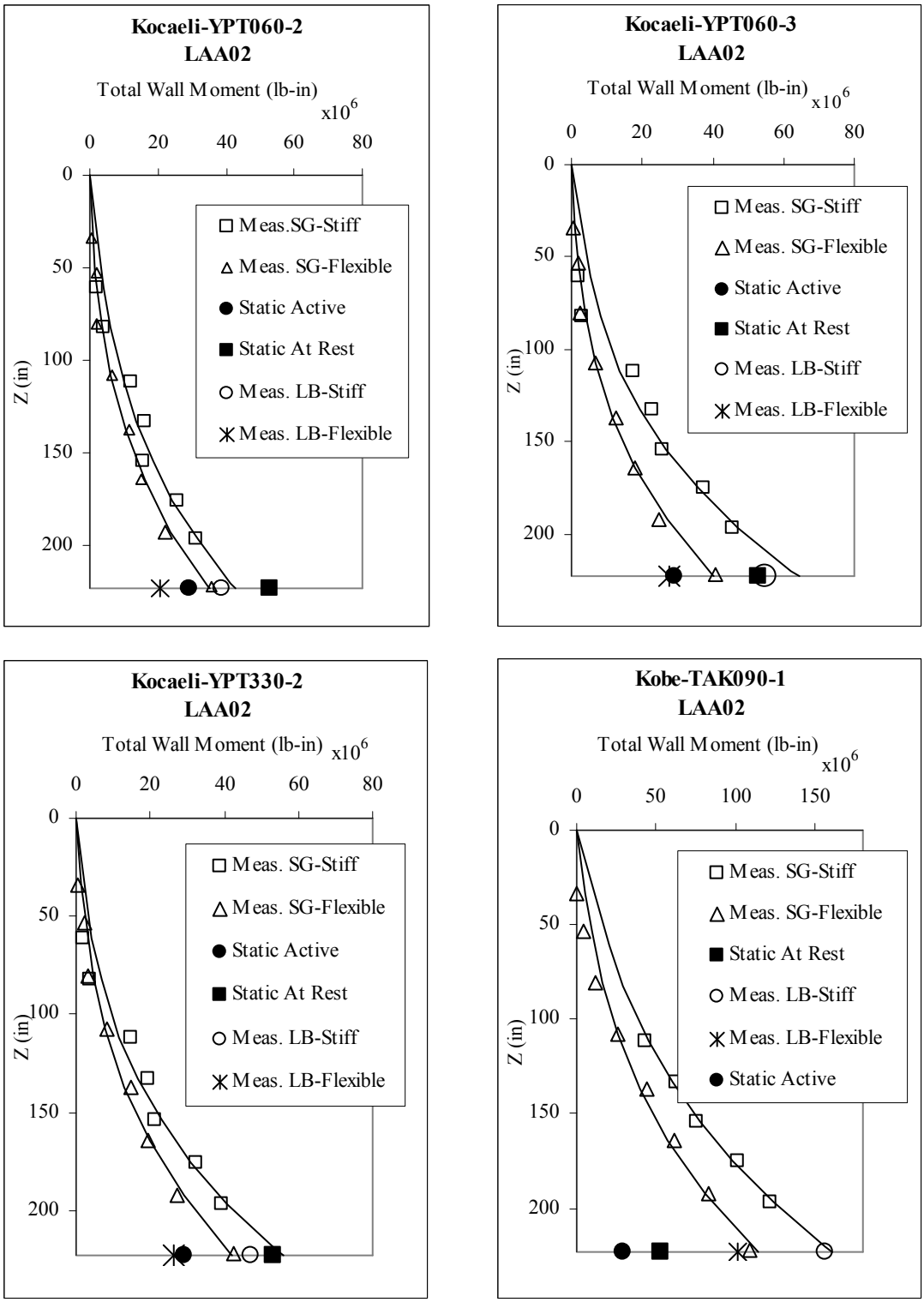

Fig. 4.18 Maximum total wall moment profiles measured by strain gages and force-sensing bolts, and static active and at-rest moment estimates on south stiff and north flexible walls for Kocaeli-YPT060-2 and 3, Kocaeli-YPT330-2 and Kobe-TAK090-1 for LAA02.

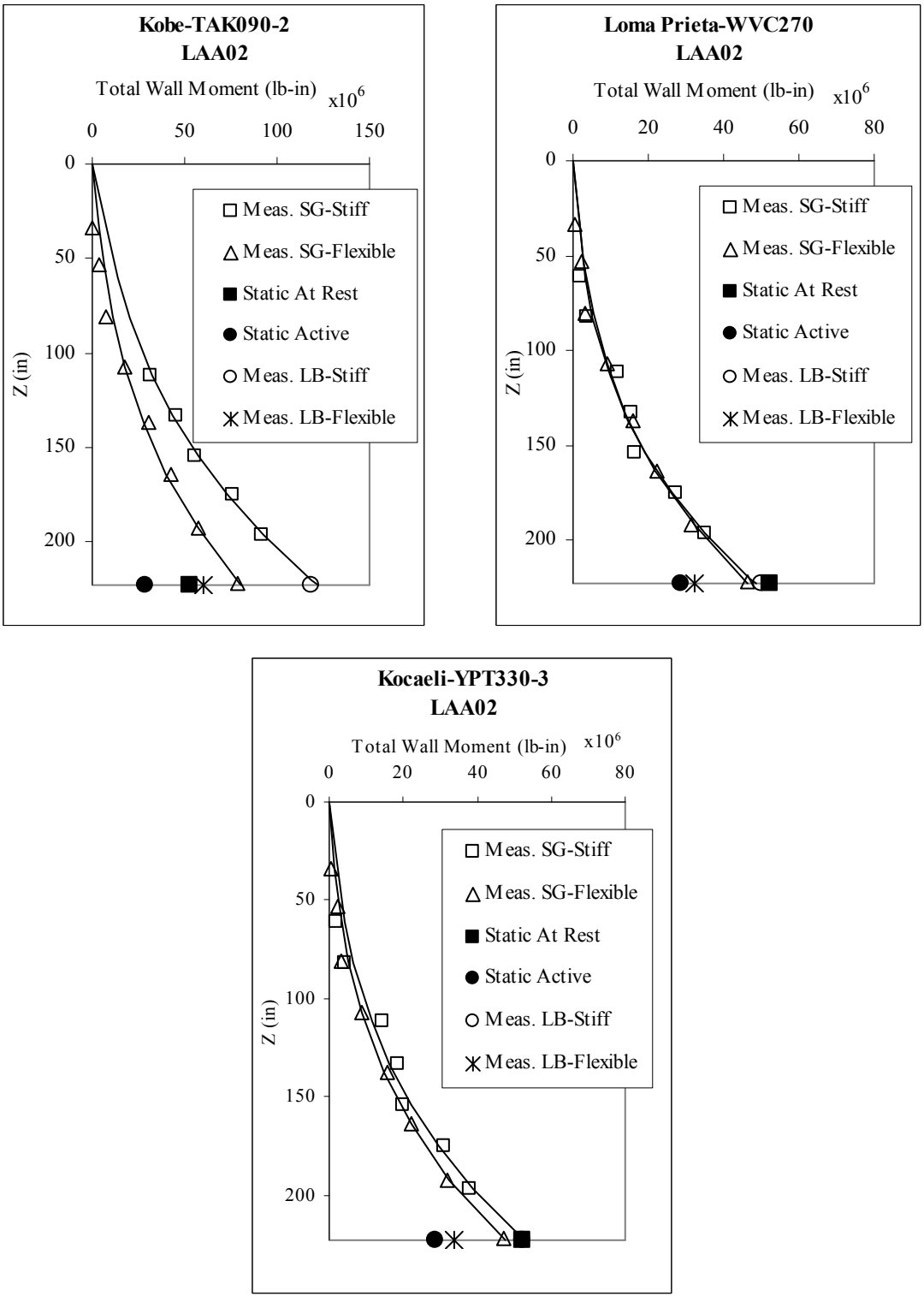

Fig. 4.19 Maximum total wall moment profiles measured by strain gages and force-sensing bolts, and static active and at-rest moment estimates on south stiff and north flexible walls for Kobe-TAK090-2, Loma Prieta-WVC270, and Kocaeli-YPT330-3 for LAA02.

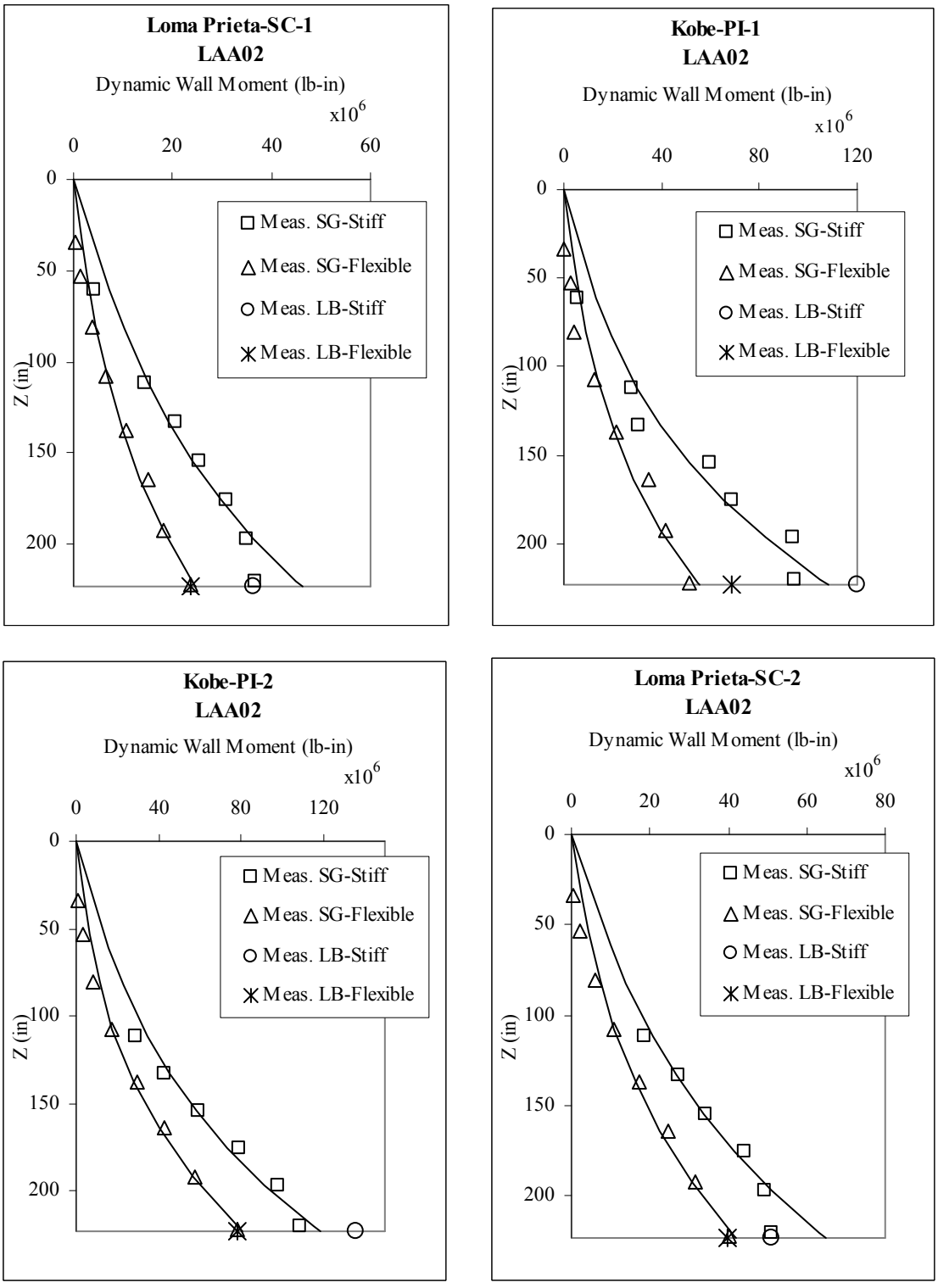

Fig. 4.20 Maximum dynamic wall moment profiles measured by strain gages and force-sensing bolts on south stiff and north flexible walls for Loma Prieta-SC-1 and 2 and Kobe-PI-1 and 2 for LAA02.

The maximum dynamic wall moment distributions interpreted from the strain gage and force-sensing bolt measurements for the south stiff and north flexible walls are presented in Figures A.30–A32 for the different shaking events in experiments LAA01 and LAA02. Figure 4.20 presents an example of the maximum dynamic moment profile figures for the Loma Prieta-SC-1 and 2 and Kobe-PI-1 and 2 shaking events. The dynamic wall moments still contain the moments due to the wall inertial forces; however they eliminate the increment in the static moment on the walls as a result of compaction of the backfill. Thus, they provide a more representative measure of the actual dynamic loading on the walls. Cubic polynomial curves usually provided the best least-squares fits for the dynamic wall moment increment profiles data with R-square generally greater than 0.98.

4.7.3 Wall Inertial Moments

In the pseudostatic method of analysis, the effect of earthquake loading is modeled by an additional set of static forces representing the inertial forces acting on the retaining wall–backfill system. As mentioned in Chapter 2 (Literature Review), inertial forces acting on retaining structures are generally ignored in most seismic earth pressures theories, especially for cantilever retaining walls. Moreover, the literature review revealed several studies wherein the total dynamic moments or forces acting on the cantilever retaining walls were reported as being induced by dynamic earth pressures without any attempt to evaluate the contribution of the wall inertial effects to the total wall forces and moments. It is important to note that the M-O and Seed and Whitman (1970) methods do not account for wall inertial effects in their dynamic earth pressure estimates. Richards and Elms (1979) observed that wall inertia for gravity retaining walls can be of the same order as that of the dynamic soil pressure computed by the M-O method and should be properly accounted for. In an attempt to provide a better understanding of the seismic behavior of cantilever retaining walls and an accurate estimate of seismically induced lateral earth pressures, wall inertial effects were evaluated in this study. Their contribution to the dynamic response of the wall was investigated based on data recorded in the dynamic centrifuge experiments.

The wall inertial moments at different locations on the stiff and the flexible walls were estimated for LAA02 according to the method outlined in Section 4.1.5. The wall inertial moments were compared to dynamic wall moments interpreted from the strain gage and force-

sensing bolt measurements and including the combined effects of both dynamic earth pressures and wall inertia. Figure 4.2 presents an example of the wall inertial contribution to the dynamic wall moment time series interpreted at the bases of the south stiff and north flexible walls and at the SG1 location for the Loma Prieta-SC-1 shaking event in LAA02. Comparison figures of the wall inertial moments and dynamic wall moment time series for all the LAA02 shaking events are included in Figures A.33–A.43. Table 4.9 presents the contribution in percentage of the estimated wall inertial moments to the dynamic wall moments interpreted from the strain gage data at the bases of the south stiff and north flexible walls for LAA02. Values presented in Table 4.9 correspond to the time at which the maximum dynamic wall moment occurred on the walls.

Table 4.9 Ratio of wall inertial moment estimates to dynamic wall moments interpreted from strain gage data at bases of south stiff and north flexible walls for LAA02.

	Wall Inertial Moment Estimate/Measured Dynamic Wall Moment	
	Stiff	**Flexible**
Loma Prieta-SC-1	50%	99%
Kobe-PI-1	23%	77%
Kobe-PI-2	31%	53%
Loma Prieta-SC-2	47%	75%
Kocaeli-YPT060-2	95%	174%
Kocaeli-YPT060-3	87%	150%
Kocaeli-YPY330-2	88%	186%
Kobe-TAK090-1	34%	10%
Kobe-TAK090-2	44%	96%
Loma Prieta-WVC270	90%	194%
Kocaeli-YPT330-3	102%	209%

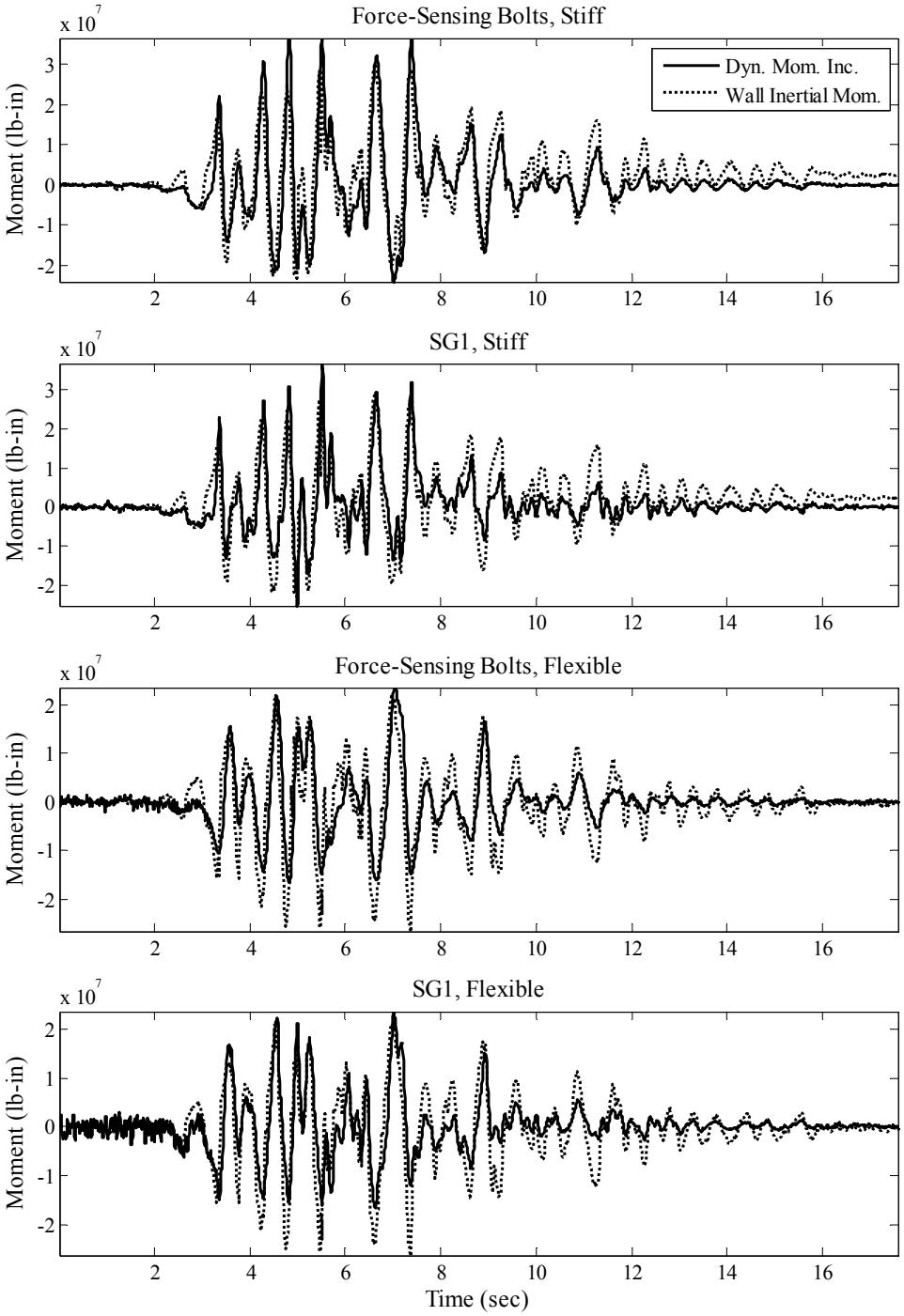

Fig. 4.21 Dynamic wall moment time series interpreted from SG1 and force-sensing bolt data and corresponding wall inertial moment estimates on south stiff and north flexible walls for Loma Prieta-SC-1 for LAA02.

As shown in Figure 4.21, the contribution of the wall inertial moments to the dynamic wall moments is substantial. The periods of the wall inertial moment time series are close to those of the dynamic wall moment time series. Table 4.9 shows that a large percentage of the maximum dynamic wall moment interpreted from the strain gage data at the bases of the stiff and flexible walls is generally induced by wall inertia. Wall inertia is therefore important and should be accounted for appropriately in the seismic design of retaining structures. Moreover, moment time series recorded by the strain gages and force-sensing bolts cannot be used directly to infer dynamic earth pressures.

4.7.4 Total and Dynamic Earth Pressure Moments

Moment time series interpreted from the strain gage measurements and directly measured by the force-sensing bolts on the south stiff and north flexible walls were corrected to reflect only static and dynamic earth pressures by subtracting the corresponding estimated wall inertial moment time series. The maximum total earth pressure moment profiles interpreted from the strain gage and force-sensing bolt data for the different shaking events in experiment LAA02 are presented in Figures A.44–A.45. Figure 4.22 presents an example of the maximum total earth pressure profile figures for the Loma Prieta-SC-1 and 2, and Kobe-PI-1 and 2 shaking events. Static active and at-rest moment estimates at the bases of the walls are included in Figure 4.22 for reference. It is important to note that the maximum moment profiles presented in this section do not correspond to the same maximum total wall moment profiles presented in Sections 4.7.2. Cubic polynomial curves usually provided good least-squares fits for the maximum total earth pressure moment profiles data with R-square generally greater than 0.98.

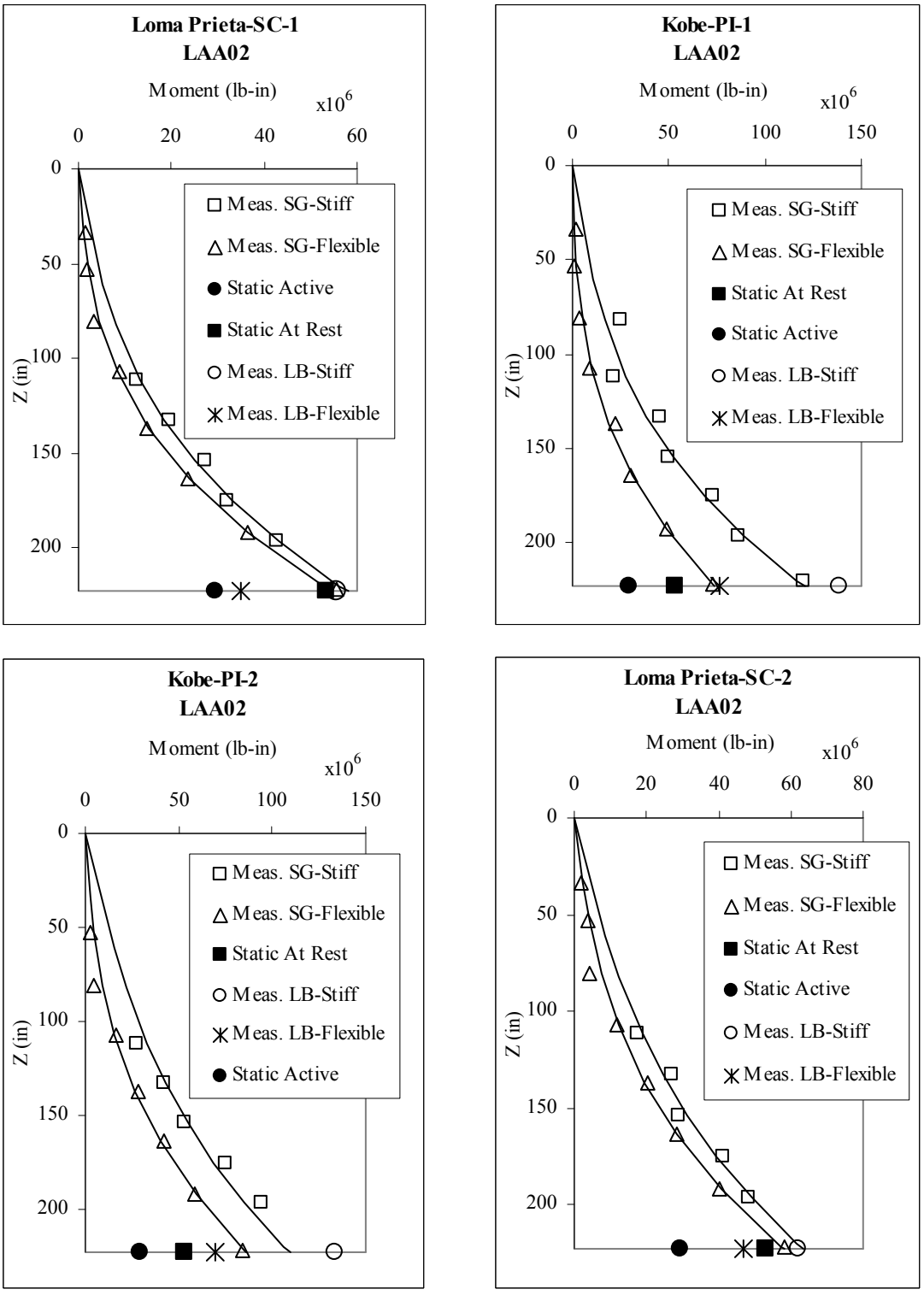

Fig. 4.22 Maximum total earth pressure moment profiles interpreted from strain gage and force-sensing bolt measurements and static active and at-rest moment estimates on south stiff and north flexible walls for Loma Prieta-SC-1 and 2, and Kobe-PI-1 and 2 for LAA02.

The maximum dynamic earth pressure moment profiles interpreted from the strain gage and force-sensing bolts data and induced by dynamic earth pressure increments on the south stiff and north flexible walls are presented in Figures A.46–A.48 for all the LAA02 shaking events. Figure 4.23 presents an example of these figures for Loma Prieta-SC-1 and Kobe-PI-1 shaking events. Cubic polynomial curves provided good least-squares fits for the corrected dynamic moment increment profiles.

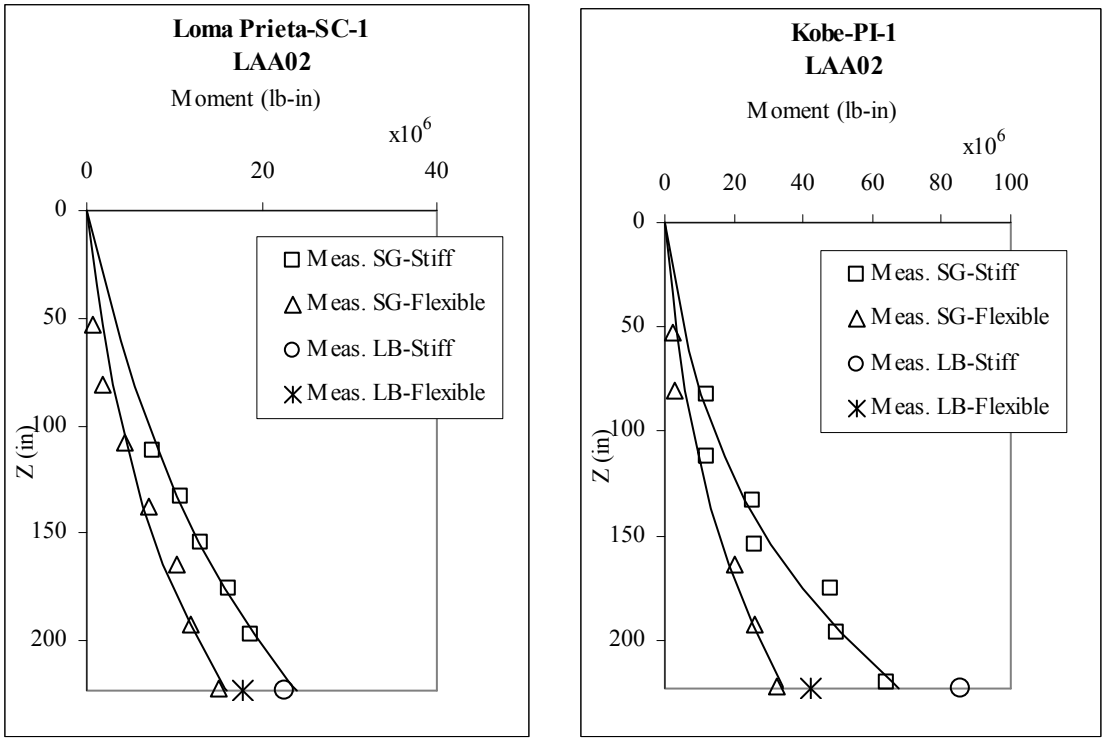

Fig. 4.23 Maximum dynamic earth pressure moment profiles interpreted from strain gage and force-sensing bolt measurements on south stiff and north flexible walls for Loma Prieta-SC-1 and Kobe-PI-1 for LAA02.

4.8 WALL DEFLECTIONS

Horizontal displacement transducers located at the tops of the stiff and flexible walls in both centrifuge experiments were used to measure deflections at the tops of the walls during shaking, as well as static offsets. The instrument rack to which displacement transducers were attached experienced vibration during spinning and shaking. This vibration resulted in large apparent deflections and its effect is obvious in the recorded displacement time series, as shown in Figure

4.24. As a result, dynamic displacement data recorded by the linear potentiometers and the LVDTs were considered inaccurate and were not used in this study. Data recorded by the displacement transducers were used only to determine static offsets.

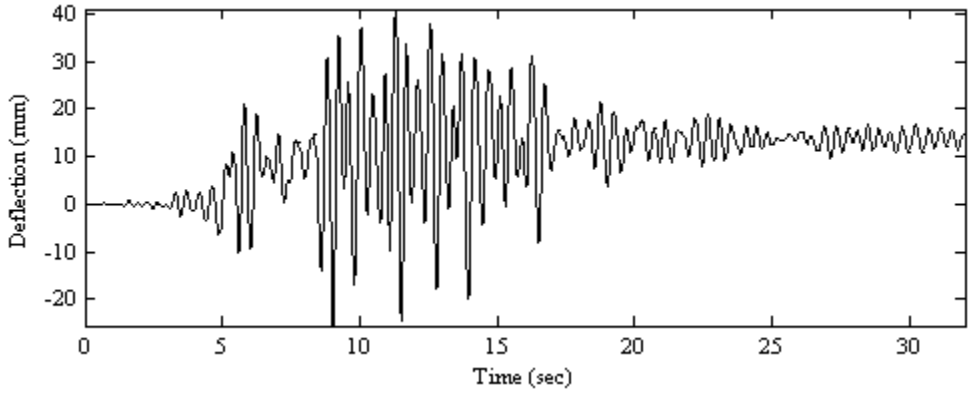

Fig. 4.24 Displacement time series recorded at top of south stiff wall by instrument L9 during Loma Prieta-1 in experiment LAA01.

Acceleration time series recorded at the tops of the walls were double-integrated to obtain displacement time series that were used to determine the transient deflections at the tops of the walls. Static offsets cannot be obtained from the double integration of the acceleration time series due to the high-pass filtering of the records. Table 4.10 presents the normalized static offsets measured at the tops of the four walls after the different shaking events in both sets of experiments. The static offsets were normalized by the heights of the walls (H = 18.6 ft). It should be noted that the displacement time series for the Kobe-PI-1 shaking event in experiment LAA02 were very noisy due to the power supply problem mentioned in Chapter 3, and therefore the static offsets could not be determined for this shaking event. Moreover, the two displacement transducers located at the top of the north flexible wall were damaged in experiment LAA02 and static offset measurements at this location are not available.

Table 4.10 Normalized static offset increments measured at tops of stiff and flexible walls after different shaking events in experiment LAA01 and LAA02.

	Normalized Static Offset at Tops of Walls			
	South Stiff	North Stiff	North Flexible	South Flexible
Loma Prieta-1, LAA01	0.003	0.001	0.006	0.000
Loma Prieta-2, LAA01	0.001	0.000	0.001	0.001
Kobe, LAA01	0.001	0.001	0.001	0.001
Loma Prieta-3, LAA01	0.000	0.000	0.000	0.001
Loma Prieta-SC-1, LAA02	0.003	0.000	-	0.000
Kobe-PI-1, LAA02	-	-	-	-
Kobe-PI-2, LAA02	0.002	0.003	-	0.029
Loma Prieta-SC-2, LAA02	0.000	0.000	-	0.000
Kocaeli-YPT060-2, LAA02	0.000	0.001	-	0.001
Kocaeli-YPT060-3, LAA02	0.000	0.000	-	0.000
Kocaeli-YPT330-2, LAA02	0.000	0.000	-	0.002
Kobe-TAK090-1, LAA02	0.001	0.000	-	0.001
Kobe-TAK090-2, LAA02	0.000	0.000	-	0.000
Loma Prieta-WVC270, LAA02	0.000	0.000	-	0.000
Kocaeli-YPT330-3, LAA02	0.000	0.000	-	0.000

Table 4.11 contains the maximum transient deflections during loading obtained by double integrating the acceleration time series and normalized by the height of the walls (H = 18.6 ft). Table 4.11 shows that the maximum normalized transient deflections at the tops of the stiff walls exceeded 0.004H only for the LAA01 shaking events and for the Kobe motions during LAA02, while the maximum normalized transient deflections at the tops of the flexible walls generally exceeded 0.004H for most shaking events.

Table 4.11 Maximum transient deflections at tops of stiff and flexible walls during different shaking events in experiment LAA01 and LAA02.

	Normalized Transient Deflection			
	North Stiff	South Stiff	North Flexible	South Flexible
Loma Prieta-1, LAA01	0.0111	0.0050	0.0096	0.0024
Loma Prieta-2, LAA01	0.0125	0.0034	0.0097	0.0033
Kobe, LAA01	0.0149	0.0057	0.0104	0.0052
Loma Prieta-3, LAA01	0.0140	0.0046	0.0125	0.0038
Loma Prieta-SC-1, LAA02	0.0024	0.0035	0.0036	0.0022
Kobe-PI-1, LAA02	0.0041	0.0041	0.0099	0.0032
Kobe-PI-2, LAA02	0.0042	0.0041	0.0084	0.0056
Loma Prieta-SC-2, LAA02	0.0016	0.0024	0.0043	0.0031
Kocaeli-YPT060-2, LAA02	0.0007	0.0013	0.0019	0.0006
Kocaeli-YPT060-3, LAA02	0.0013	0.0019	0.0032	0.0013
Kocaeli-YPT330-2, LAA02	0.0032	0.0033	0.0039	0.0031
Kobe-TAK090-1, LAA02	0.0062	0.0080	0.0155	0.0069
Kobe-TAK090-2, LAA02	0.0146	0.0201	0.0194	0.0230
Loma Prieta-WVC270, LAA02	0.0008	0.0014	0.0032	0.0008
Kocaeli-YPT330-3, LAA02	0.0009	0.0016	0.0023	0.0007

4.9 SUMMARY

Recorded data from the series of centrifuge experiments in this study show that ground motions are consistently amplified at the tops of the walls and that acceleration at the top of the soil crosses over the 45° line, indicating attenuation of the large-magnitude input shaking events. Moreover, soil settlement and densification occurred as a result of shaking, especially after large shaking events such as Kobe. The dynamic wall moments recorded by the strain gages and the force-sensing bolts include the combined effects of earth pressures and wall inertia. Estimates of wall inertial moments were used to back out the contribution of dynamic earth pressures to the overall dynamic moments. The data show that the contribution of wall inertial moments to the dynamic wall moments is significant and should be properly accounted for in the design of retaining walls. Recorded dynamic moment profiles have a cubic distribution with depth. Earth pressures measured using the Flexiforce sensors were compared to those interpreted from the strain gage measurements. The results show that the total earth pressures consistently increase monotonically downward, in a manner that is typically observed and assumed under static

conditions. This observation runs counter to the typical assumptions made in the current design methods and requires careful consideration in any future design methodologies.

Most importantly, comparisons of recorded accelerations, bending moments, and earth pressures show that inertial forces do not act simultaneously on the retaining wall and the backfill. When the inertial force is at its maximum, the dynamic wall moment is at its maximum as well, but the dynamic earth pressure increment is at its minimum at or around zero. The interpretation of this observation is that when the retaining wall is moving in the active direction, total earth pressure is equal to or less than the static earth pressure. Total earth pressure is at its maximum when the wall is at rest or moving in the passive direction. These observations are important in that they provide a better understanding of the seismic behavior of the retaining wall–backfill system and should serve as a basis for the seismic design criteria of cantilever retaining walls.

5 Nonlinear Dynamic Finite Element Model

Numerical models offer a very efficient and cost-effective alternative to experiments and can be used to extend the range of existing data. However, they need to be calibrated against well-documented case histories or experiments. Centrifuge test results provide an excellent database that can be used in calibrating and evaluating dynamic numerical tools, which then can be used for parametric studies and evaluation of various design alternatives.

Therefore a 2-D nonlinear FE model was built to simulate dynamic centrifuge experiment LAA02 and to study the seismic behavior of retaining wall–backfill systems. The model consists of a dry, elasto-plastic 2-D plane-strain quadratic soil mesh with elastic beam-column models of U-shaped cantilever retaining structures attached to the soil mesh with nonlinear springs. The main objective of this effort was to explore how well a numerical model could match observed and recorded data and to develop a predictive capability. Specifically, the FE model was evaluated for its capacity to capture the essential features of the seismic behavior of the retaining wall–backfill systems by comparing the computed responses to those measured in the centrifuge experiments. The sensitivity and the limitations of the FE model were evaluated as well, and are discussed in this chapter. The calibrated FE model was then used for a preliminary evaluation of the scenario of U-shaped retaining structures with dry dense sand backfill which is of interest in future applications.

5.1 OVERVIEW OF OPENSEES

The Open System for Earthquake Engineering Simulations (OpenSees) is an open-source, object-oriented software framework developed by the Pacific Earthquake Engineering Research (PEER) Center. OpenSees allows users to create finite element applications to simulate the response of structural and geotechnical systems subjected to earthquakes (http://opensees.berkeley.edu). It consists of a set of modules to perform the creation of the FE model, specification of an analysis

procedure, selection of responses to be monitored during the analysis, and the output of the results. OpenSees has the additional benefit of containing a large library of linear and nonlinear geotechnical and structural materials that facilitate the realistic simulation of earthquake engineering problems.

Matlab was used to develop the OpenSees mesh and to create soil and structures nodes, and elements. Tcl scripts were written to input the nodes and the elements created by Matlab, and to assign boundary conditions, record different responses, create static and dynamic loading patterns, specify analysis procedure, and perform finite element analysis. The results obtained from OpenSees were processed using Matlab codes to plot different computed responses and compare them to recorded ones.

5.2 DEVELOPMENT AND CALIBRATION OF FINITE ELEMENT MODEL

The 2-D plane-strain FE model of the U-shaped cantilever retaining structures and the backfill and base soil for experiment LAA02 are presented in Figure 5.1. The centrifuge model configuration for experiment LAA02 was presented in profile view and model scale in Figure 3.4. The finite element mesh consisted of a total of 1120 soil nodes, 1020 soil elements, 70 wall nodes, 68 wall elements, and 70 spring elements. The FE model has the same prototype configuration as that of experiment LAA02.

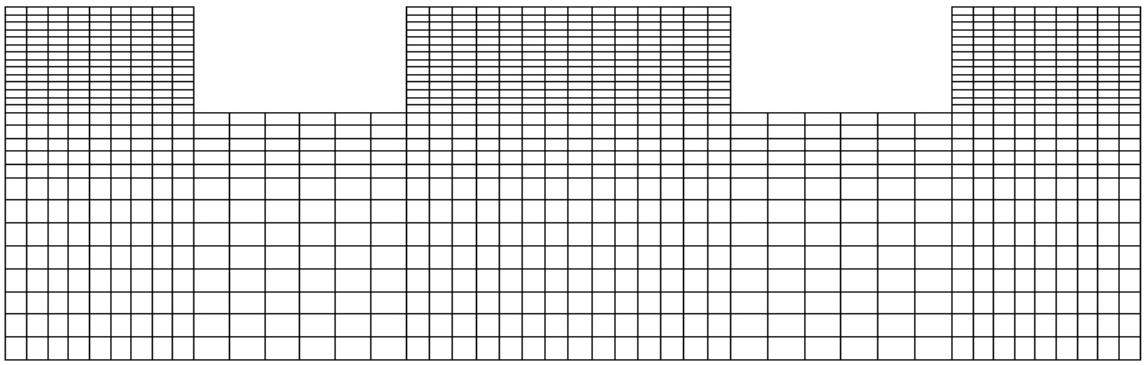

Fig. 5.1 Two-dimensional plane-strain finite element mesh developed for OpenSees.

The U-shaped retaining structures were modeled as linear elastic elements. A 2-D plane-strain, pressure-dependent, elasto-plastic material was used to model the nonlinear response of the dry Nevada sand. Nonlinear springs were used to simulate soil-structure interaction. Detailed

properties of the different components of the FE model and calibration procedures of the various input parameters are described in the following sections.

5.2.1 Properties of Retaining Structures

The properties of the stiff and flexible U-shaped cantilever retaining structures used in both centrifuge experiments are given in Chapter 3. The walls and the bases of these retaining structures were modeled in OpenSees using elastic BeamColumn elements. Each wall consisted of 15 nodes and 14 elements, while each base consisted of 7 nodes and 6 elements. The retaining structures used in the FE model had the same prototype dimensions, mass, and properties as the aluminum structures used in the centrifuge experiments. The FE model parameters of the stiff and flexible retaining structures are given in Tables 5.1 and 5.2, respectively. The connections between the wall and the base of each structure were modeled as rigid moment connections in OpenSees, which means that no rotational flexibility was allowed at the connections.

Table 5.1 FE model properties for stiff retaining structure.

	North Stiff	South Stiff	Base
Height (m)	5.67	5.67	-
Width (m)	-	-	10.86
Thickness (m)	0.30	0.30	0.30
Mass (kg)	3334.34	3452.11	12044.31
Area (m^2)	0.14	0.14	0.25
E (KPa)	7.0E+07	7.0E+07	7.0E+07
I (m^4)	2.43E-03	2.43E-03	1.42E-02

5.2.2 Soil Constitutive Model and Parameter Calibration

The uniform-density dry sand of experiment LAA02 was modeled by single-phase FourNodeQuad elements to simulate dry soil response. A total of 1120 soil nodes and 1020 soil elements were used in the soil mesh as shown in Figure 5.1. PressureDependMultiYield (PDMY) nDMaterial was used to simulate the nonlinear response of sand under general loading conditions (http://opensees.berkeley.edu/OpenSees/manuals/usermanual/).

Table 5.2 FE model properties for flexible retaining structure.

	North Flexible	South Flexible	Base
Height (m)	5.67	5.67	-
Width (m)	-	-	11.32
Thickness (m)	0.30	0.30	0.30
Mass (kg)	2890.39	2937.50	12353.95
Area (m^2)	0.08	0.08	0.25
E (KPa)	7.0E+07	7.0E+07	7.0E+07
I (m^4)	4.26E-04	4.26E-04	1.42E-02

The PDMY soil material is an elasto-plastic material that simulates the essential response characteristics of pressure-sensitive soils subjected to loading. This constitutive soil model is based on the framework of multi-yield surface plasticity, in which a number of conical yield surfaces with different tangent moduli are employed to represent shear stress-strain nonlinearity and confinement dependence of shear strength. The yield surfaces are of the Drucker-Prager type. The model assumes that material elasticity is linear and isotropic, while nonlinearity and anisotropy result from plasticity (Yang 2000). This plasticity-based constitutive soil model is capable of capturing response characteristics such as non-flow liquefaction (cyclic mobility), dilatancy (shear-induced volume contraction or dilation), and the associated shear strain accumulation. The PDMY soil model can be employed to simulate dry, drained, or fully undrained soil responses. During the application of gravity and static loads, the material behavior is linear elastic. In the subsequent dynamic loading phases, the material response is elastic-plastic. A schematic of the PDMY constitutive model response is presented in Figure 5.2. A detailed description of the soil material and the model parameters are given in Yang (2000), Yang et al. (2002, 2003, 2008) and Elgamal et al. (2002, 2003).

The parameters associated with the PDMY constitutive soil model can be grouped into three categories: (1) multi-yield parameters describing the nonlinear shear stress-strain relations and volumetric stress-strain relations, (2) non-associativity parameters describing the coupling of shear-volumetric deformations (contraction and dilation), and (3) liquefaction parameters describing the evolution of liquefaction slip strains. Overall, fifteen major parameters are needed to define the PDMY material. The recommended ranges of PDMY parameter values for sand with different relative densities given by Yang et al. (2008) are presented in Table 5.3.

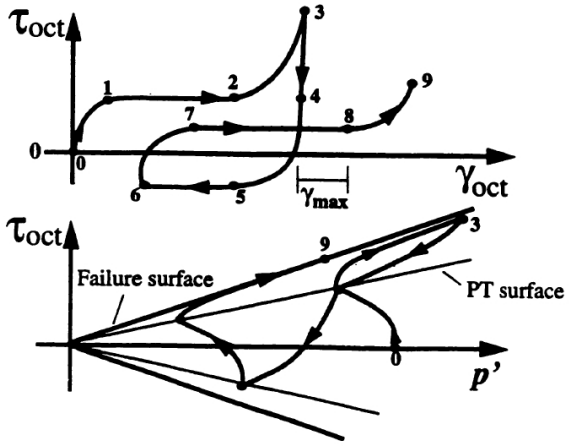

Stage:
0–1: Contractive phase (stress space)
1–2: Perfectly plastic phase (strain space)
2–3: Dilative phase (stress space)
3–4: Unloading phase (stress space)
4–5: Contractive phase in opposite direction
5–6: Neutral strain phase in opposite direction
6–9: Logic of 0–3

Fig. 5.2 Schematic of PressureDependMultiYield soil model (source: Yang 2000).

Table 5.3 Recommended parameters for PDMY material by Yang et al. (2008).

Model Parameters	Loose Sand (15% - 35%)	Medium Sand (35% - 65%)	Medium-Dense Sand (65% - 85%)	Dense Sand (85% -100%)
Mass Density (ton/m^3)	1.7	1.9	2	2.1
Ref. Confining Pressure, P'r (KPa)	80	80	80	80
Ref. Shear Modulus, Gr at P'r (KPa)	5.50E+04	7.50E+04	1.00E+05	1.30E+05
Ref. Bulk Modulus, Br at P'r (KPa)	1.50E+05	2.00E+05	3.00E+05	3.90E+05
Peak Shear Strain	0.1	0.1	0.1	0.1
Pressure Dependent Coefficient	0.5	0.5	0.5	0.5
Friction Angle (deg.)	29	33	37	40
Phase Transformation Angle (deg.)	29	27	27	27
Contraction Constant	0.21	0.07	0.05	0.03
Dilation Constants	d1=0, d2=0	d1=0.4, d2=2	d1=0.6, d2=3	d1=0.8, d2=5
Liquefaction-Induced Strain Constants	liq1=10, liq2=0.02, liq3=1	liq1=10, liq2=0.01, liq3=1	liq1=5, liq2=0.003, liq3=1	liq1=0, liq2=0, liq3=0
Void Ratio	0.85	0.7	0.55	0.45

The PDMY material was used with FourNodeQuad elements, and the input parameter values were based mainly on the centrifuge measurements. The recommendations by Yang et al. (2008), presented in Table 5.3, and Arulmoli et al. (1992) for dry medium-dense Nevada sand, were also considered in the parameter selection and calibration. The initial PDMY parameter values for the medium-dense Nevada sand used in centrifuge experiment LAA02 are presented in Table 5.4. Calibration and selection of the material parameters were performed as follows:

Table 5.4 Initial input parameters for PDMY soil properties in FE model.

Model Parameters	**Dry Medium-Dense Nevada sand (Dr = 74%)**
Initial Mass Density (kg/m^3)	1692
Reference Shear Modulus, G_r (kPa)	5.30E+04
Poisson's Ratio	0.3
Reference Bulk Modulus, B_r (kPa)	1.15E+05
Reference Confining Stress, P'_r (kPa)	54
Peak Shear Strain	0.1
Pressure Dependent Coefficient	0.5
Shear Strain and G/Gmax pairs	Based on Figure 5.4
Friction Angle	35°
Phase Transformation Angle	27°
Contraction Constant	0.05
Dilation Constants	d_1=0.6, d_2=3.0
Liquefaction Induced Strain Constants	0
Number of Yield Surfaces	11
Void Ratio	0.566

1. The dry soil mass density for the medium-dense Nevada sand was measured during experiment LAA02. The initial (before shaking) relative density of the sand was measured to be about 72% with a dry mass density of about 1692 kg/m^3.

2. The low strain shear modulus of soil is defined by $G = G_r \cdot \left(\frac{P'}{P'_r} \right)^d$, where Gr, P′, P′$_r$ and d represent the reference shear modulus, the effective confining pressure, the reference mean effective confining pressure, and the pressure-dependent coefficient, respectively. The pressure-dependent coefficient, d, which defines the variation of G and B as a function of depth or effective confinement P′, is usually assumed to be equal to 0.5. P′$_r$

was taken as 54 KPa corresponding to the middle of the backfill. G_r was calculated based on the shear-wave velocity (Vs) measurements from experiment LAA02 using $G_r = \rho * Vs^2$, where ρ is the soil mass density. The measured value of Vs in the backfill before shaking was about 177 m/sec, and the corresponding G_r was calculated to be around 0.53E+05 KPa.

3. The low strain bulk modulus B_r was defined according to the elastic relation $B_r = \frac{2(1+\mu)}{3(1-2\mu)} \cdot G_r$, where μ is Poisson's ratio taken as $\mu = \frac{Ko}{1+Ko}$. Ko represents the coefficient of the lateral earth pressure at rest, which can be approximated by $Ko = 1 - \sin\phi$ for normally consolidated sand (Jaky 1948).
4. The initial friction angle for the PDMY material was set to 35° based on calibration against the centrifuge results and on values presented in Arulmoli et al. (1992). Once the low strain shear modulus and the modulus reduction curve are specified in OpenSees, the friction angle is automatically computed as $\sin\phi = \frac{3\sqrt{3} \cdot \sigma_m / P'_r}{6 + \sqrt{3} \cdot \sigma_m / P'_r}$, where σ_m is the product of the last modulus and strain pair in the modulus reduction curve and P′r is the reference mean confining pressure. The phase transformation angle defining the boundary between contraction and dilation was set to 27°.
5. The peak octahedral shear strain, γr, at which the maximum shear strength is mobilized at the reference mean effective confining pressure P′r, was set to 0.1 as recommended by Yang et al. (2008).
6. The contraction parameter defining the rate of shear-induced volume decrease for the dry sand model was set to 0.05. The dilation parameters defining the rate of shear-induced volume increase were set to 0.6 and 3.
7. The liquefaction-induced strain constants were set to zero in order to deactivate the liquefaction mechanism.
8. The void ratio was calculated based on the minimum and maximum Nevada sand void ratios and the measured relative density of the sand in experiment LAA02.
9. The number of yield surfaces was set to 11. The yield surfaces were defined in OpenSees based on the shear modulus reduction curve specified as G/Gmax and shear strain pairs. According to the procedure outlined in Zeghal et al. (1995) and Elgamal et al. (2005), the shear stress and shear strain responses at different depths along the centerline of the soil

were estimated using the recorded lateral downhole accelerations (at A24, A26, A27, A30, and A31) for the different shaking events during centrifuge experiment LAA02. The evaluation of the shear stress time series was based on the 1-D shear beam idealization used to describe the site seismic lateral response as $\frac{\partial \tau}{\partial z} = \rho \cdot ii$, where z, τ, ρ, and ii are depth, horizontal shear stress, mass density, and absolute horizontal acceleration, respectively. Applying shear and displacement boundary conditions and utilizing linear interpolation between the downhole accelerations and the shear stress time series were estimated as described in Zeghal et al. (1995). The shear strain time series were evaluated by first double-integrating the acceleration records to obtain absolute displacements, and then dividing the displacement difference between two adjacent downhole stations by the vertical distance between them. The shear stress and shear strain estimates are of second-order accuracy and are representative of the average response midway between the accelerometer locations. The interpreted shear stress-strain loops at accelerometer locations A27 and A30 along the centerline of the sand are shown in Figure 5.3 for shaking events Loma-Prieta-SC-1, Kocaeli-YPT330-1, and Kocaeli-YPT330-2. These events represent strong (maximum shear strain of about 0.2%), weak (maximum shear strain of about 0.02%), and moderate (maximum shear strain of about 0.08%) shaking conditions, respectively. In all three cases, the initial low-strain shear stiffness appears to increase with depth, indicating confinement dependence. As expected, Figure 5.3 shows that the level of damping and of soil nonlinearity increases going from the weak to the moderate and the strong shaking events.

The evaluated shear stress-strain time series were used to estimate the equivalent (secant) shear modulus (G) and the damping ratio (ξ). Figure 5.4 presents the modulus reduction curve G/Gmax evaluated from the selected shear stress-strain loops at location A27. The employed Gmax was defined based on shear-wave velocity measurements as described above. Figure 5.5 presents the damping ratio data evaluated from the corresponding shear stress-strain loops used to estimate G. The Seed and Idriss (1970) modulus reduction and damping curves are presented for comparison in Figures 5.4 and 5.5, respectively.

As shown in Figure 5.5, considerable scatter exists in the damping ratio data and the estimated damping ratio is noticeably higher than the Seed and Idriss (1970) curves.

This observed higher damping can be explained by the fact that the damping ratio data presented in Figure 5.5 do not reflect the soil material damping alone. The estimated damping represents the combination of material damping and additional loss of energy within the centrifuge test system. Moreover, the damping ratio at low shear strain (0.002%) is observed to be around 2.5–3%.

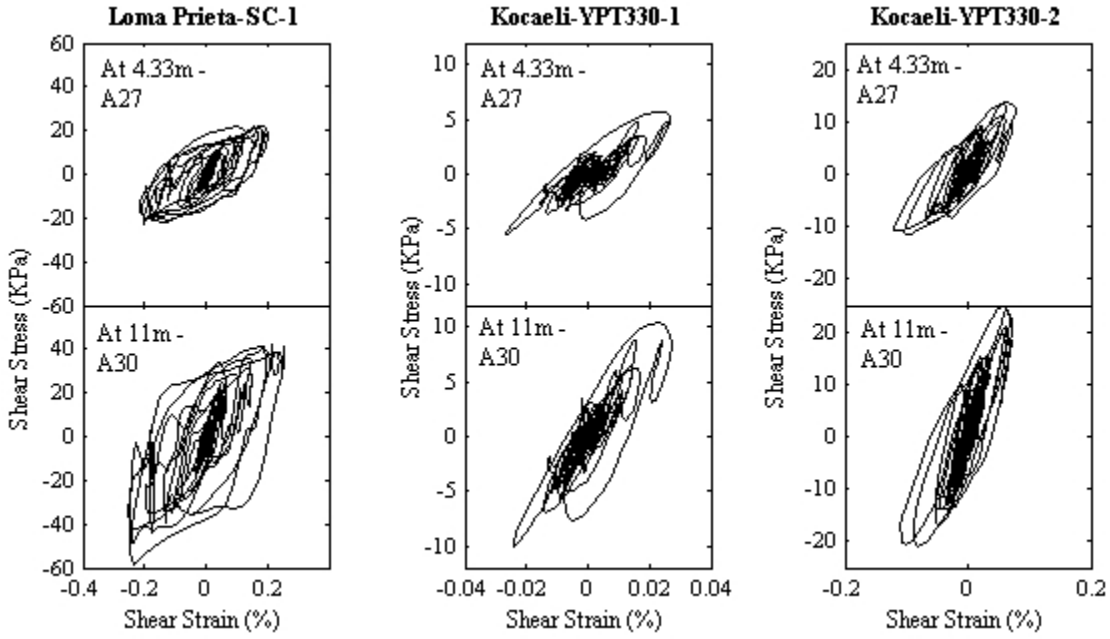

Fig. 5.3 Shear stress-strain time series interpreted from acceleration time series recorded at A27 and A30 for Loma Prieta-SC-1, Kocaeli-YPT330-1, and Kocaeli-YPT330-2 during experiment LAA02.

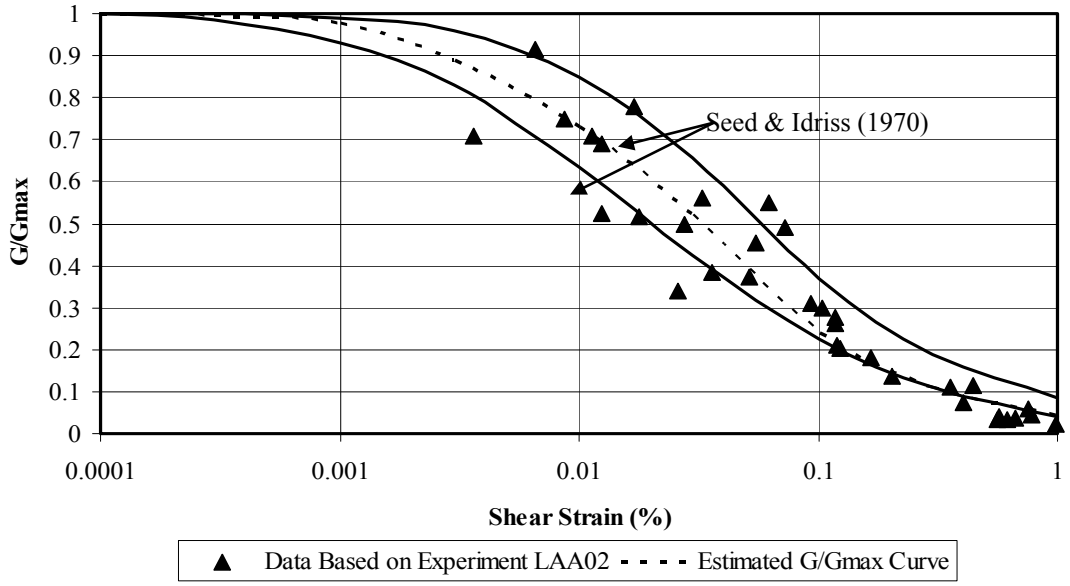

Fig. 5.4 Modulus reduction curve estimated based on acceleration data recorded during different shaking events of centrifuge experiment LAA02.

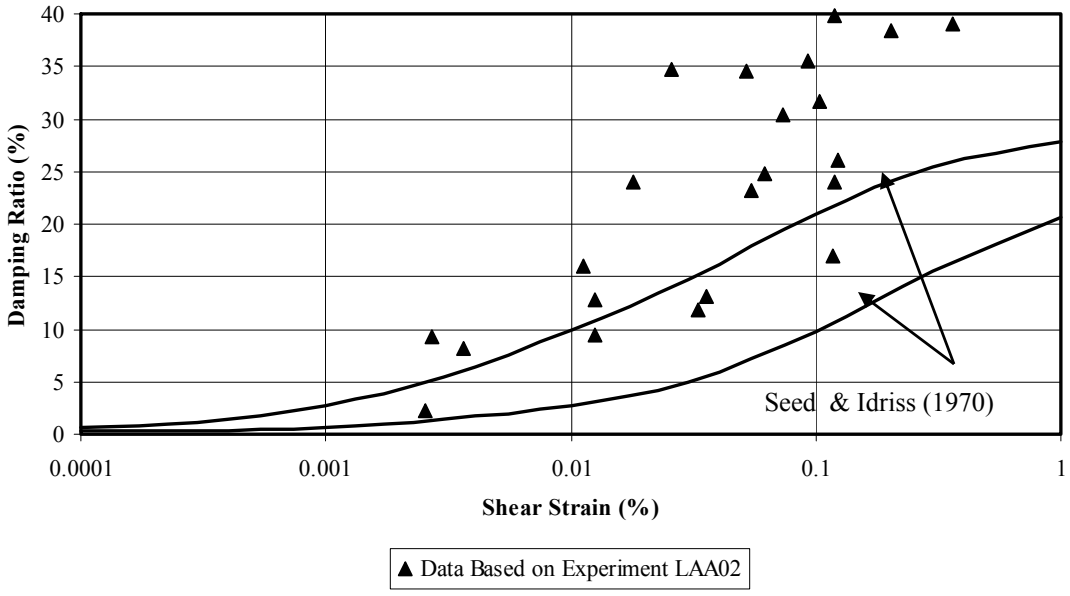

Fig. 5.5 Damping ratio estimated based on acceleration data recorded during different shaking events of centrifuge experiment LAA02.

5.2.3 Soil-Structure-Interface Elements

The soil-structure interaction was simulated by zero-length nonlinear springs. Each nonlinear spring consisted of an elastic-no-tension component in parallel with a viscous component or a dashpot representing radiation damping. The properties of the nonlinear springs were generally selected to be proportional to the strength and the damping of the adjacent soil elements. Horizontal springs were used to connect the backfill soil to the retaining walls while vertical springs were used to connect the bases of the retaining structures to the base soil as shown in Figure 5.6. Both stiff and flexible retaining structures had the same springs' layout for soil-structure interaction. Figure 5.7 presents a close-up view of the backfill soil-retaining wall connection mechanism.

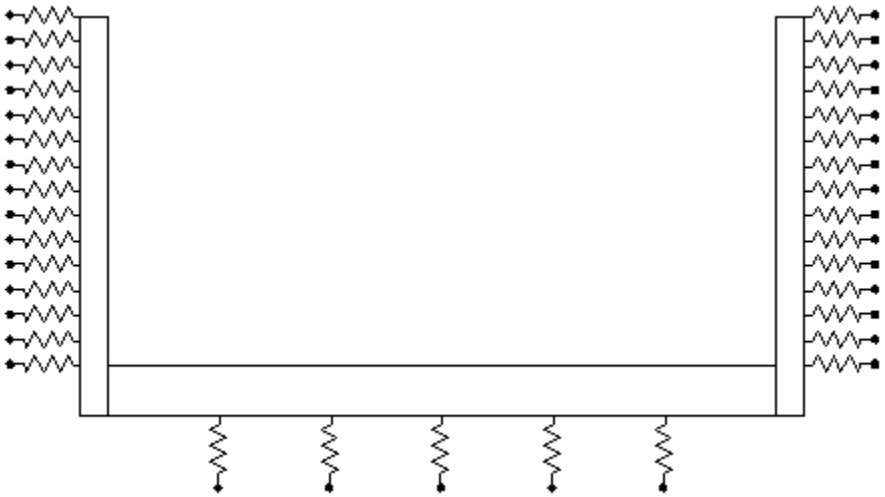

Fig. 5.6 Schematic of retaining structure with soil-structure-spring connections.

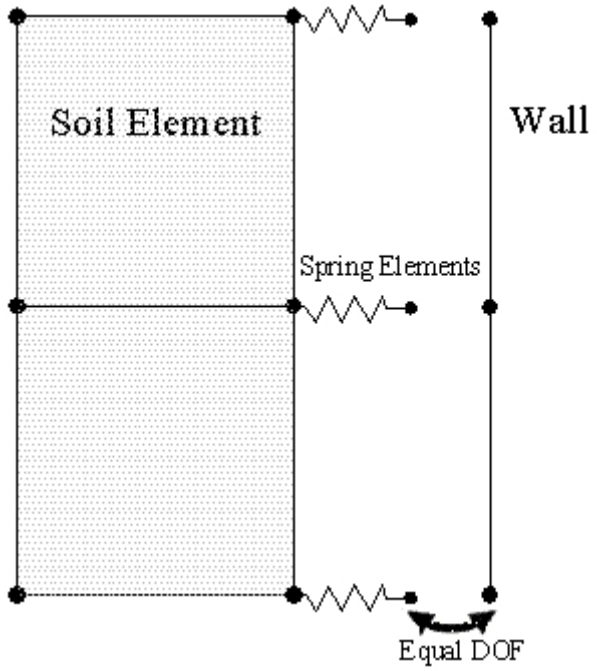

Fig. 5.7 Schematic of backfill soil-retaining wall connections in FE model.

5.2.4 Container and Boundary Conditions

Centrifuge models LAA01 and LAA02 were tested in a flexible shear-beam model container (FSB2), which consists of an aluminum base plate and a series of five stacked aluminum rings separated by soft neoprene rubber providing lateral flexibility. To minimize boundary effects, the container was designed such that its natural frequency is less than the initial natural frequency of the soil (Kutter 1995). The behavior of flexible shear-beam model containers was evaluated in Wilson et al. (1997), Lai et al. (2004), Yang et al. (2004), and Ilankatharan and Kutter (2008). Although Ilankatharan and Kutter (2008) observed that more accurate 2-D modeling of the container boundary conditions results in a more accurate numerical simulation of dynamic centrifuge experiments, researchers agree that flexible model containers do not have a significant impact on the experimental results. Flexible containers are typically regarded as representative of field conditions.

The boundary conditions in the 2-D finite element mesh used herein consisted of (1) base nodes of the soil continuum that were fixed both horizontally and vertically to reproduce the fixed-base conditions of the model container, (2) displacement degrees of freedom of the lateral boundary nodes of the soil continuum that were tied together both horizontally and vertically

using the equalDOF command and penalty method, (3) a traction-free surface, and (4) dynamic excitation defined as the recorded base acceleration.

5.2.5 System Damping

Energy supplied to the centrifuge models is dissipated in a complex manner. In the 2-D FE model, energy is mainly dissipated by hysteresis damping and viscous damping. Hysteretic damping is generally the main energy-dissipation mechanism and is generated in the FE model by the shear stress-strain loops of the PDMY soil material. However, at very low strains, hysteretic damping alone is not sufficient, which can cause unrealistic resonance during wave propagation. Viscous damping becomes the main energy-dissipation mechanism and is modeled using the Rayleigh command. The Rayleigh damping matrix consists of a combination of stiffness and mass-proportional damping matrices described by $[C] = \alpha \cdot [M] + \beta \cdot [K]$, where [M] and [K] are the mass and the stiffness matrices and α and β are the mass and stiffness proportional coefficients, respectively. In the FE model, viscous damping is assumed to be only stiffness proportional, whereby the stiffness proportional coefficient is obtained using an average of 3.5% damping ratio at the soil natural frequency. A stiffness proportional damping coefficient of 0.0044 was used in the FE model.

5.2.6 Input Earthquake Motions

Accelerations recorded during centrifuge testing at the base of the model container were used as input accelerations to the 2-D FE model using the UniformExcitation command in OpenSees. The simulated input earthquakes included input acceleration time series recorded during the Loma Prieta-SC-1, Kobe-PI-2, and Loma Prieta-SC-2 shaking events in experiment LAA02. Peak accelerations varied from 0.49 to 0.8 g. The input acceleration time series and characteristics of the different shaking events used for the FE model can be found in Section 4.2 and Figures A.10, A.12, and A.13.

5.2.7 Finite Element Analysis

The sequence of the finite element analysis included the following steps:

1. The soil mesh was first generated and the base and lateral boundary conditions were specified;
2. Soil behavior was first set to the linear elastic stage;
3. The stiff and flexible retaining structures' nodes and elements were added to the FE model, along with the corresponding soil-structures springs;
4. Structure self-weight was applied as nodal vertical loads and static gravity-loading was applied to the FE model, now including the soil mesh and the retaining structures;
5. Soil behavior was updated to the plastic stage;
6. Based on Yang (2000), it is possible to have a stress point outside the failure surface after the gravity application to the soil model with elastic properties. Adjustment to the stress state in the soil model introduces a force imbalance in the finite element equation system. Yang (2000) recommended including an intermediate plastic phase with high numerical damping in the finite element analysis in order to rapidly dissipate the force imbalance effect. Therefore, gravity loading was applied again to the developed FE model with high numerical damping.
7. Input ground motion was applied to the FE model, and the transient system responses were recorded.

Numbering of nodal degrees of freedom was performed using the reverse Cuthill-Mckee algorithm. Penalty constraints were used to enforce the prescribed displacement boundary conditions using the transformation method. A norm displacement increment test was used to determine whether or not convergence had been achieved at the end of an iterative step. Generally, only several steps were required to converge on a solution for the finite element analysis. A general sparse system of equations was set up and solved using the NewtonLineSearch algorithm, which uses the Newton-Raphson method with line search to advance to the next time step of analysis. A Newmark integrator was used for the transient analysis with γ and β coefficients set to 0.6 and 0.3025, respectively. Rayleigh damping was included in the analysis as described in Section 5.2.5.

5.3 COMPARISON BETWEEN COMPUTED AND RECORDED SYSTEM RESPONSES

One baseline set of parameters (Table 5.4) selected using the calibration procedures described in Section 5.2 was used to analyze three cases consisting of two retaining structures, stiff and flexible, and three shaking events. The shaking events consisted of Loma Prieta-SC-1, Kobe-PI-2 and Loma Prieta-SC-2. Soil mass density, low strain shear modulus, and Poisson ratio were specified for the different cases as measured or interpreted from the corresponding centrifuge shaking events. While the initial friction angle was set as 35° for the Loma Prieta-SC-1 shaking event, friction angle values for the subsequent events were computed in OpenSees based on the specified low strain shear modulus and the modulus reduction curve.

Recorded and computed responses are presented in this section for the three analyzed scenarios. The comparisons include time series of soil and structure accelerations, bending moments and earth pressures on the walls, soil shear stresses and strains, as well as acceleration response spectra. All recorded and computed results are presented in a prototype scale. The deformed meshes, five times magnified, for each of the three scenarios show the soil settlement and permanent wall deflection patterns for the stiff and flexible retaining structures, as presented in Figures 5.8–5.10.

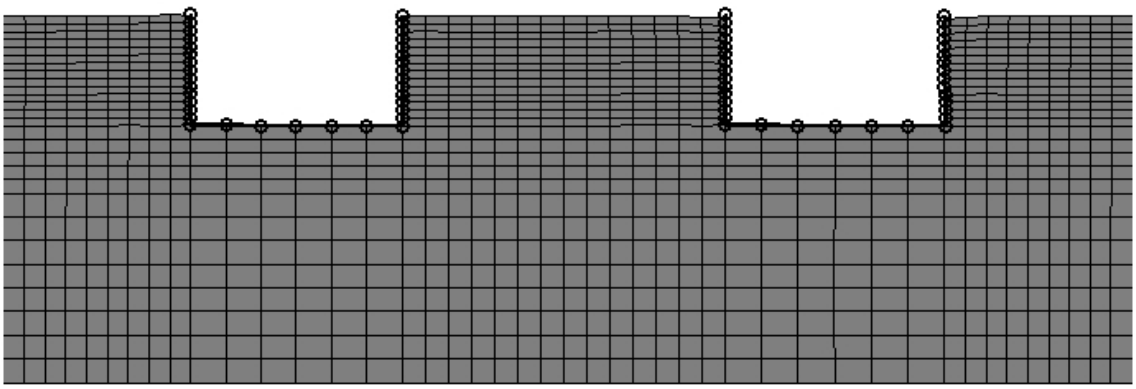

Fig. 5.8 Deformed finite element mesh for Loma Prieta-SC-1 shaking event.

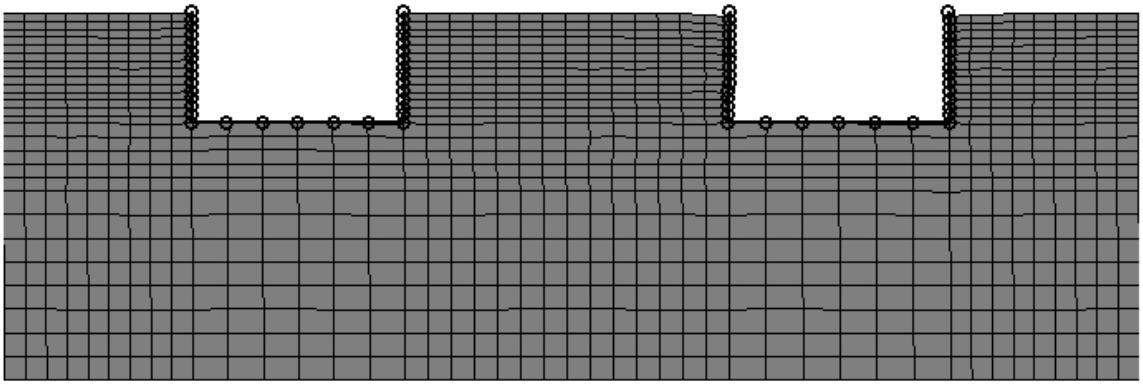

Fig. 5.9 Deformed finite element mesh for Kobe-PI-2 shaking event.

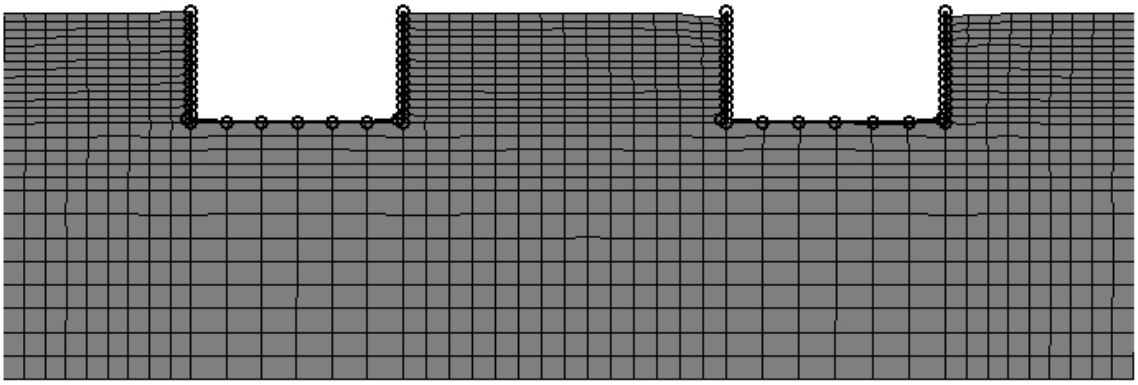

Fig. 5.10 Deformed finite element mesh for Loma Prieta-SC-2 shaking event.

5.3.1 Acceleration and Response Spectra

Figures 5.11–5.13 present the comparisons of the computed and recorded horizontal acceleration time series at the top of the soil in the free field, and at the tops of the stiff and flexible retaining walls. The input acceleration time series for the different shaking events are also presented in these figures. All acceleration time series were corrected such that the horizontal acceleration is positive toward the north end of the model container. Figures 5.14–5.16 present the acceleration response spectra at 5% damping for the recorded and computed acceleration time series at the tops of the south stiff and north flexible walls, at the top of the ground surface in the free field, and within the soil deposit.

As shown in Figures 5.11–5.13, the computed and recorded acceleration time series at the tops of the retaining structures and the soil in the free field were in excellent agreement in terms of the phase and magnitude of accelerations for the three shaking scenarios. Figures 5.14–5.16 show that the computed and recorded acceleration response spectra are in reasonably good agreement. While the computed acceleration response spectra agree very well with the recorded ones at long periods, the computed response consistently underestimates the measured response at shorter periods in Figures 5.14–5.16. This behavior can be explained by the use of an approximation of the Rayleigh damping in the FE model, which consists of only the stiffness proportional component obtained using the first natural mode of the soil column. Since the Rayleigh damping formulation is frequency dependent, the stiffness proportional damping introduces an artificially high damping that filters high-frequency motion content. The use of the extended Rayleigh formulation would possibly reduce the overdamping effect at short periods.

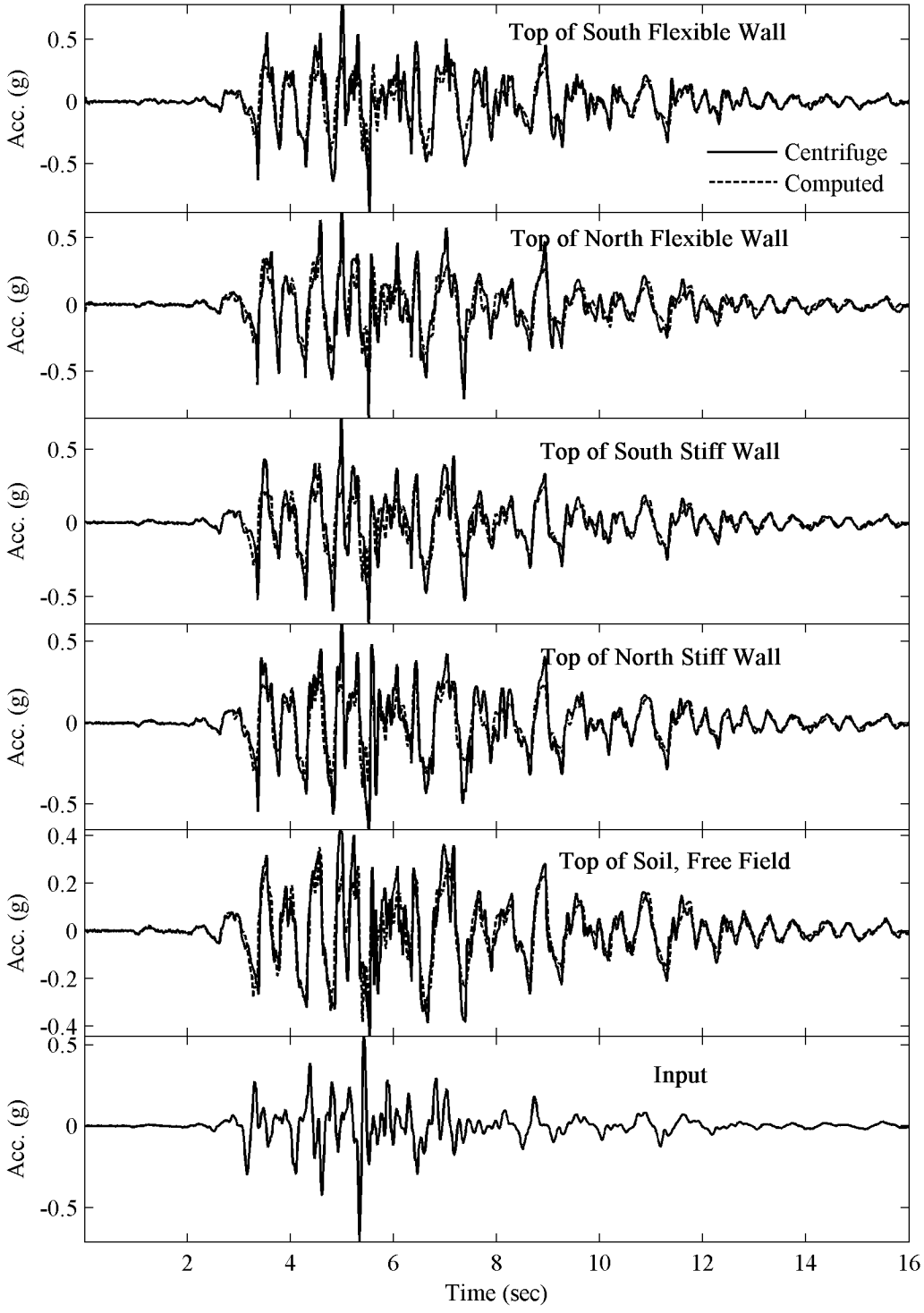

Fig. 5.11 Comparison of recorded and computed accelerations at top of soil in free field and at tops of south stiff and north flexible walls during Loma Prieta-SC-1.

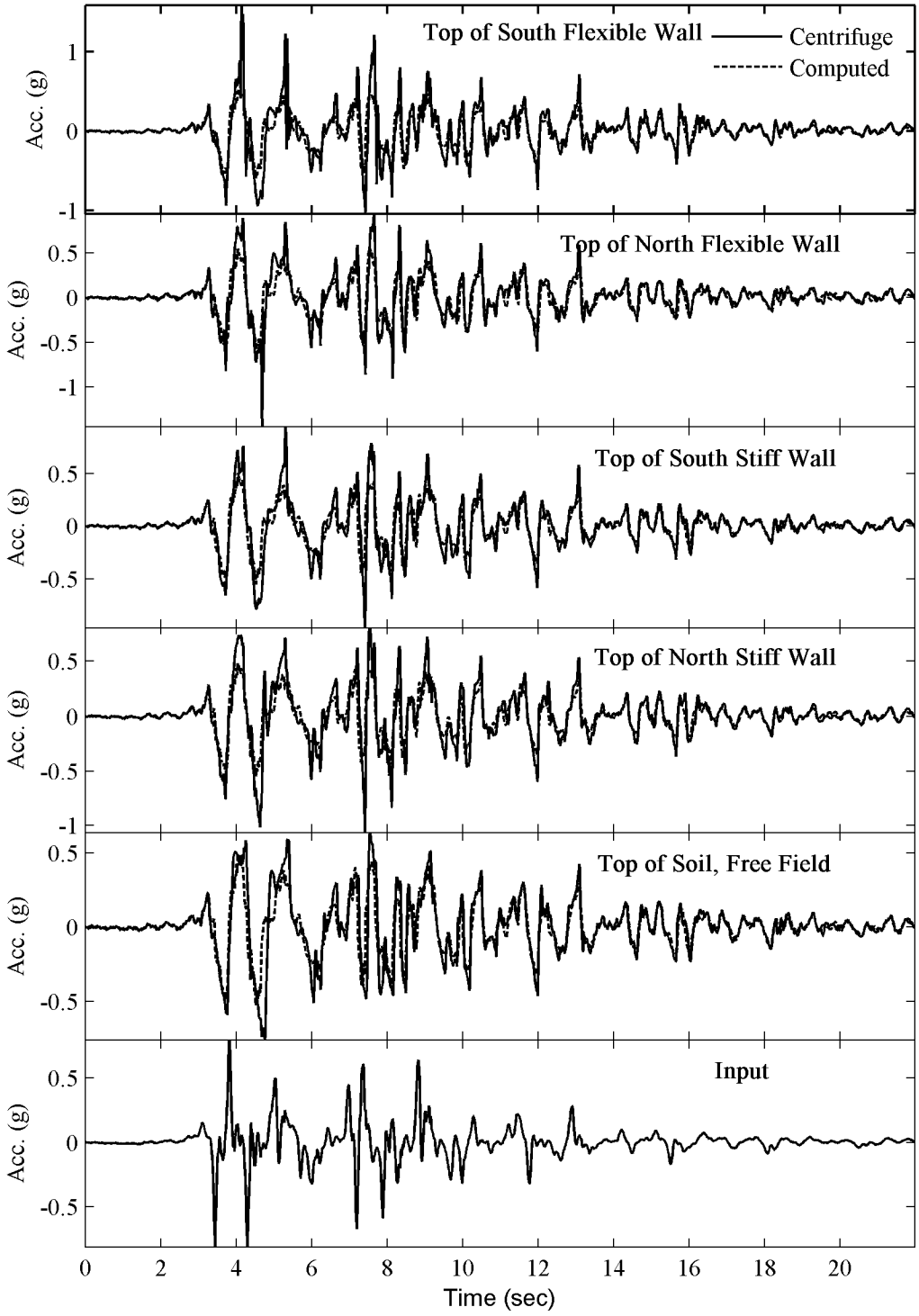

Fig. 5.12 Comparison of recorded and computed accelerations at top of soil in free field and at tops of south stiff and north flexible walls during Kobe-PI-2.

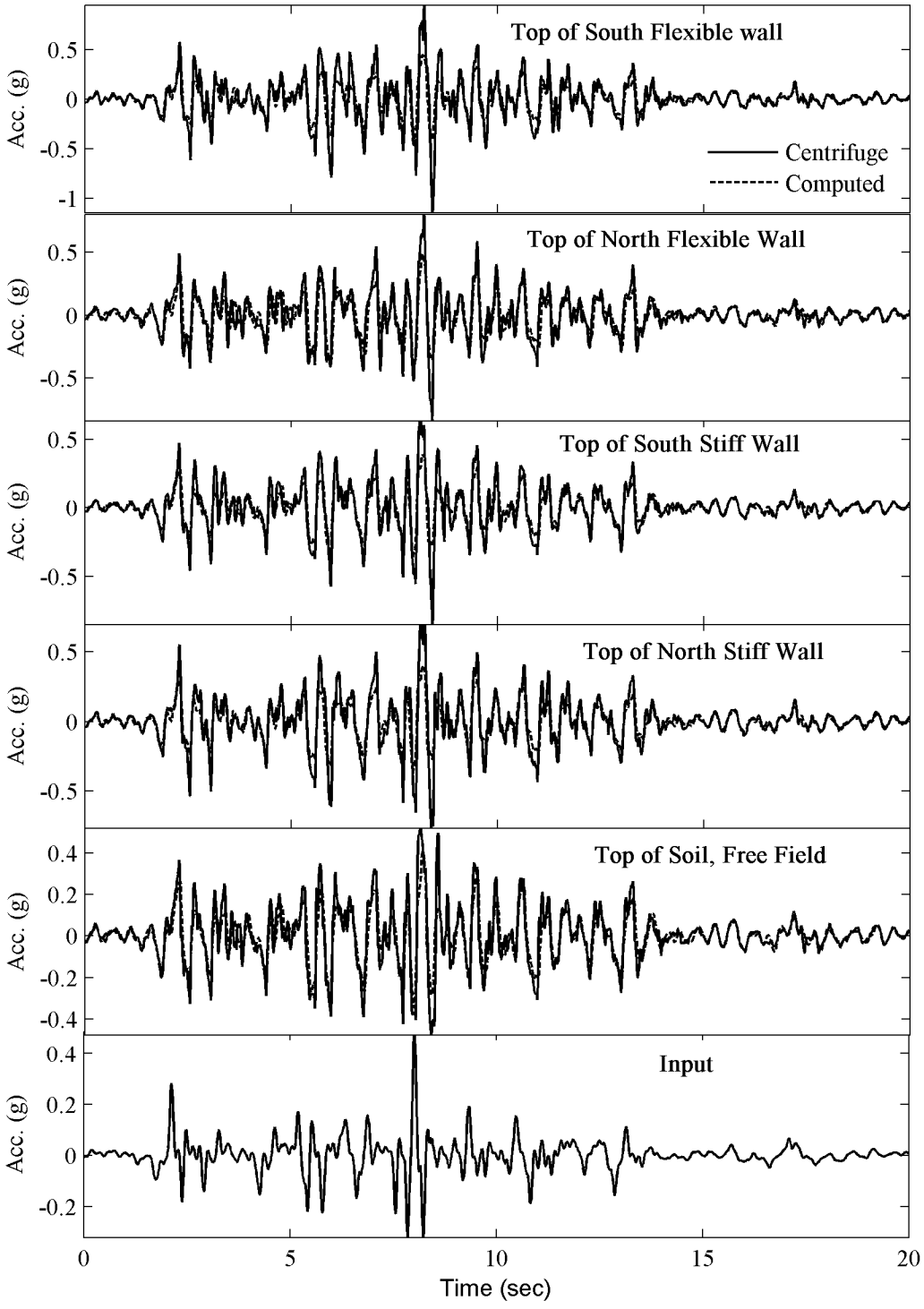

Fig. 5.13 Comparison of recorded and computed accelerations at top of soil in free field and at tops of south stiff and north flexible walls during Loma Prieta-SC-2.

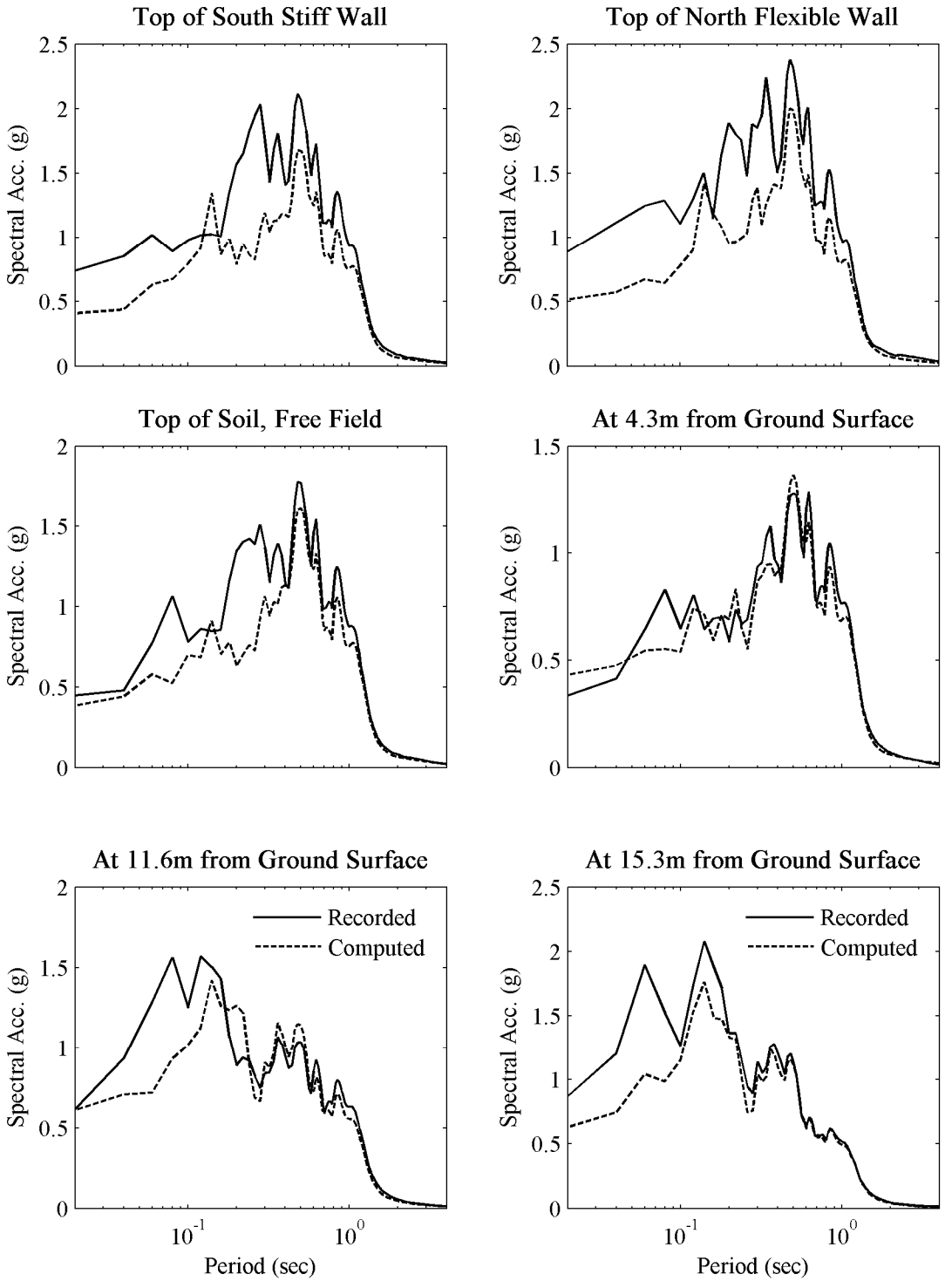

Fig. 5.14 Comparison of recorded and computed acceleration response spectra at 5% damping at top of south stiff and north flexible walls, at top of soil in free field and within base soil during Loma Prieta-SC-1.

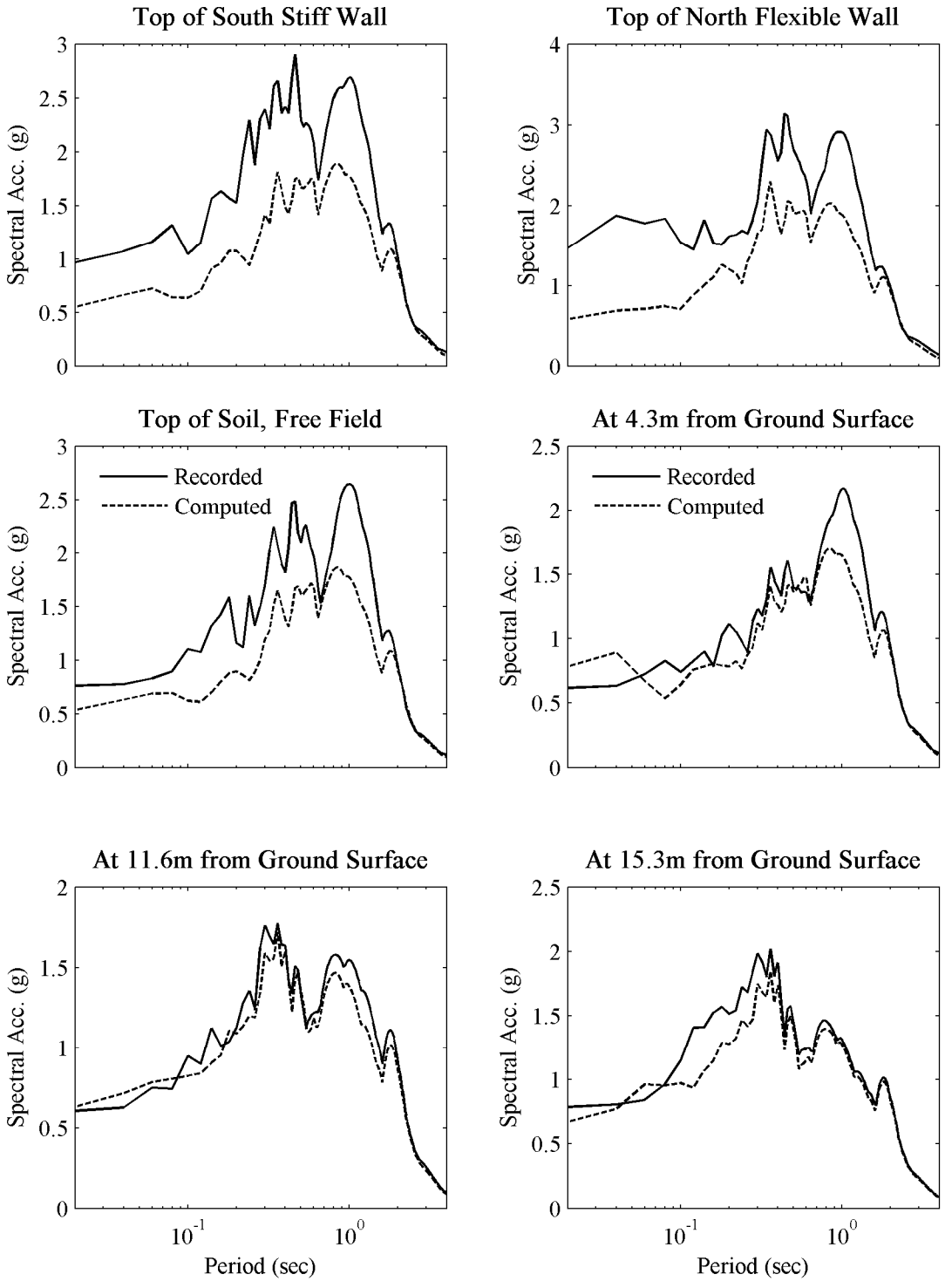

Fig. 5.15 Comparison of recorded and computed acceleration response spectra at 5% damping at top of south stiff and north flexible walls, at top of soil in free field and within base soil during Kobe-PI-2.

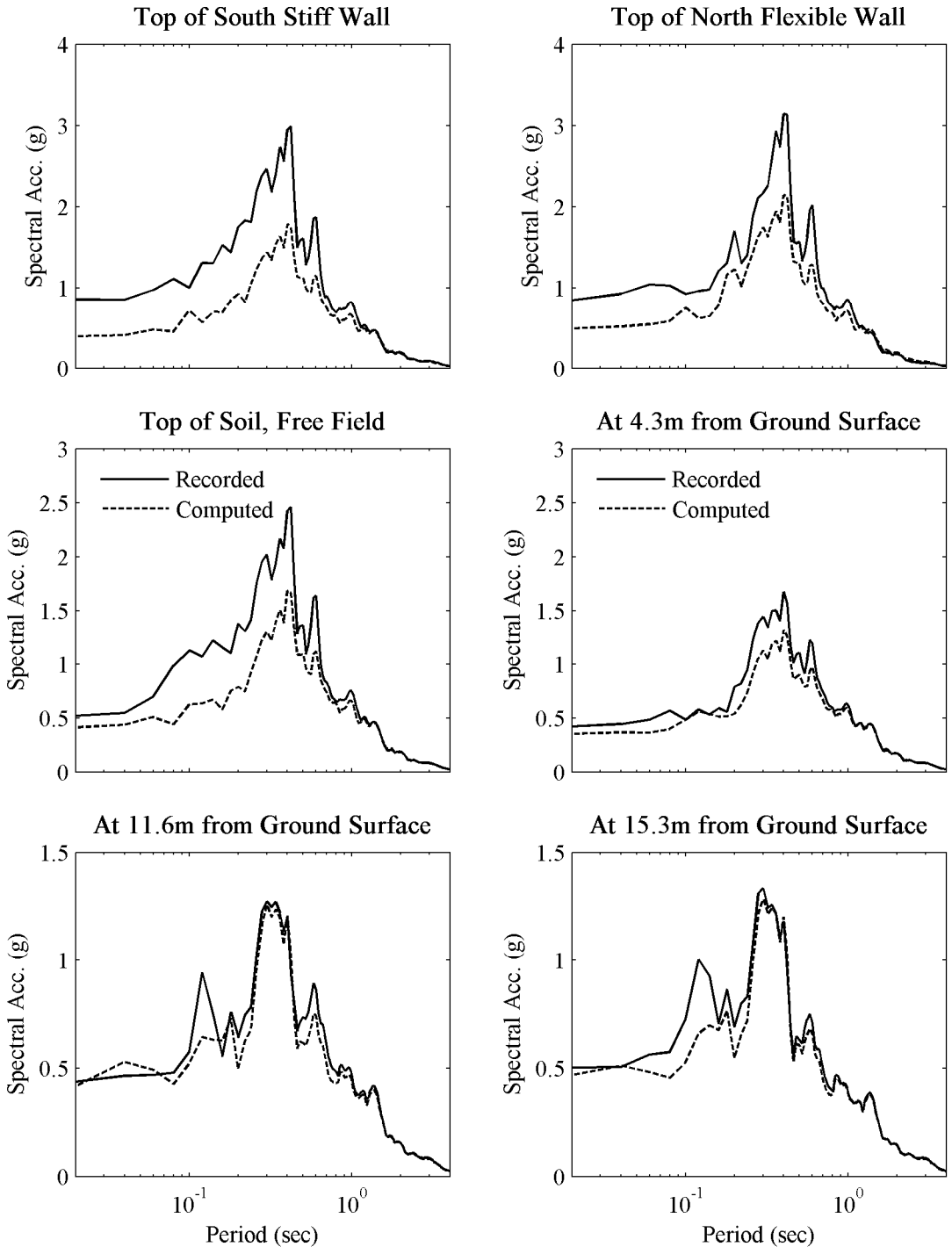

Fig. 5.16 Comparison of recorded and computed acceleration response spectra at 5% damping at tops of south stiff and north flexible walls, at top of soil in free field and within base soil during Loma Prieta-SC-2.

5.3.2 Bending Moments

Figures 5.17–5.19 present recorded and computed total wall moment time series on the south stiff and north flexible retaining walls during the Loma-Prieta-SC-1, Kobe-PI-2, and Loma Prieta-SC-2 shaking scenarios. Figures 5.20–5.22 present the recorded and computed static moment profiles before and after the different shaking events, as well as the maximum total wall moment profiles on the stiff and the flexible walls. The recorded total wall moment time series are interpreted from the strain gage measurements and include contributions from wall inertia as well as static and dynamic earth pressures. The computed total wall moment time series are obtained in OpenSees by using the wall element recorder, and also include effects from wall inertia, and from static and dynamic lateral earth pressures. The moments presented in Figures 5.17–5.22 were corrected such that the positive moment corresponds to wall rotation away from the soil for both stiff and flexible walls.

As shown in Figures 5.17–5.19, the computed and recorded total wall moments agree reasonably well at various strain gage locations on the stiff and flexible walls for the three analyzed shaking events. The computed moments well reproduced the phase and magnitude of the moment responses of the stiff and flexible walls. Moreover, the FE model successfully simulated the gradual increase in the static moment observed in Figures 5.17 and 5.18, as a result of shaking and soil densification.

Figures 5.20–5.22 show that the computed and recorded static and maximum total wall moment profiles agree reasonably well in magnitude and distribution on the stiff and flexible walls. Computed moments on the stiff wall appear to consistently overestimate the static recorded moments before and after shaking. The same behavior was not generally observed on the flexible wall. A possible explanation for this observation is that the wall-base connections were modeled in OpenSees as perfectly rigid, while in actual structures, connections never behave in a perfectly rigid or hinged manner. Moreover, in both centrifuge experiments, the retaining walls were bolted to the bases by applying a measured torque to the force-sensing bolts. This torque was selected in order to avoid excessive pre-loading of the bolts. This process may have introduced a certain degree of rotation flexibility in the connections. Since the degree of flexibility in the wall-base connections was not measured in the centrifuge experiments, it was difficult to incorporate a certain degree of flexibility in the wall-base connections of the FE

model. The above conditions could explain the relatively small observed differences between the computed and recorded moments, especially in the static loading.

Overall, the FE model was able to capture the main features observed in the centrifuge recorded moments in terms of the magnitude and the phase of the time series, the increase of static moments after shaking, and the cubic distributions of the static and total moments along the depth of the walls.

5.3.3 Lateral Earth Pressures on Retaining Walls

Figures 5.23–5.25 present a comparison of the computed and recorded total lateral earth pressures at various locations on the south stiff and north flexible walls for the three analyzed shaking scenarios. Earth pressure time series recorded by the Flexiforce sensors during centrifuge experiment LAA02 are also presented in these figures. Computed earth pressure time series were obtained from the spring forces by dividing each force by the contributing area to obtain corresponding lateral earth pressure. Lateral earth pressures, presented in Figures 5.23–5.25, were corrected such that positive earth pressure corresponds to a force acting on the wall in the direction away from the backfill.

As shown in these figures, there was a varying degree of agreement between the computed and recorded total earth pressures on the stiff and the flexible walls for the different shaking scenarios. Static earth pressures before shaking were not always adequately estimated by the FE model. Observed differences in the static earth pressures before and after shaking can be attributed to the fact that the wall-base connections were modeled in OpenSees as rigid connections, while in reality a small degree of flexibility is likely to have been experienced at the connections as discussed in Section 5.3.2. Moreover, the computed earth pressure time series show an increase in static earth pressure after the Loma Prieta-SC-1 and Kobe-PI-2 shaking scenarios. A similar type of response is observed in the recorded earth pressures.

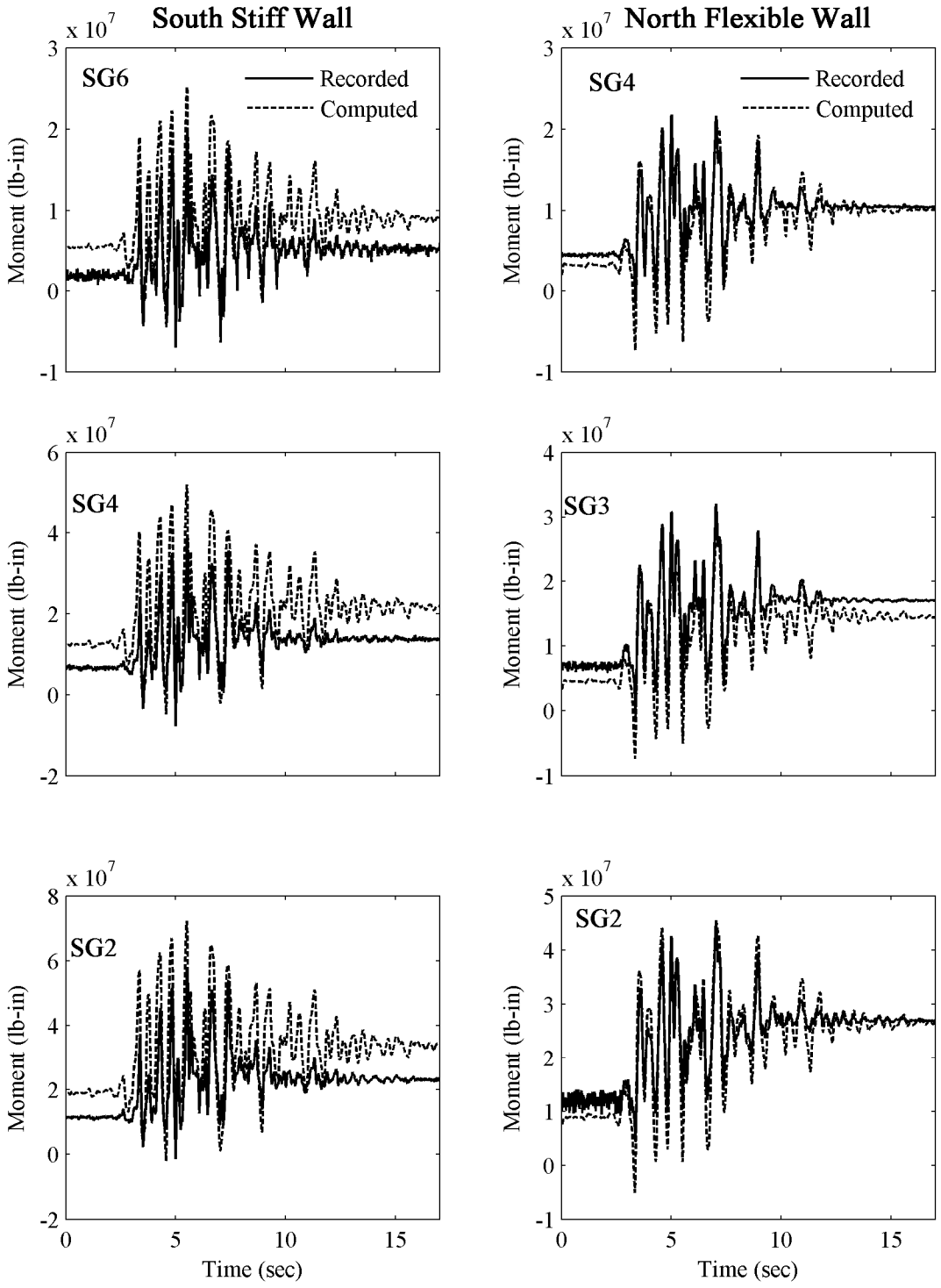

Fig. 5.17 Comparison of computed and recorded total wall moment time series at different strain gage locations on south stiff and north flexible wall during Loma Prieta-SC-1.

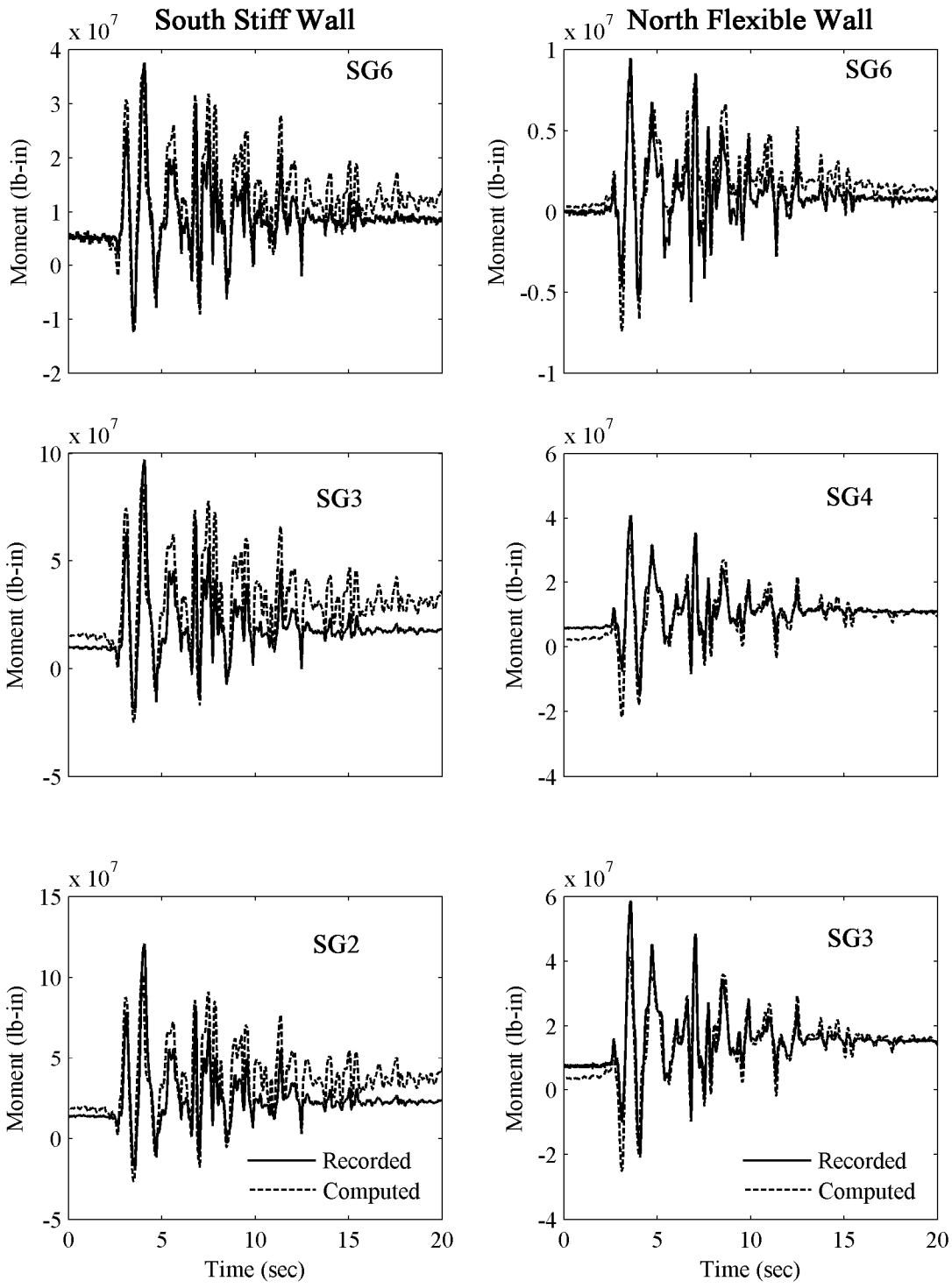

Fig. 5.18 Comparison of computed and recorded total wall moment time series at different strain gage locations on south stiff and north flexible wall during Kobe-PI-2.

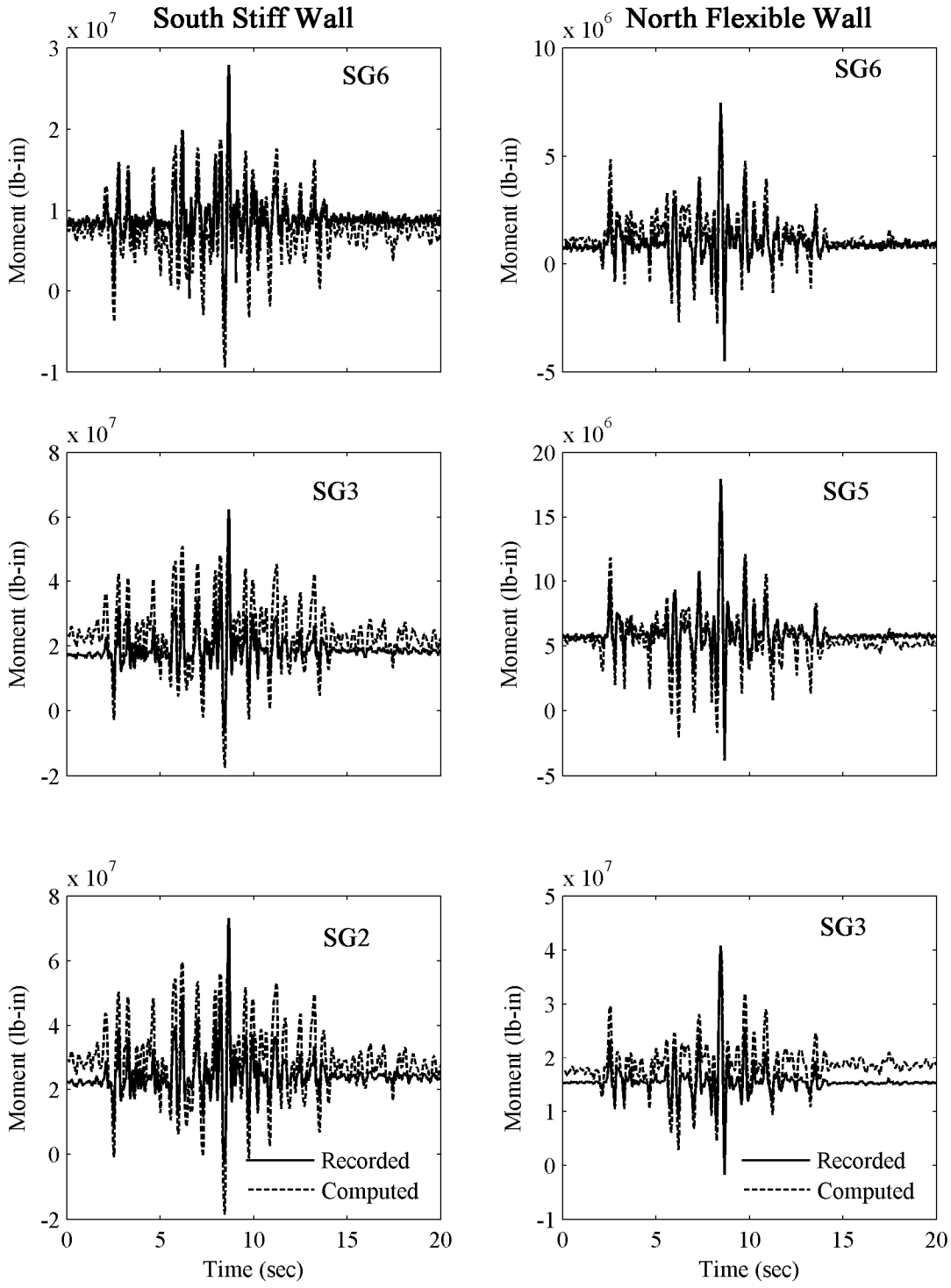

Fig. 5.19 Comparison of computed and recorded total wall moment time series at different strain gage locations on south stiff and north flexible wall during Loma Prieta-SC-2.

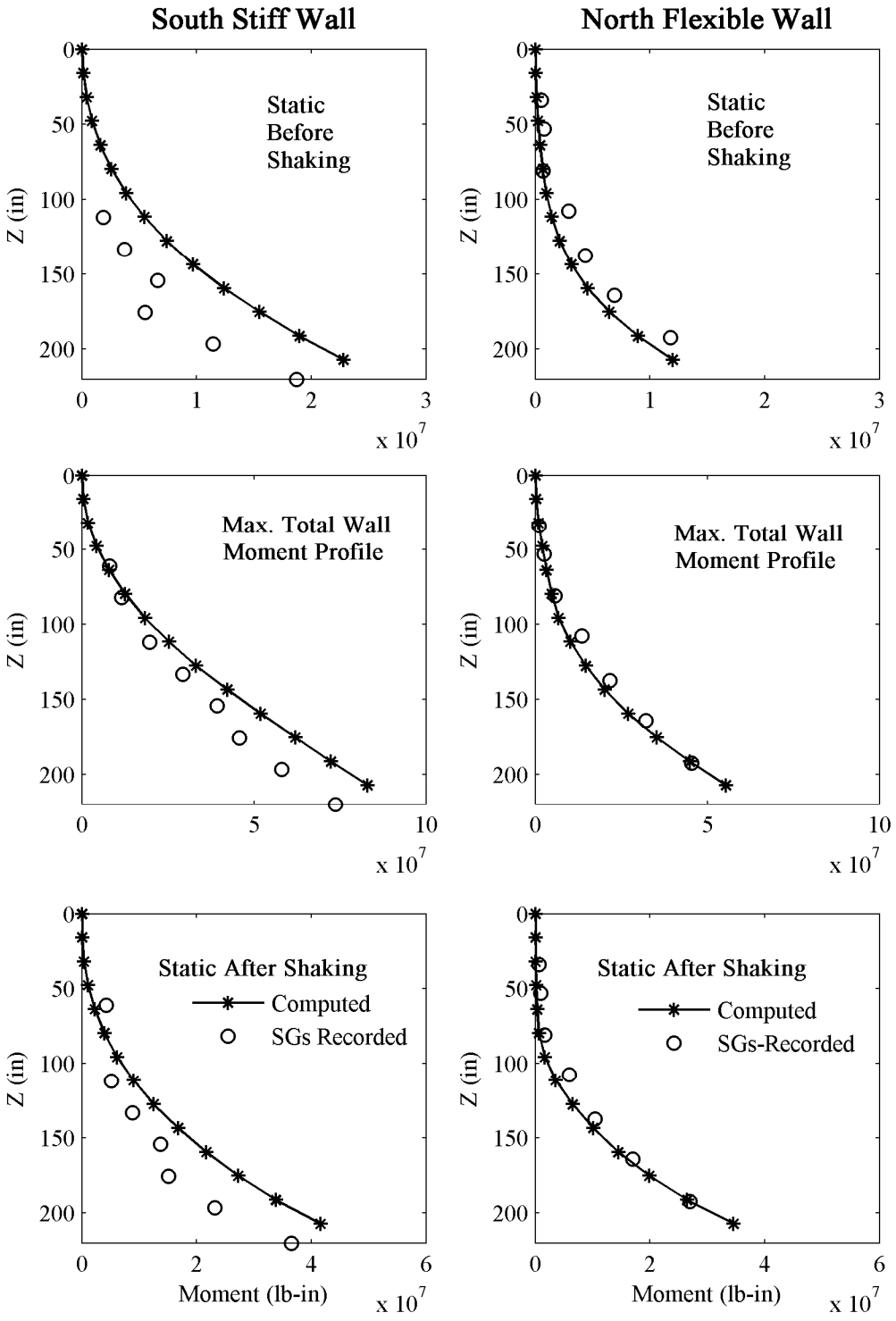

Fig. 5.20 Comparison of computed and recorded static moment profiles before and after shaking and maximum total wall moment profiles on south stiff and north flexible walls during Loma Prieta-SC-1.

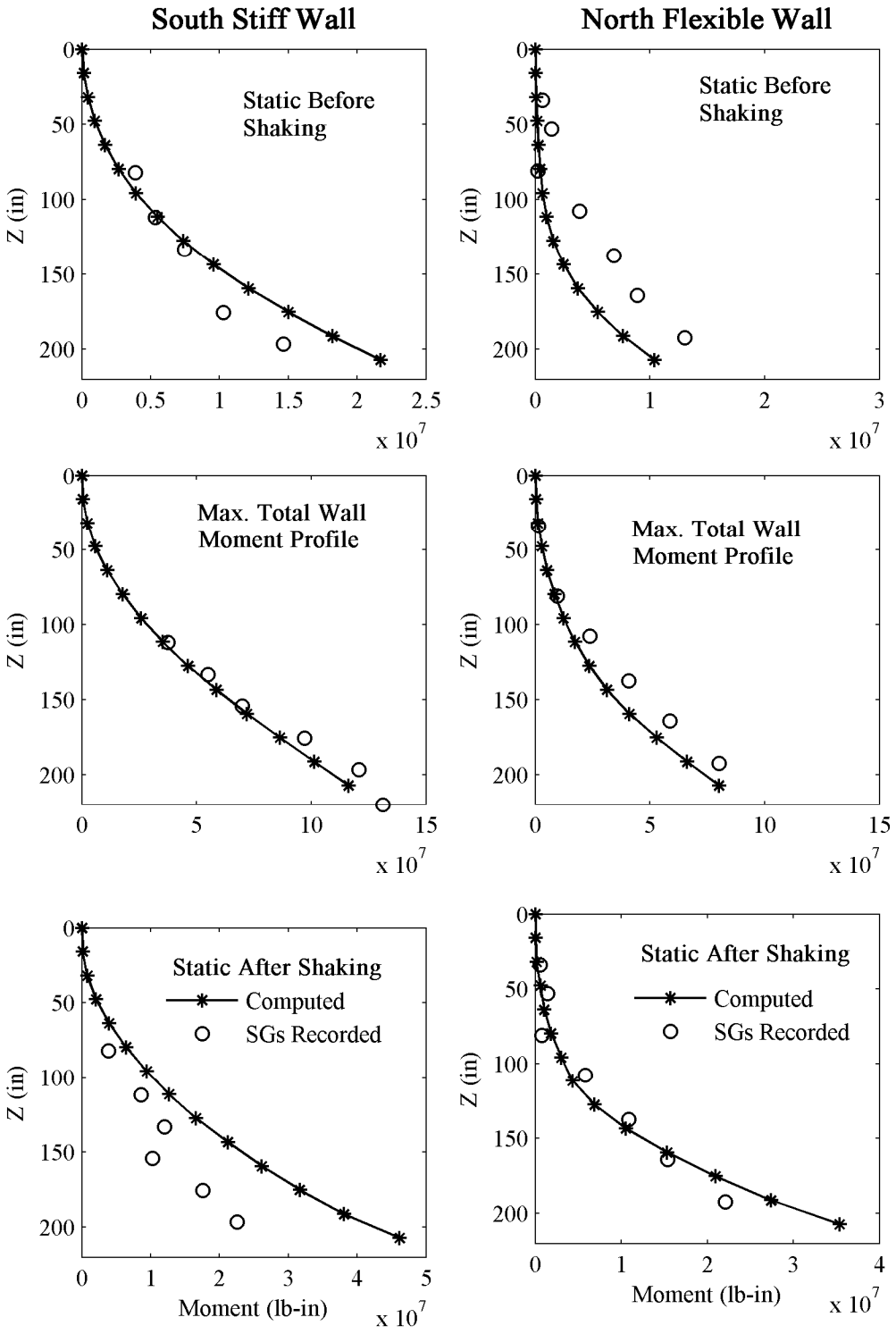

Fig. 5.21 Comparison of computed and recorded static moment profiles before and after shaking and maximum total wall moment profiles on south stiff and north flexible walls during Kobe-PI-2.

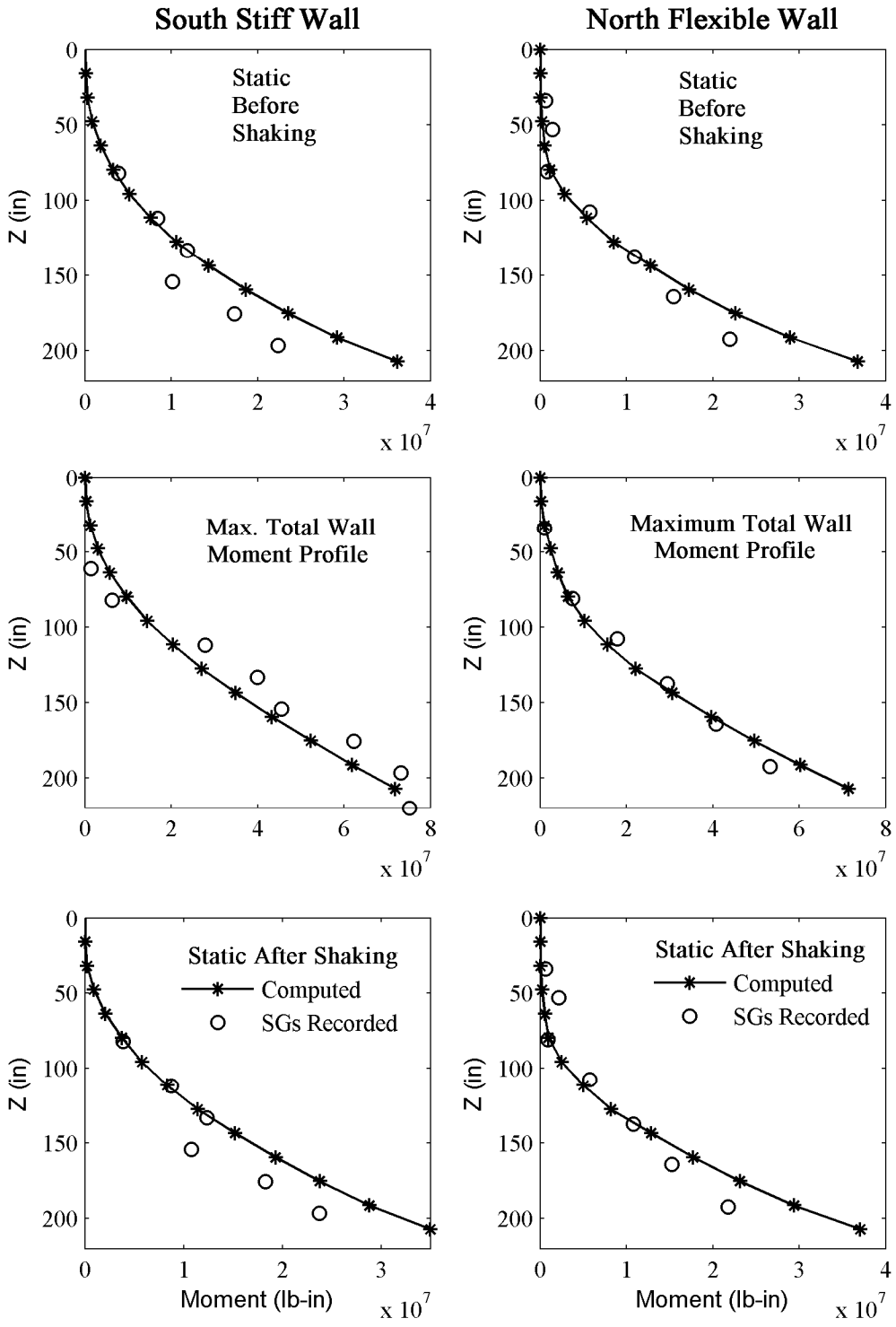

Fig. 5.22 Comparison of computed and recorded static moment profiles before and after shaking and maximum total wall moment profiles on south stiff and north flexible walls during Loma Prieta-SC-2.

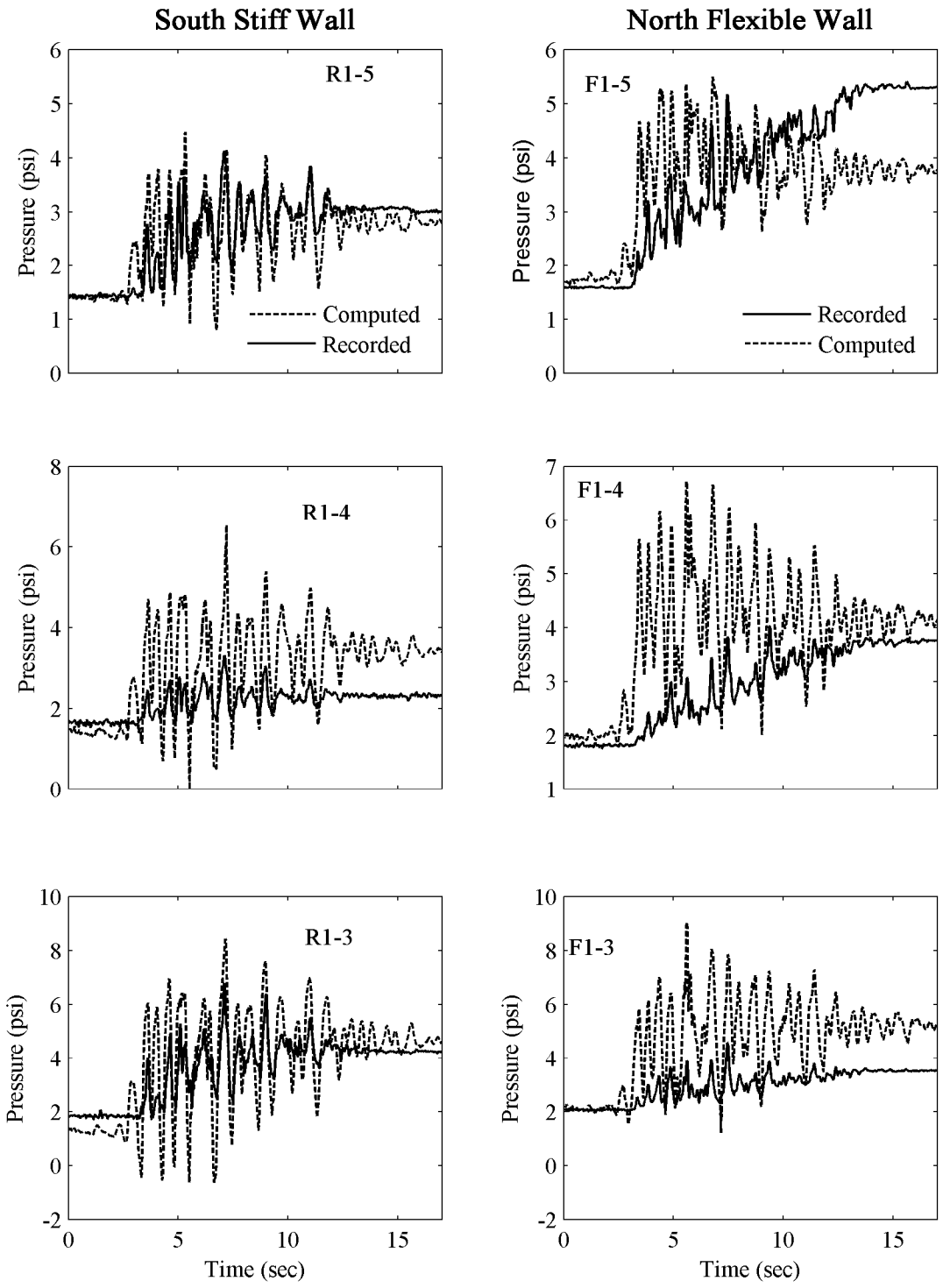

Fig. 5.23 Comparison of computed and recorded total earth pressure time series at different Flexiforce locations on south stiff and north flexible walls during Loma Prieta-SC-1.

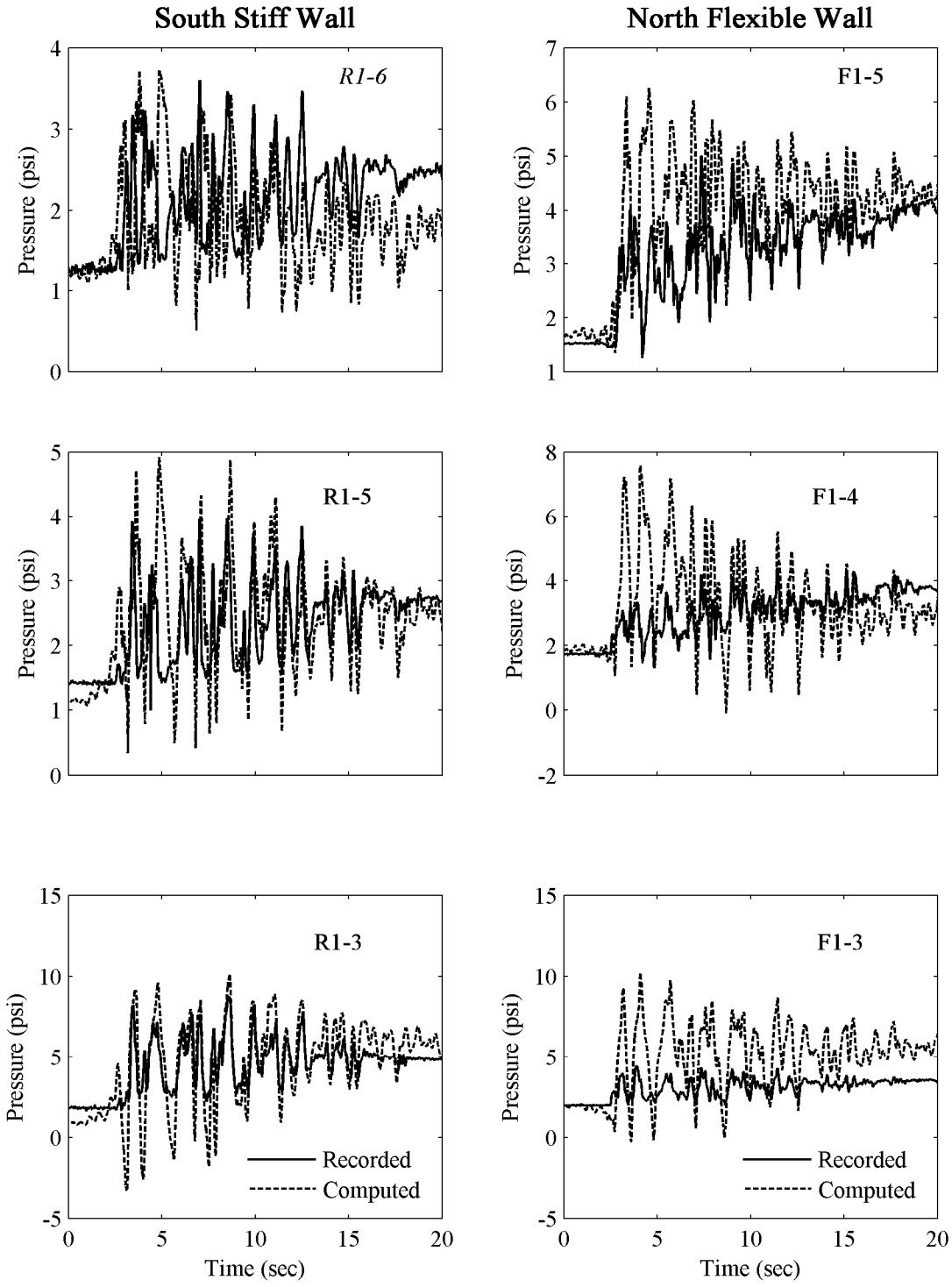

Fig. 5.24 Comparison of computed and recorded total earth pressure time series at different Flexiforce locations on south stiff and north flexible walls during Kobe-PI-2.

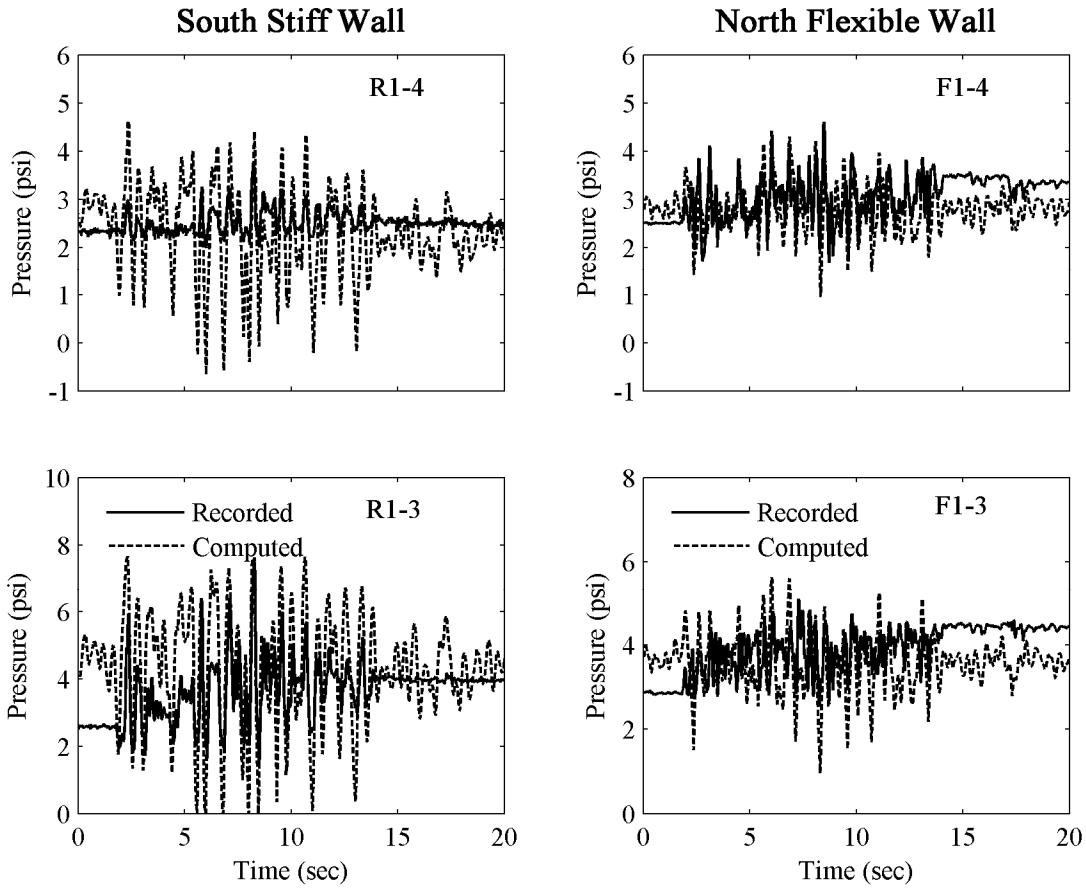

Fig. 5.25 Comparison of computed and recorded total earth pressure time series at different Flexiforce locations on south stiff and north flexible walls during Loma Prieta-SC-2.

While there was a reasonable phase agreement between the recorded and computed total earth pressure time series, the computed values usually overestimated the magnitude of the recorded total earth pressures. It should be noted that the accuracy of the earth pressure magnitudes measured by the Flexiforce sensors is limited due to the problems encountered with these sensors, as described in Section 3.11.2. This limitation possibly contributed to the differences observed between the computed and recorded earth pressure responses. Moreover, the computed earth pressures in OpenSees were sensitive to small variations in the properties of the wall-soil springs and the type of soil-structure interaction. While the soil-wall spring properties were carefully selected to obtain a good overall agreement in the computed and recorded moment and pressure responses, a more elaborate modeling of the soil-structure interaction could possibly produce better results. Overall and despite the mentioned limitations,

the main observed characteristics of the static and total earth pressures acting on the stiff and the flexible retaining walls in the centrifuge experiments were reasonably simulated by the FE model.

5.3.4 Soil Shear Stress and Strain Responses

Figures 5.26–5.28 present comparisons of interpreted and computed shear stress (τ_{xy}) and shear strain (ε_{xy}) time series in the middle of the backfill in the free field for the different analyzed shaking scenarios. The computed shear stresses and strains were obtained using the element recorder in OpenSees at a particular integration point in the soil element. The interpreted shear stress and strain time series presented in Figures 5.26–5.28 were estimated using the recorded lateral downhole accelerations as described in Section 5.2.2. The evaluation of shear stresses was based on the 1-D shear beam idealization. Shear strain time series were evaluated based on the displacement time series obtained by double-integrating the acceleration records. This method of estimating the shear strain time series eliminates any residual static shear strain after shaking because of the high-pass filtering and double integration of the acceleration records. It should be noted that shear stress and shear strain estimates based on the centrifuge recorded accelerations are of second-order accuracy. As shown in Figures 5.26–5.28, the computed and interpreted shear stress strain time series in the middle of the soil backfill are in very good agreement for the three analyzed shaking events.

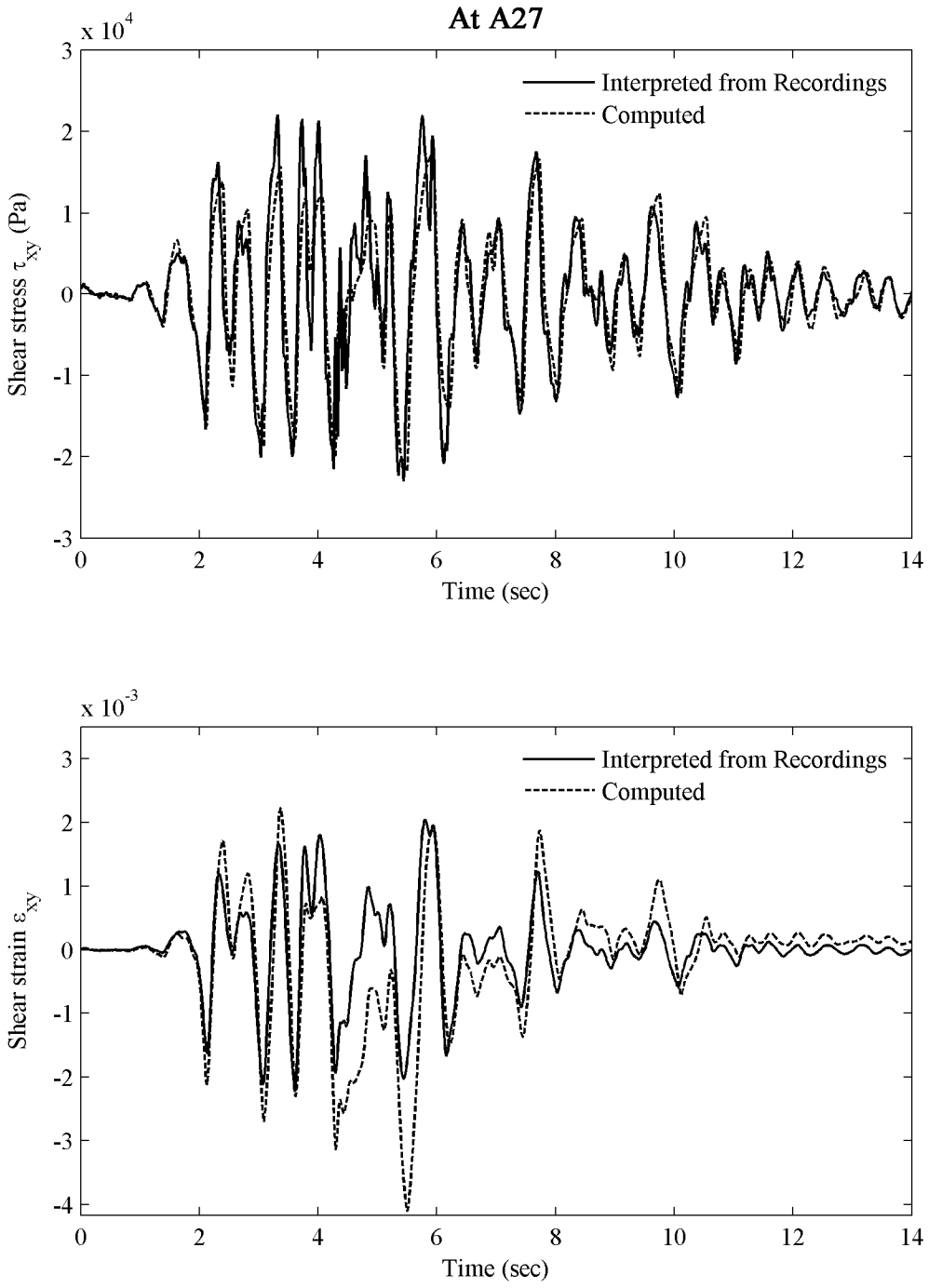

Fig. 5.26 Comparison of computed and recorded shear stress and strain time series in middle of soil backfill during Loma Prieta-SC-1.

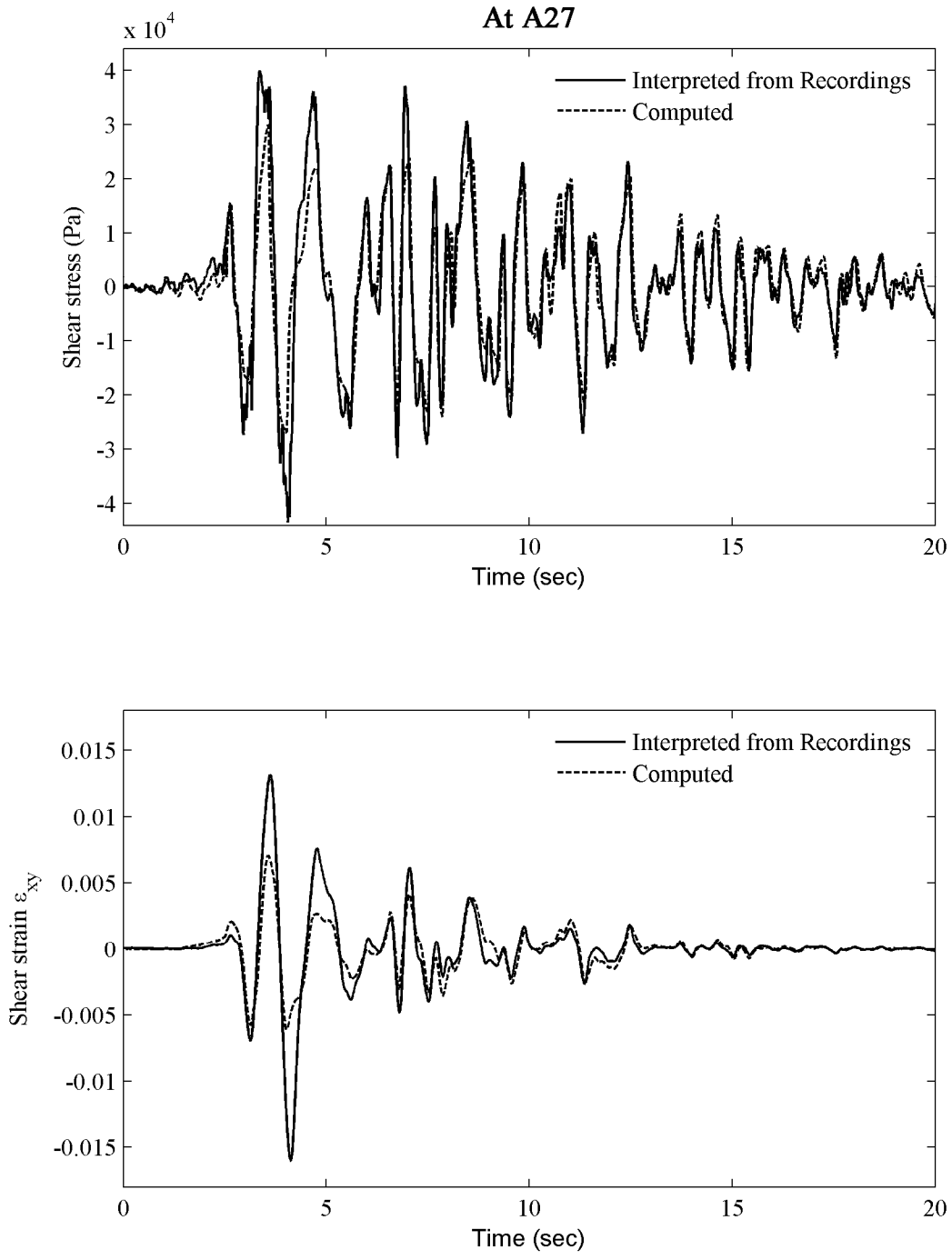

Fig. 5.27 Comparison of computed and recorded shear stress and strain time series in middle of soil backfill during Kobe-PI-2.

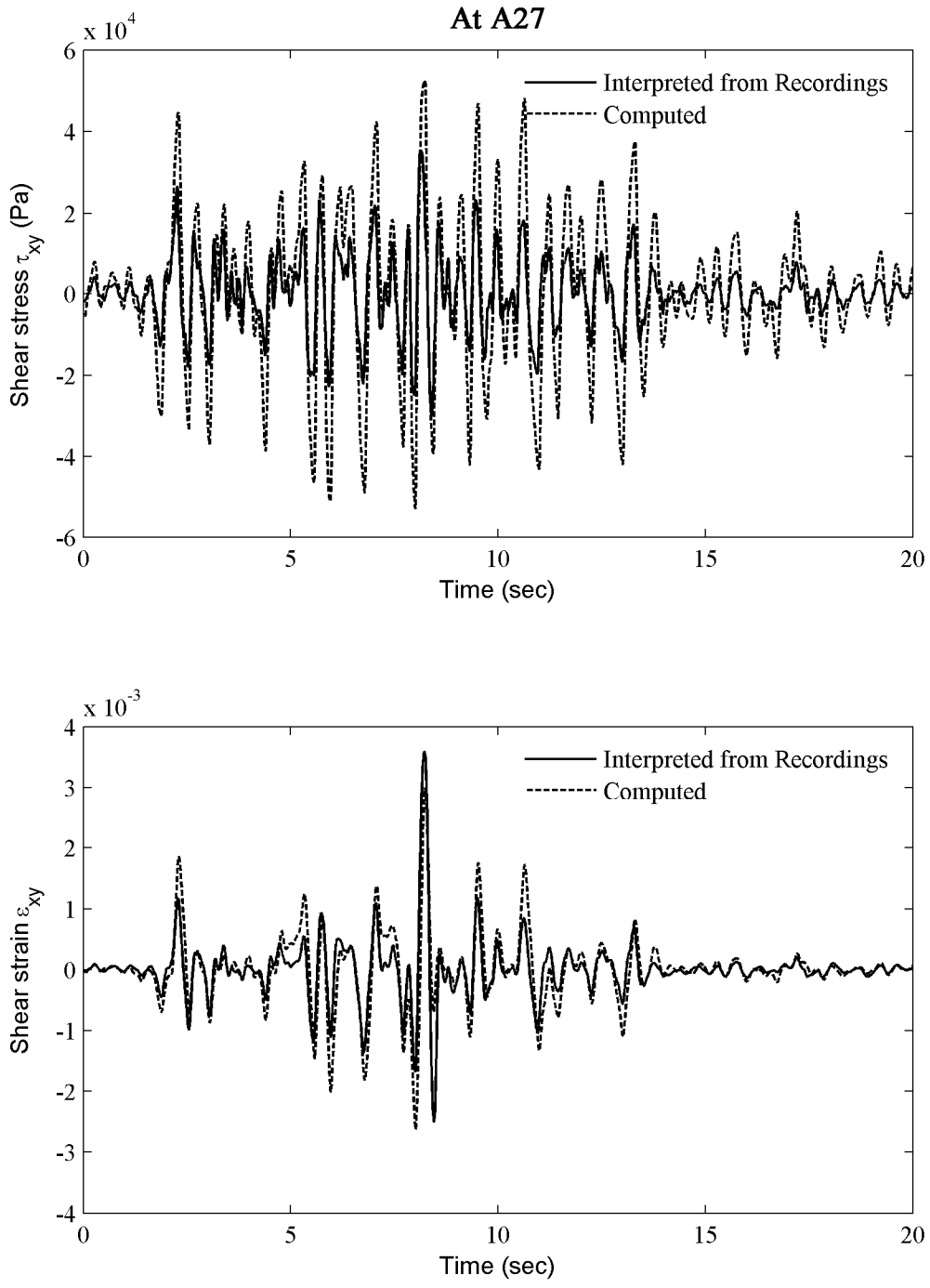

Fig. 5.28 Comparison of computed and recorded shear stress and strain time series in middle of soil backfill during Loma Prieta-SC-2.

5.4 SENSITIVITY OF FINITE ELEMENT MODEL

The FE model was tested with a range of input variables and scenarios to evaluate the influence of various parameters on key responses such as accelerations in the soil and on the structures, as well as bending moments and earth pressures on the walls. The initial FE model represented the two retaining structures, stiff and flexible, together as was the case in the centrifuge experiments. The potential for interaction between the two structures was then evaluated by modeling the stiff and flexible structures separately. Differences of less than 5% were generally observed in the acceleration, moment, and earth pressures responses, indicating that having the two structures together in one centrifuge model does not have a significant effect on the results. However, as expected, soil properties such as low strain shear modulus, low strain bulk modulus, friction angle and modulus reduction curve have a significant effect on the computed results. This emphasizes the importance and necessity of having reliable estimates of the soil properties in numerical modeling. Moreover, the calibrated FE model was able to reasonably well capture the influence of frequency content of the different analyzed base ground motions.

Finally, the type and parameters of soil-structure interface elements had a considerable effect on the bending moments and earth pressures computed on the walls. As discussed in Section 5.2.3, elastic-no-tension springs in parallel with dashpots were used to model the soil-structures interaction. Other types of interface elements such as elastic springs, elastic-no-tension springs, or soil and structure directly attached were evaluated as well. These types of interface elements tended to overestimate the earth pressures acting on the walls and did not match the phase of the recorded total earth pressure time series. Moreover, the stiffness and radiation damping parameters for the soil-structure interface elements had an effect on the computed earth pressures acting on the walls with high radiation damping coefficients and lower stiffness values resulting in lower earth pressures on the walls. More elaborate soil-structure interface models, such as those described in Gomez et al. (2003) and Green et al. (2008), could possibly better model the retaining wall–soil interaction, but their application was beyond the scope of this study. It should be noted that the effects of the interface element properties on the computed bending moments on the walls were not as pronounced as for the earth pressures, since computed moments on the walls were significantly affected by the inertia of the wall itself. This response is consistent with observations from the centrifuge experiments presented in Chapter 4.

5.5 ALTERNATIVE SOIL PROPERTIES STUDY

The calibrated model was used as a baseline for a preliminary evaluation of dynamic earth pressures and moments for U-shaped cantilever retaining structures with dry dense sand backfill. The results of this scenario are used to evaluate the effect of higher soil strength on the lateral loads computed on the walls. Other retaining wall–backfill scenarios such as rigid walls and basement walls are beyond the scope of the current study and require more elaborate treatment of soil-structure interface.

5.5.1 U-Shaped Cantilever Retaining Structures with Dense Sand Backfill

Description

For the stiff and flexible U-shaped cantilever retaining structures in a dry dense sand backfill scenario, a 2-D plane-strain finite element mesh identical to the one used in the development and the calibration of the FE model, presented in Figure 5.29, was employed. The elasto-plastic PDMY material with FourNodeQuad elements was used to model the uniform-density dry dense Nevada sand. Input parameters for the soil model were based on Yang et al. (2008) and Elgamal et al. (2005) and are presented in Table 5.5. The input ground motion consisted of the input accelerations recorded during the Loma Prieta-SC-1 shaking event of centrifuge experiment LAA02.

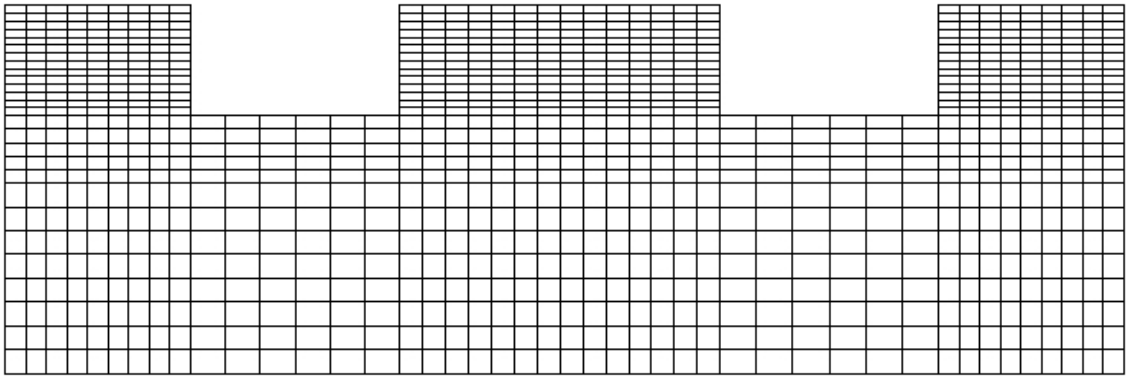

Fig. 5.29 Two-dimensional plane-strain finite element mesh for U-shaped cantilever retaining structures with dry dense sand backfill scenario.

Table 5.5 Input parameters for PDMY soil properties in FE model.

Model Parameters	Dry Dense Nevada Sand
Initial Mass Density (kg/m^3)	1767
Reference Shear Modulus, G_r (kPa)	6.60E+04
Poisson's Ratio	0.248
Reference Bulk Modulus, B_r (kPa)	1.09E+05
Reference Confining Stress, P'_r (kPa)	80
Peak Shear Strain	0.1
Pressure Dependent Coefficient	0.5
Friction Angle	42°
Phase Transformation Angle	27°
Contraction Constant	0.03
Dilation Constants	d_1=0.8, d_2=10.0
Liquefaction Induced Strain Constants	0
Number of Yield Surfaces	11
Void Ratio	0.511

Analytical Results and Observations

The deformed mesh, five times magnified, for the Loma Prieta-SC-1 scenario shows soil settlement and permanent wall deflection patterns for the stiff and the flexible retaining structures and is presented in Figure 5.30. The computed acceleration time series at the top of the soil in the free field, and at the tops of the south stiff and north flexible walls are presented in Figure 5.31.

The computed total wall moments and earth pressure time series on the stiff and flexible retaining walls supporting dry dense sand backfill were evaluated and compared to the results obtained for the stiff and flexible U-shaped structures retaining dry medium-dense sand. A comparison of the total wall moment time series at different locations on the south stiff and north flexible walls with the dense and the medium-dense sand backfill is shown in Figure 5.22. The corresponding comparison of total earth pressure time series at different locations on the south stiff and north flexible walls for the dense and medium-dense dry backfill is presented in Figure 5.33. Figure 5.32 shows that the moments computed for the case with dense sand backfill decrease by about 25–30 % relative to the corresponding moments for the medium-dense sand backfill. Similarly, Figure 5.33 shows that the total earth pressures on the stiff and the flexible

walls exerted by the medium-dense sand backfill significantly exceed those induced by the dense sand backfill.

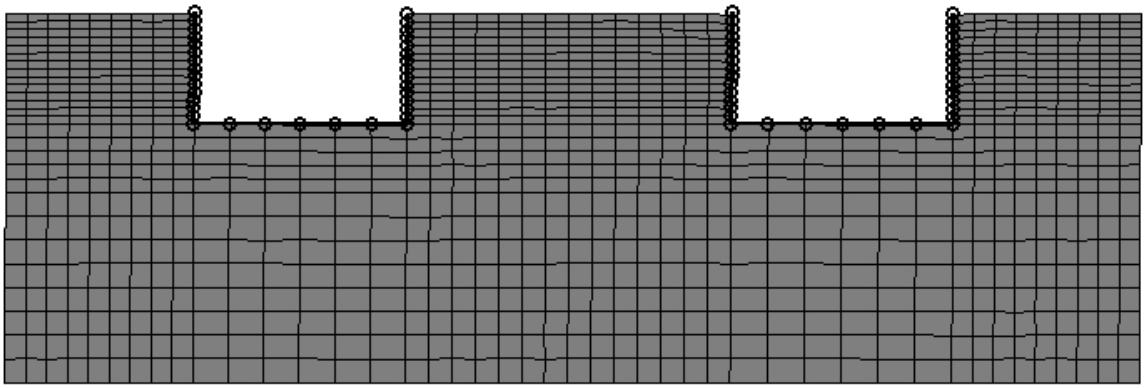

Fig. 5.30 Deformed finite element mesh for Loma Prieta-SC-1 shaking event.

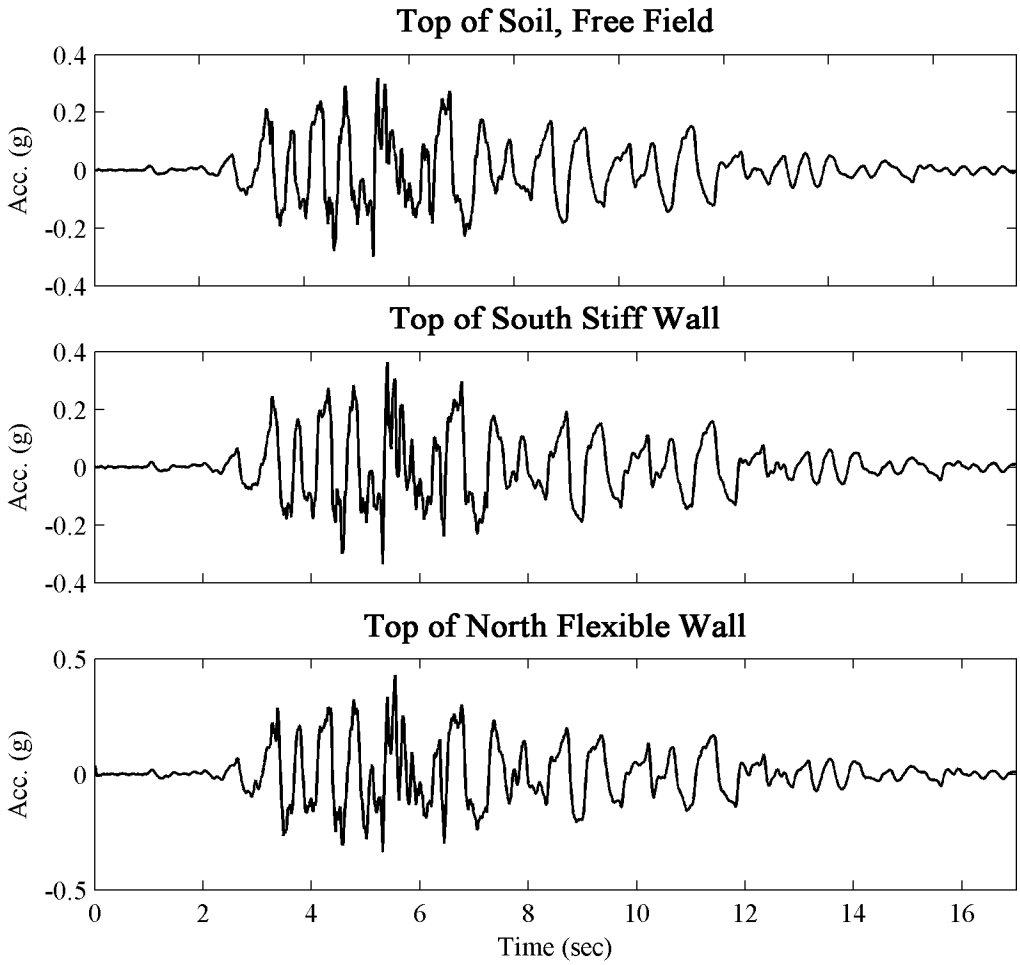

Fig. 5.31 Computed acceleration time series at top of soil in free field and at tops of south stiff and north flexible walls.

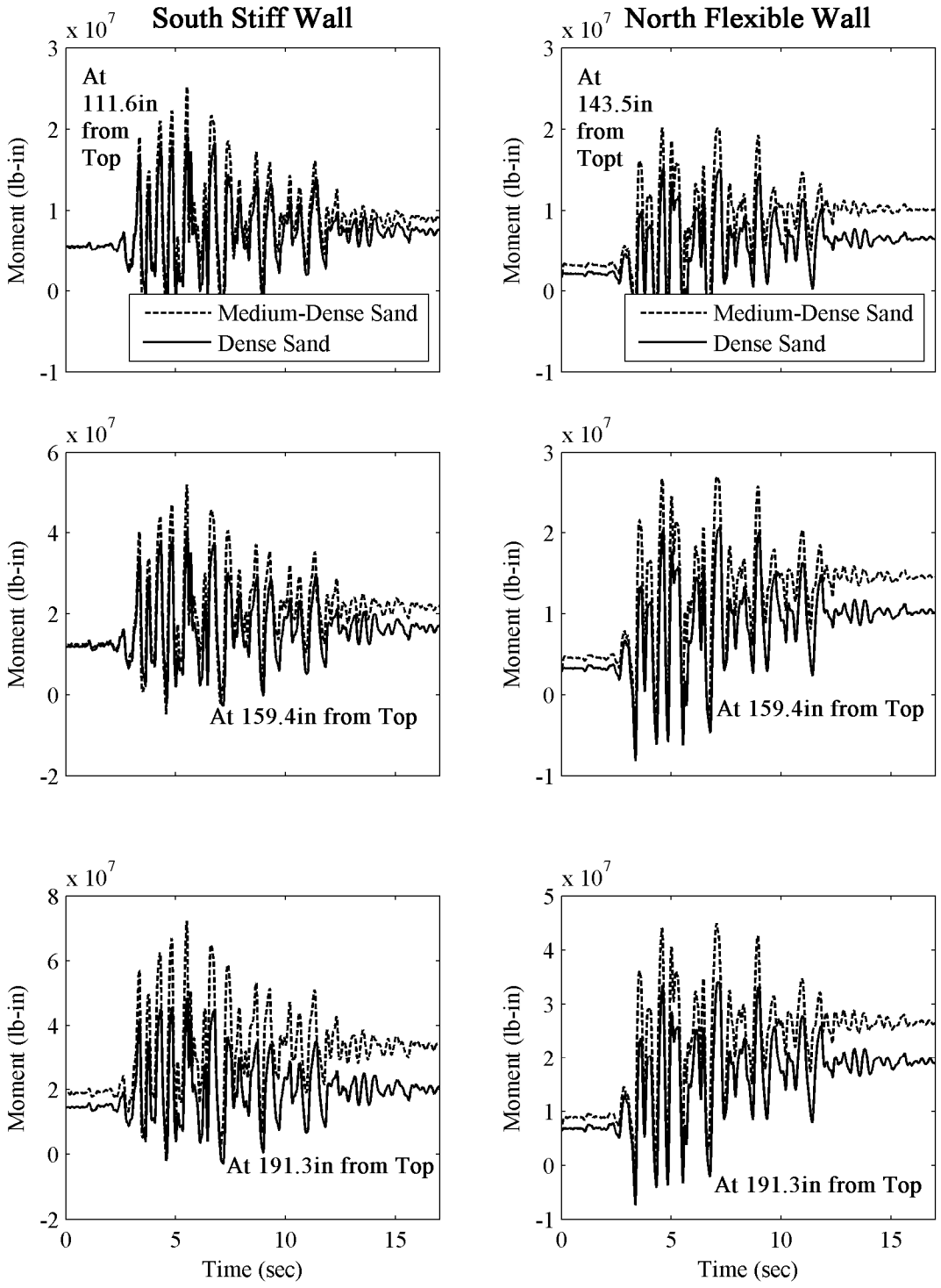

Fig. 5.32 Comparison of computed total moments at different locations on south stiff and north flexible walls with dry dense and medium-dense sand backfill.

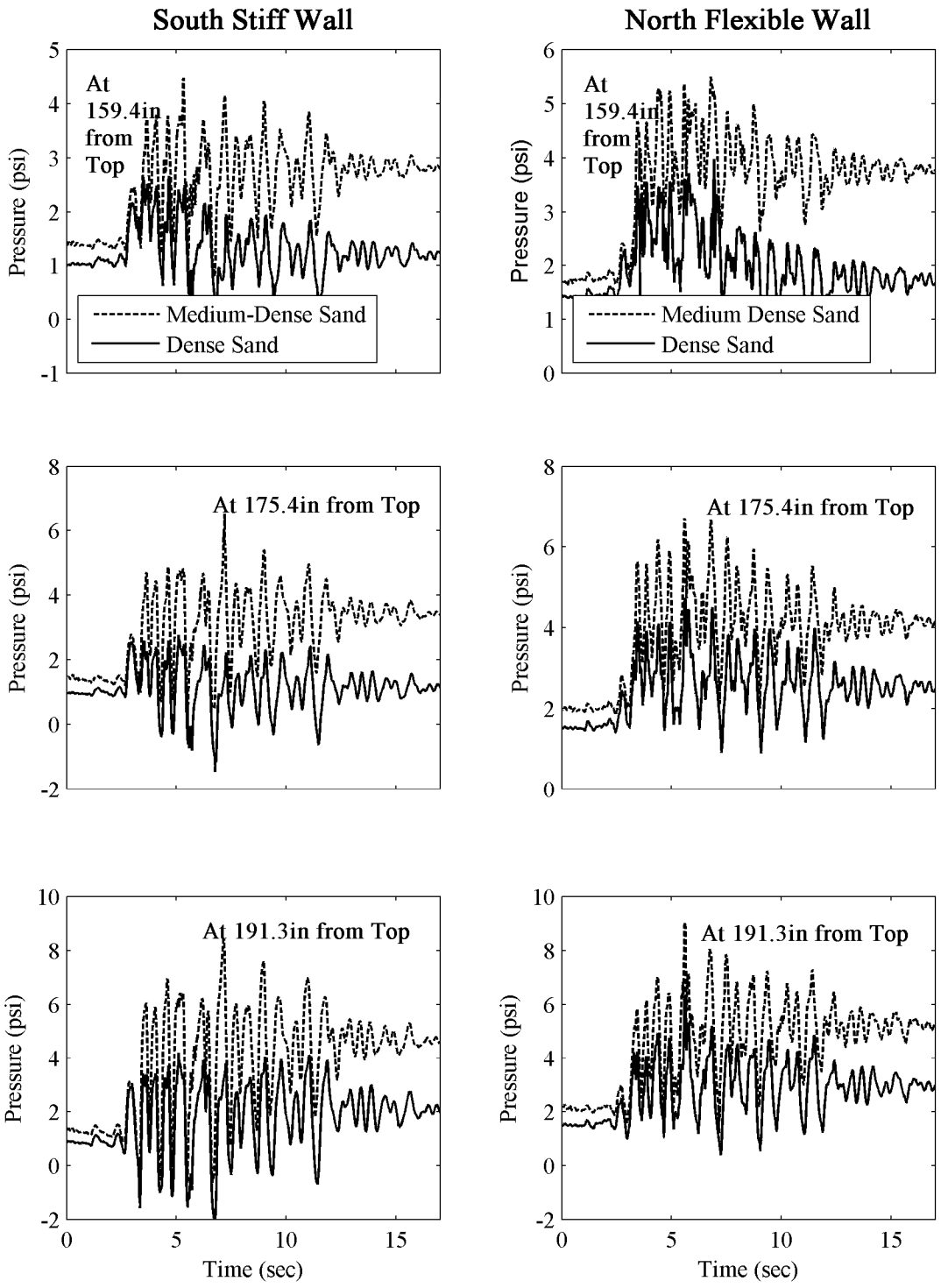

Fig. 5.33 Comparison of computed total earth pressures at different locations on south stiff and north flexible walls with dry dense and medium-dense sand backfill.

5.6 SUMMARY

A 2-D plane-strain FE model was developed on the OpenSees platform and was calibrated and evaluated against a set of centrifuge model results for three shaking events from experiment LAA02. The computed and recorded results consisting of acceleration, response spectra, bending moments, earth pressures, and shear stress and strain time series were compared with the experimental results. Despite the simplifications and inherent limitations in the FE model as well as the uncertainties in the input parameters, the computed results show that the finite element analysis is able to capture reasonably well the essential system responses observed in the centrifuge experiments. Most importantly, the resulting model was then available to perform a preliminary analysis of a case with denser soil backfill. The results of the numerical studies show that increasing the soil density and hence its shear strength does indeed lead to a better performance and lesser loads on the retaining structures, as would be expected. In all studied cases, the pressure profiles consistently increase with depth along the height of the walls.

Nevertheless, the FE model had a number of important limitations must be acknowledged and reconciled before extending these results further, including:

- Inherent uncertainties in the input parameters;
- Simplifications adopted in modeling of the rather complex soil-structure interaction;
- Challenges in accurately capturing the soil stress and strain conditions resulting from previous shakings. Measured soil properties before a specific shaking event such as mass density and low strain shear modulus were used as input parameters for the particular scenario. In this study, the cumulative effects of previous shakings on the other soil properties could not be accurately modeled, since consideration of previous loading is not possible in the current sand models in OpenSees;
- The centrifuge model container was simplified;
- The wall-base connections were assumed to be perfectly rigid; and
- Possible 3-D effects were not captured in the 2-D plane-strain analysis.

6 Implications for Existing Design Methods and Recommendations

One of the principal objectives of this research was to evaluate the validity of the assumptions used in the current seismic design methods and to assess the overall quality of the design methodology. To this end, the lateral earth pressures and moments observed during centrifuge experiments LAA01 and LAA02 were compared to estimates obtained using the most commonly applied dynamic earth pressure theories. Based on these comparisons, and based on the experimental observations and measurements, recommendations are provided for future seismic design of cantilever retaining walls.

6.1 EVALUATION OF MONONOBE-OKABE AND SEED AND WHITMAN (1970) METHODS

As discussed in the literature review of Chapter 2, the M-O theory assumes that the backfill is in a state of plastic equilibrium under dynamic loading, and treats the seismic forces on the wall as equivalent static forces. While there is no clear empirical basis for these assumptions, the M-O theory along with its simplified version presented in Seed and Whitman (1970) has become the established theory for estimating seismic earth pressures on retaining walls.

Based on the experimental findings presented in Section 4.5, the M-O hypothetical idealization that seismic response occurs simultaneously and uniformly in the retaining wall and backfill without any phase difference does not correctly represent the real seismic behavior of the retaining wall–backfill system. Moreover, the M-O theory assumes that the maximum earth pressure and the inertial force occur simultaneously, and that a stability analysis of the retaining wall is usually conducted for this case. In contrast, the experimental data show that the dynamic earth pressure is at its local maximum when the inertial force and dynamic wall moment reach their local minimum values or zero. While the M-O theory suggests that a retaining wall is

subjected to the seismic active earth pressure when the wall and the backfill are loaded by the inertial force in the active direction, experimental data suggest that this hypothesis is clearly flawed. When the retaining wall and the backfill are loaded in the active direction, the dynamic earth pressure is around its minimum, or around zero.

6.1.1 Total Moments

Tables 6.1 and 6.2 present total earth pressure moments estimated using the M-O, and Seed and Whitman (1970) methods as a ratio in percent of the maximum total moments interpreted from the strain gage data at the bases of the south stiff and north flexible walls, respectively, for the different shaking events in experiments LAA01 and LAA02. While maximum total moments for centrifuge experiment LAA01 include contributions from the earth pressure and wall inertial effects and therefore represent the total wall moments, the total moments for experiment LAA02 were corrected to remove wall inertial effects, and represent total earth pressure moments. In the M-O method, the resultant force of the estimated total dynamic pressure distribution was applied at one third the height of the wall from its base. In the Seed and Whitman (1970) method, the M-O pressure distribution was used with the resultant force of the dynamic increment applied at two thirds the height of the wall from the base. The M-O and Seed and Whitman (1970) moment estimates were calculated with peak and 65% of the peak ground accelerations measured at the top of the soil in the free field. It should be noted that Seed and Whitman (1970) recommend using 85% rather than the more commonly assumed 65% of the peak ground acceleration. For some of the shaking events, the total dynamic moments estimated using the M-O method were indeterminate due to the high peak ground acceleration. Whenever the total earth pressure moment underestimates the measured maximum total moments, the corresponding values are presented in bold in Tables 6.1 and 6.2. Tabulated values of the maximum total moments at the bases of the south stiff and north flexible walls interpreted from the strain gage and force-sensing bolt measurements during the different shaking events for centrifuge experiments LAA01 and LAA02 are presented in Appendix B (Tables B.1–B.4). These tables also contain the total earth pressure moments at the bases of the walls estimated using the M-O and Seed and Whitman (1970) methods with total and 65% peak ground acceleration.

For experiment LAA01, Tables 6.1 and 6.2 show that both the M-O and Seed and Whitman (1970) methods used with total PGA typically overestimate the maximum measured total wall moments (including wall inertial moments). For experiment LAA02, the M-O and Seed and Whitman (1970) methods overestimate the maximum total earth pressure moments at the bases of the stiff and flexible walls. Using 65% of the total peak ground acceleration, the M-O and Seed and Whitman (1970) methods slightly underestimate the observed total earth pressure moments for the very strong shaking events, such as Kobe and Loma Prieta on the stiff wall, but overestimate the moments for the rest of the shaking events. The ratio of computed to observed total earth pressure moments appears to be a function of the flexibility of the wall, the magnitude of shaking, and the density of the backfill. As expected, this ratio is the lowest for the stiff wall with a large magnitude of shaking and a looser backfill.

Table 6.1 Ratio of computed total earth pressure moments to maximum total moments interpreted from strain gage measurements at base of south stiff wall during different shaking events for LAA01 and LAA02.

	Moment Estimate / Measured Moment			
	M-O Method with a_{max}	**M-O Method with 65% a_{max}**	**Seed & Whitman Method with a_{max}**	**Seed & Whitman Method with 65% a_{max}**
Loma Prieta-1, LAA01	102%	**67%**	127%	**95%**
Loma Prieta-2, LAA01	**96%**	**63%**	120%	**89%**
Kobe, LAA01	INDET.*	**61%**	106%	**76%**
Loma Prieta-3, LAA01	107%	**66%**	125%	**92%**
Loma Prieta-SC-1, LAA02	135%	**94%**	186%	139%
Kobe-PI-1, LAA02	143%	**65%**	125%	**90%**
Kobe-PI-2, LAA02	INDET.*	**82%**	153%	109%
Loma Prieta-SC-2, LAA02	152%	**97%**	194%	143%
Kocaeli-YPT060-2, LAA02	160%	129%	238%	186%
Kocaeli-YPT060-3, LAA02	175%	127%	251%	189%
Kocaeli-YPT330-2, LAA02	161%	118%	233%	175%
Kobe-TAK090-1, LAA02	INDET.*	**85%**	147%	103%
Kobe-TAK090-2, LAA02	151%	**80%**	159%	115%
Loma Prieta-WVC270, LAA02	118%	**93%**	178%	137%
Kocaeli-YPT330-3, LAA02	148%	112%	219%	166%

* Total earth pressure moment estimate is indeterminate by the M-O method due to the high peak ground acceleration

The overall performance of the walls can be further evaluated by inspecting the measured total moment time series and comparing them to limit values estimated using the M-O and Seed and Whitman (1970) methods. Figures 6.1–6.2 present the total moment time series measured by the force-sensing bolts and by SG2 on the south stiff and north flexible walls for the Loma Prieta-1 and the Loma Prieta-SC-1 shaking events in experiments LAA01 and LAA02, respectively. Total earth pressure moment estimates using the M-O and Seed and Whitman (1970) methods with total peak ground accelerations are also presented in the figures at the corresponding locations on the walls. Plots comparing the observed total moment time series to the M-O and Seed and Whitman (1970) total earth pressure moment estimates for the rest of the LAA01 and LAA02 shaking events are included in Figures A.49–A.61.

Table 6.2 Ratio of computed total earth pressure moments to maximum total moments interpreted from strain gage measurements at base of north flexible wall during different shaking events for LAA01 and LAA02.

	Moment Estimate / Measured Moment			
	M-O Method with a_{max}	**M-O Method with 65% a_{max}**	**Seed & Whitman Method with a_{max}**	**Seed & Whitman Method with 65% a_{max}**
Loma Prieta-1, LAA01	107%	**70%**	133%	**99%**
Loma Prieta-2, LAA01	102%	**67%**	127%	**95%**
Kobe, LAA01	INDET.*	**73%**	128%	**92%**
Loma Prieta-3, LAA01	112%	**70%**	131%	**97%**
Loma Prieta-SC-1, LAA02	144%	101%	199%	148%
Kobe-PI-1, LAA02	233%	106%	204%	146%
Kobe-PI-2, LAA02	INDET.*	194%	194%	138%
Loma Prieta-SC-2, LAA02	166%	106%	212%	156%
Kocaeli-YPT060-2, LAA02	142%	114%	211%	164%
Kocaeli-YPT060-3, LAA02	161%	117%	231%	174%
Kocaeli-YPT330-2, LAA02	165%	121%	238%	179%
Kobe-TAK090-1, LAA02	INDET.*	**75%**	130%	**91%**
Kobe-TAK090-2, LAA02	192%	102%	202%	146%
Loma Prieta-WVC270, LAA02	124%	**98%**	186%	143%
Kocaeli-YPT330-3, LAA02	129%	**97%**	191%	145%

*Total earth pressure moment estimate is indeterminate by the M-O method due to the high peak ground acceleration

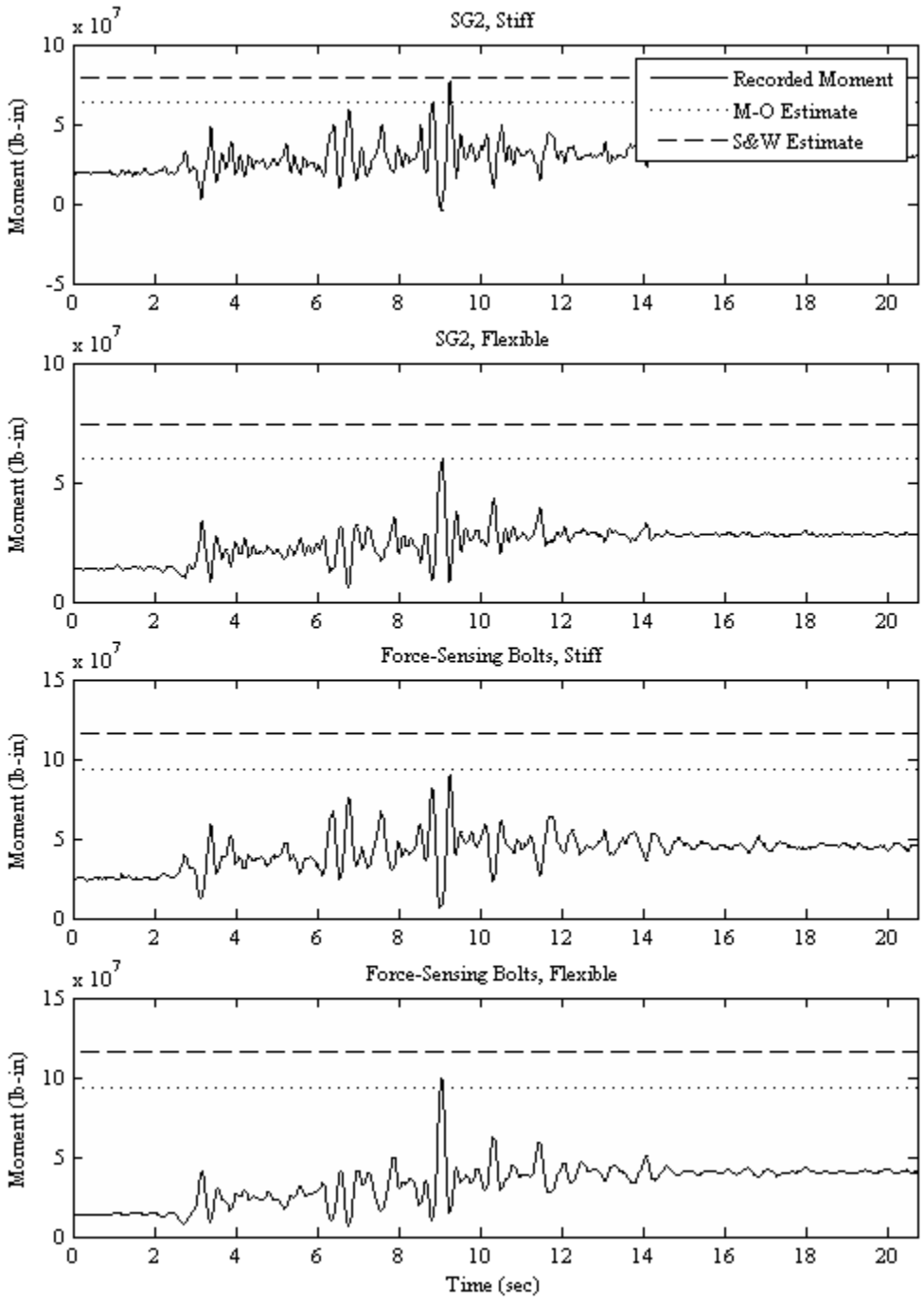

Fig. 6.1 Comparison of total wall moment time series recorded at SG2 on south stiff and north flexible walls and at bases of walls by force-sensing bolts with M-O and Seed and Whitman (1970) total moment estimates for Loma Prieta-1, LAA01.

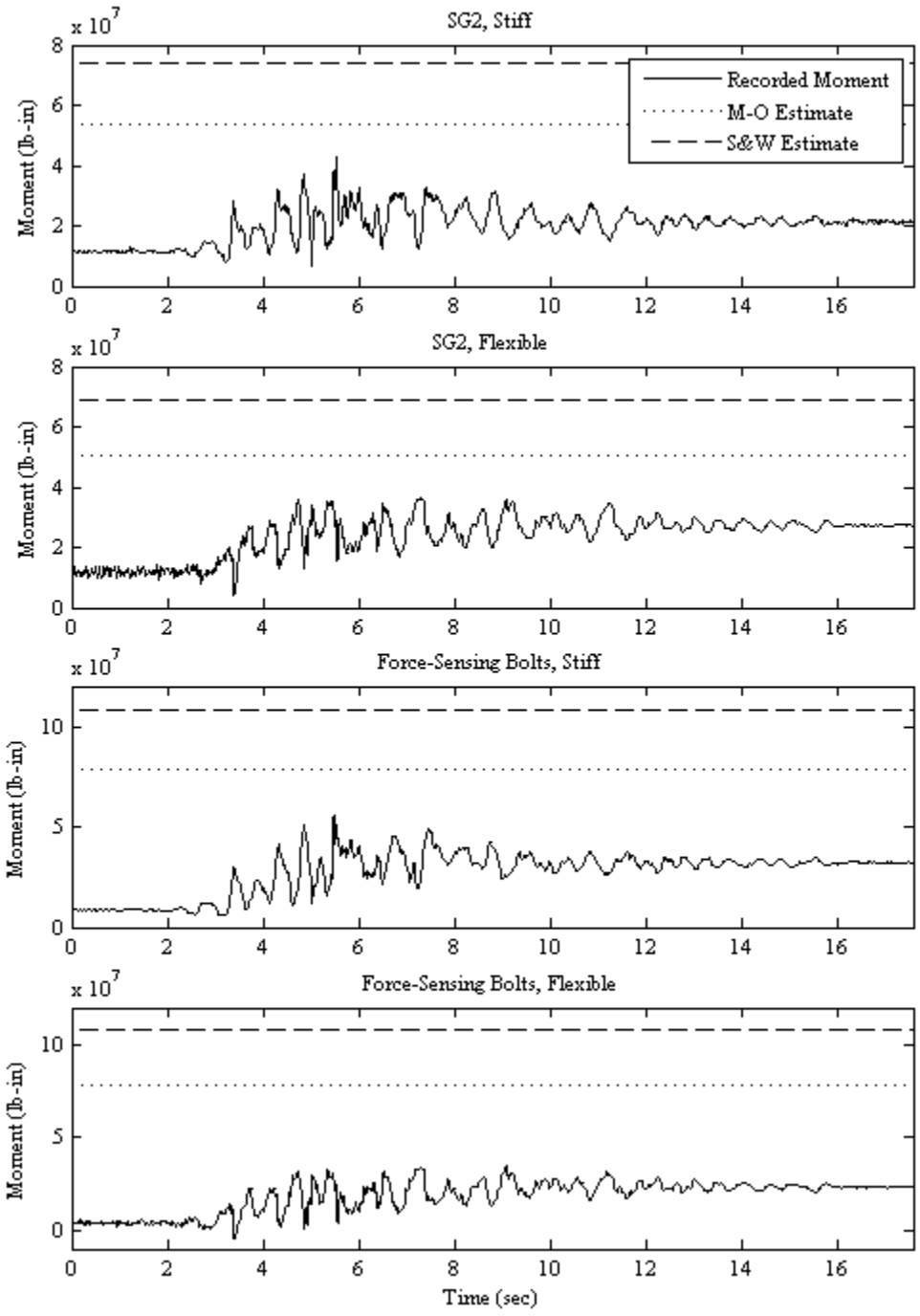

Fig. 6.2 Comparison of total earth pressure moment time series recorded at SG2 on south stiff and north flexible walls and at bases of walls by force-sensing bolts with M-O and Seed and Whitman (1970) moment estimates for Loma Prieta-SC-1, LAA02.

For centrifuge experiment LAA01, the total wall moments measured at the bases of the stiff and flexible walls and at the SG2 location including wall inertial effects are generally adequately estimated or slightly underestimated by the M-O method and overestimated by the Seed and Whitman (1970) method. For centrifuge experiment LAA02, the M-O and Seed and Whitman methods overestimate the total earth pressure moments at all times and for all shaking events. In addition, the total moment time series clearly show the effect of soil densification during shaking as the static moment on the walls increases under seismic loading. This effect is most pronounced for the strongest shaking events with the largest amount of settlement. Such an effect would be less pronounced in soils that are less susceptible to compaction either due to greater density or presence of cohesion. Finally, the time series show that the total wall moments rarely exceed the design criteria in more than one cycle. Overall, the total wall moments tend to be significantly overestimated by current design methods.

6.1.2 Dynamic Moments

Tables 6.3 and 6.4 present estimates of the dynamic component of the moment due to earth pressure using the M-O and Seed and Whitman (1970) methods. The results are given as a ratio (in percent) of the maximum dynamic moments interpreted from the strain gage measurements at the bases of the south stiff and the north flexible walls for the different shaking events for experiments LAA01 and LAA02. While recorded maximum dynamic moments for LAA01 shaking events include wall inertial effects, recorded moments for the LAA02 shaking events were corrected to reflect only the earth pressure effects. The M-O and Seed and Whitman (1970) dynamic earth pressure moment estimates were calculated with peak and 65% of the peak ground accelerations measured at the top of the soil in the free field. Whenever the dynamic earth pressure moment estimates underestimate the measured maximum dynamic moments, the corresponding values are presented in bold. Tabulated values of the dynamic moments at the bases of the south stiff and north flexible walls interpreted from the strain gage and force-sensing bolt measurements during the different shaking events for LAA01 and LAA02 are presented in Tables B.5–B.8. These tables also contain the values of dynamic earth pressure moments estimated using the M-O and Seed and Whitman (1970) methods with total and 65% peak ground acceleration.

As previously observed in the total moment comparisons, Tables 6.3 and 6.4 show that the maximum dynamic wall moments recorded at the bases of the stiff and flexible walls during the LAA01 shaking events generally tend to be overestimated by the M-O and Seed and Whitman methods using PGA values. For experiment LAA02, the maximum earth pressure dynamic moments are overestimated by the M-O and Seed and Whitman (1970) methods used with PGA. The M-O method with 65% PGA tends to underestimate the dynamic earth pressure moments for the strong shaking events such as Kobe but adequately estimates those for the rest of the shaking events. The Seed and Whitman (1970) method used with 65% PGA generally overestimates the dynamic earth pressure moments at the bases of the stiff and flexible walls.

Table 6.3 Ratio of computed dynamic earth pressure moments to maximum dynamic moments interpreted from strain gage measurements at base of south stiff wall during different shaking events for LAA01 and LAA02.

	Moment Estimate / Measured Moment			
	M-O Method with a_{max}	**M-O Method with 65% a_{max}**	**Seed & Whitman Method with a_{max}**	**Seed & Whitman Method with 65% a_{max}**
Loma Prieta-1, LAA01	104%	**50%**	141%	**92%**
Loma Prieta-2, LAA01	**96%**	**47%**	132%	**86%**
Kobe, LAA01	INDET.*	**47%**	100%	**65%**
Loma Prieta-3, LAA01	116%	**53%**	143%	**93%**
Loma Prieta-SC-1, LAA02	204%	105%	327%	212%
Kobe-PI-1, LAA02	210%	**72%**	179%	116%
Kobe-PI-2, LAA02	INDET.*	**88%**	198%	129%
Loma Prieta-SC-2, LAA02	230%	110%	323%	210%
Kocaeli-YPT060-2, LAA02	239%	138%	493%	320%
Kocaeli-YPT060-3, LAA02	316%	169%	553%	359%
Kocaeli-YPT330-2, LAA02	313%	168%	555%	361%
Kobe-TAK090-1, LAA02	INDET.*	106%	212%	137%
Kobe-TAK090-2, LAA02	215%	**87%**	231%	150%
Loma Prieta-WVC270, LAA02	179%	102%	362%	235%
Kocaeli-YPT330-3, LAA02	302%	166%	568%	369%

*The dynamic earth pressure moment estimate is indeterminate by the M-O method due to the high peak ground acceleration

Figures 6.3–6.4 present the dynamic moment time series measured by the force-sensing bolts and by SG2 on the south stiff and north flexible walls for the Loma Prieta-1 and the Loma Prieta-SC-1 shaking events for LAA01 and LAA02, respectively. The dynamic earth pressure moment estimates using the M-O and Seed and Whitman (1970) methods with total PGA values are also presented in the figures. Performance figures comparing the observed dynamic moment time series to the M-O and Seed and Whitman (1970) estimates for the rest of the LAA01 and LAA02 shaking events are included in Figures A.62–A.74. As expected, the dynamic moment results show a pattern generally consistent with that observed for the maximum total moments discussed in Section 6.1.1.

Table 6.4 Ratio of computed dynamic earth pressure moments to maximum dynamic moments interpreted from strain gage measurements at base of north flexible wall during different shaking events for LAA01 and LAA02.

	Moment Estimate / Measured Moment			
	M-O Method with a_{max}	**M-O Method with 65% a_{max}**	**Seed & Whitman Method with a_{max}**	**Seed & Whitman Method with 65% a_{max}**
Loma Prieta-1, LAA01	137%	**67%**	187%	122%
Loma Prieta-2, LAA01	139%	**67%**	190%	123%
Kobe, LAA01	INDET.*	**73%**	155%	101%
Loma Prieta-3, LAA01	175%	**80%**	217%	141%
Loma Prieta-SC-1, LAA02	308%	159%	494%	321%
Kobe-PI-1, LAA02	413%	142%	352%	229%
Kobe-PI-2, LAA02	INDET.*	277%	277%	180%
Loma Prieta-SC-2, LAA02	295%	141%	415%	270%
Kocaeli-YPT060-2, LAA02	211%	122%	435%	283%
Kocaeli-YPT060-3, LAA02	266%	143%	466%	303%
Kocaeli-YPT330-2, LAA02	325%	175%	576%	374%
Kobe-TAK090-1, LAA02	INDET.*	**82%**	163%	106%
Kobe-TAK090-2, LAA02	329%	133%	354%	229%
Loma Prieta-WVC270, LAA02	243%	138%	491%	318%
Kocaeli-YPT330-3, LAA02	269%	148%	506%	329%

*The dynamic earth pressure moment estimate is indeterminate by the M-O method due to the high peak ground acceleration

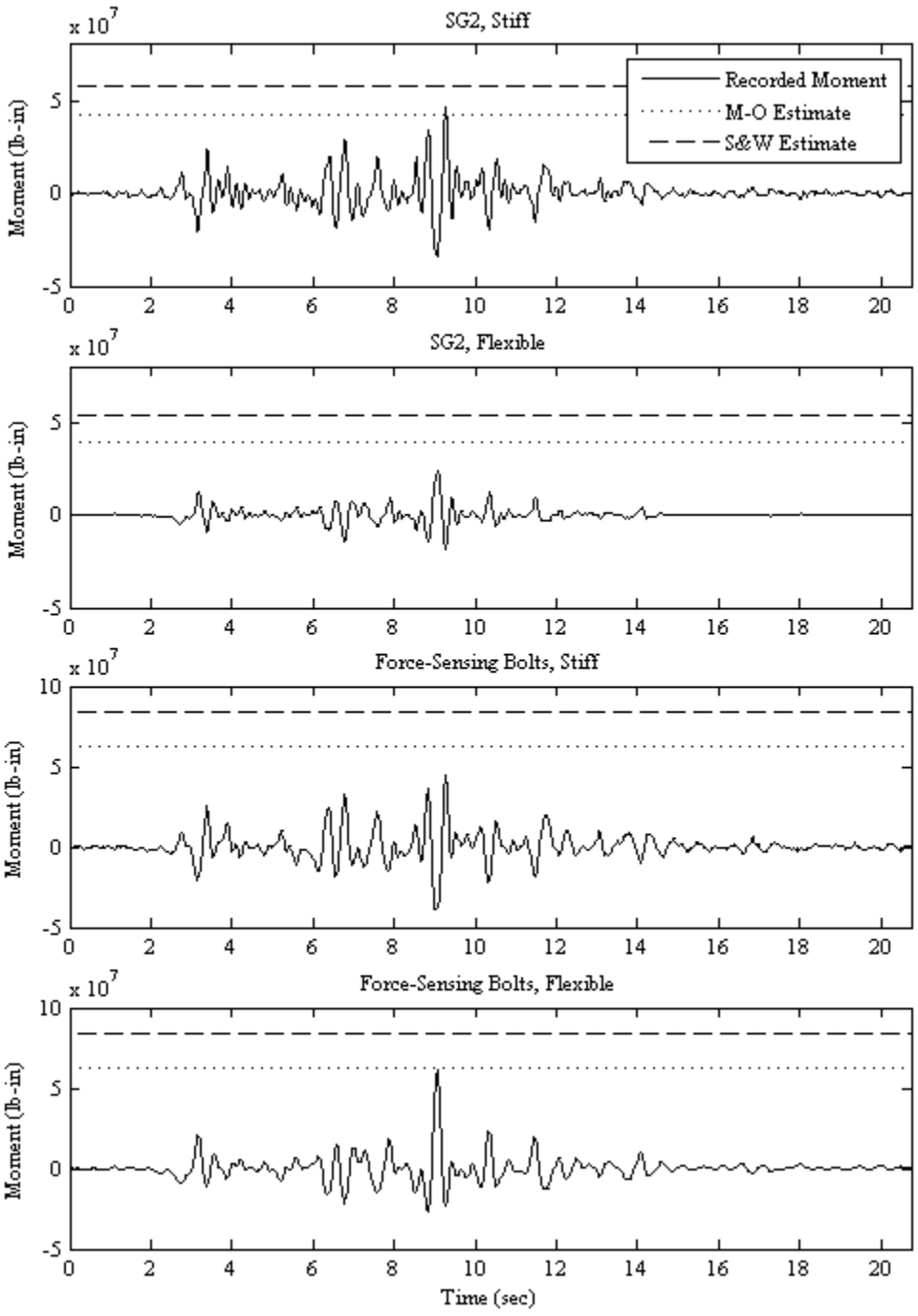

Fig. 6.3 Comparison of dynamic wall moment time series recorded at SG2 on south stiff and north flexible walls and at bases of walls by force-sensing bolts with M-O and Seed and Whitman (1970) moment estimates for Loma Prieta-1, LAA01.

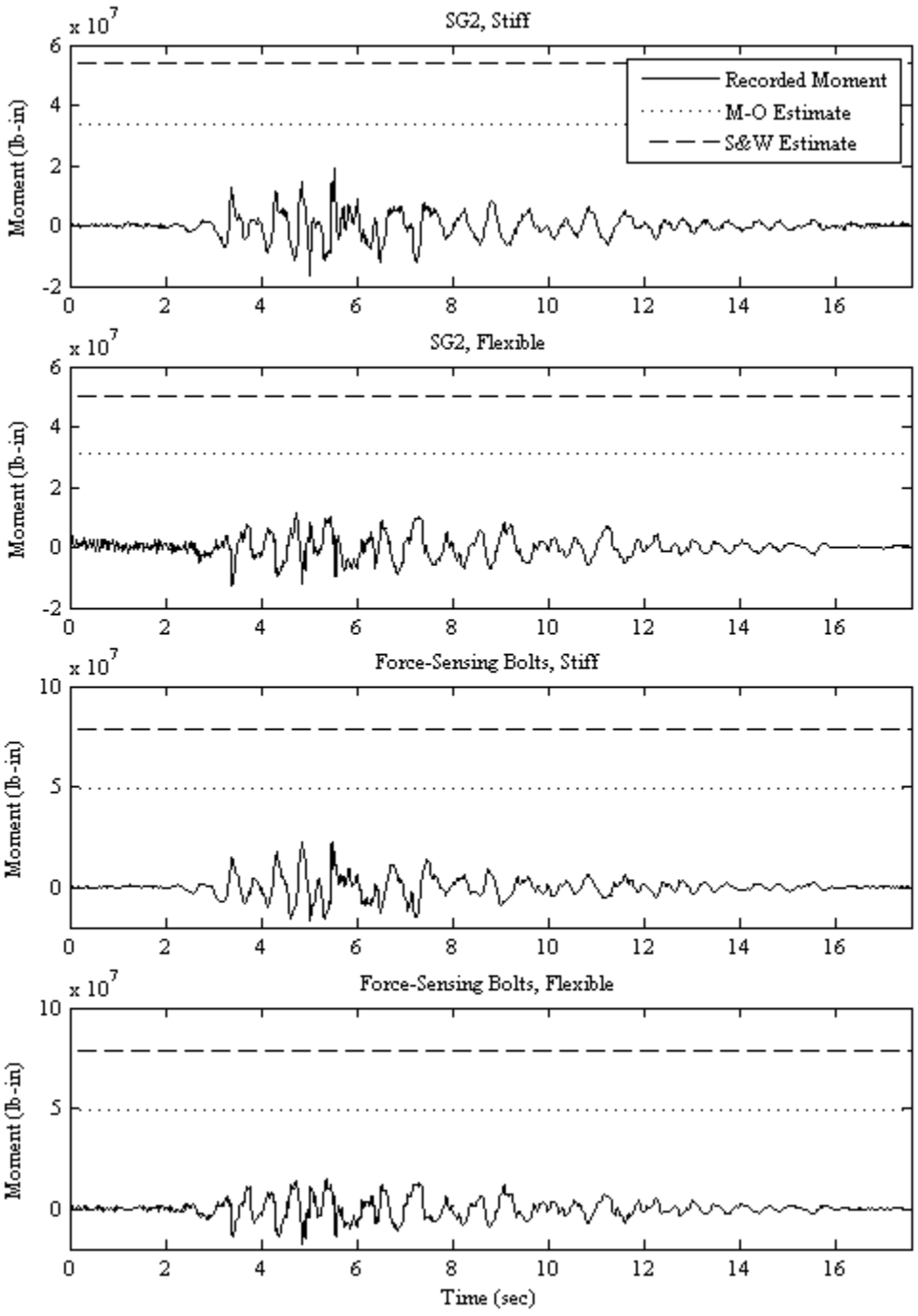

Fig. 6.4 Comparison of dynamic earth pressure moment time series recorded at SG2 on south stiff and north flexible walls and at bases of walls by force-sensing bolts with M-O and Seed and Whitman (1970) moment estimates for Loma Prieta-SC-1, LAA02.

6.1.3 Total Lateral Earth Pressures

Figures 6.5–6.7 present the maximum total pressure distributions recorded by the Flexiforce sensors and interpreted from the strain gage measurements on the south stiff and north flexible walls during the different LAA01 and LAA02 shaking events. The total pressure profiles obtained from the strain gage measurements were corrected to remove the wall inertial effects for the shaking events in experiment LAA02. The total earth pressure distributions estimated by the M-O method using peak and 65% peak ground accelerations are displayed in these figures for comparison.

Figure 6.8 presents comparisons of the maximum total earth pressure distributions recorded by the Flexiforce sensors and interpreted from the strain gage measurements to those estimated by the Seed and Whitman (1970) method using peak and 65% peak ground accelerations for selected shaking events from experiment LAA02. Seed and Whitman (1970) suggest that the point of application of the dynamic increment thrust should be between one half and two thirds the wall height above its base; hence the total earth pressure profile estimates in Figure 6.8 were calculated using an inverted triangular dynamic increment pressure distribution with depth. Figure 6.8 shows that the dynamic earth pressure increment distribution suggested by Seed and Whitman (1970) is not in agreement with the triangular earth pressure profiles observed in the centrifuge experiments. To evaluate the magnitude of the total earth pressures estimated by the Seed and Whitman (1970) method, Figures 6.9–6.11 present comparisons of the maximum recorded and interpreted total pressure distributions to those estimated by the Seed and Whitman (1970) method using a triangular distribution with depth.

Overall, Figures 6.5–6.11 show that the maximum total pressure distributions measured on the stiff and flexible walls are generally lower than those estimated by the M-O method using total PGA. Moreover, the maximum measured total pressure distributions are also lower than those estimated by the Seed and Whitman (1970) method using total PGA, with the exception of the pressure distributions observed for the LAA01 shaking events that include wall inertial effects. Using a reduced PGA value in the M-O and Seed and Whitman (1970) methods generally results in better estimates of the maximum observed total earth pressures. Finally, it is important to note that recorded total earth pressures consistently increase monotonically downward in a manner that is typically observed and assumed under static conditions.

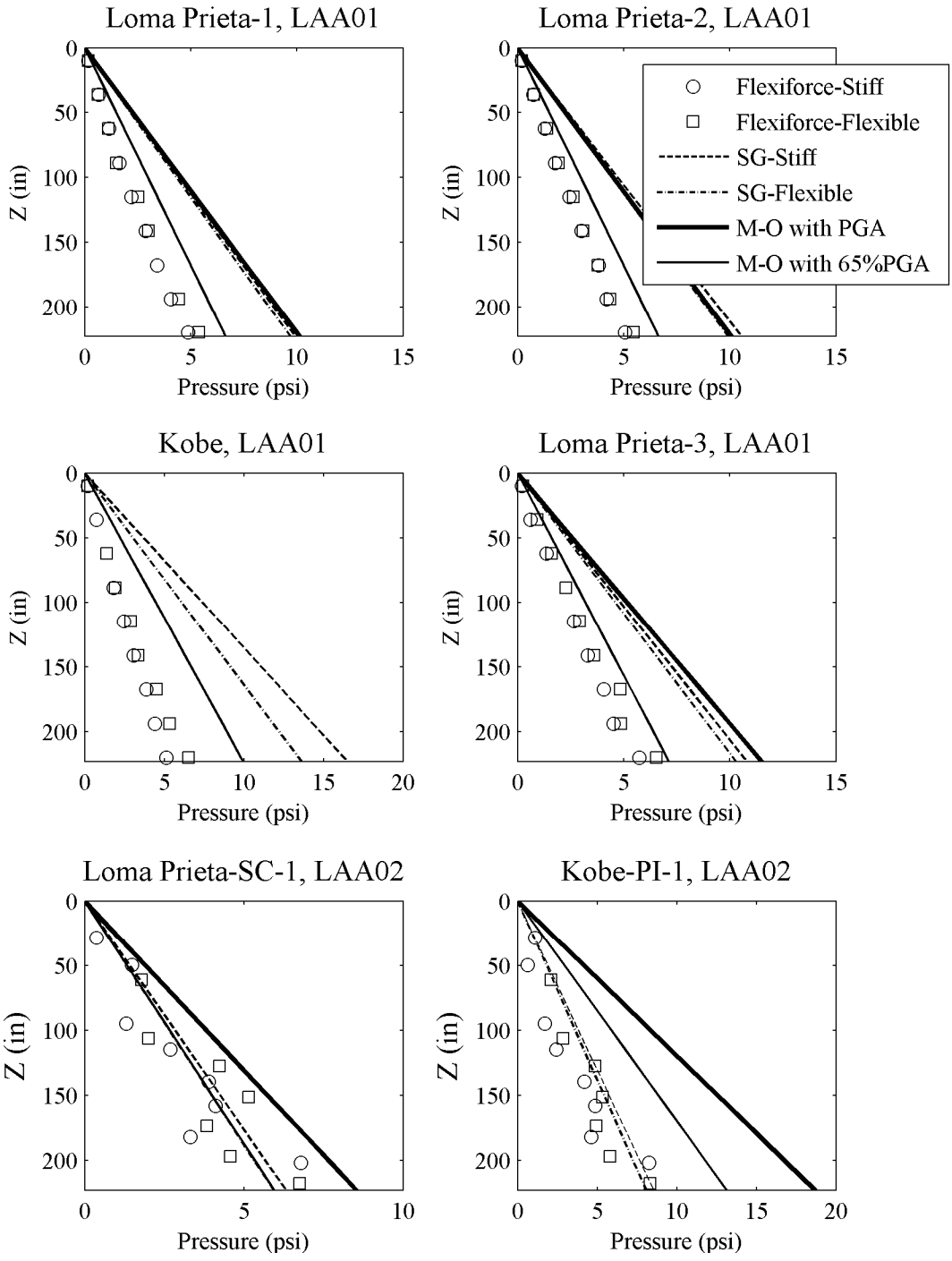

Fig. 6.5 Maximum total pressure distributions directly measured and interpreted from Flexiforce sensors and strain gage data, and estimated using M-O method[1] on south stiff and north flexible walls for all Loma Prieta and Kobe shaking events for LAA01 and for Loma Prieta-SC-1 and Kobe-PI-1 for LAA02.

[1] Total earth pressure profile for Kobe, LAA01 is indeterminate by the M-O method due to the high peak ground acceleration.

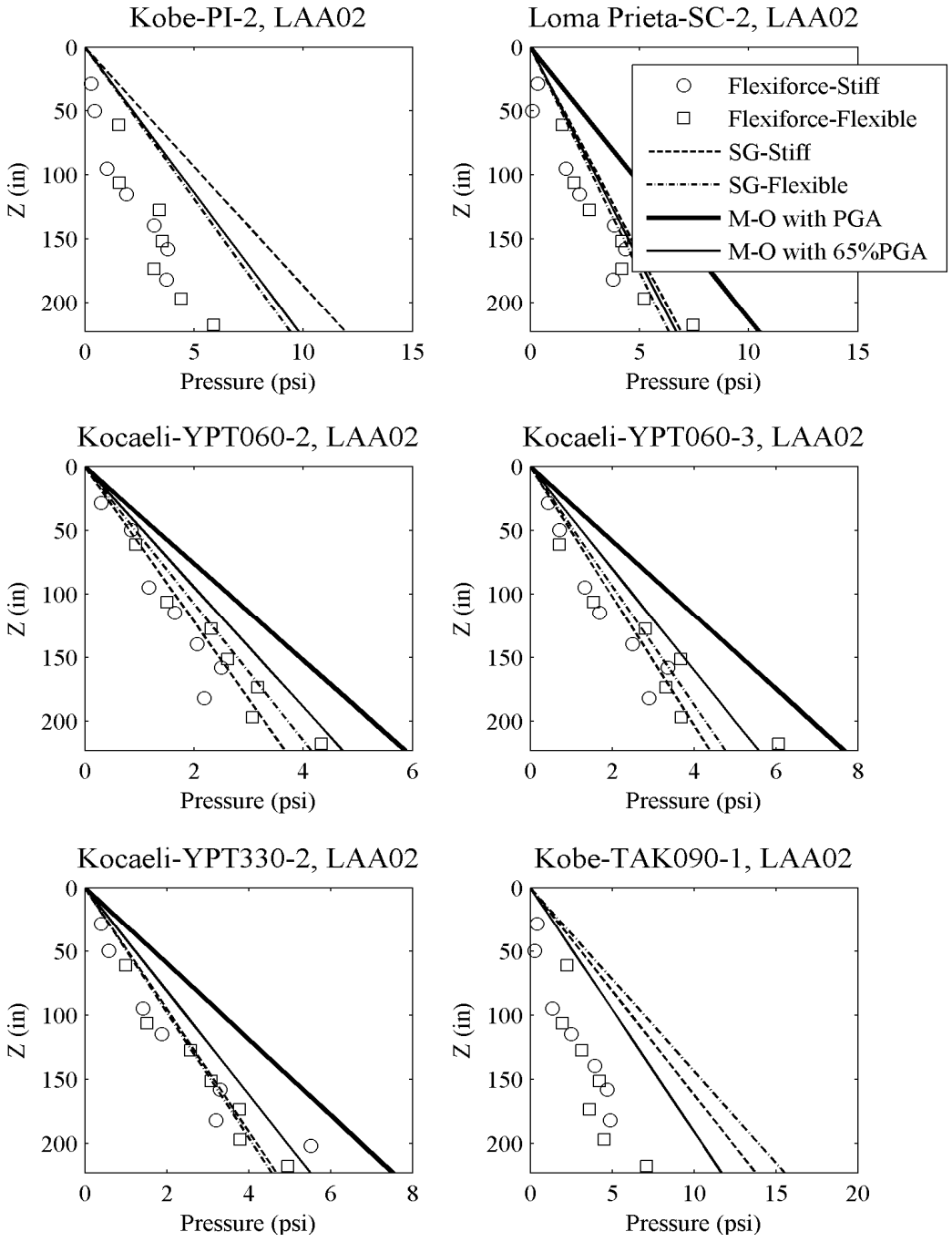

Fig. 6.6 Maximum total earth pressure distributions directly measured and interpreted from Flexiforce sensors and strain gage data, and estimated using M-O method[*] on south stiff and north flexible walls for Kobe-PI-2, Loma Prieta-SC-2, Kocaeli-YPT060-2 and 3, Kocaeli-YPT330-2 and Kobe-TAK090-1 for LAA02.

[*]Total earth pressure profiles for Kobe-PI-2, LAA02 and Kobe-TAK090-1, LAA02 are indeterminate by the M-O method due to the high peak ground acceleration.

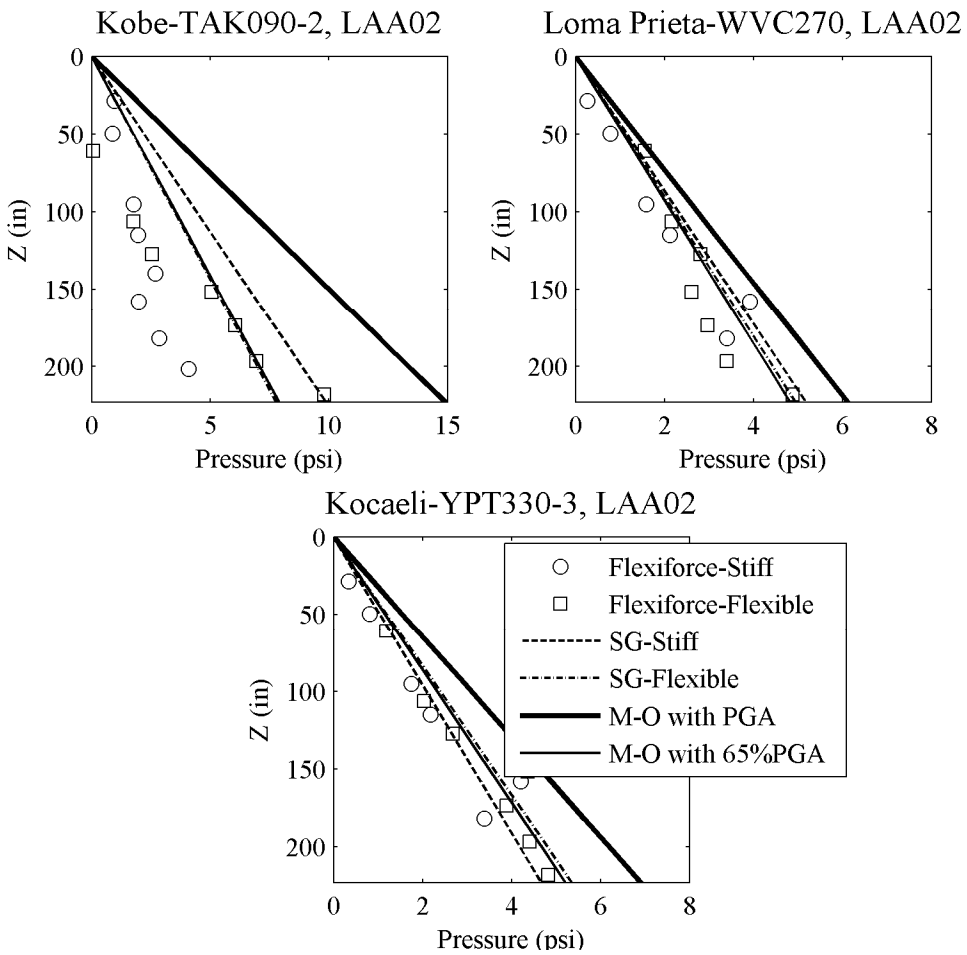

Fig. 6.7 Maximum total earth pressure distributions directly measured and interpreted from Flexiforce sensors and strain gage data, and estimated using M-O method on south stiff and north flexible walls for Kobe-TAK090-2, Loma Prieta-WVC270, and Kocaeli-YPT330-3 for LAA02.

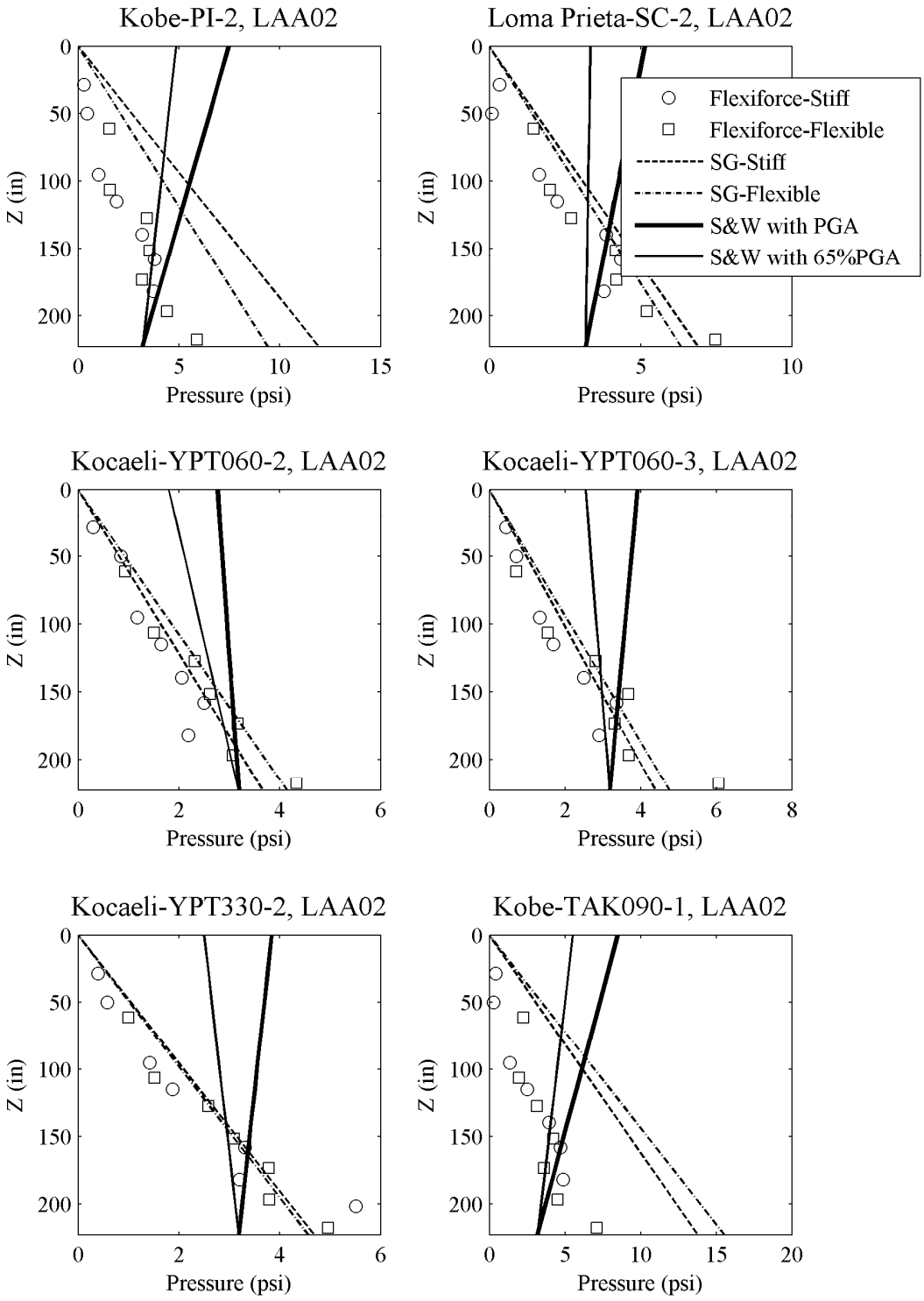

Fig. 6.8 Maximum total earth pressure distributions directly measured and interpreted from Flexiforce sensors and strain gage data, and estimated using Seed and Whitman (1970) method on south stiff and north flexible walls for Kobe-PI-2, Loma Prieta-SC-2, Kocaeli-YPT060-2 and 3, Kocaeli-YPT330-2 and Kobe-TAK090-1 for LAA02.

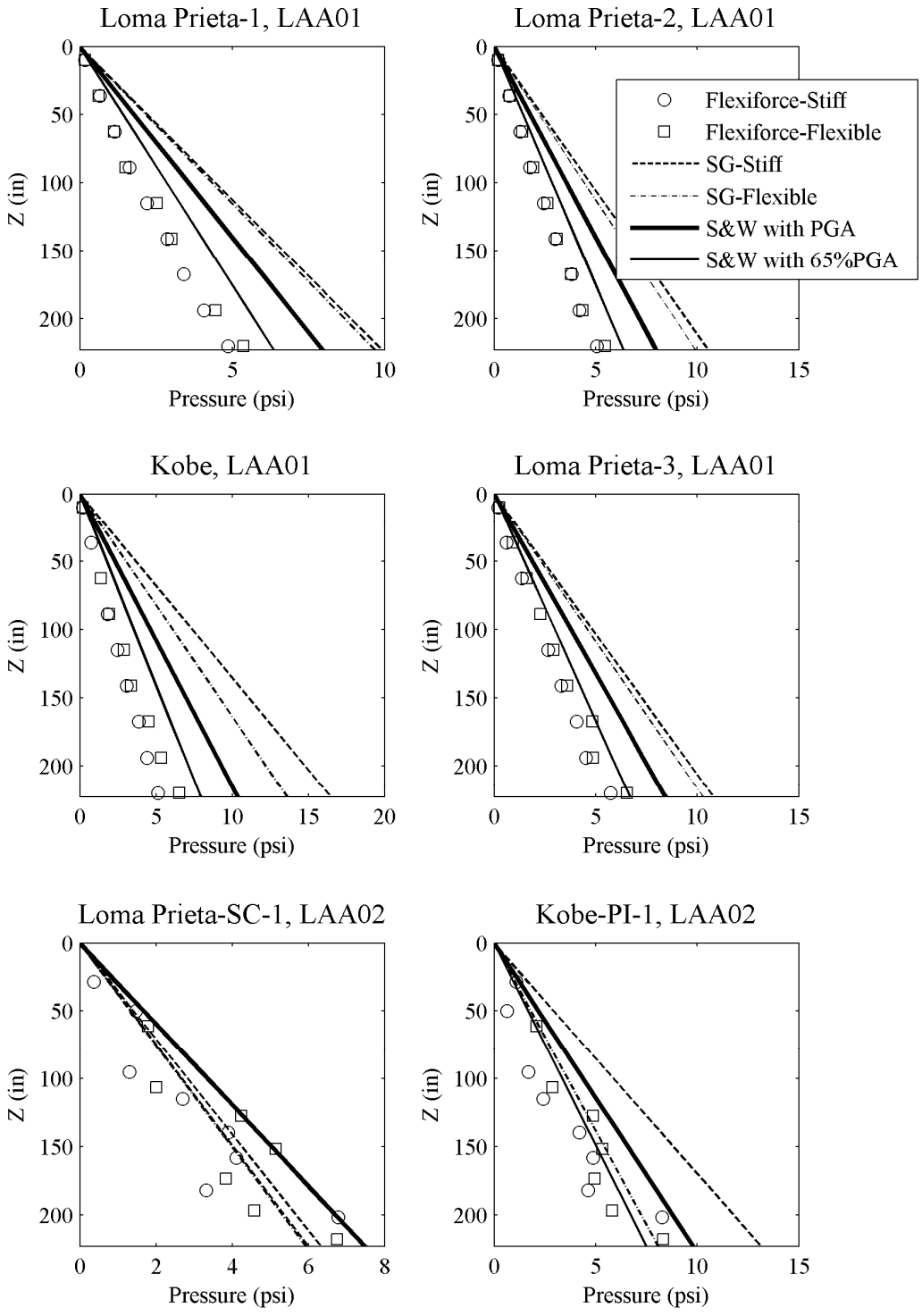

Fig. 6.9 Maximum total pressure distributions directly measured and interpreted from Flexiforce sensors and strain gage data, and estimated using Seed and Whitman (1970) method with triangular pressure profiles on south stiff and north flexible walls for all Loma Prieta and Kobe shaking events for LAA01 and for Loma Prieta-SC-1 and Kobe-PI-1 for LAA02.

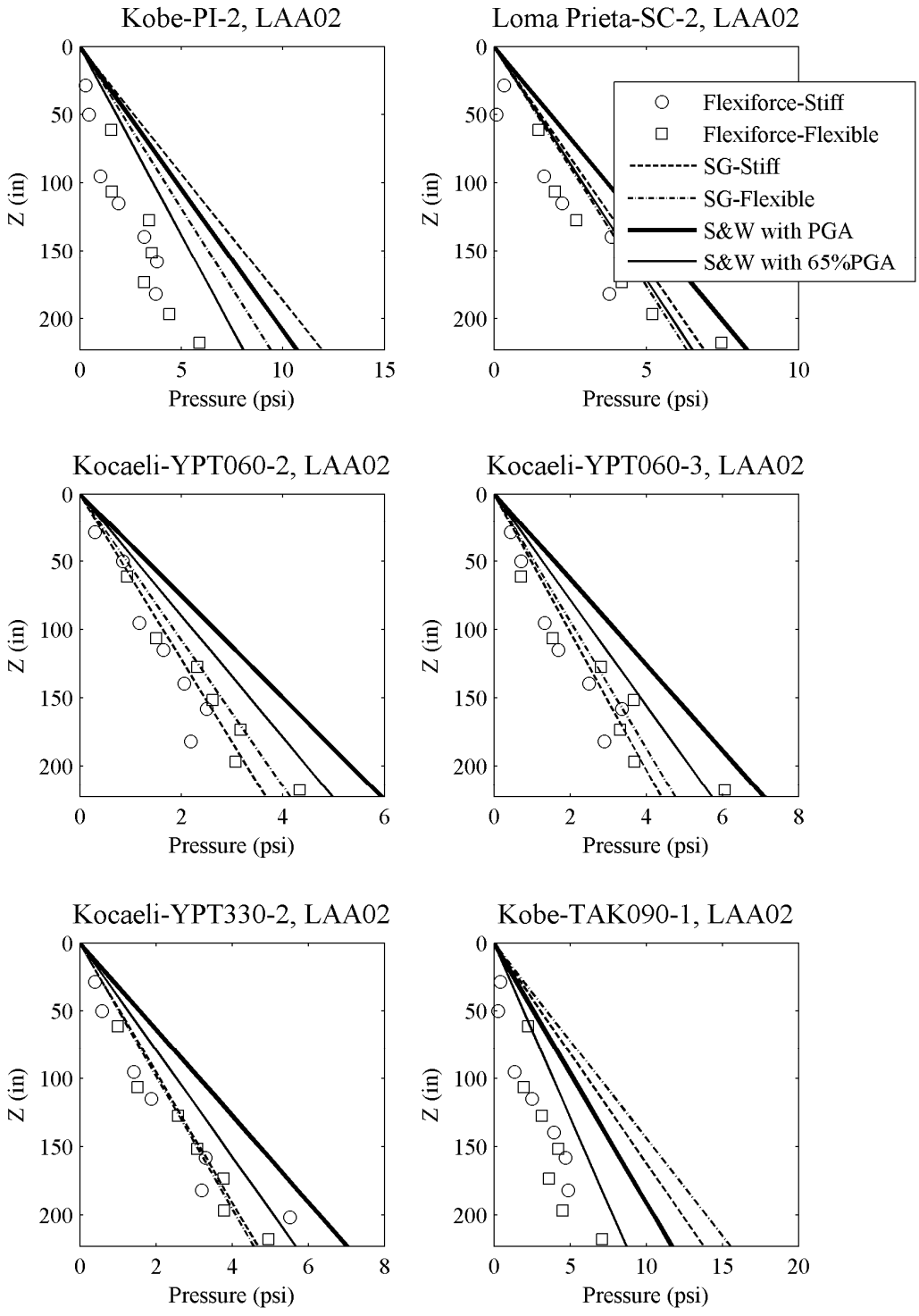

Fig. 6.10 Maximum total earth pressure distributions directly measured and interpreted from Flexiforce sensors and strain gage data, and estimated using Seed and Whitman (1970) method with triangular pressure profiles on south stiff and north flexible walls for Kobe-PI-2, Loma Prieta-SC-2, Kocaeli-YPT060-2 and 3, Kocaeli-YPT330-2 and Kobe-TAK090-1 for LAA02.

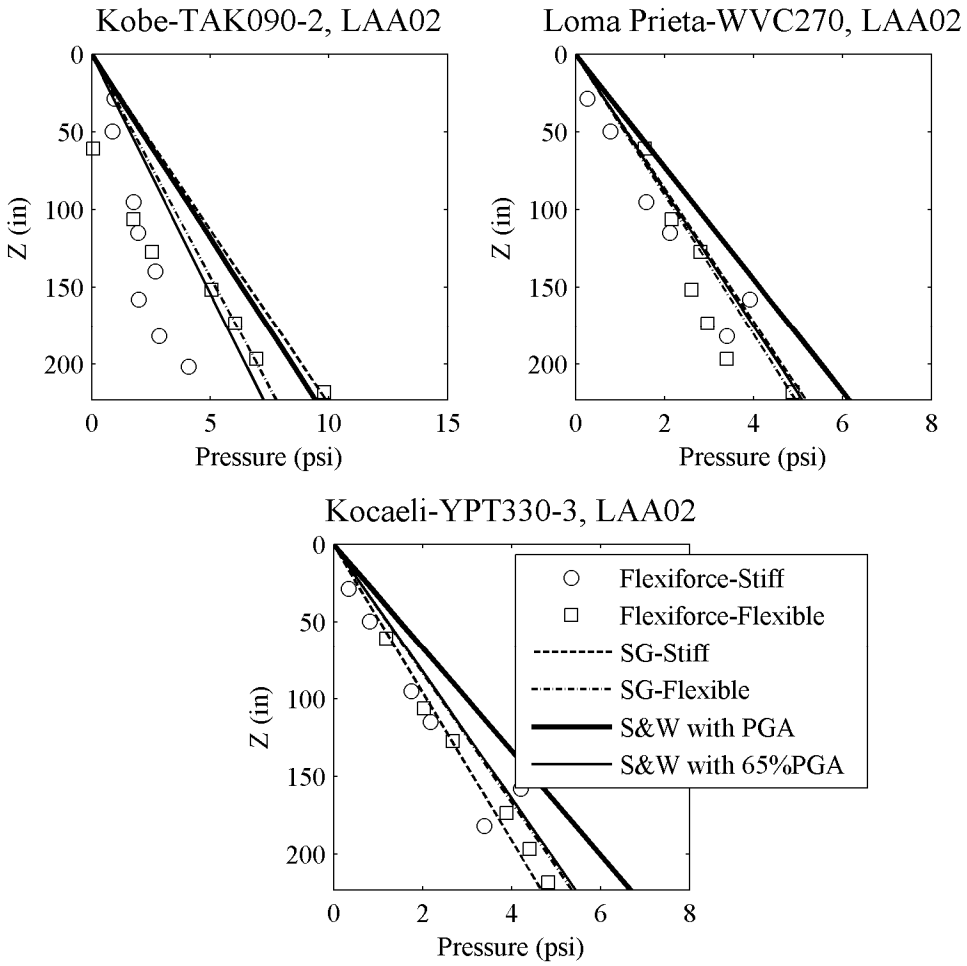

Fig. 6.11 Maximum total earth pressure distributions directly measured and interpreted from Flexiforce sensors and strain gage data, and estimated using Seed and Whitman (1970) method with triangular pressure profiles on south stiff and north flexible walls for Kobe-TAK090-2, Loma Prieta-WVC270, and Kocaeli-YPT330-3 for LAA02.

6.2 EVALUATION OF TYPICAL SEISMIC DESIGN: PROPOSED BART STRUCTURES

Based on the results obtained from the centrifuge experiments, the Bay Area Rapid Transit (BART) designs were evaluated in order to assess their adequacy in estimating the distribution and magnitude of dynamic earth pressures and moments on retaining structures. The cantilever U-shaped retaining structures used in both centrifuge experiments are representative of typical designs currently under consideration by BART and the Valley Transportation Authority (VTA). U-shaped cantilever retaining walls designed by BART are classified as either “yielding” (also

called “flexible”) or “rigid.” According to the BART design criteria, a cantilever retaining wall is considered “yielding” when the top of the wall moves a distance equal to or greater than 0.4% the height of the wall during seismic loading. The top of a “rigid” U-wall deflects less than 0.4% the height of the wall during loading. The BART design criteria for “rigid” walls assume at-rest (Ko) earth pressures for static loads and 1.5 times the M-O inverted triangular dynamic pressure for seismic loads. For “flexible” walls, BART design criteria assume active earth pressures for static loads and the M-O inverted triangular dynamic pressure for seismic loads. For both stiff and flexible walls, half the peak ground accelerations measured at the top of the soil in the free field are used for estimates of earth pressures using the BART design criteria.

Based on the maximum transient deflections for the different shaking events presented in Table 4.11, the stiff retaining structure used in the centrifuge experiments generally classifies as “rigid” per BART’s criteria for most of the shaking events. The flexible retaining structure classifies as “yielding.” Table 6.5 presents computed total earth pressure moments based on the BART design criteria as a ratio in percent of the maximum total moments interpreted from the strain gage measurements at the bases of the south stiff and the north flexible walls for the different shaking events in experiments LAA01 and LAA02. Table 6.6 presents BART estimates for dynamic earth pressure moments as a ratio in percent of the maximum dynamic moments interpreted at the bases of the walls from the strain gage measurements. It should be noted that moment measurements for LAA01 in Tables 6.5 and 6.6 include wall inertial effects, while recorded moments for LAA02 were corrected to remove wall inertial effects.

As shown in Tables 6.5 and 6.6, BART design criteria generally overestimate the maximum total earth pressure moments and the maximum dynamic earth pressure moments interpreted at the bases of the stiff and flexible walls for LAA02 shaking events. The maximum total moments and dynamic moments measured at the bases of the walls for some shaking events during experiment LAA01 are underestimated by BART’s criteria because they contain wall inertial effects. Figures 6.12 and 6.13 show that BART’s design criteria with triangular pressure distributions generally overestimate the maximum total earth pressures on the stiff wall but slightly underestimate those on the flexible wall.

Table 6.5 Ratio of computed total earth pressure moments using BART design criteria to maximum total moments interpreted from strain gage measurements at bases of south stiff and north flexible walls during different shaking events for LAA01 and LAA02.

	Moment Estimate / Measured Moment	
	Stiff Wall	**Flexible Wall**
Loma Prieta-1, LAA01	130%	**83%**
Loma Prieta-2, LAA01	122%	**80%**
Kobe, LAA01	113%	**86%**
Loma Prieta-3, LAA01	128%	**83%**
Loma Prieta-SC-1, LAA02	184%	120%
Kobe-PI-1, LAA02	125%	127%
Kobe-PI-2, LAA02	154%	123%
Loma Prieta-SC-2, LAA02	190%	127%
Kocaeli-YPT060-2, LAA02	251%	132%
Kocaeli-YPT060-3, LAA02	248%	139%
Kocaeli-YPT330-2, LAA02	231%	143%
Kobe-TAK090-1, LAA02	154%	**86%**
Kobe-TAK090-2, LAA02	155%	122%
Loma Prieta-WVC270	182%	114%
Kocaeli-YPT330-3, LAA02	209%	110%

Comparisons of the maximum total earth pressure profiles measured by the Flexiforce sensors and interpreted from the strain gage measurements on the south stiff and north flexible walls to those estimated using the BART design criteria are presented in Figure 6.12 for selected shaking events from experiment LAA02. Figure 6.12 shows that the inverted triangular dynamic earth pressure distribution assumed in the BART design criteria is not in agreement with the trend observed in the recorded total earth pressure profiles. Figures 6.13 and 6.14 present comparisons of the recorded and interpreted maximum total earth pressure profiles on the south stiff and north flexible walls to those estimated using the BART design criteria assuming triangular pressure distribution for some of the LAA02 shaking events.

While the assumptions in the methodology used to develop the seismic design of U-shaped stiff and flexible cantilever retaining structures for BART are clearly flawed, they are overly conservative in estimating the maximum total dynamic moments at the bases of the walls.

The experimental results show that dynamic pressure profiles have a triangular distribution with depth and there is no basis for the inverted triangular distribution assumption.

Table 6.6 Ratio of computed dynamic earth pressure moments using BART design criteria to maximum dynamic moments interpreted from strain gage measurements at bases of south stiff and north flexible walls during different shaking events for LAA01 and LAA02.

	Moment Estimate / Measured Moment	
	Stiff Wall	**Flexible Wall**
Loma Prieta-1, LAA01	105%	**92%**
Loma Prieta-2, LAA01	**97%**	**93%**
Kobe, LAA01	**89%**	**92%**
Loma Prieta-3, LAA01	109%	110%
Loma Prieta-SC-1, LAA02	223%	225%
Kobe-PI-1, LAA02	142%	187%
Kobe-PI-2, LAA02	166%	156%
Loma Prieta-SC-2, LAA02	229%	196%
Kocaeli-YPT060-2, LAA02	302%	177%
Kocaeli-YPT060-3, LAA02	362%	203%
Kocaeli-YPT330-2, LAA02	362%	250%
Kobe-TAK090-1, LAA02	192%	**98%**
Kobe-TAK090-2, LAA02	174%	178%
Loma Prieta-WVC270	222%	200%
Kocaeli-YPT330-3, LAA02	359%	213%

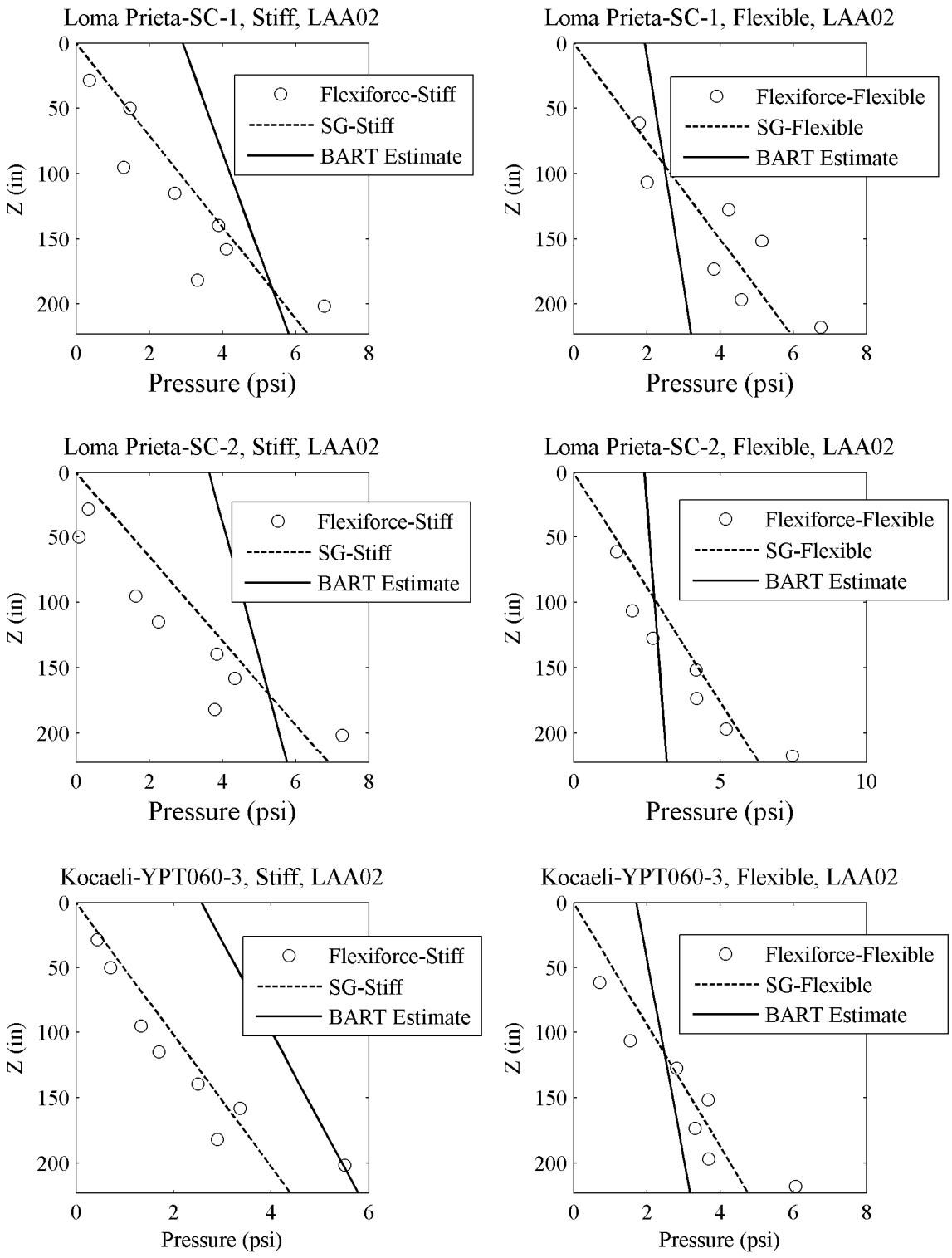

Fig. 6.12 Maximum total earth pressure distributions directly measured and interpreted from Flexiforce sensors and strain gage data, and estimated using BART design criteria on south stiff and north flexible walls for Loma Prieta-SC-1, Loma Prieta-SC-2, and Kocaeli-YPT060-3 shaking events for LAA02.

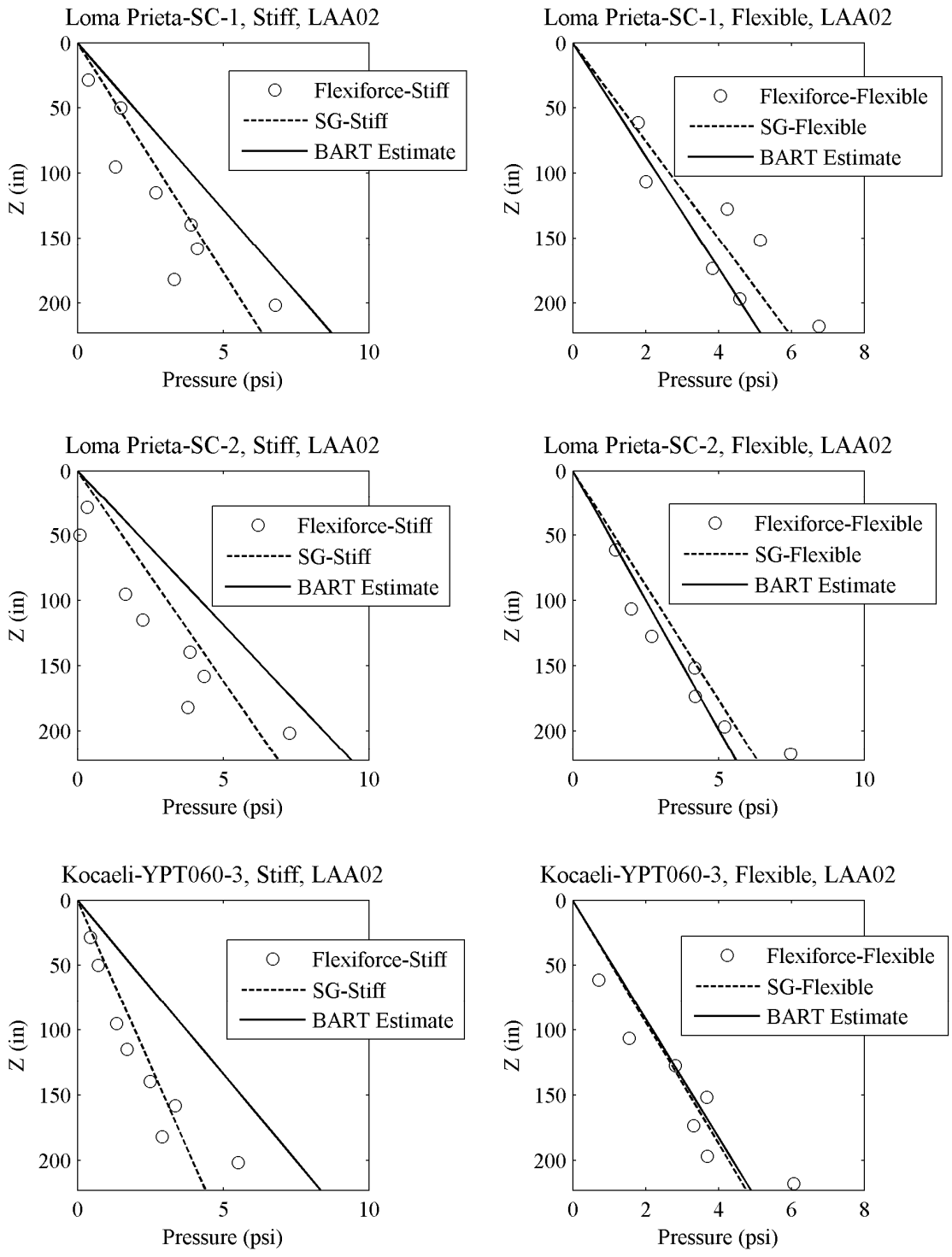

Fig. 6.13 Maximum total earth pressure distributions directly measured and interpreted from Flexiforce sensors and strain gage data, and estimated using BART design criteria with triangular pressure profiles on south stiff and north flexible walls for Loma Prieta-SC-1, Loma Prieta-SC-2, and Kocaeli-YPT060-3 shaking events for LAA02.

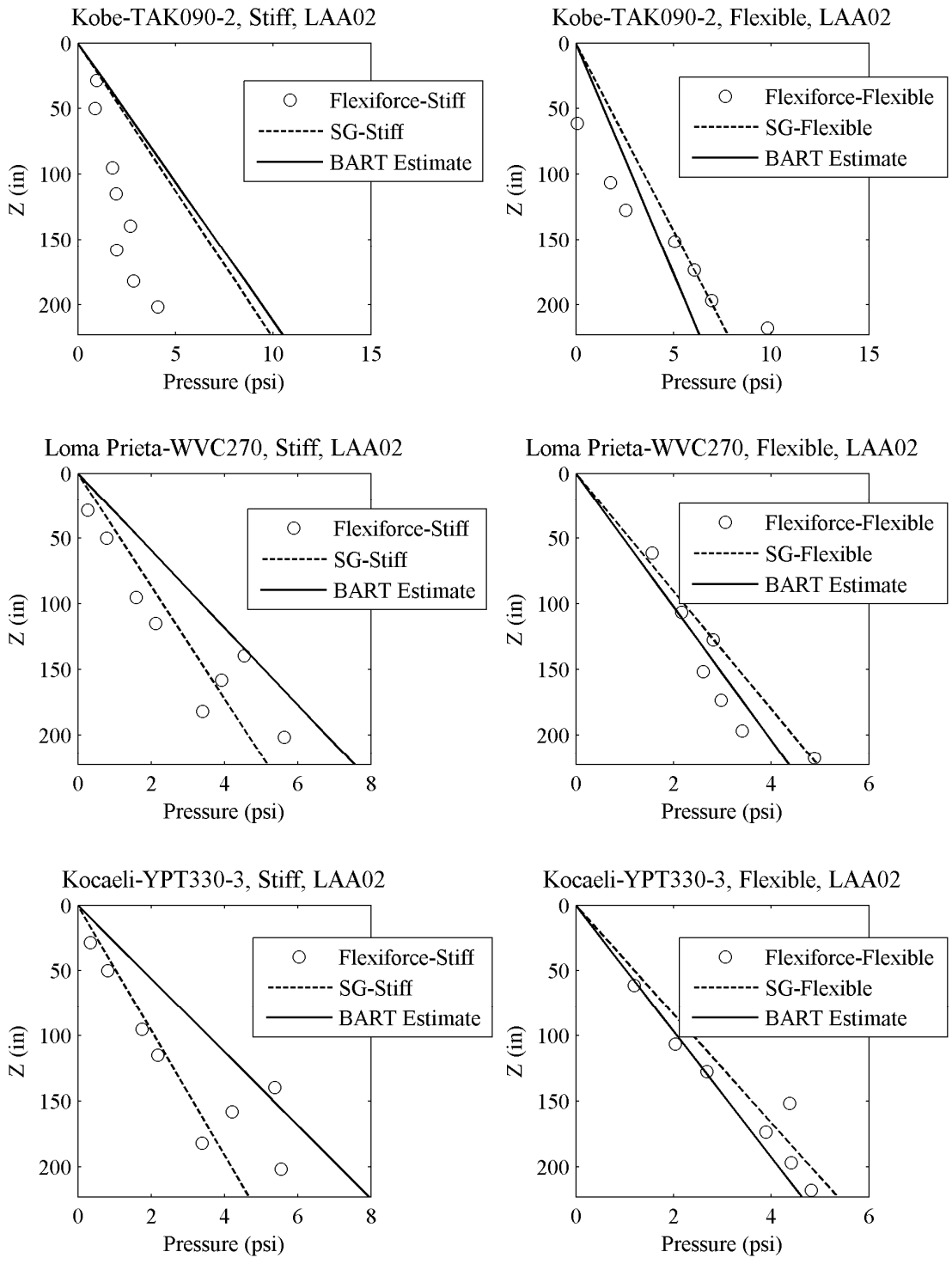

Fig. 6.14 Maximum total earth pressure distributions directly measured and interpreted from Flexiforce sensors and strain gage data, and estimated using BART design criteria with triangular pressure profiles on south stiff and north flexible walls for Kobe-TAK090-2, Loma Prieta-WVC270, and Kocaeli-YPT330-3 shaking events for LAA02.

6.3 BACK-CALCULATED DYNAMIC EARTH PRESSURE COEFFICIENTS

6.3.1 Design Considerations

As discussed in the literature review of Chapter 2, retaining walls are traditionally designed for maximum total earth pressures that consist of static and maximum dynamic earth pressures. However, designing retaining structures for both, the maximum dynamic earth pressures and the maximum wall inertia is inconsistent with experimental data which show that the earth pressures and the wall inertial forces are not in phase, as discussed in Section 4.5.2. Since moments are usually more relevant to the structural design of cantilever retaining walls, a more rational approach is to design retaining walls for maximum total wall moments reflecting the combined effects of both earth pressures and wall inertia. Figures 6.15 and 6.16 present an example of recorded dynamic wall moment time series compared to computed wall inertial moment and recorded dynamic earth pressure time series acting on the south stiff and north flexible walls during Loma Prieta-SC-1. As discussed in Section 4.5.2 and shown in these figures, dynamic wall moments are generally in phase with wall inertial moments but not in phase with dynamic earth pressures. Therefore, based on the observed performance of the retaining walls under earthquake loading, it is more appropriate to design cantilever retaining walls for the maximum dynamic wall moment, which consists of maximum wall inertia and a dynamic earth pressure contribution that is lower than the maximum dynamic earth pressure acting on the walls. The appropriate dynamic earth pressure coefficients can be back-calculated based on the earth pressures interpreted from the maximum wall moments as observed in the centrifuge experiments.

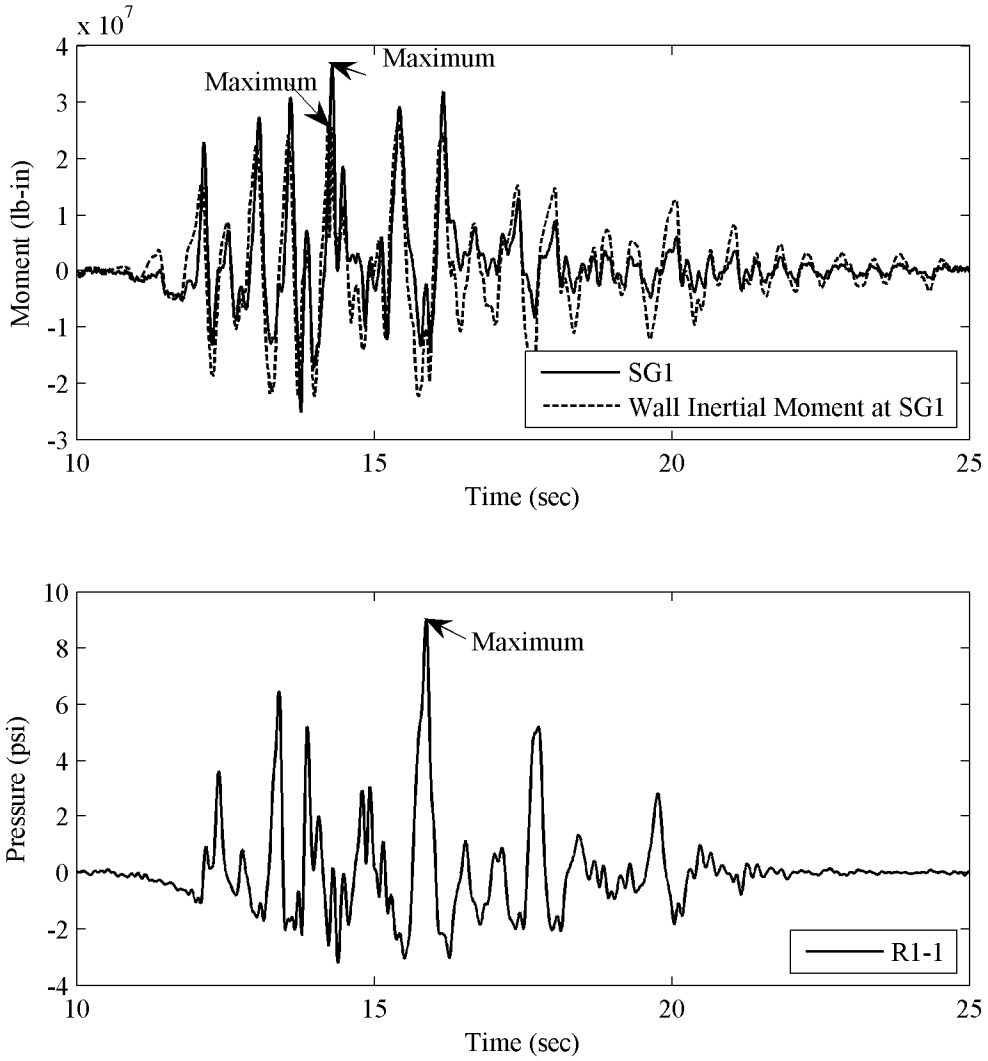

Fig. 6.15 Comparison of dynamic wall moment recorded by SG1, estimated wall inertial moment at SG1 location, and dynamic earth pressure recorded by R1-1 on south stiff wall during Loma Prieta-SC-1.

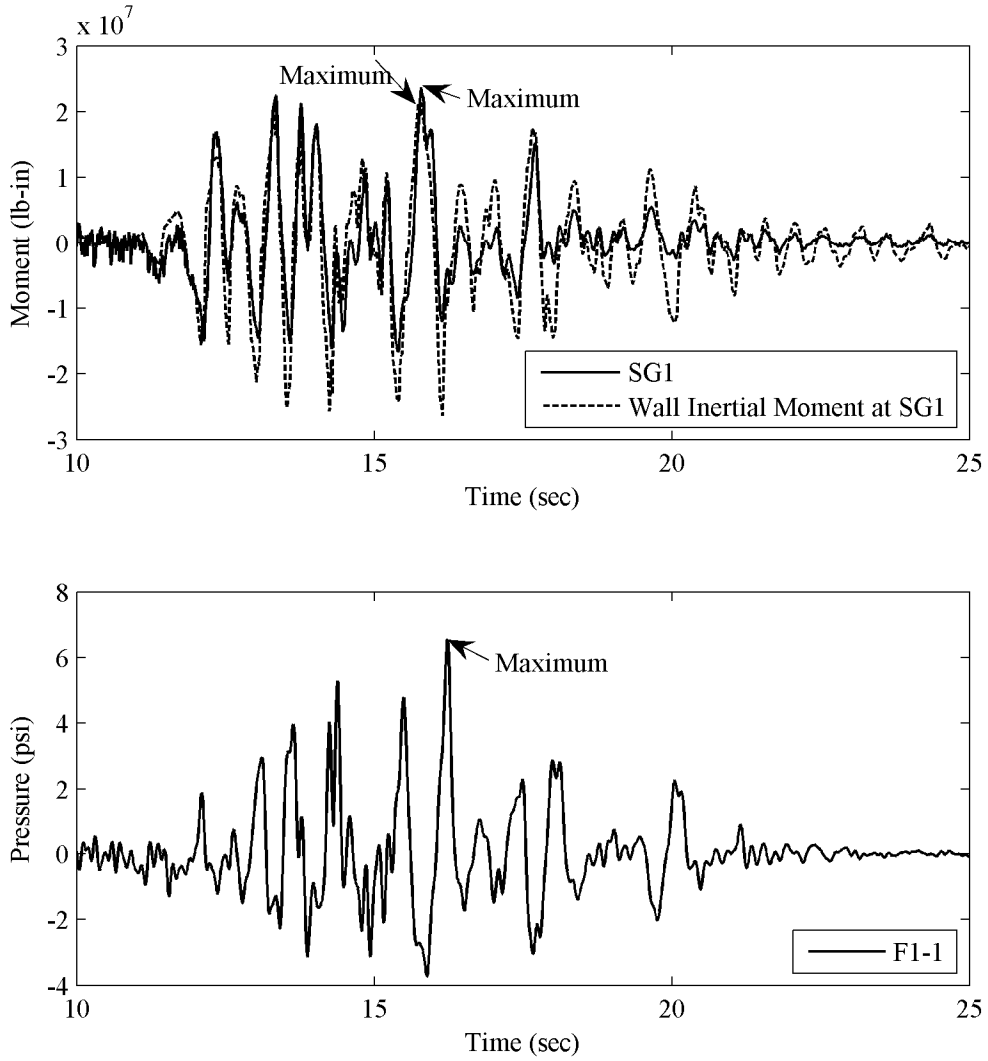

Fig. 6.16 Comparison of dynamic wall moment recorded by SG1, estimated wall inertial moment at SG1 location, and dynamic earth pressure recorded by F1-1 on north flexible wall during Loma Prieta-SC-1.

6.3.2 Dynamic Earth Pressure Coefficients

The dynamic earth pressure coefficients (ΔK_{AE}) can be calculated from the strain gage and force-sensing bolt measurements at the time of the maximum dynamic wall moments. Figure 6.17 presents ΔK_{AE} relationships for the stiff and flexible walls as a function of the peak ground acceleration measured at the top of the soil in the free field. Maximum ΔK_{AE} values corresponding to maximum dynamic earth pressures are also presented in Figure 6.17 for

comparison. It should be noted that using maximum ΔK_{AE} values for design purposes is overly conservative when added to the maximum wall inertial response.

Figure 6.17 shows that ΔK_{AE} values increase linearly with increasing peak ground acceleration measured at the top of the soil in the free field. Moreover, dynamic effects at the maximum dynamic wall moments do not appear to be significant when the peak ground acceleration is less than about 0.4 g. This suggests that for peak ground accelerations less than 0.4 g, the maximum dynamic wall moment is mainly due to the inertia of the wall itself. Total earth pressures acting on the walls at that time are slightly lower than static earth pressures. It is important to note that the back-calculated ΔK_{AE} values presented in Figure 6.17 do not include any factor of safety that would normally be incorporated in seismic designs. Such factors of safety when included in seismic designs would allow retaining walls to resist peak ground accelerations greater than 0.4 g without significant increase in dynamic earth pressures. Similar conclusions were stated by Seed and Whitman (1970), who observed that gravity retaining structures designed to a reasonable static factor of safety should be able to resist seismic loads up to 0.3 g.

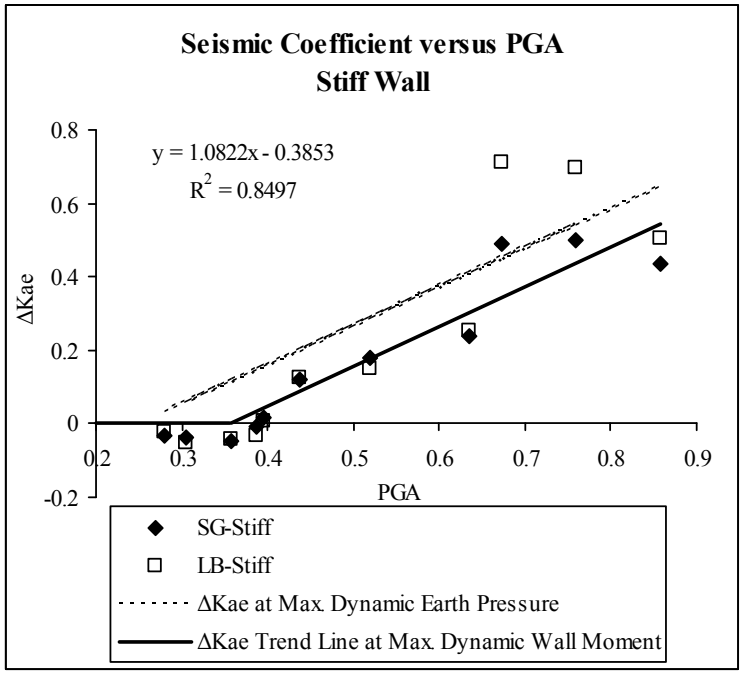

(a)

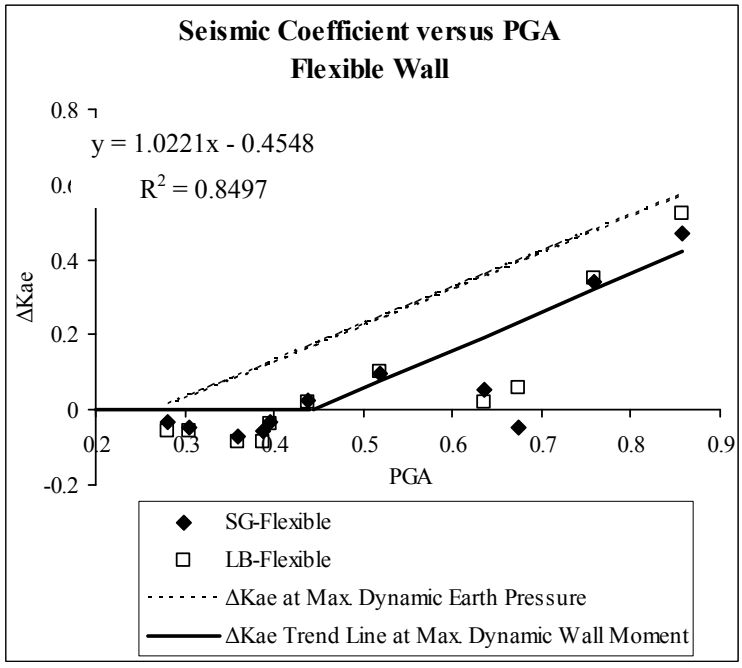

(b)

Fig. 6.17 Back-calculated dynamic earth pressure coefficients at time of maximum dynamic wall moments and maximum dynamic earth pressures on stiff and flexible walls as function of peak ground acceleration measured at top of soil in free field.

The relationships between the ΔK_{AE} values at the time of the maximum dynamic wall moments and backfill relative density, the amplification/attenuation of the ground motions, and the Arias intensity are presented in Figures 6.18–6.20. As shown in Figure 6.18, the effect of changing relative density on ΔK_{AE} is somewhat indistinct because of the relatively small range of relative densities (72–81%) in experiment LAA02. While it appears that there is a decrease in ΔK_{AE} with increasing relative density, this trend is not very clear and is probably masked by the fact that different ground motions of different intensities were used at different stages of the experiment. Another way to look at the results is to plot ΔK_{AE} as a function of the amplification of the input ground motion in the free field. The plots in Figure 6.15 show that the seismic earth pressure coefficient is generally highest when the ground motion is attenuated (stronger shaking), and decreases as the magnitude of the ground motion amplification increases. This effect is more clearly evident in Figure 6.16, which shows that the seismic earth pressure coefficient increases with the intensity of shaking represented by I_a.

Finally, the relationships presented in Figure 6.17 can be applied to estimate the dynamic earth pressures at the time of maximum dynamic wall moments as a function of the PGA at the top of the soil in the free field. This estimated dynamic earth pressure can be used for the seismic design of a cantilever retaining wall with dry medium-dense sand backfill.

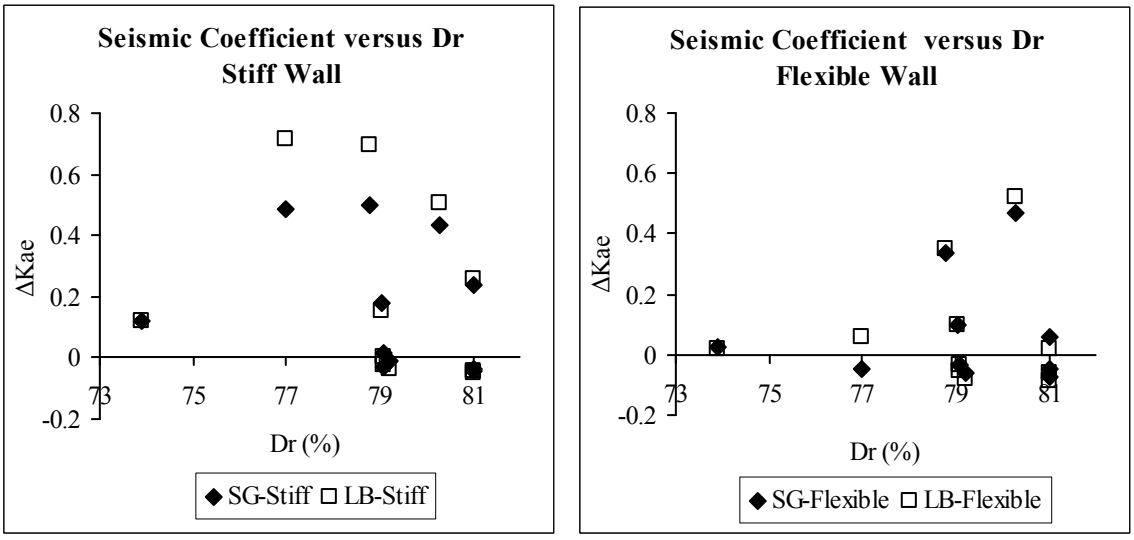

Fig. 6.18 Back-calculated dynamic earth pressure coefficient at time of maximum dynamic wall moments on stiff and flexible walls as function of relative density of soil backfill.

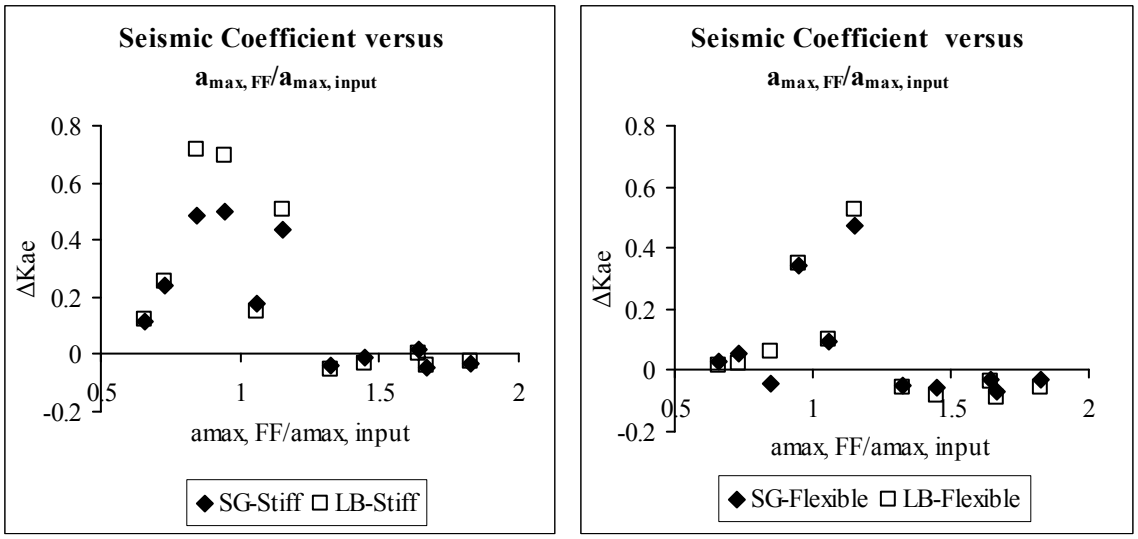

Fig. 6.19 Back-calculated dynamic earth pressure coefficient at time of maximum dynamic wall moments on stiff and flexible walls as function of amplification/attenuation of ground motion.

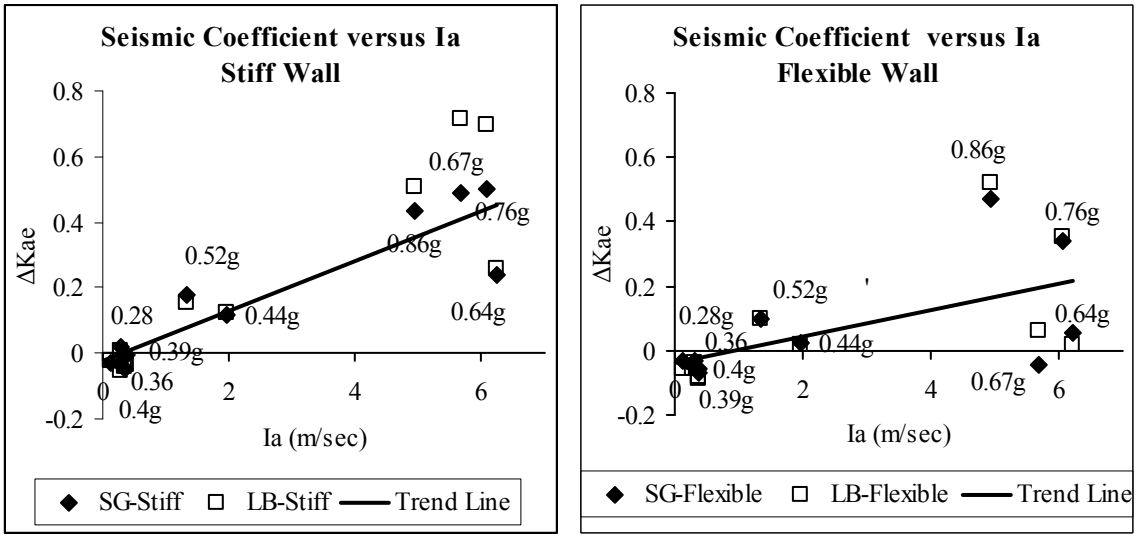

Fig. 6.20 Back-calculated dynamic earth pressure coefficient at time of maximum dynamic wall moments on stiff and flexible walls as function of intensity of shaking.

7 Summary and Conclusions

7.1 OVERVIEW

A review of the basic assumptions and criteria used for the analysis and design of retaining structures subjected to seismic loading shows that most of the methods are based on or comparable to procedures that have roots in experimental and analytical work performed in the 1920s and 1940s. Although the basic method is commonly referred to as the Mononobe-Okabe (M-O) method, the experimental basis for the method is the work of Mononobe and Matuso (1929) and Matsuo (1941), while the theoretical underpinnings are presented by Okabe (1926). The approach presented in these early papers was reviewed by Seed and Whitman (1970), who carefully considered field evidence and available experimental data to that date, and proposed a modified approach that has been extensively adopted since then. Later, Richards and Elms (1979, 1980) suggested a modification of the methodology to deal specifically with gravity walls, and included wall inertial effects as an important parameter in the design. While many other researchers have addressed this topic since, the basic premise of the method, that a Coulomb wedge adequately represents the mobilized soil mass during seismic loading, has been accepted.

With the increased awareness of seismic risks and a better understanding of the magnitude of potential ground motions, designers of retaining structures in regions in proximity to seismic sources have increasingly faced the challenge of having to consider very large seismic forces based on the M-O methodology or its variants. Yet, no significant failures of retaining structures designed for seismic loading and supporting level backfill have occurred in recent large earthquakes. Case histories show that retaining structures underdesigned with respect to seismic forces performed quite well under seismic loading with peak ground acceleration up to 0.5 g.

Thus, the purpose of this study was to obtain a set of experimental data that could be used to evaluate whether the basic assumptions derived from the shaking table experiments on relatively dry loose sand, as performed by Mononobe and Matsuo (1929) and Matsuo (1941), were being appropriately extended to modern design. While shaking table experiments have been extensively used for various types of studies, they present a very difficult scaling challenge for frictional materials such as sand, since the strength and hence all other dynamic properties of the material are directly proportional to confining stress. As a result, correct scaling of dynamic effects using natural material such as sand is virtually impossible in 1-g shaking table experiments without resorting to full-scale models. Therefore, the approach adopted in this study was to use the geotechnical centrifuge to perform two sets of experiments on model walls with medium-dense dry sand backfill. While scaling and instrumentation issues still come up, the dynamic properties of the prototype structures and soil backfill can be correctly scaled, so a significantly better insight can be obtained into the mechanism of seismic earth pressure development.

The centrifuge experiments results and observations were later used to develop and calibrate a 2-D FE model on the OpenSees platform to study the behavior of retaining walls and backfill under seismic loading. While many analytical studies have been conducted on the subject of seismic earth pressures in the last eighty years, many have been validated using oversimplified or very limited experimental or field data. The purpose of the analytical phase of this study was to evaluate the ability of FE models to capture the essential features and response characteristics of the retaining wall–backfill system under seismic loading. Once adequately calibrated, such models can be further used to perform more specific parametric studies and design evaluations.

7.2 DYNAMIC CENTRIFUGE EXPERIMENTS OBSERVATIONS AND CONCLUSIONS

The results of the two centrifuge experiments on model U-shaped stiff and flexible cantilever retaining structures with medium-dense dry Nevada sand backfill with relative density of 61% and 72%, respectively, provide a number of important observations and conclusions, as follows.

7.2.1 Seismic Behavior of Retaining Wall–Backfill Systems

While the M-O theory assumes that the seismic response occurs simultaneously and uniformly in the backfill and the retaining walls, the experimental results show that the inertial forces do not in fact occur at the same time in the backfill and the walls. Moreover, accelerations are not uniform in the backfill or on the walls.

The M-O theory further assumes that the maximums of dynamic earth pressures and inertial forces occur simultaneously, and stability analyses of retaining walls are conducted for such a case. Comparisons of the dynamic wall moments, dynamic earth pressures, and inertial forces acting on the walls suggest that when the inertial force is at its local maximum, the dynamic wall moment (due to dynamic earth pressures and wall inertia) is at its local maximum as well, but the dynamic earth pressure increment is at its local minimum at or around zero. On the other hand, when the dynamic earth pressure is at its local maximum, the inertial force and dynamic wall moment reach their local minimum values near or at zero. This observation is very important in that it shows that designing retaining walls for maximum dynamic earth pressures and maximum wall inertia is inherently very conservative and does not reflect the true seismic performance of retaining structures. Since wall inertial forces and dynamic earth pressures are not in phase, their cumulative effect is to reduce overall moments acting on the walls. Retaining walls should therefore be designed for dynamic wall moments that include the combined effects of the inertial forces on the wall and the backfill.

7.2.2 Dynamic Moments on Retaining Walls

The computation of the dynamic moments acting on the walls is probably the most challenging aspect of this study in that there are a number of important factors that come into play as follows: (a) the elevation of the wall at which the dynamic force due to the dynamic earth pressure should be applied; (b) the magnitude of the dynamic earth pressure; and (c) the moment due to inertia of the wall itself.

The dynamic moments measured by the strain gages and the force-sensing bolts in the centrifuge experiments represent the combined effects of both dynamic earth pressures and wall inertial forces. An important contribution to the overall dynamic wall moments is the mass of the wall itself. While Richards and Elms (1979 and 1980) make a strong case for the consideration

of the inertial forces due to the mass of the retaining structure in the design of gravity walls, cantilever walls have not received similar attention (Vallenas, personal communication). To better understand the moment response of the walls, the dynamic earth pressures and wall inertial effects on the wall moments were separated by estimating the wall inertial moments using the acceleration records on the walls. The results show that the wall inertial moment contribution to the overall dynamic wall moments is substantial and should be specifically accounted for. Moreover, wall inertial moments are generally in phase with dynamic wall moments. This suggests that dynamic wall moments are largely influenced by the inertia of the wall itself. The experimental results show that the conventional analysis methods tend to give estimates of dynamic earth pressure induced moments that are larger than the measured dynamic wall moments. When these dynamic moment estimates are added to wall inertial moments, the wall moments are routinely significantly overestimated.

The issue of the point of application of the force representing the dynamic earth pressure increment has received significant attention over the years with most authors suggesting that 0.6 - 0.7H is a reasonable range (e.g., Seed and Whitman 1970). The exact origin of this idea is not clear, although early experimental results seem to have provided much of the impetus for the assumption that seismic earth pressure increases upward due to soil amplification. While this effect may have been observed in rigid-base shaking table tests, as already discussed, it has not been observed in the centrifuge results. Both dynamic wall moments and dynamic earth pressure moments exhibit cubic distributions with depth. This suggests that the point of application of the resultant force of the dynamic earth pressure increment is around 0.3H above the base of the wall. Moreover, the analyses of the moments in the centrifuge tests show that the M-O and Seed and Whitman (1970) methods of analysis result in very conservative estimates of the maximum induced dynamic moments when used with full peak ground accelerations.

7.2.3 Seismic Earth Pressure Distribution

The centrifuge data consistently show that the maximum dynamic earth pressures increase with depth and can be reasonably approximated by a triangular distribution analogous to that used to represent static earth pressures. This result is contrary to the assumption made by Seed and Whitman (1970), who based their approach on the experimental work of Matsuo (1941) and other similar types of experiments. Matsuo's experiments were on dry relatively loose sand in a

rigid shaking table container up to 6 ft deep. While these experiments were very meticulous and pioneering in their scope, they cannot be simply scaled to taller structures. More importantly, the observed amplification of ground motion and the observed increase in earth pressure upward are a direct result of the physical layout of the geometry of the shaking table box and the properties of the sand. In that sense, Matsuo's results are correct for the given geometry and material, and are directly applicable to walls up to 6 ft in height with relatively loose granular backfill that rest on a rigid foundation.

7.2.4 Seismic Earth Pressure Magnitude

In general, the magnitude of the seismic earth pressures depends on the magnitude and intensity of shaking, the density of the backfill soil, and the flexibility of the retaining walls. A comparison of the maximum dynamic earth pressure magnitudes measured in this study to the pressure estimates based on commonly used design methods shows that designing retaining walls for maximum dynamic earth pressures is overly conservative when considering the fact that dynamic earth pressures and inertial forces are not in phase. Designing retaining walls for dynamic earth pressures corresponding to the maximum dynamic wall moments is more appropriate. The relationship between the back-calculated seismic earth pressure coefficient (ΔK_{AE}) at the time of maximum dynamic wall moment and peak ground acceleration (Fig. 6.17) suggests that seismic earth pressures can be neglected at accelerations below 0.4 g. While similar conclusions and recommendations were made by Seed and Whitman (1970), their approach assumed that a wall designed to a reasonable static factor of safety should be able to resist seismic loads up 0.3 g. In the present study, experimental data suggest that seismic loads higher than 0.4 g could be resisted by cantilever walls designed to an adequate factor of safety. This observation is consistent with the observations and analyses performed by Clough and Fragaszy (1977) and Fragaszy and Clough (1980) who concluded that conventionally designed cantilever walls with granular backfill could be reasonably expected to resist seismic loads at accelerations up to 0.5 g.

Since peak ground acceleration does not fully represent all aspects of the ground motion, a better alternative may be to use the Arias intensity as a representative parameter. Figure 6.20 presents the observed relationship between the seismic earth pressure coefficient (ΔK_{AE}) at the time of maximum dynamic wall moment and Arias intensity. In either case, however, it is

important to note that these results are applicable to medium-dense sand backfill, and therefore represent a fairly severe loading condition that may not occur in denser materials or materials with some degree of cohesion. Similarly, the effect of the wall stiffness cannot be fully assessed with the present data, since both flexible and stiff retaining structures studied are relatively flexible. Thus, while it would appear prudent to use the relationships obtained for the stiff wall, it may still be overly conservative for most retaining structures in well-consolidated or cohesive deposits. Finally, it is important to note that the traditional M-O method, and the Seed and Whitman (1970) method currently used in practice, provide very, if not overly, conservative estimates of the maximum induced seismic earth pressures.

7.2.5 Effective Duration of Loading

One of the important aspects of seismic loading is its transient nature that is evident from the time histories of dynamic moments. However, the currently available methods of analysis treat the dynamic loading in terms of an envelope containing the maximum response at any given height independent of time. While most walls are not tall enough to experience full incoherence of motion, this fact should not be neglected in the design of very tall retaining structures. More importantly, depending on the phase lag between the soil and the wall, the maximum moment on the wall may not occur at the same time as the maximum soil pressure and maximum shear. Similarly, the fact that the maximum loading occurs only for a very brief period needs to be carefully considered, especially if performance-based design methodology is considered. As it is, the current design methods do not consider the effective duration of loading, and consequently introduce an additional level of conservatism.

7.3 RESULTS OF FINITE ELEMENT SIMULATIONS

A 2-D nonlinear FE model was developed on the OpenSees platform and calibrated to simulate dynamic centrifuge experiment LAA02 and study the seismic behavior of retaining wall–backfill systems. The FE model assumes a dry, elasto-plastic 2-D plane-strain soil mesh with elastic beam-column models of U-shaped cantilever retaining structures attached to the soil mesh with nonlinear springs. The FE model was calibrated and evaluated against a set of centrifuge results for three shaking events from experiment LAA02. Computed and centrifuge-recorded results

consisting of acceleration, response spectra, bending moments, earth pressures, and shear stress and strain time series were compared. Despite the simplifications and inherent limitations in the FE model, as well as the uncertainties in the input parameters, the computed results show that the finite element analysis is able to capture reasonably well the essential system responses observed in the centrifuge experiments. A preliminary analysis with denser soil backfill shows that the dynamic earth pressures drop on the order of 25–30 % due to higher strength of the backfill.

Overall, the results of this study shows that well calibrated FE models can be used as a predictive tool for seismic earth pressures and moments on retaining walls. However, calibrating the FE model with real data is essential for the validation of the computed results. The results from the FE model are sensitive to input soil properties and constitutive models used. Therefore, the reliability of analytical seismic earth pressures and moment results is subject to having reliable estimates of soil properties, good soil constitutive models that are able to capture the nonlinear soil response under seismic loading, and a set of experimental or field data for the calibration of the model.

7.4 DESIGN RECOMMENDATIONS

The results and observations from the centrifuge experiments can be used to provide performance-based recommendations for better and more efficient seismic design of cantilever retaining walls with dry medium-dense sand backfill. For the design of retaining walls, the effects of static earth pressures, the dynamic earth pressure increments, and the wall inertial forces should be estimated and accounted for as follows. The experimental results show that both stiff and flexible retaining walls considered in this study experience enough deflection to generate static active earth pressures. In fact, observed static earth pressures before the various shaking events generally lie between static active and static at-rest earth pressure estimates. Static earth pressures on retaining walls increase for relatively loose sand backfill as a result of shaking.

The centrifuge results show that dynamic earth pressures and inertial forces do not act simultaneously on the walls and that the overall dynamic wall moments are generally in phase with the inertial forces acting on the walls. While relations of back-calculated maximum dynamic earth pressure coefficients (ΔK_{AE}) with peak ground accelerations are provided in Section 6.3.2, designing retaining walls for maximum dynamic earth pressures and maximum

wall inertia is overly conservative and unnecessary. Since moment is usually more relevant for the design of retaining walls, it is more appropriate to consider the maximum dynamic wall moment as a design criterion for cantilever retaining walls. Seismic earth pressure corresponding to the time of the maximum dynamic wall moment can be estimated using the relation in Figure 6.17 and then added to the maximum estimated wall inertial effects. It is important to note that ground motions with peak ground accelerations less than 0.4 g do not have a significant effect on the maximum dynamic wall moments and that their resulting seismic earth pressure can be ignored. In the present study, experimental data suggest that even higher seismic loads could be resisted by cantilever walls designed to an adequate factor of safety.

7.5 LIMITATIONS AND RECOMMENDATIONS FOR FUTURE WORK

The results of the centrifuge experiments and FE modeling presented herein are limited to cantilever retaining structures with dry medium-dense sand backfill and level ground surface. The dry medium-dense sand used in the experiments has a pronounced tendency to compact during shaking, and it provides a more severe loading than would be encountered in denser, cemented or well-consolidated deposits. Hence, the results of the experiments are likely quite conservative and significant savings could be realized by further experimental work with denser or cohesive materials. Moreover, both stiff and flexible retaining structures used in this study are considered relatively flexible, and conducting further centrifuge experiments on fully rigid type of retaining walls, such as basement walls, is needed in order to better understand the seismic behavior of such structures. Such experiments would help in clarifying the effect of the relative flexibility of the wall and the retained medium on the seismic response of the system.

The data presented in this study clearly show a triangular distribution of seismic earth pressures increasing with depth, and it would appear reasonable to consider the point of application of the resultant seismic force on cantilever retaining walls at 1/3 H above the base of the wall. Further experimental work is needed in order to verify the point of application of the resultant seismic force on rigid walls. Since many retaining structures are built in sloping ground and have sloping backfill, this case remains an important area of further study. Experience in recent earthquakes shows that structures on sloping ground and retaining sloping backfill are at significant risk of failure due to a variety of factors that deserve careful scrutiny and experimental work. In addition, further experimental work is needed to study dynamic earth

pressures on retaining walls supporting saturated backfill and to evaluate the effects of near-field ground motions on the wall-backfill response.

Although computed and recorded results presented in this study are in relatively good agreement, limitations were encountered in developing and calibrating the FE model. Such limitations include inherent uncertainties in the input parameters and simplifications adopted in modeling the rather complex seismic retaining wall–backfill behavior and interaction. Possible improvements on the FE model would include more elaborate modeling of the centrifuge model container, studying the possible 3-D effects on the model, more elaborate modeling of the soil-structure interaction, and including a certain degree of flexibility in the wall-base moment connections. Despite the mentioned limitations and simplifications, the FE model was able to capture the main response features of the retaining wall–backfill system. A parametric study can be conducted to study further the effects of the different parameters on the induced seismic earth pressures and moments on the walls.

REFERENCES

Aggour, M. S., and Brown, C. B. 1973. Retaining walls in seismic areas. *Proceedings, 5th World Conference on Earthquake Engineering*, Rome, Italy, 2624-2627.

Arulmoli, K., Muraleetharan, K. K., Hosain, M. M., and Fruth, L. S. 1992. *VELACS laboratory testing program.* Soil Data Report. The Earth Technology Corporation, Irvine, California, Washington D.C.

Arulnathan, R., Boulanger, R. W., Kutter, B. L., and Sluis, W. K. 2000. New tool for shear wave velocity measurements in model tests. *Geotechnical Testing Journal* GTJODJ, 23(4): 444-453.

Boardman, T. 2006. *Seismic Earth pressures on below grade retaining structures*. PEER/UC Berkeley Seismic Earth Pressures Workshop.

Bolton M. D., and Steedman, R. S. 1982. Centrifugal testing of micro-concrete retaining walls subject to base shaking. *Proceedings of Conference on Soil dynamics and Earthquake Engineering*, Southampton, 1, 311-329, Balkema.

Bolton M. D., and Steedman, R. S. 1985. The behavior of fixed cantilever walls subject to lateral loading. *Application of Centrifuge Modeling to Geotechnical Design*, Craig (ed.), Balkema, Rotterdam.

Chang, C. Y., Power, M. S., Mok, C. M., Tang, Y. K., and Tang, H. T. 1990. Analysis of dynamic lateral earth pressures recorded on Lotung reactor containment model structure. *Proceedings, 4th U.S. National Conference on Earthquake Engineering*, *Oalm Springs, California*.

Chopra, A. K. 2007. *Dynamics of structures: theory and applications to earthquake engineering*. Third Edition, New Jersey: Prentice Hall, Upper Saddle River.

Clough, G. W., and Duncan, J. M. 1971. Finite element analyses of retaining wall behavior. *ASCE Journal of Soil Mechanics* 97(12): 1657-1673.

Clough, G. W., and Fragaszy, R. F. 1977. A study of earth loadings on floodway retaining structures in the 1971 San Fernando Valley earthquake. *Proceedings of the Sixth World Conference on Earthquake Engineering*, 3.

Coulomb, C. A. 1776. Essai sur une application des regles des maximis et minimis a quelques problemes de statique relatifs a l'architecture. *Memoires de l'Academie Royale pres Divers Savants* 7.

Dewoolkar, M. M., Ko, H., and Pak R. Y. S. 2001. Seismic behavior of cantilever retaining walls with liquefiable backfills. *Journal of Geotechnical and Geoenvironmental Engineering, ASCE* 127(5): 424-435.

Dobry, R., and Liu, L. 1994. Centrifuge modeling of soil liquefaction. *Proceedings of the Tenth World Conference on earthquake Engineering*, Balkema, Rotterdam, 6801-6809.

Elgamal, A., Yang, Z., and Parra, E. 2002. Computational modeling of cyclic mobility and post-liquefaction site response. *Soil Dynamics and Earthquake Engineering* 22: 259-271.

Elgamal, A., Yang, Z., Lai, T., Kutter, B., and Wilson, D. 2005. Dynamic response of saturated dense sand in laminated centrifuge container. *Journal of Geotechnical and Geoenvironmental Engineering*, *ASCE* 131(5): 598-609.

Elgamal, A., Yang, Z., Parra, E., and Ragheb, A. 2003. Modeling of cyclic mobility in saturated cohesionless soils. *International Journal of Plasticity*, 19: 883-905.

Fragaszy, R. F., and Clough, G. W. 1980. Seismic behavior of gravity retaining walls – discussion. *Journal of the Geotechnical Engineering Division, ASCE*, 106 (GT6):734-735.

Gazetas, G., Psarropoulos, P. N., Anastasopoulos, I., and Gerolymos, N. 2004. Seismic behaviour of flexible retaining systems subjected to short-duration moderately strong excitation. *Soil Dynamics and Earthquake Engineering* 24: 537-550.

Gomez, J. E., Filz, G. M., and Ebeling, R. M. 2003. Extended hyperbolic model for sand-to-concrete interfaces. *Journal of Geotechnical and Geoenvironmental Engineering, ASCE* 129(11): 993-1000.

Green, R. A., Olgun, C. G., Ebeling, R. M., and Cameron, W. I. 2003. Seismically induced lateral earth pressures on a cantilever retaining wall. *Earthquake Engineering*.

Green, R. A., Olgun, C. G., and Cameron, W. I. 2008. Response and modeling of cantilever retaining walls subjected to seismic motions. *Computer-Aided Civil and Infrastructure Engineering* 23: 309-322.

Hausler, E. 2002. Influence of ground improvement on settlement and liquefaction: a study based on field case history evidence and dynamic geotechnical centrifuge tests. *PhD Thesis*.

Ilankatharan, M., and Kutter, B. L. 2008. Numerical simulation of soil model-model container-centrifuge shaking table system. *Proceedings of Geotechnical Earthquake Engineering and Soil Dynamics-IV*, *Sacramento, California*.

Ishibashi, I., and Fang, Y. S. 1987. Dynamic earth pressures with different wall movement modes. *Soils and Foundations* 27(4): 11-22.

Ishii, Y., Arai, H., Tsuchida, H. 1980. *Lateral earth pressure in an earthquake*. Research Report 80-9. University of Canterbury, New Zealand.

Jacobson, P. N. 1980. *Translational behavior of gravity retaining walls during earthquakes*. Research Report 80-9. University of Canterbury, New Zealand.

Jaky, J. 1948. Pressure in soils. *Proceedings, 2nd International Conference on Soil Mechanics and Foundation Engineering,* 2: 43-45.

Kammerer, A. M., Wu, J., Pestana, J. M., Riemer, M., and Seed, R. B. 2000. *Cyclic simple shear testing of Nevada sand for PEER center project 2051999*. Geotechnical Engineering Report No. UCB/GT/00-01, University of California, Berkeley.

Koseki, J., Tatsuoka, F., Munaf, Y., Tateyama, M., and Kojima, K. 1998. A modified procedure to evaluate active earth pressure at high seismic loads. Soils *and Foundations, Special Issue on Geotechnical Aspects of the January 17, 1996 Hyogoken-Nambu Earthquake*, 2: 209-216.

Kutter, B. L, Idriss, I. M., Kohnke, T., Lakeland, J., Li, X.S., Sluis, W., Zeng, X., Tauscher, R.C., Goto, Y., and Kubodera, I. 1994. Design of a large earthquake simulator at UC Davis. *Centrifuge 94*, Leung, Lee, and Tan (eds.), Balkema, 169-175.

Kutter, B. L. 1995. Recent advances in centrifuge modeling of seismic shaking. *Proceedings., St. Louis*, 2: 927-941.

Lai, T., Elgamal, A., Yang, Z., Wilson, D. W., and Kutter, B. L. 2004. Numerical modeling of dynamic centrifuge experiments on a saturated dense sand stratum. *Proceedings of 11th Conference on Soil Dynamics and earthquake Engineering and 3rd International Conference on Earthquake Geotechnical Engineering, University of California, Berkeley*.

Lew, M., Simantob, E., and Hudson, M. E. 1995. Performance of shored earth retaining systems during the January 17, 1994, Northridge Earthquake. *Proceedings of the Third International Conference on Recent Advances in Geotechnical Earthquake Engineering and Soil Dynamics*, *St Louis, Missouri*, 3.

Ling, H. I., Leshchinsky, D., and Chou, N. 2001. Post-earthquake investigation on several geosynthetic-reinforced soil retaining walls and slopes during the Ji-Ji Earthquake in Taiwan. *Soil Dynamics and Earthquake Engineering* 21: 297-313.

Matsuo, H. 1941. Experimental study on the distribution of earth pressures acting on a vertical wall during earthquakes. *Journal of the Japanese Society of Civil Engineers* 27(2).

Matsuo, H., and Ohara, S. 1960. Lateral earth pressure and stability of quay walls during earthquakes. *Proceedings, Earthquake Engineering, Second World Conference, Tokyo, Japan*, 1.

Mononobe, N., and Matsuo M. 1929. On the determination of earth pressures during earthquakes. *Proceedings, World Engineering Congress* 9: 179-187.

Nakamura, S. 2006. Reexamination of Mononobe-Okabe theory of gravity retaining walls using centrifuge model tests. *Soils and Foundations* 46(2): 135-146.

Newmark, N. M. 1965. Effects of earthquakes on dams and embankments. Fifth Rankine Lecture, *Geotechnique* 15(2): 139-160.

Okabe S. 1926. General theory of earth pressure," *Journal of the Japanese Society of Civil Engineers*, Tokyo, Japan 12(1).

Ortiz, L. A., Scott, R. F., and Lee, J. 1983. Dynamic centrifuge testing of a cantilever retaining wall. *Earthquake Engineering and Structural Dynamics* 11: 251–268.

Ostadan, F. 2005. Seismic soil pressure for building walls – an updated approach. *Journal of Soil Dynamics and Earthquake Engineering* 25: 785-793.

Prakash, S. and Basavanna, B. M. 1969. Earth pressure distribution behind retaining wall during earthquakes. *Proceedings of the Fourth World Conference on Earthquake Engineering*, *Santiago, Chile*.

Rankine, W. 1857. On the stability of loose earth. *Philosophical Transactions of the Royal Society of London* 147.

Rathje, E. M., Abrahamson, N. A., and Bray, J. D. 1998. Simplified frequency content estimates of earthquake ground motions. *Journal of Geotechnical and Geoenvironmental Engineering* 124(2): 150-159.

Richards, R., and Elms, D. G. 1979. Seismic behavior of gravity retaining walls. *Journal of the Geotechnical Engineering Division, ASCE* 105(GT4): 449–64.

Richards, R., and Elms, D. G. 1980. Seismic behavior of gravity retaining wallsg1

closure. *Journal of the Geotechnical Engineering Division, ASCE* 106(GT6): 737-738.

Scott, R. F. 1973. Earthquake-induced earth pressures on retaining walls. *Proceedings, Earthquake Engineering, Fifth World Conference*, *Rome, Italy, 2*.

Scott, R. F. Centrifuge modeling and technology: a survey. *Revue Francaise de Geotechnique*, 48: 15-34.

Seed, H. B., and Idriss, I. M. 1970. *Soil moduli and damping factors for dynamic response analyses*. Earthquake Research Center, Report EERC 70-10, University of California, Berkeley, California.

Seed, H. B., and Whitman, R. V. 1970. Design of earth retaining structures for dynamic loads. *ASCE Specialty Conference*, *Lateral Stresses in the Ground and Design of Earth Retaining Structures*, Cornell Univ., Ithaca, New York, 103–147.

Sherif, M. A., Fang, Y. S., 1984. Dynamic earth pressures on walls rotating about the top. *Soils and Foundations* 24(4): 109-117.

Sherif, M. A., Ishibashi, I., and Lee, C. D. 1982. Earth pressure against stiff retaining walls. Journal *of Geotechnical Engineering, ASCE* 108: 679-695.

Siddharthan, R., and Maragakis, E. M. 1989. Performance of flexible retaining walls supporting dry cohesionless soils under cyclic loads. *International Journal for Numerical and Analytical Methods in Geomechanics* 13: 309-326.

Stadler A. T. 1996. Dynamic centrifuge testing of cantilever retaining walls. *PhD Thesis*, University of Colorado at Boulder.

Steedman, R.S. 1984. Modeling the behavior of retaining walls in earthquakes. *PhD Thesis*, Cambridge University, Cambridge, England.

Steedman, R. S., and Zeng, X. 1990. The seismic response of waterfront retaining walls. *Design and Performance of Earth Retaining Structures, Conference Proceedings*, Cornell University, Ithaca, New York, June 18-21, ASCE Geotechnical Special Publication No. 25.

Steedman, R. S., and Zeng, X. 1991. Centrifuge modeling of the effects of earthquakes on free cantilever walls. *Centrifuge'91*, Ko (ed.), Balkema, Rotterdam.

Stevens, D. K., Wilson, D. W., and Kutter, B. L. 1999. *Comprehensive investigation of nonlinear site response – centrifuge data report for DKS03*. Center for Geotechnical Modeling, Report No. UCD/CGMDR-99/03.

Tajimi, H. 1973. Dynamic earth pressures on basement wall. *Proceedings, Earthquake Engineering, Fifth World Conference*, *Rome, Italy,* 2.

Tekscan. 2005. *Flexiforce sensors user manual*. http://www.tekscan.com/pdfs/FlexiforceUserManual.pdf.

Veletsos, A. S., and Younan, A. H. 1997. Dynamic response of cantilever retaining walls. *Journal of Geotechnical and Geoenvironmental Engineering* 123(2): 161-172.

Wilson, D. W., Boulanger, R. W., Kutter, B. L., and Abghari, A. 1997. Aspects of dynamic centrifuge testing of soil-pile-superstructure interaction. *Observation and Modeling in Numerical Analysis and Model Tests in Dynamic Soil-Structure Interaction Problems*, Geotechnical Special Publication, ASCE (64): 47-63.

Wood, J. H. 1973. Earthquake induced soil pressures on structures. *PhD Thesis*, California Institute of Technology, Pasadena, CA.

Yang, Z. 2000. Numerical modeling of earthquake site response including dilation and liquefaction. *PhD Dissertation*, Department of Civil Engineering and Engineering Mechanics, Columbia University, New York.

Yang, Z., and Elgamal, A. 2002. Influence of permeability on liquefaction-induced shear deformation. *Journal of Geotechnical and Geoenvironmental Engineering, ASCE*: 720-729.

Yang, Z., Elgamal, A., Adaliar, K., and Sharp, M. 2004. Effect of container boundary on seismic embankment response in centrifuge model tests. *Proceedings of 11th Conference on Soil Dynamics and earthquake*

Engineering and 3rd International Conference on Earthquake Geotechnical Engineering, University of California, Berkeley.

Yang, Z., Lu, J., and Elgamal, A. 2008. *OpenSees manual for PDMY and PIMY materials*. http://cyclic.ucsd.edu/opensees/.

Yang, Z., Elgamal, A., and Parra, E. 2003. A computational model for liquefaction and associated shear deformation. *Journal of Geotechnical and Geoenvironmental Engineering*, *ASCE* 129(12): 1119-1127.

Zarrabi, K. 1979. Sliding of gravity retaining wall during earthquakes considering vertical acceleration and changing inclination of failure surface. *Master's Thesis*, M.I.T, Cambridge, Mass.

Zeghal, M., Elgamal, A. W., Tang, H. T., and Stepp, J. C. 1995. Lotung downhole array. II: evaluation of soil nonlinear properties. *Journal of Geotechnical Engineering* 121(4): 363-378.

Zeng, X. 1990. Modeling behavior of quay walls in earthquakes. *PhD Thesis*, Cambridge University, Cambridge, England.

Appendix A: Additional Figures

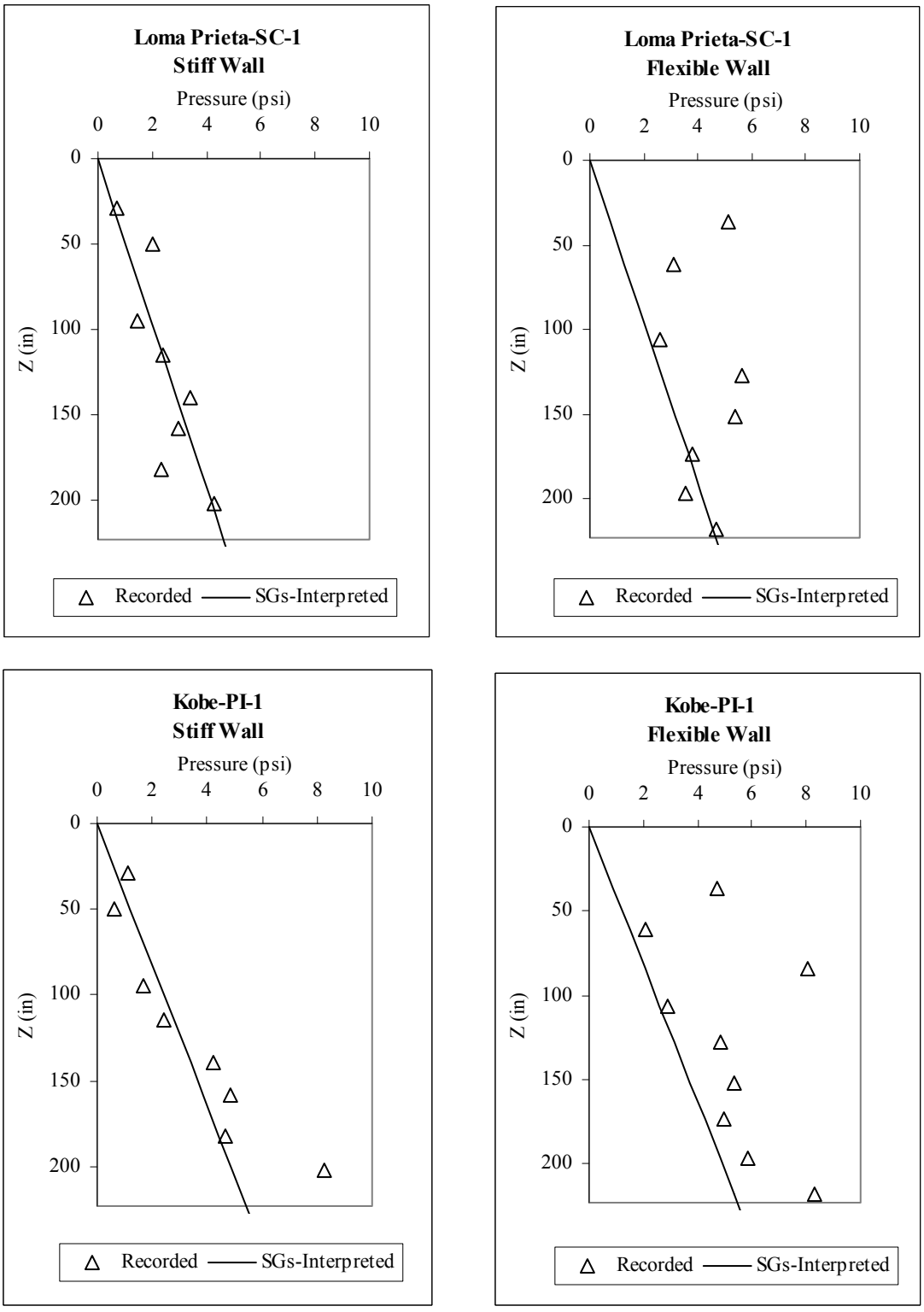

Fig. A.1 Comparison of static earth pressure profiles recorded by Flexiforce sensors and interpreted from strain gage measurements on south stiff and north flexible walls after Loma Prieta-SC-1 and Kobe-PI-1.

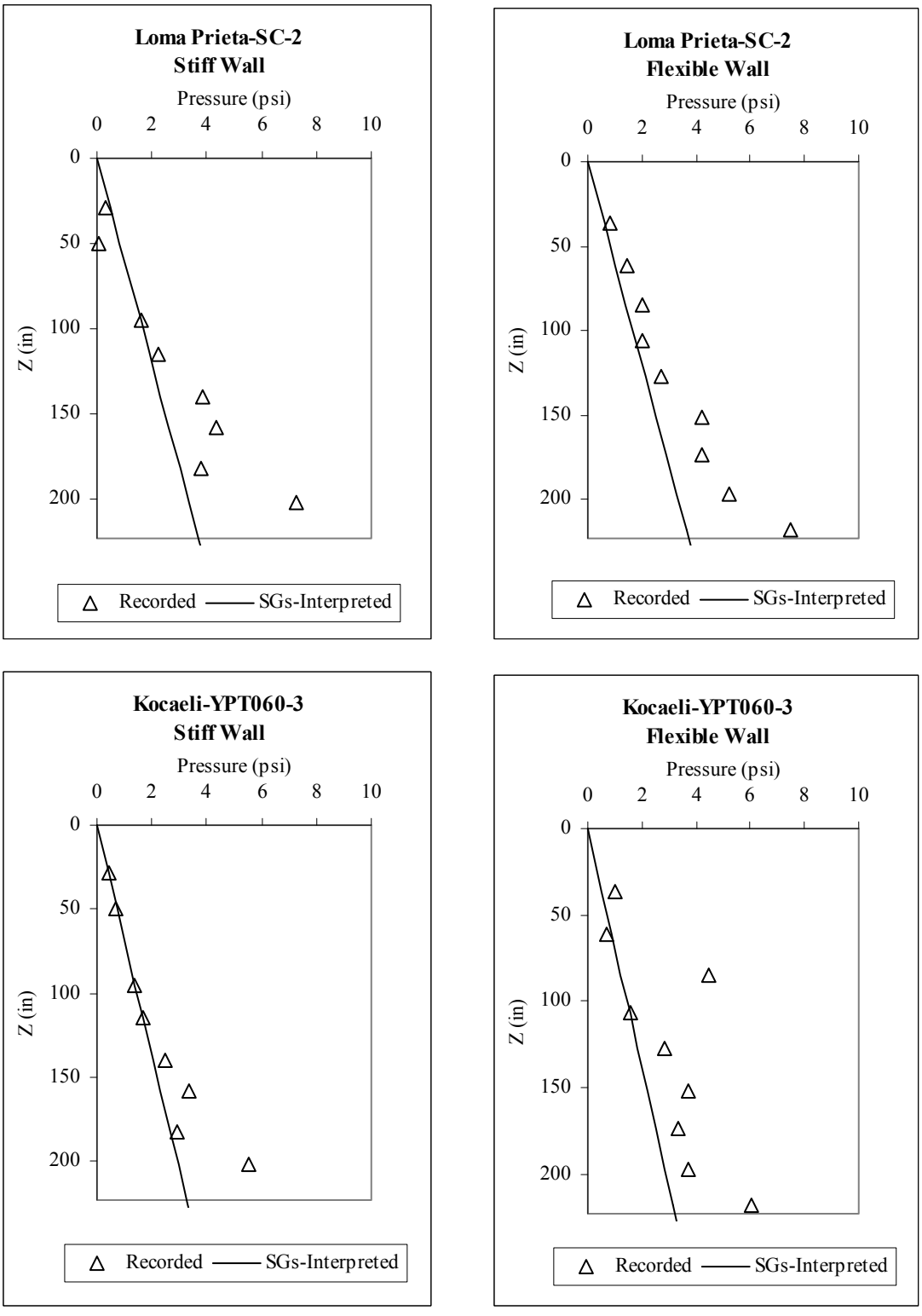

Fig. A.2 Comparison of static earth pressure profiles recorded by Flexiforce sensors and interpreted from strain gage measurements on south stiff and north flexible walls after Loma Prieta-SC-2 and Kocaeli-YPT060-3.

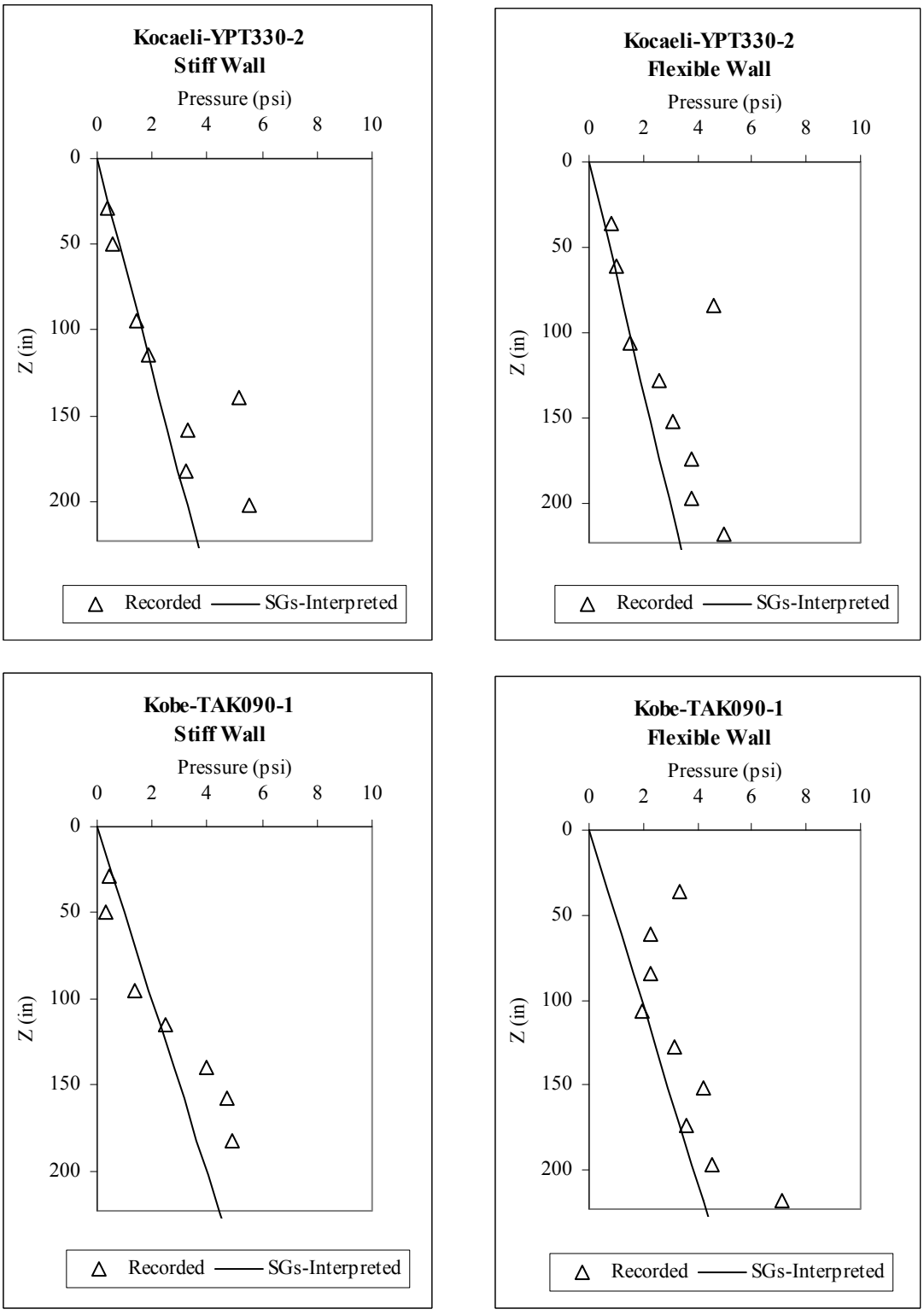

Fig. A.3 Comparison of static earth pressure profiles recorded by Flexiforce sensors and interpreted from strain gage measurements on south stiff and north flexible walls after Kocaeli-YPT330-2 and Kobe-TAK090-1.

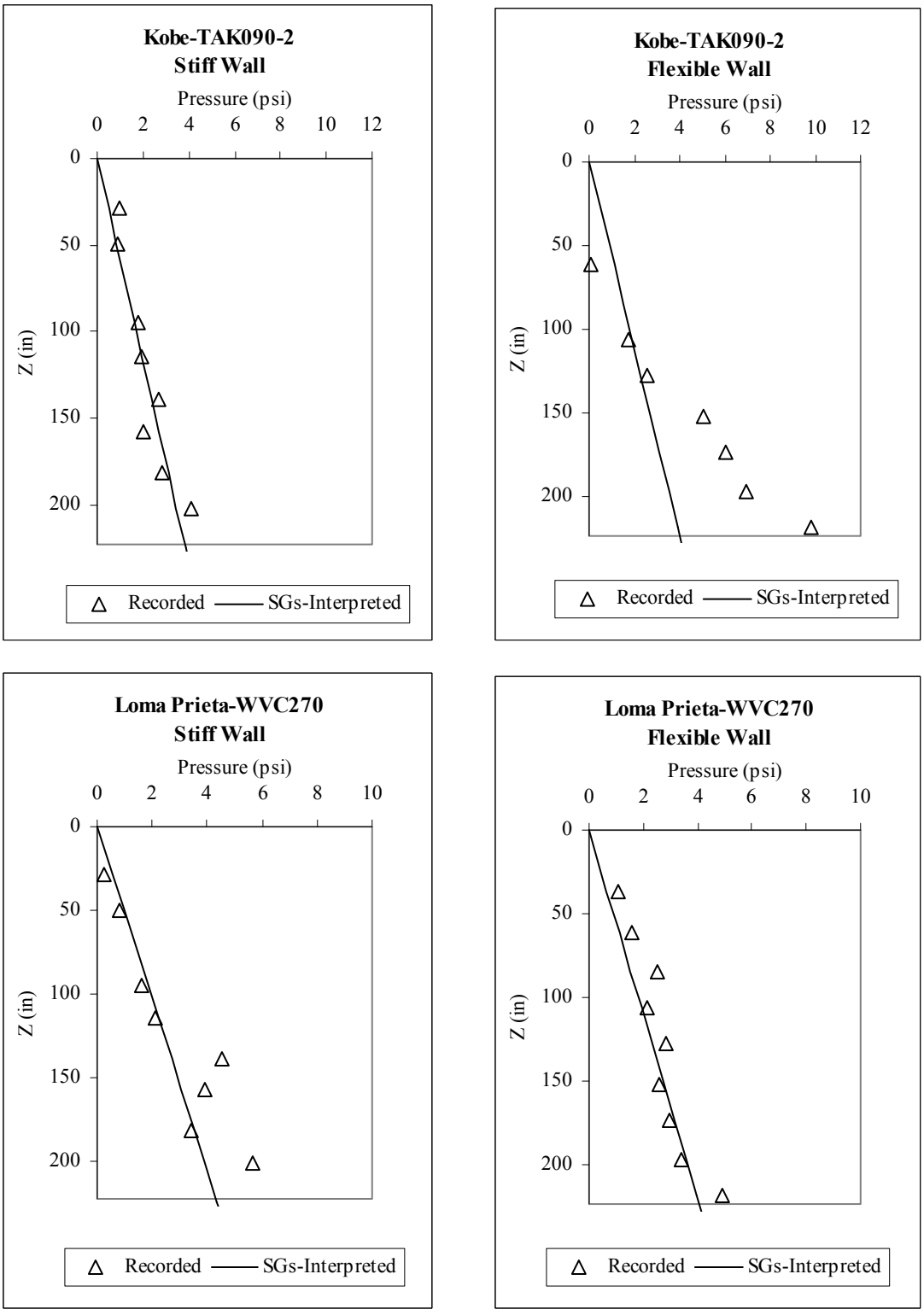

Fig. A.4 Comparison of static earth pressure profiles recorded by Flexiforce sensors and interpreted from strain gage measurements on south stiff and north flexible walls after Kobe-TAK090-2 and Loma Prieta-WVC270.

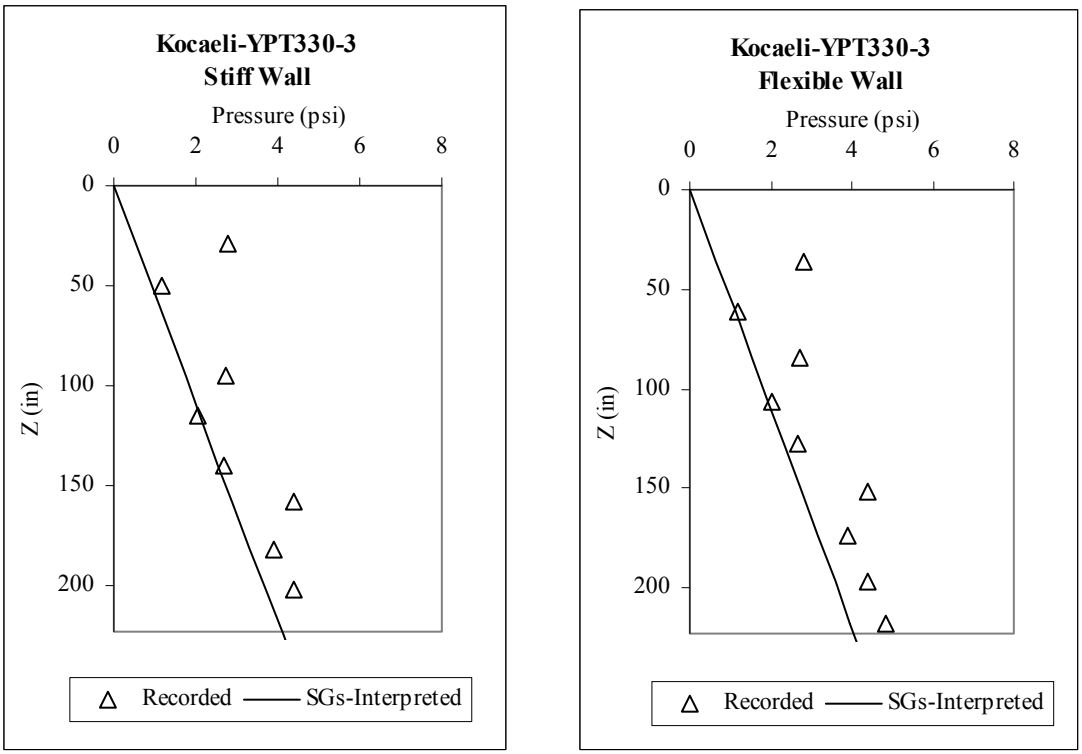

Fig. A.5 Comparison of static earth pressure profiles recorded by Flexiforce sensors and interpreted from strain gage measurements on south stiff and north flexible walls after Kocaeli-YPT330-3.

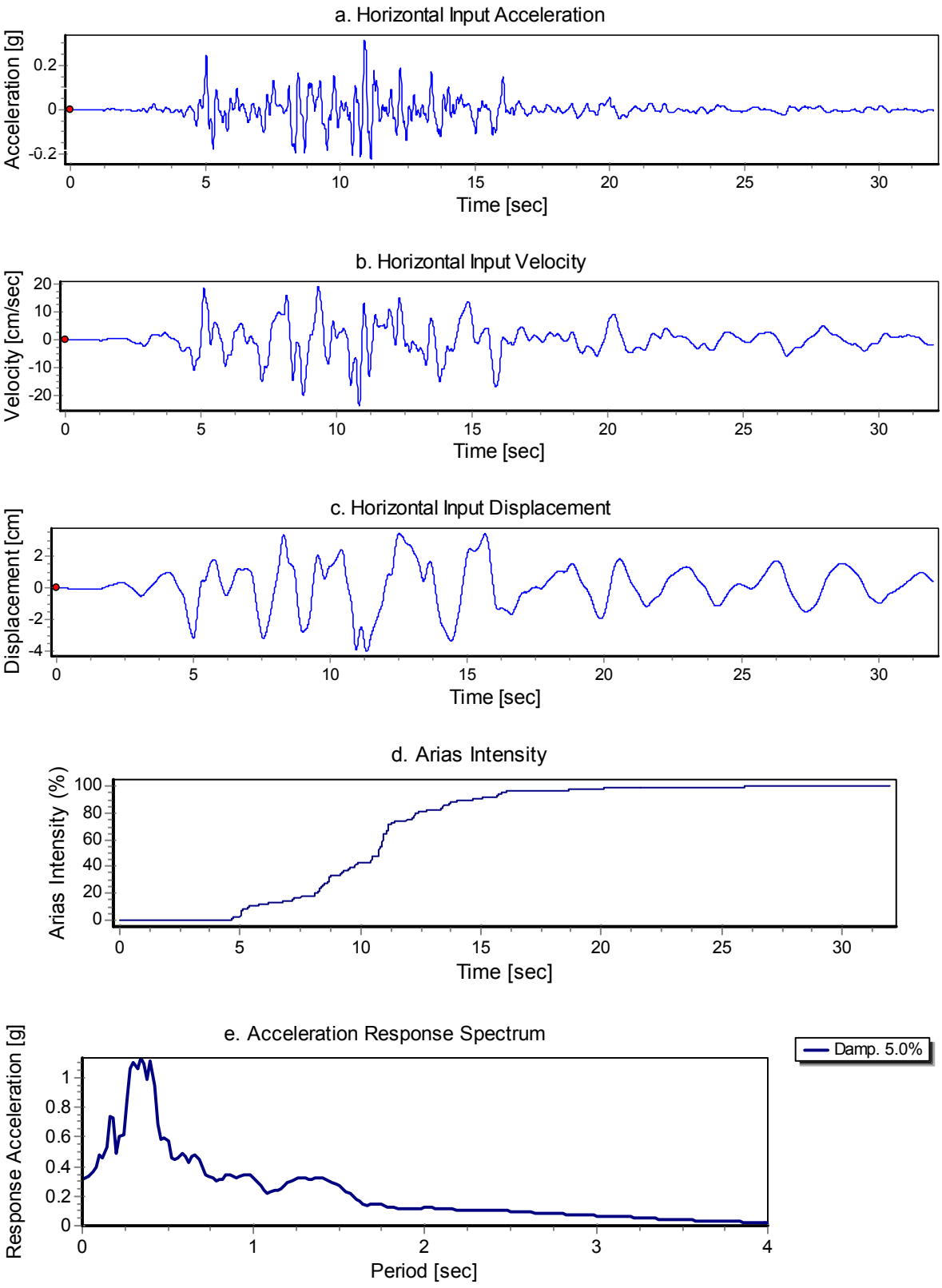

Fig. A.6 Horizontal acceleration, velocity, displacement, Arias intensity, and response spectrum of Loma Prieta-1 input ground motion for LAA01.

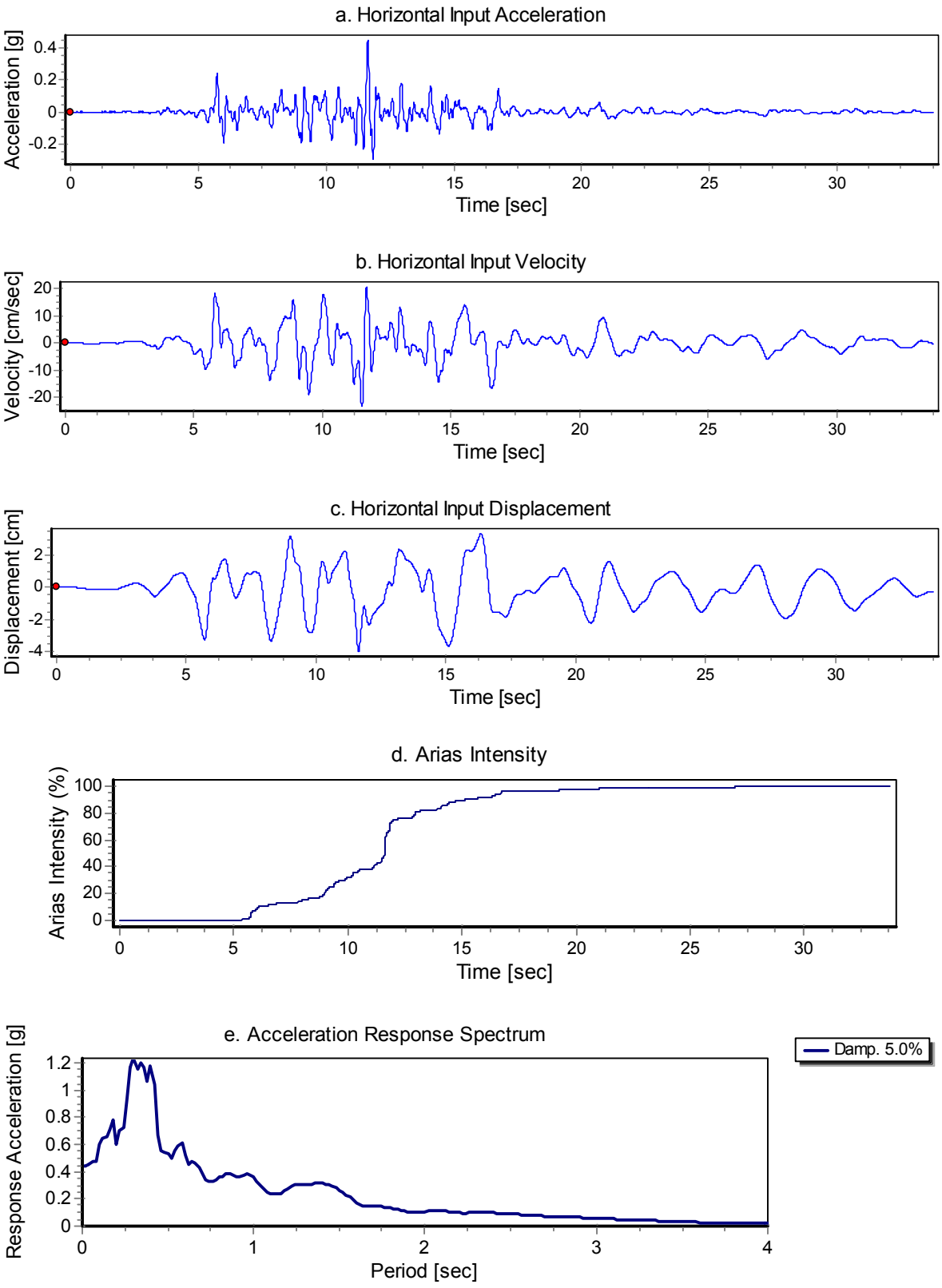

Fig. A.7 Horizontal acceleration, velocity, displacement, Arias intensity, and response spectrum of Loma Prieta-2 input ground motion for LAA01.

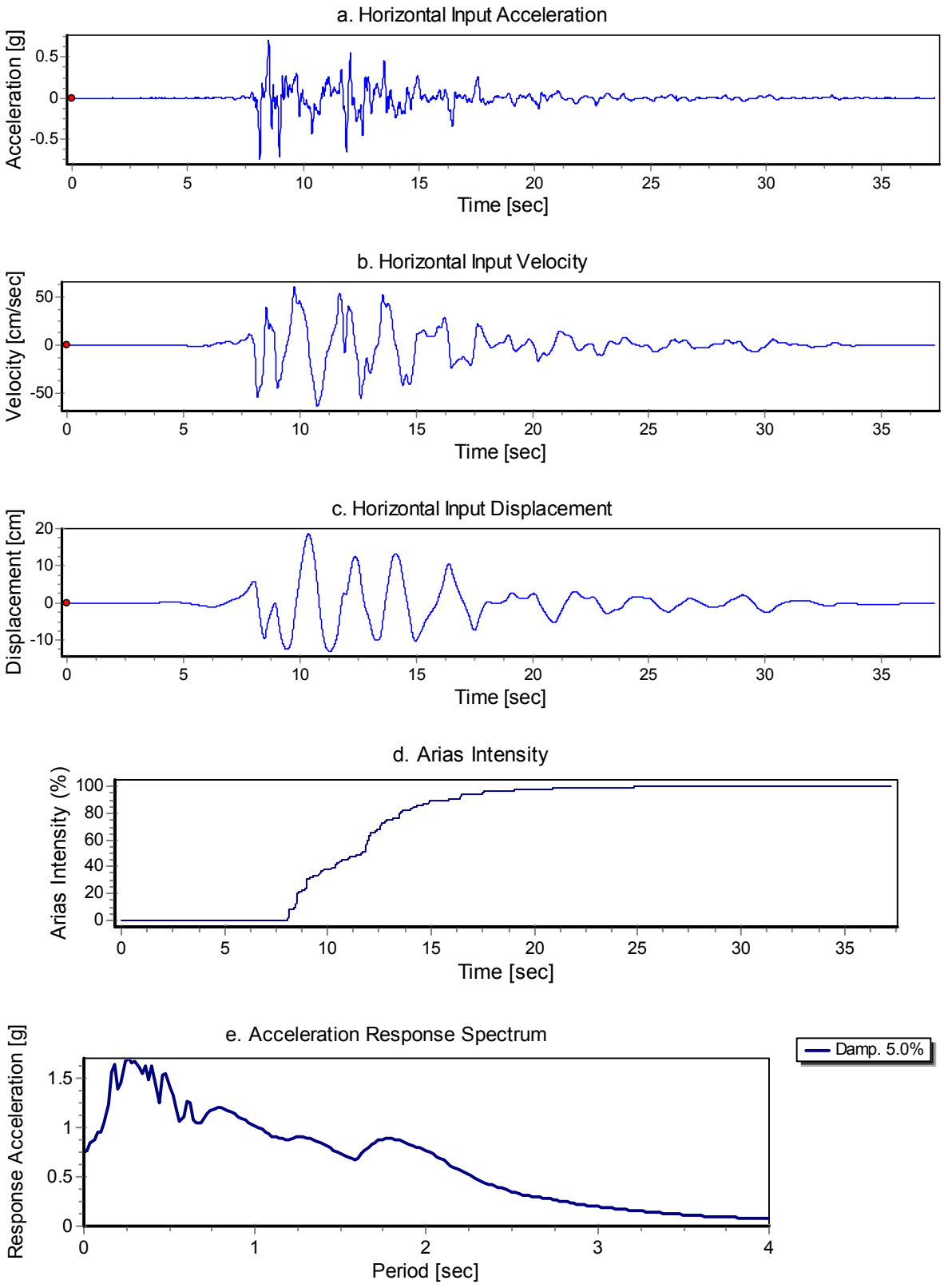

Fig. A.8 Horizontal acceleration, velocity, displacement, Arias intensity, and response spectrum of Kobe input ground motion for LAA01.

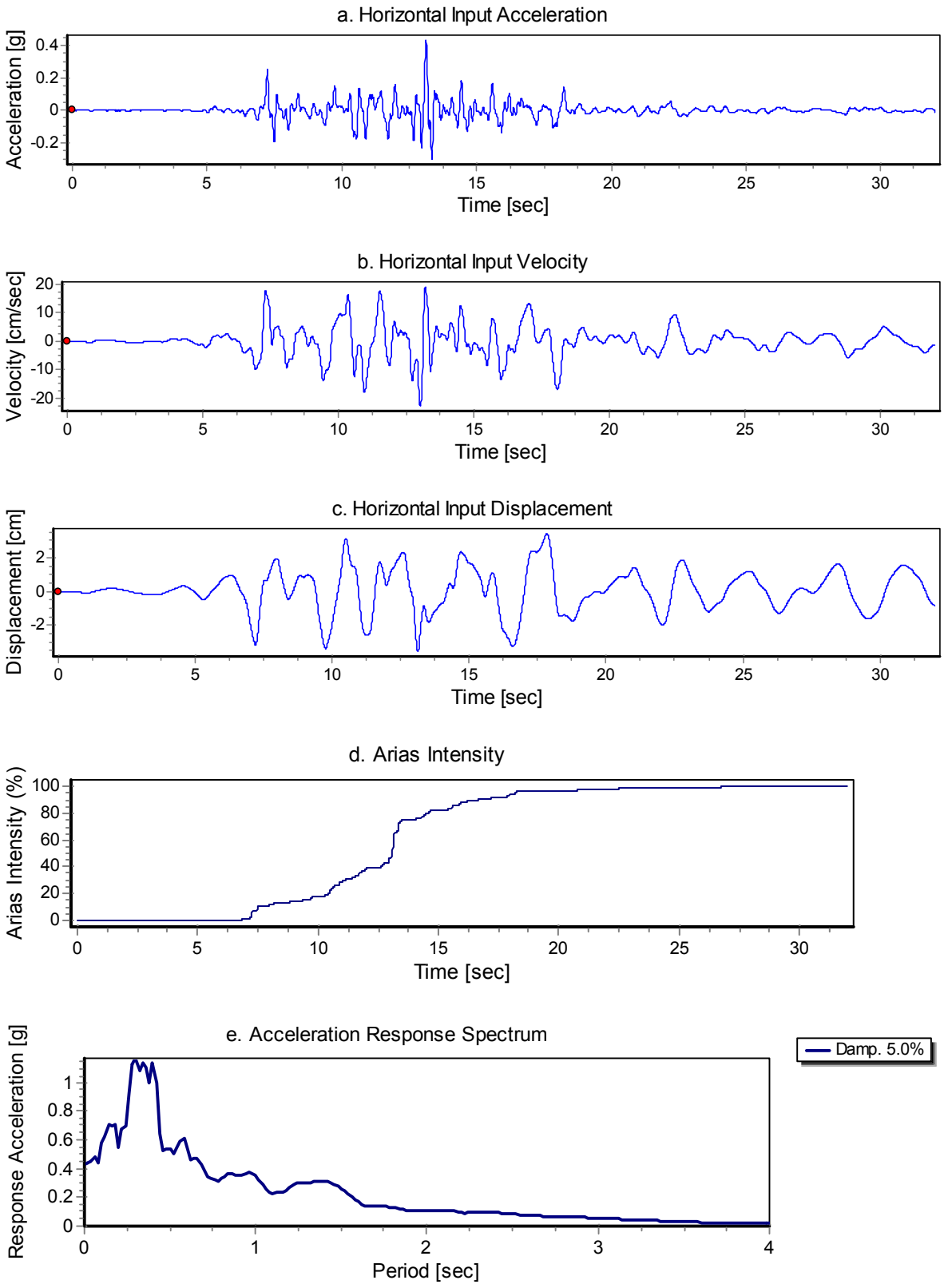

Fig. A.9 Horizontal acceleration, velocity, displacement, Arias intensity, and response spectrum of Loma Prieta-3 input ground motion for LAA01.

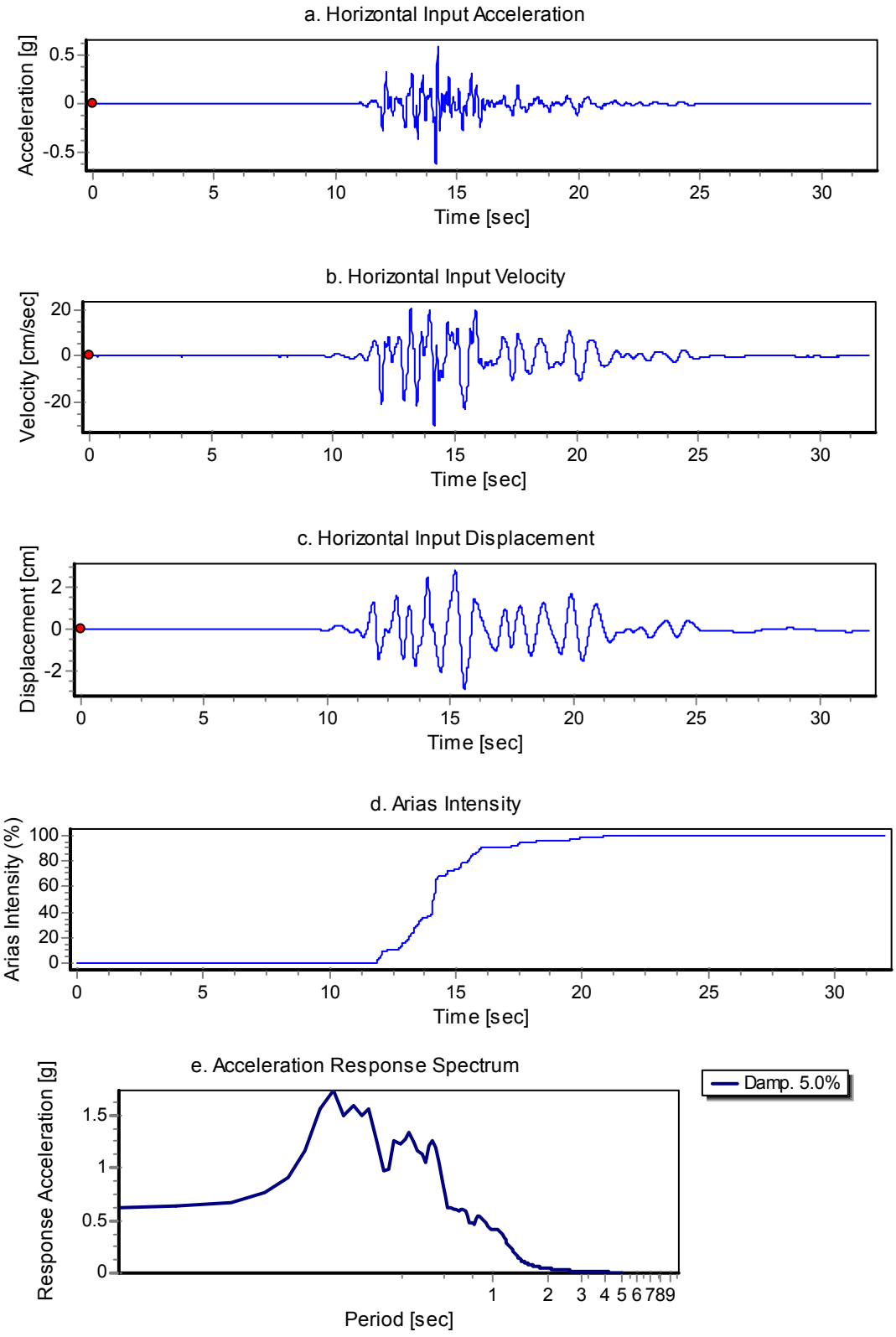

Fig. A.10 Horizontal acceleration, velocity, displacement, Arias intensity, and response spectrum of Loma Prieta-SC-1 input ground motion during LAA02.

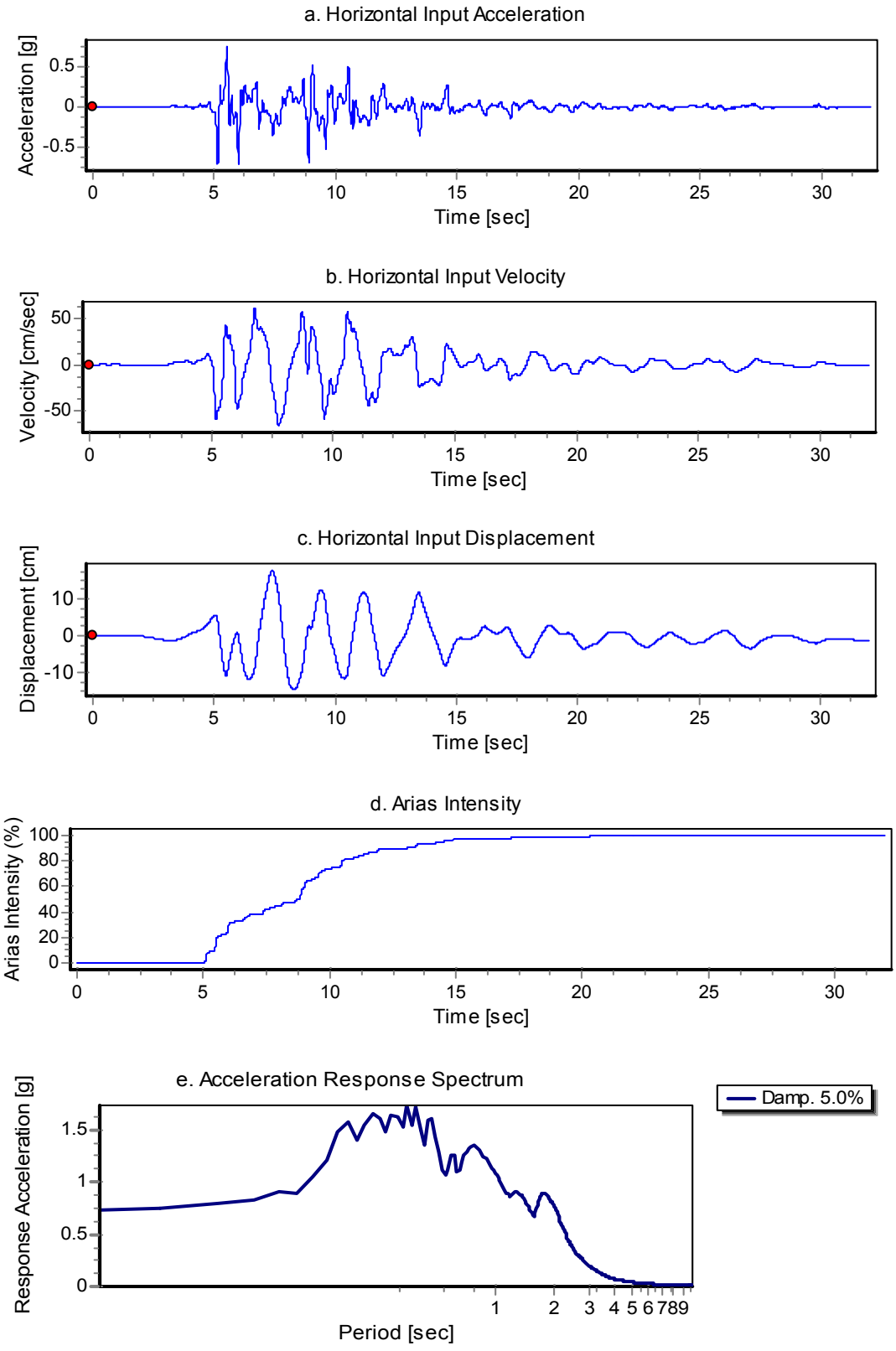

Fig. A.11 Horizontal acceleration, velocity, displacement, Arias intensity, and response spectrum of Kobe-PI-1 input ground motion during LAA02.

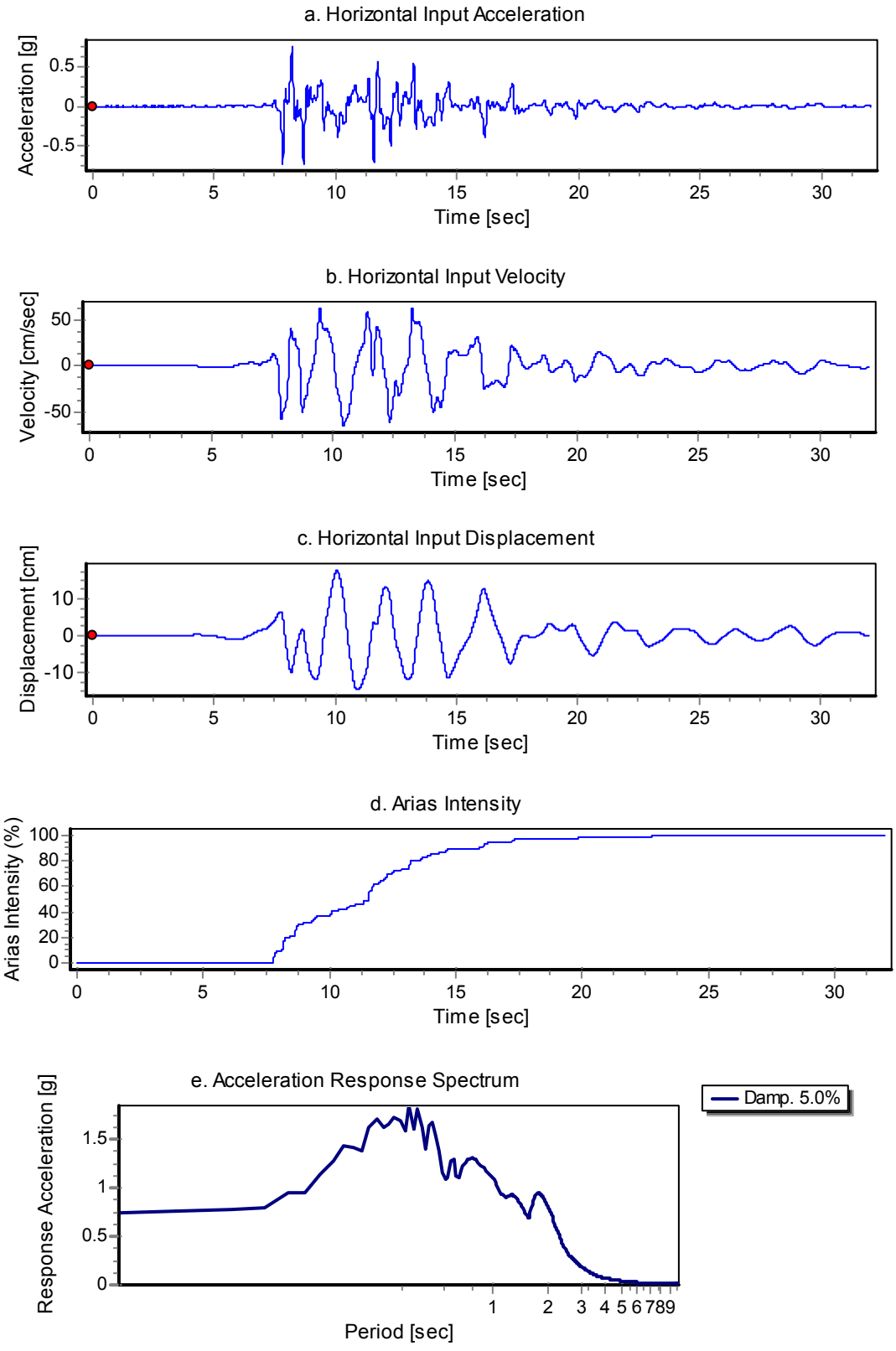

Fig. A.12 Horizontal acceleration, velocity, displacement, Arias intensity, and response spectrum of Kobe-PI-2 input ground motion during LAA02.

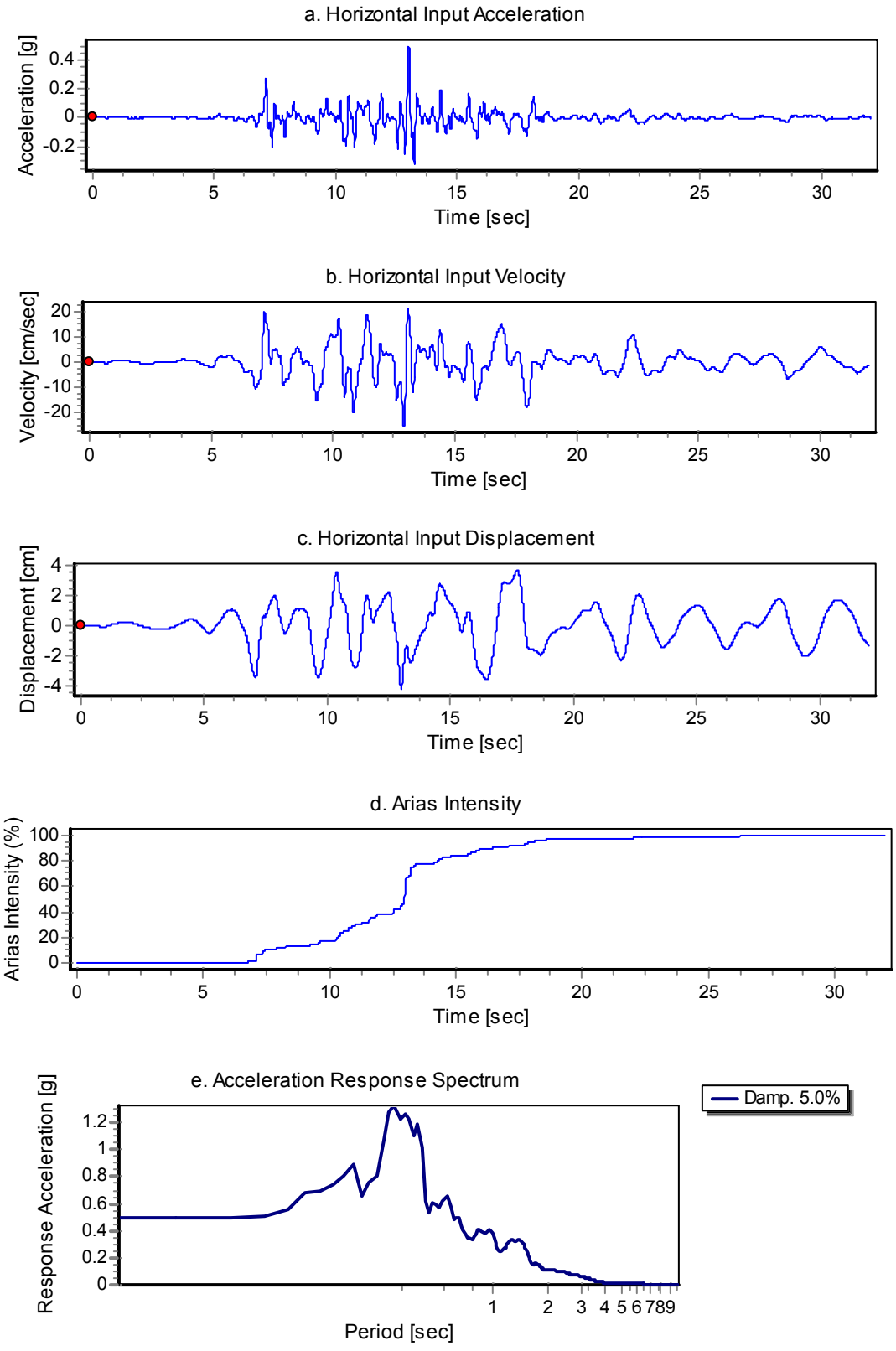

Fig. A.13 Horizontal acceleration, velocity, displacement, Arias intensity, and response spectrum of Loma Prieta-SC-2 input ground motion during LAA02.

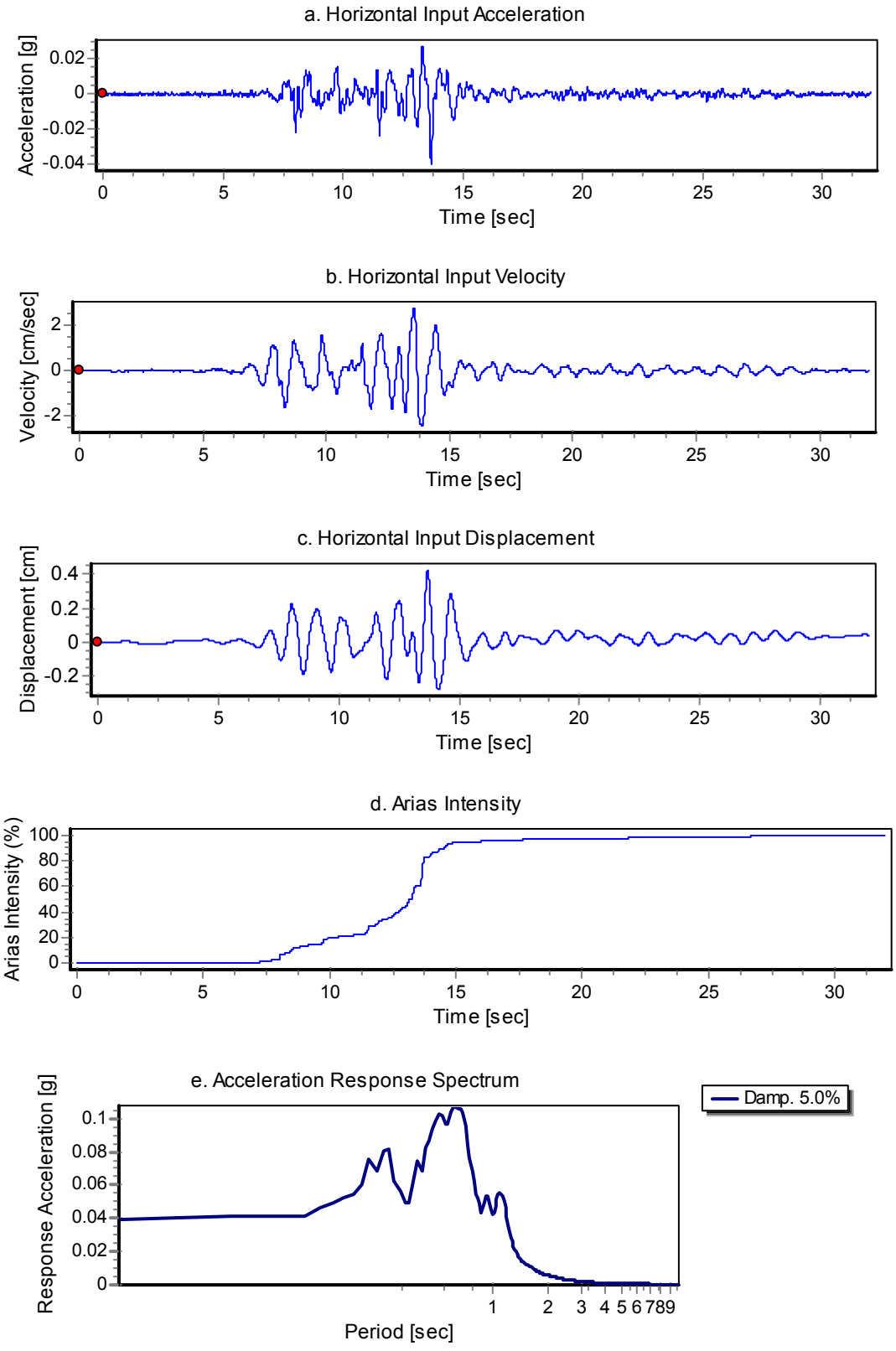

Fig. A.14 Horizontal acceleration, velocity, displacement, Arias intensity, and response spectrum of Kocaeli-YPT060-1 input ground motion during LAA02.

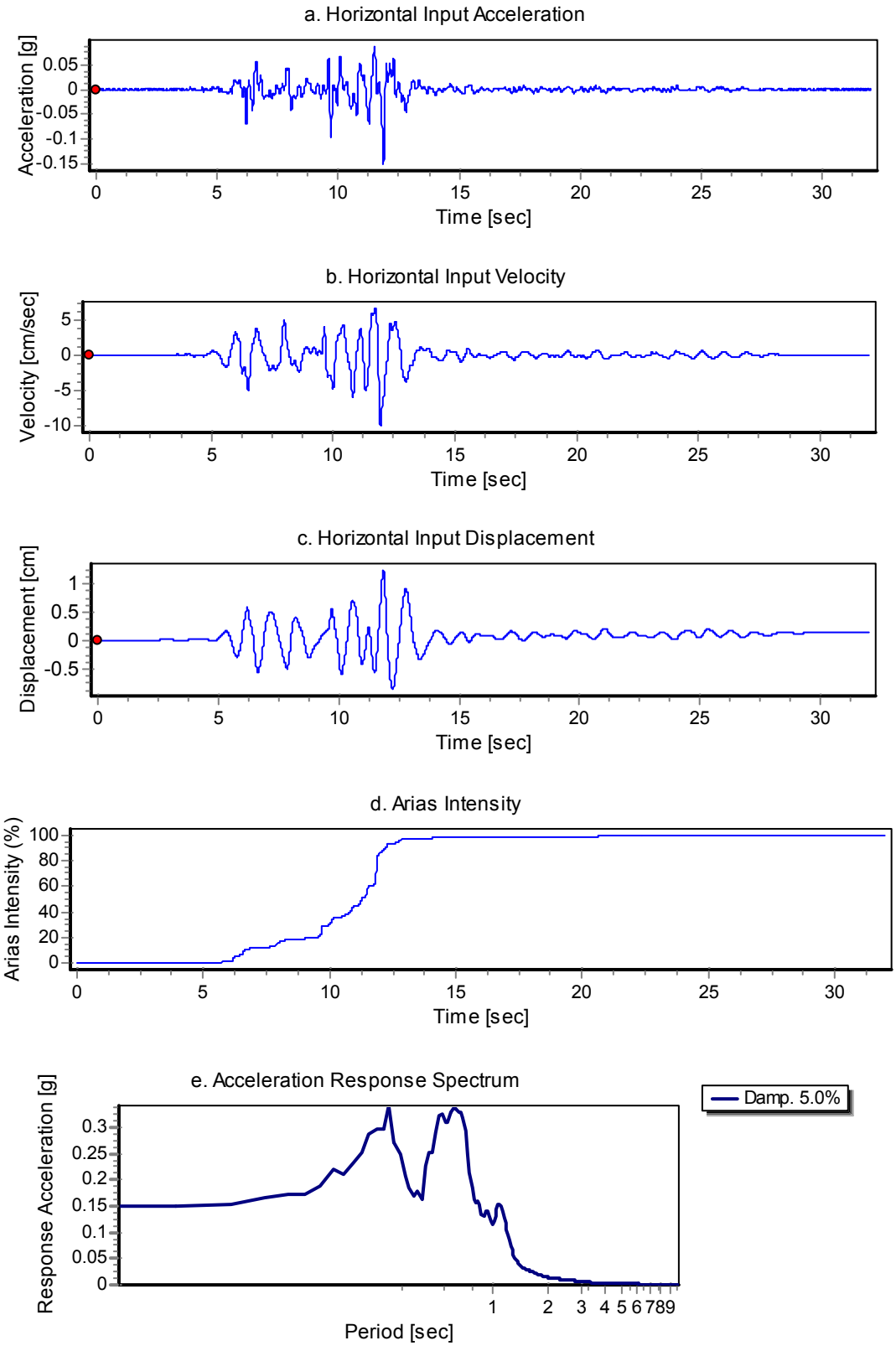

Fig. A.15 Horizontal acceleration, velocity, displacement, Arias intensity, and response spectrum of Kocaeli-YPT060-2 input ground motion during LAA02.

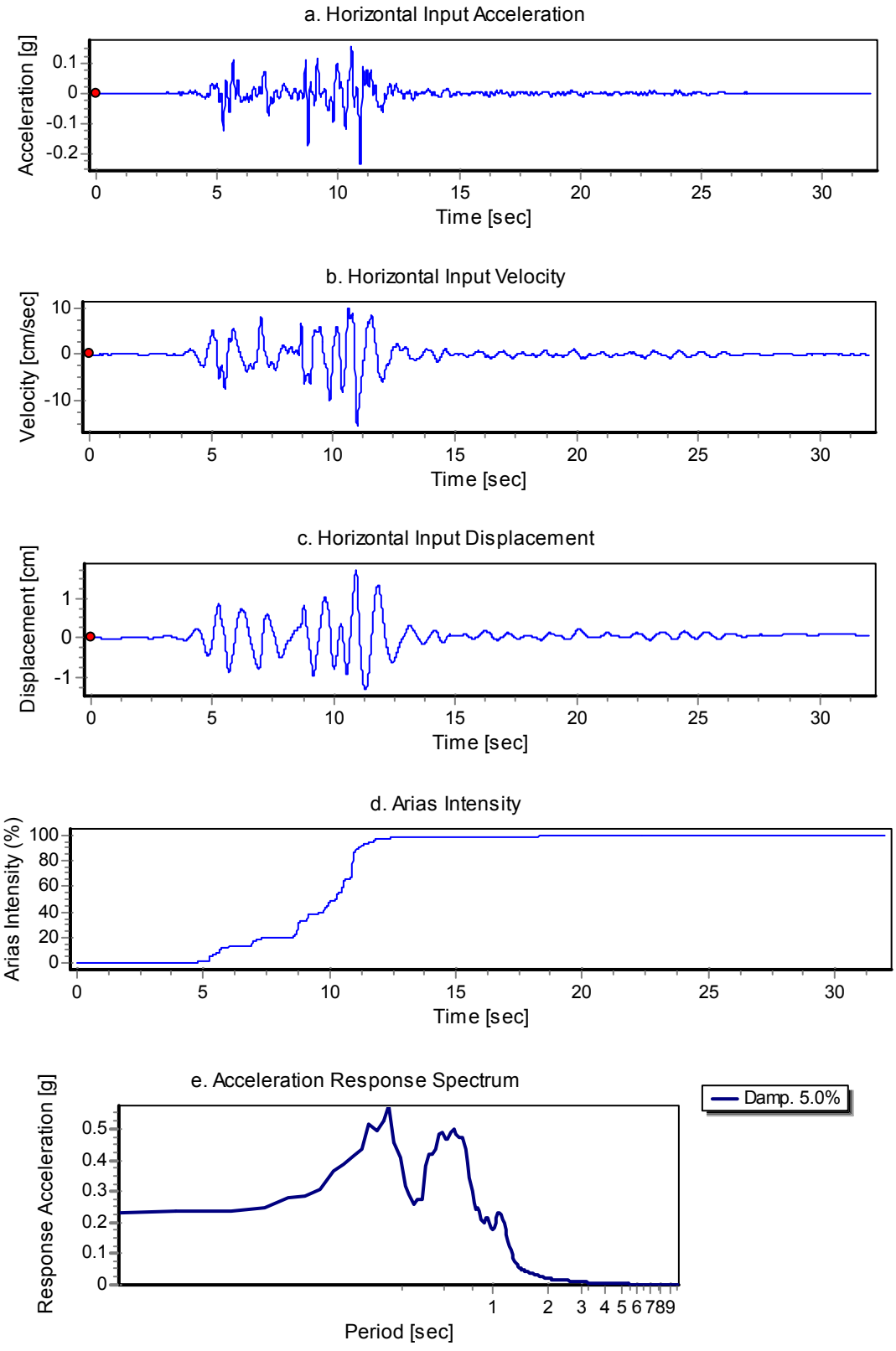

Fig. A.16 Horizontal acceleration, velocity, displacement, Arias intensity, and response spectrum of Kocaeli-YPT060-3 input ground motion during LAA02.

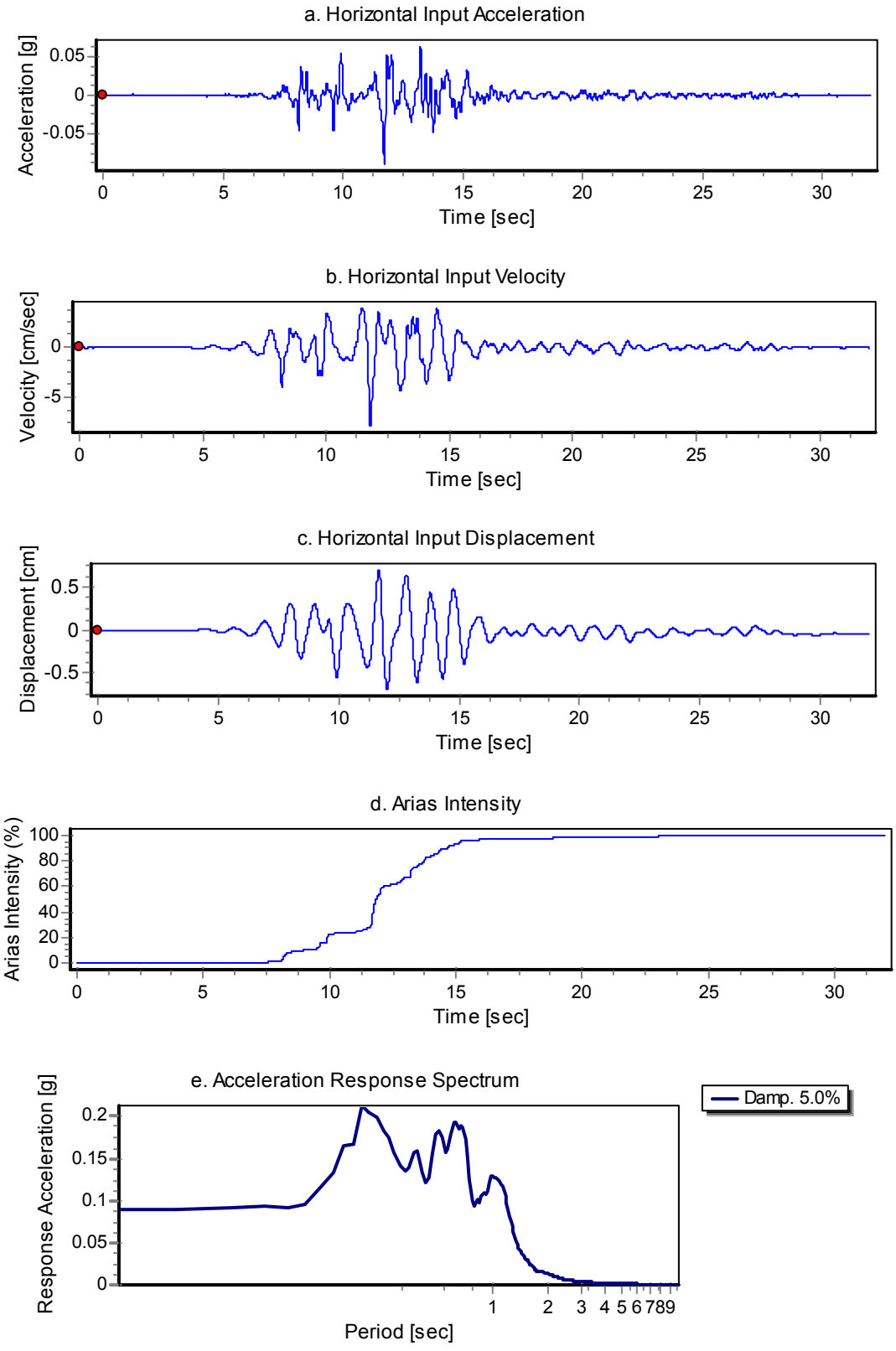

Fig. A.17 Horizontal acceleration, velocity, displacement, Arias intensity, and response spectrum of Kocaeli-YPT330-1 input ground motion during LAA02.

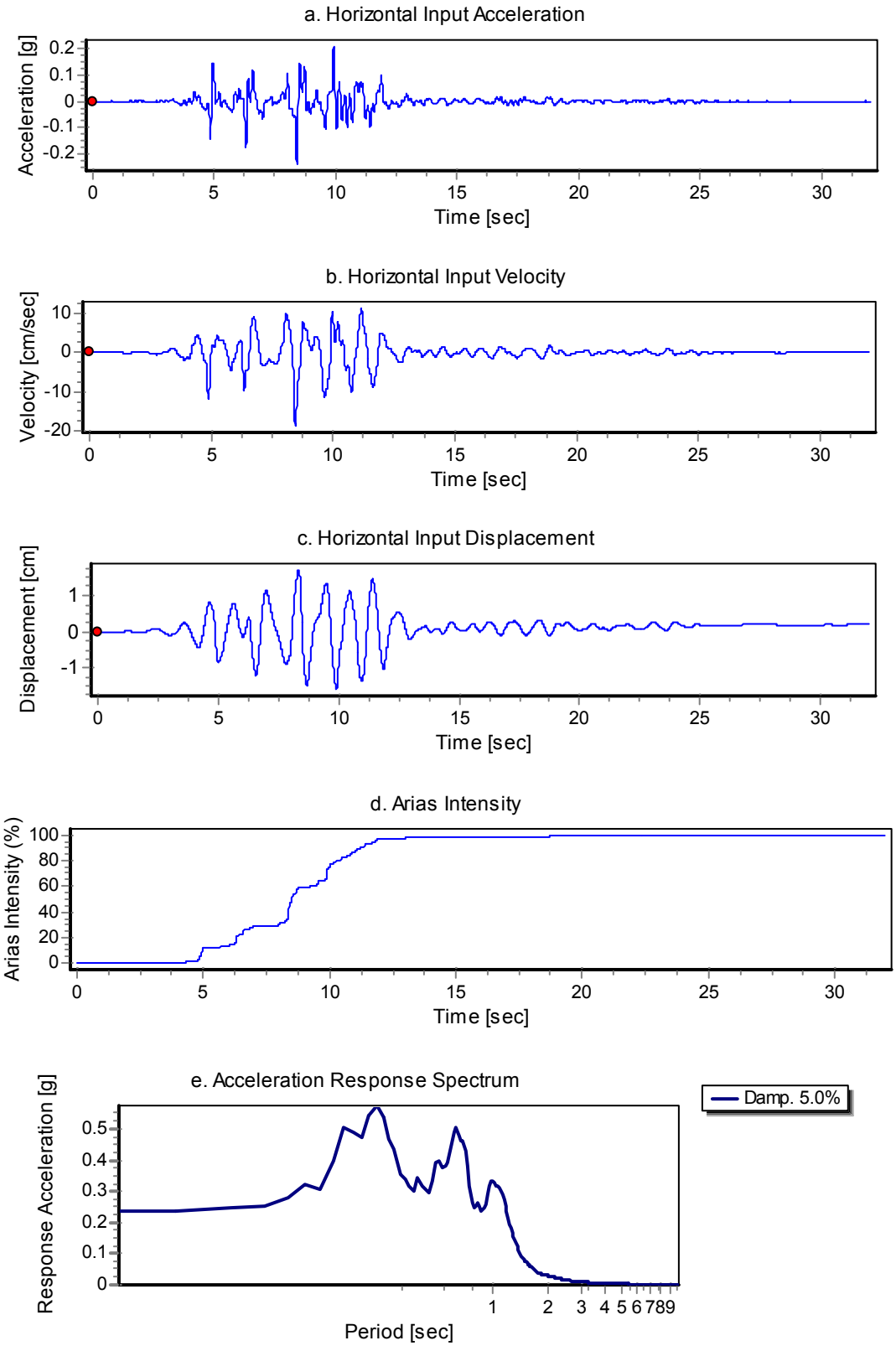

Fig. A.18 Horizontal acceleration, velocity, displacement, Arias intensity, and response spectrum of Kocaeli-YPT330-2 input ground motion during LAA02.

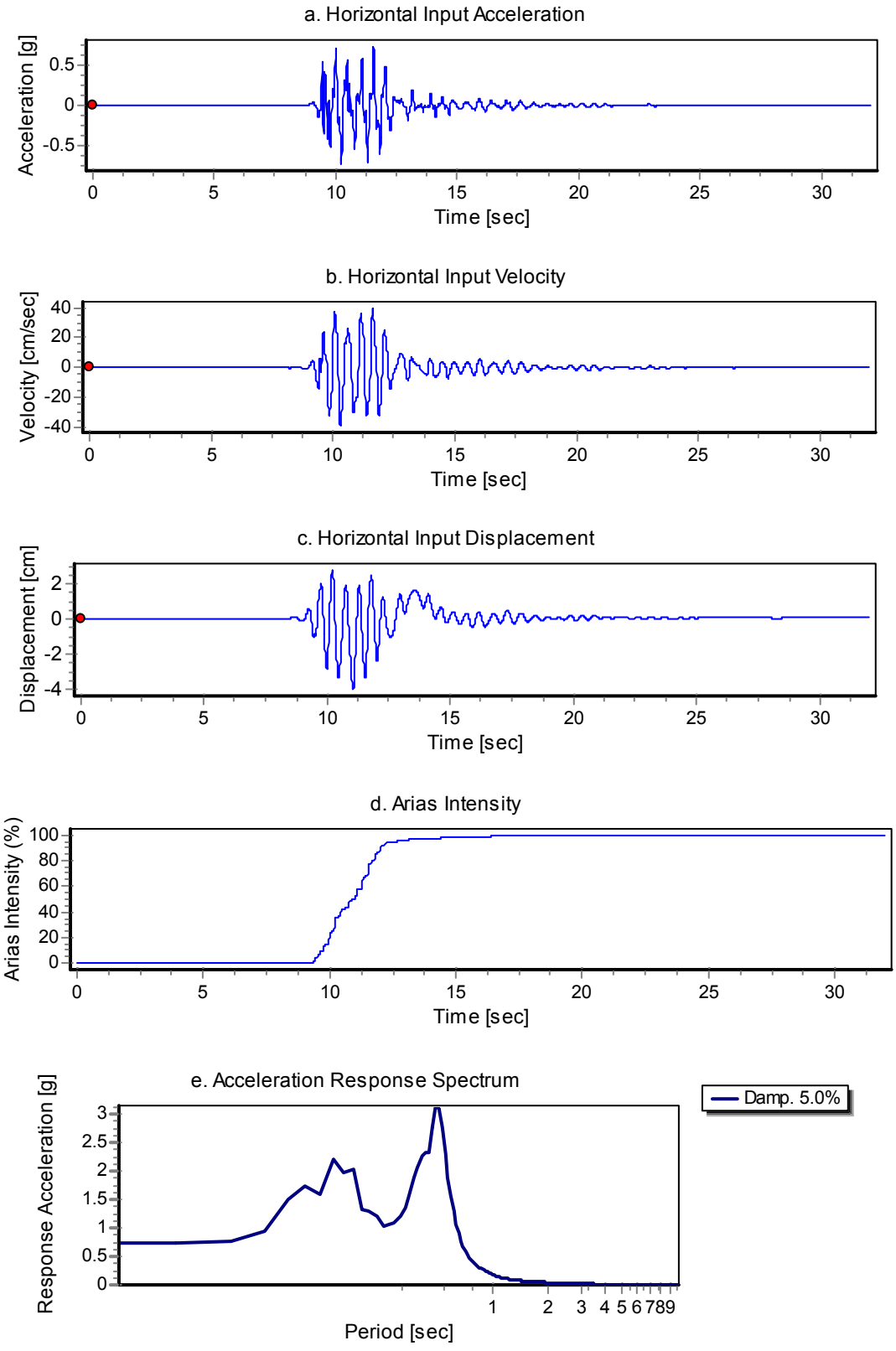

Fig. A.19 Horizontal acceleration, velocity, displacement, Arias intensity, and response spectrum of Kobe-TAK090-1 input ground motion during LAA02.

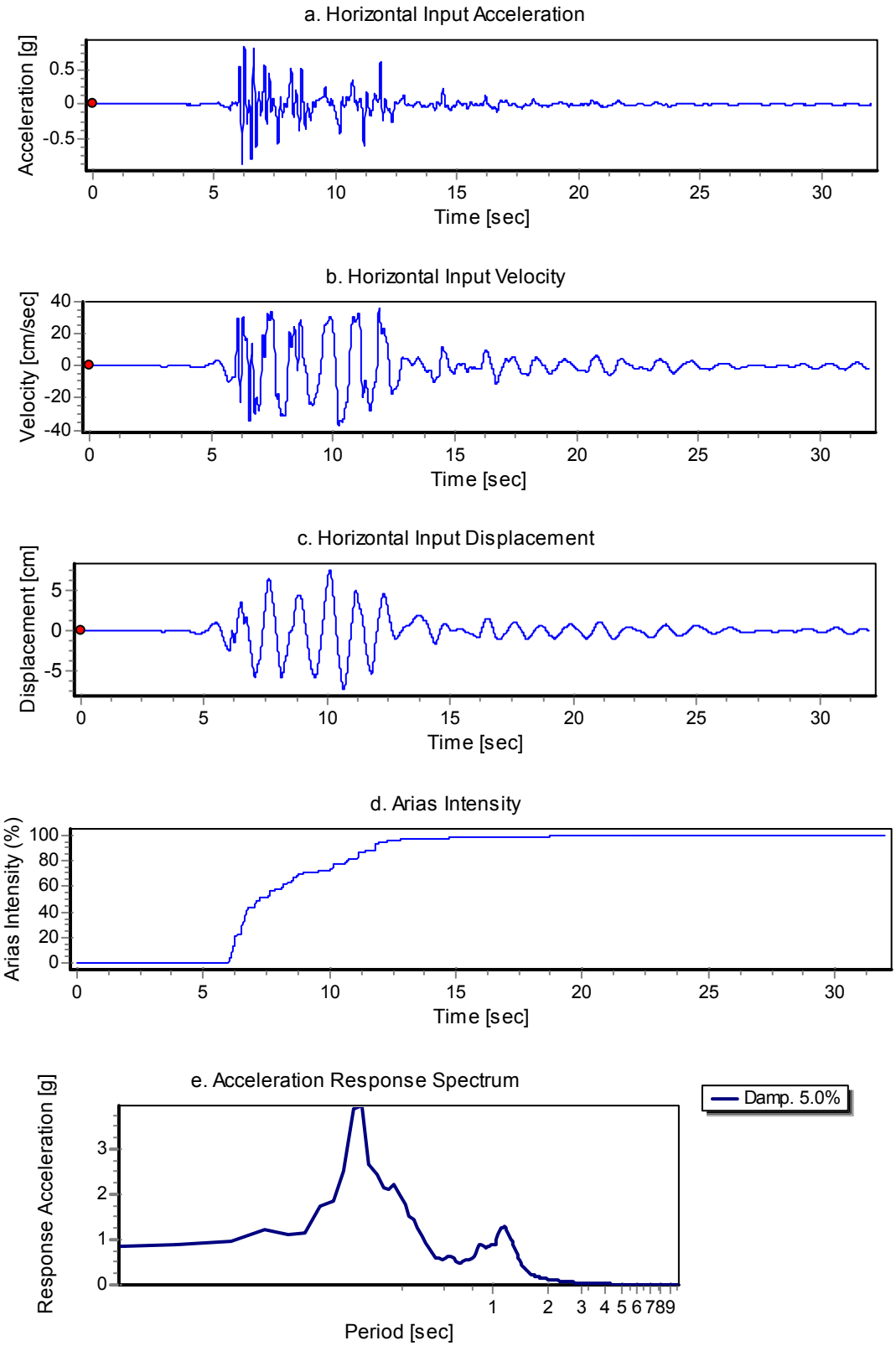

Fig. A.20 Horizontal acceleration, velocity, displacement, Arias intensity, and response spectrum of Kobe-TAK090-2 input ground motion during LAA02.

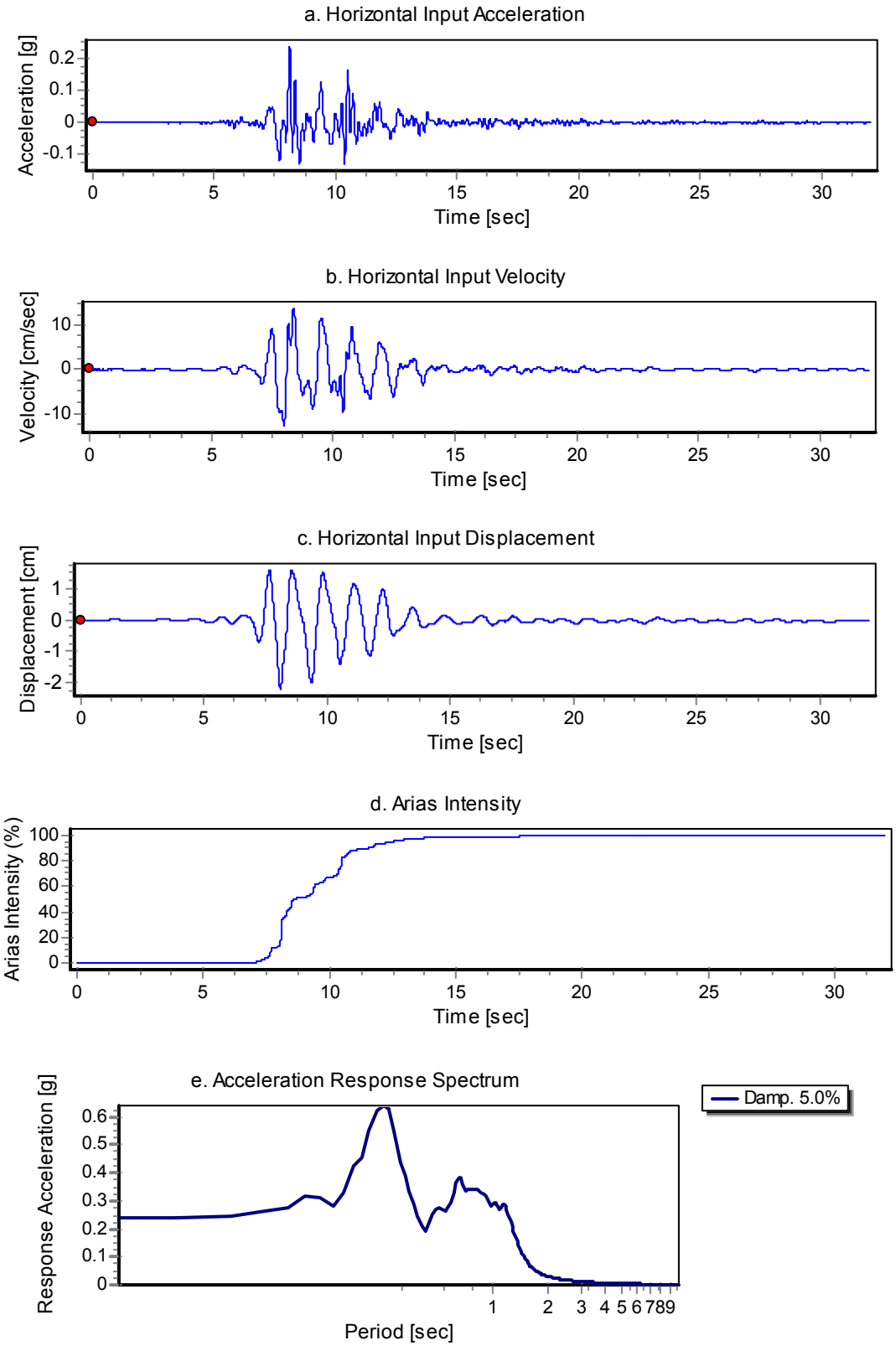

Fig. A.21 Horizontal acceleration, velocity, displacement, Arias intensity, and response spectrum of Loma Prieta-WVC270 input ground motion during LAA02.

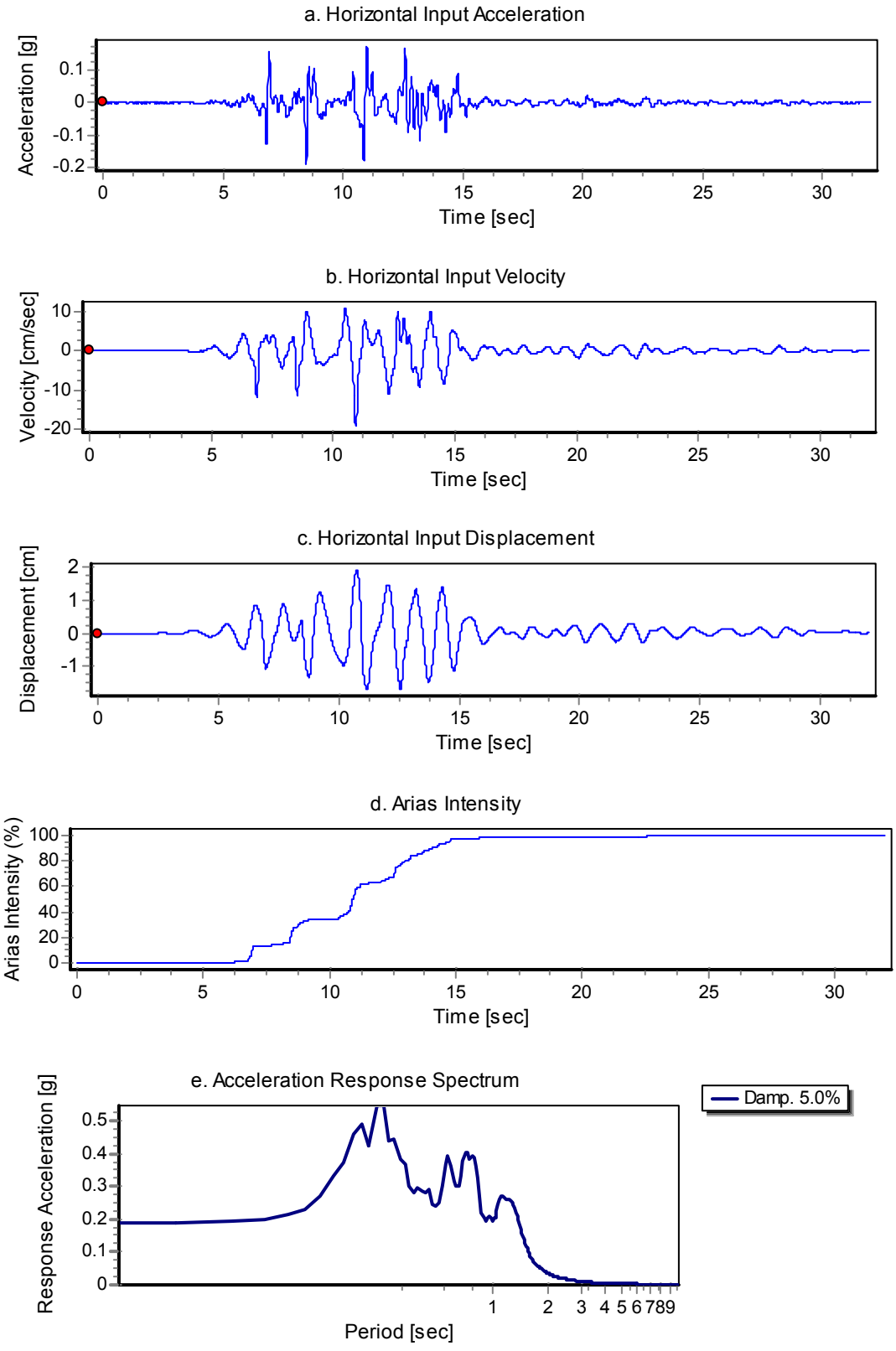

Fig. A.22 Horizontal acceleration, velocity, displacement, Arias intensity, and response spectrum of Kocaeli-YPT330-3 input ground motion during LAA02.

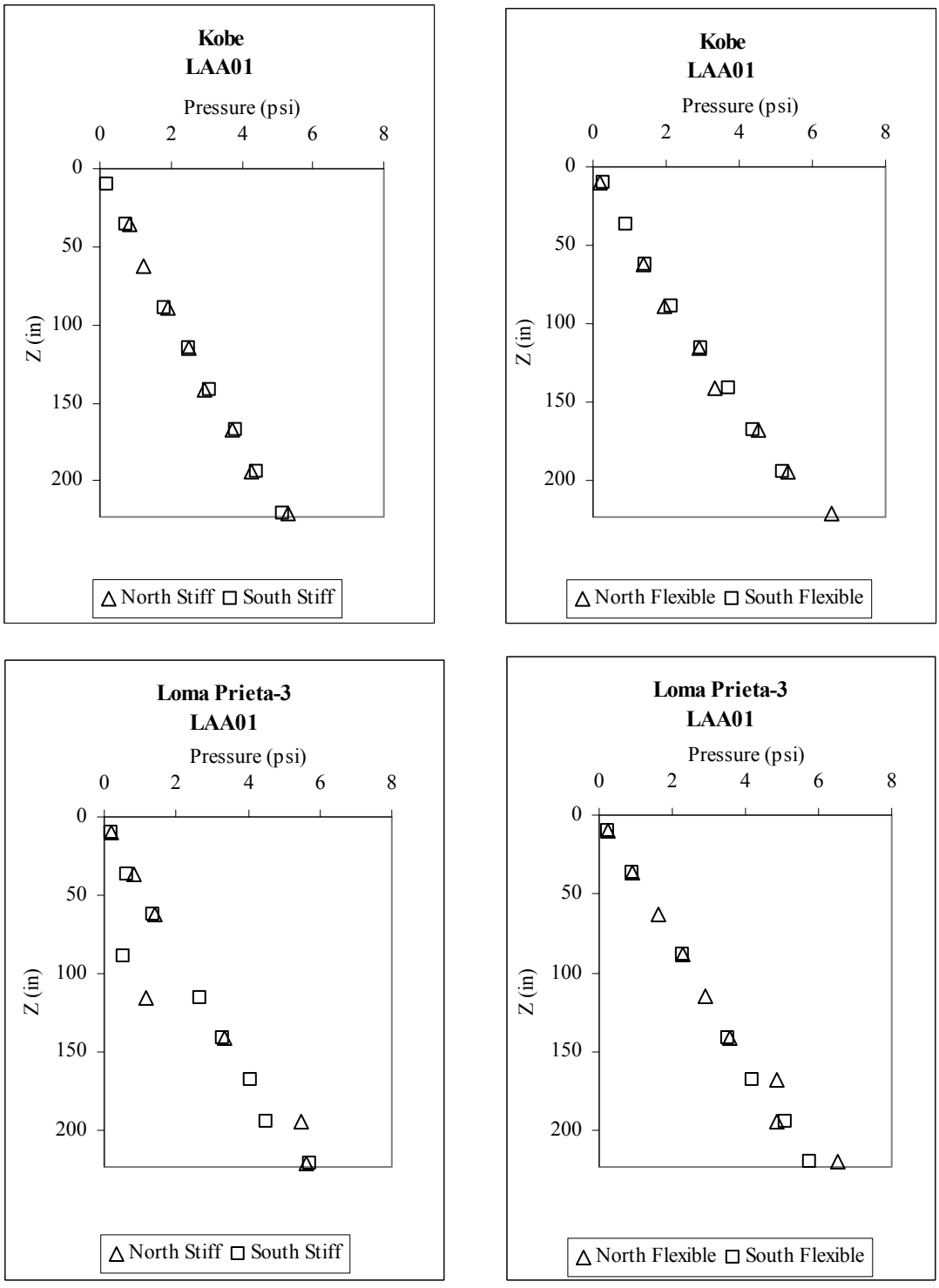

Fig. A.23 Maximum total lateral earth pressure profiles measured by Flexiforce sensors on stiff and flexible walls during Kobe and Loma Prieta-3 shaking events for LAA01.

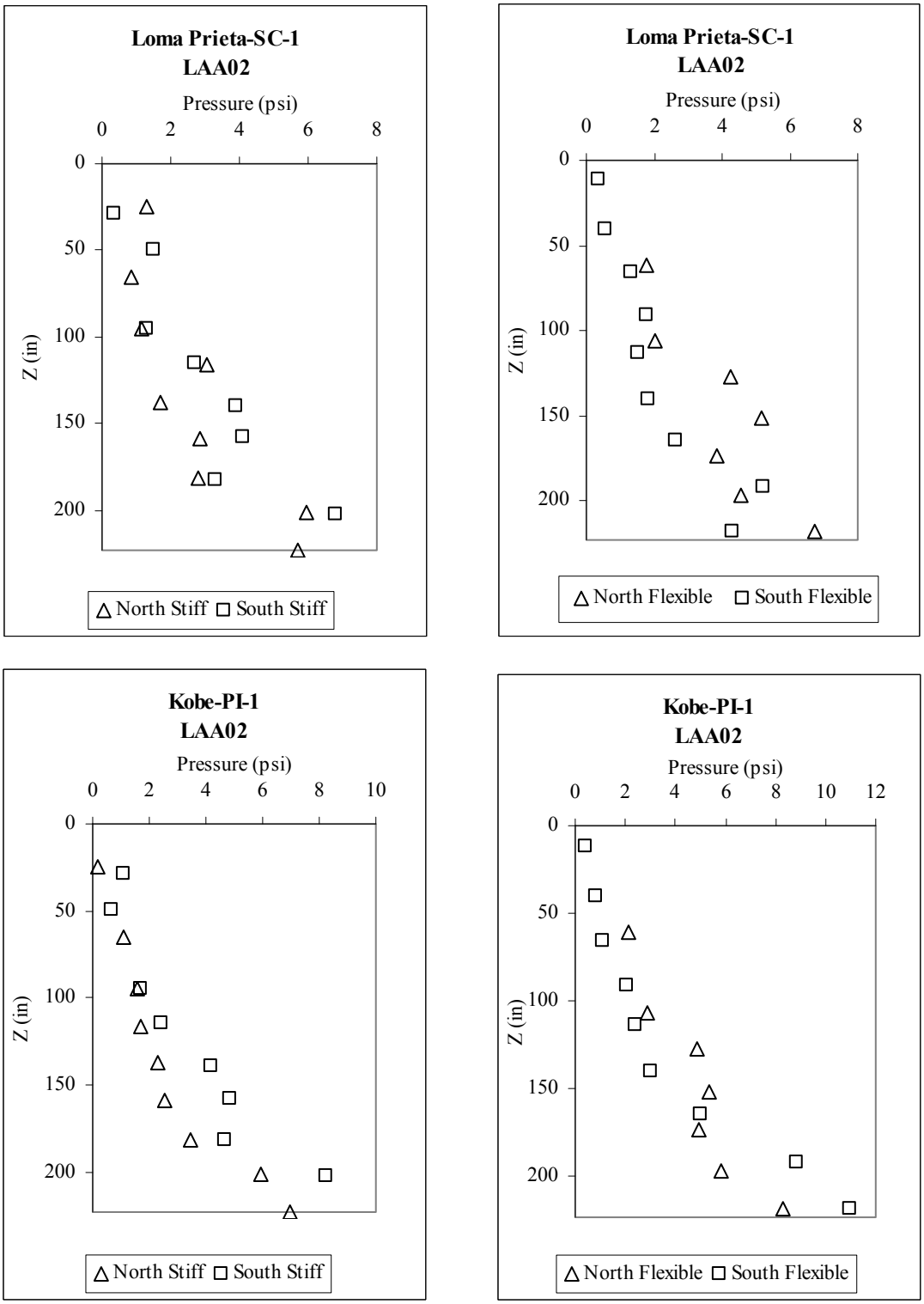

Fig. A.24 Maximum total lateral earth pressure profiles measured by Flexiforce sensors on stiff and flexible walls during Loma Prieta-SC-1 and Kobe-PI-1 shaking events for LAA02.

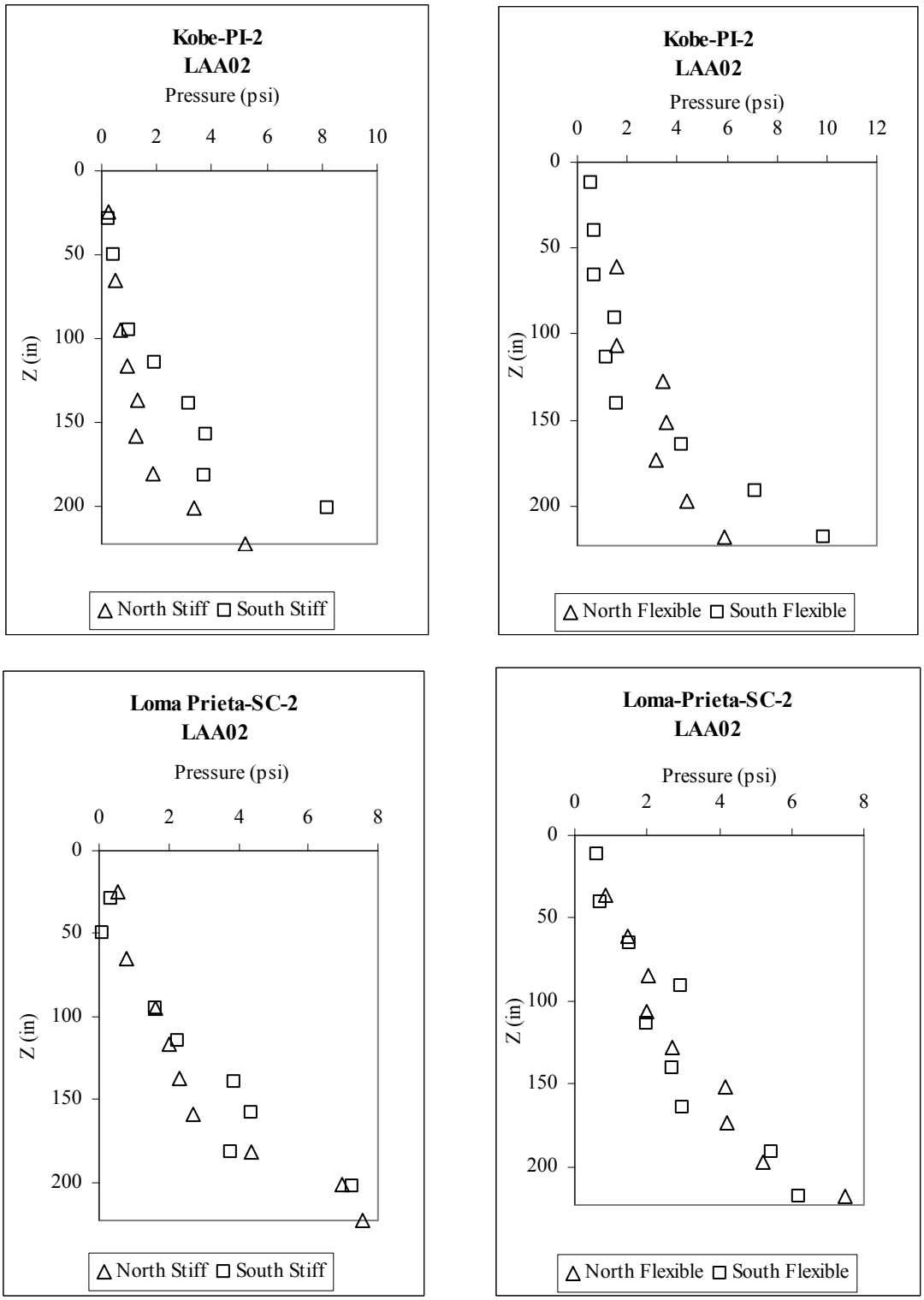

Fig. A.25 Maximum total lateral earth pressure profiles measured by Flexiforce sensors on stiff and flexible walls during Kobe-PI-2 and Loma Prieta-SC-2 shaking events for LAA02.

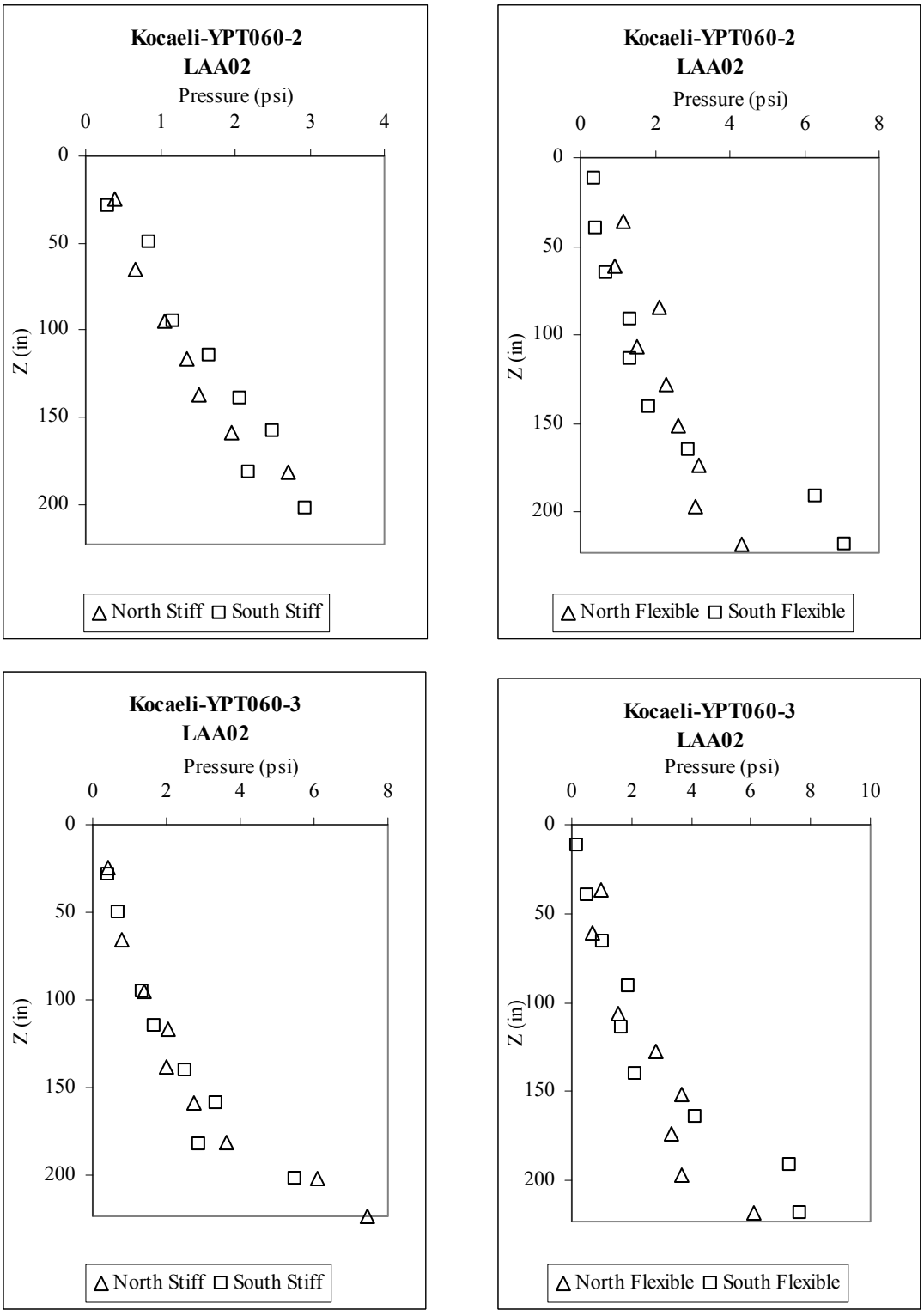

Fig. A.26 Maximum total lateral earth pressure profiles measured by Flexiforce sensors on stiff and flexible walls during Kocaeli-YPT060-2 and 3 shaking events for LAA02.

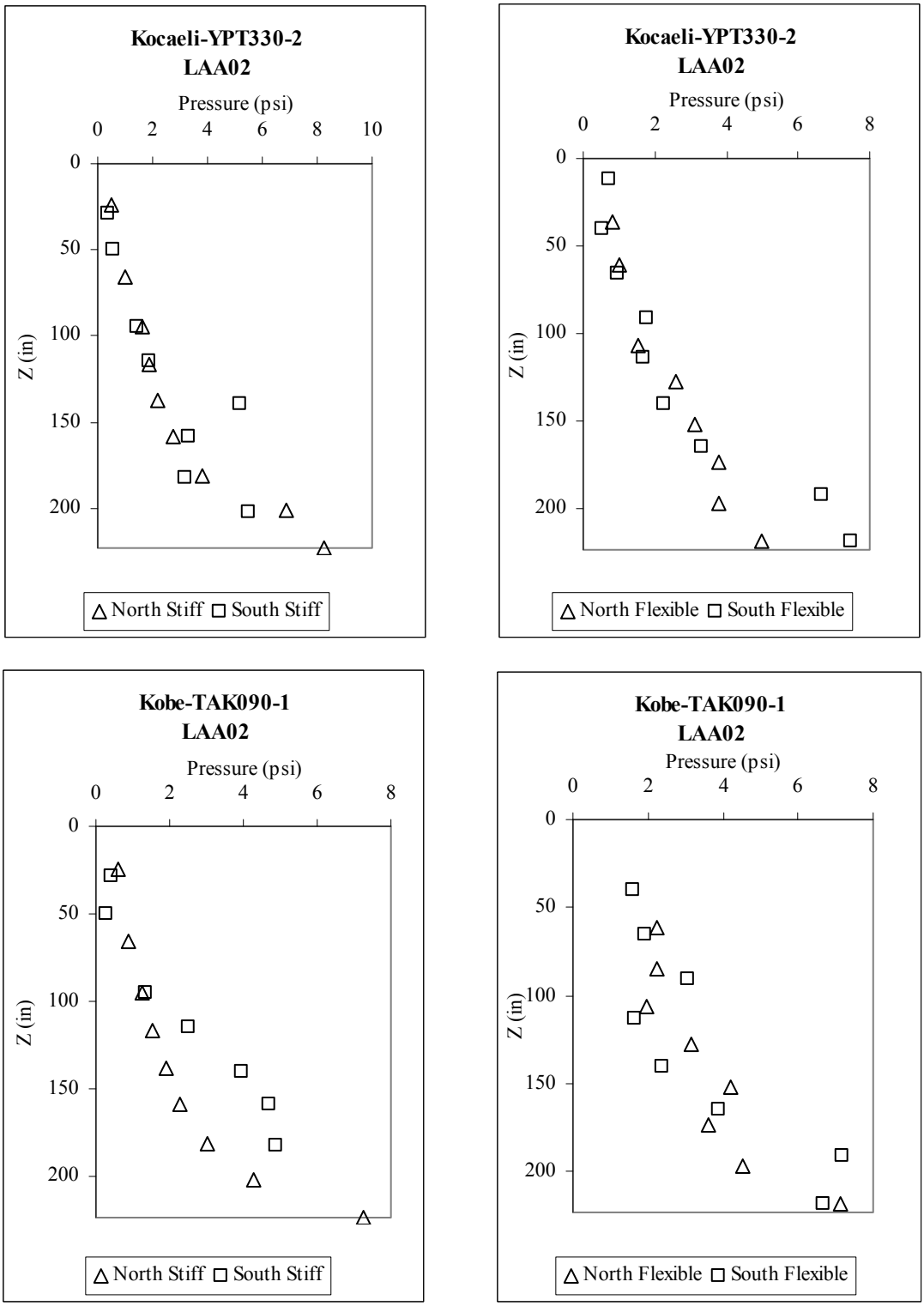

Fig. A.27 Maximum total lateral earth pressure profiles measured by Flexiforce sensors on stiff and flexible walls during Kocaeli-YPT330-2 and Kobe-TAK090-1 shaking events for LAA02.

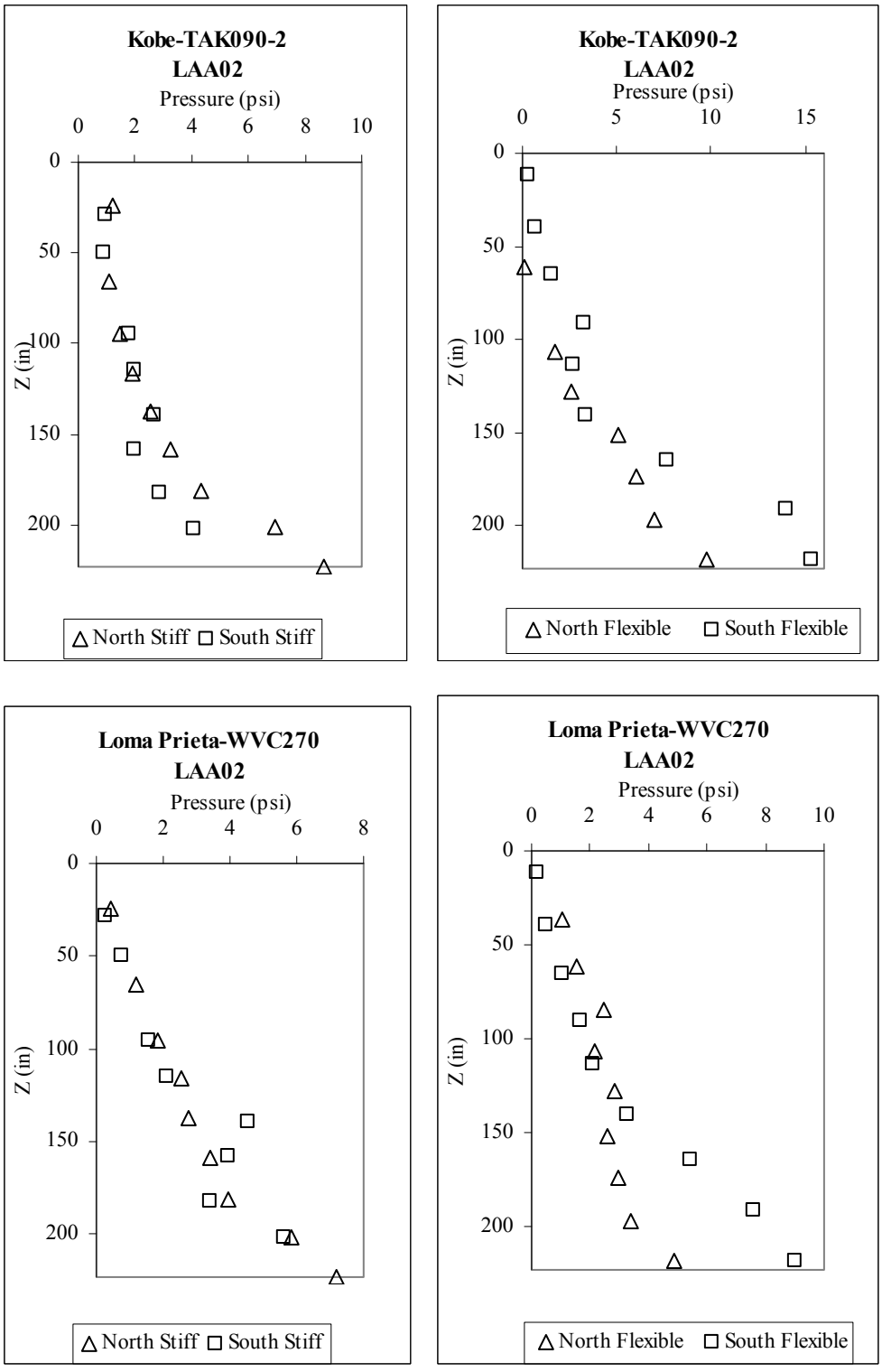

Fig. A.28 Maximum total lateral earth pressure profiles measured by Flexiforce sensors on stiff and flexible walls during Kobe-TAK090-2 and Loma Prieta-WVC270 shaking events for LAA02.

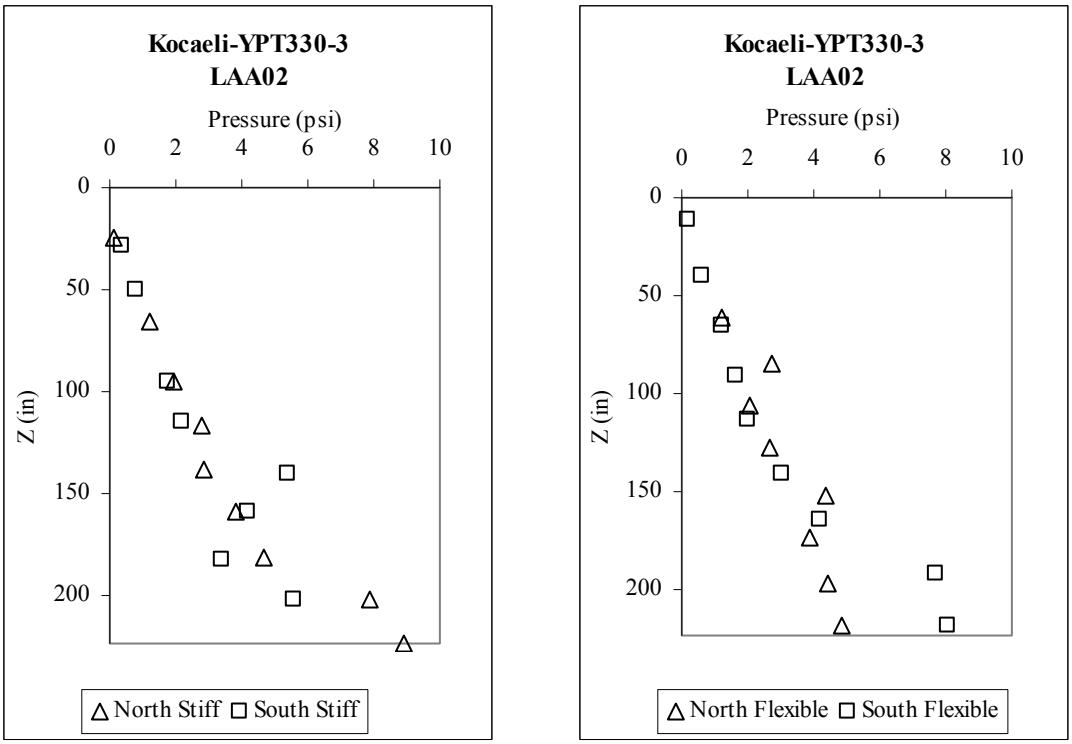

Fig. A.29 Maximum total lateral earth pressure profiles measured by Flexiforce sensors on stiff and flexible walls during Kocaeli-YPT330-3 shaking event for LAA02.

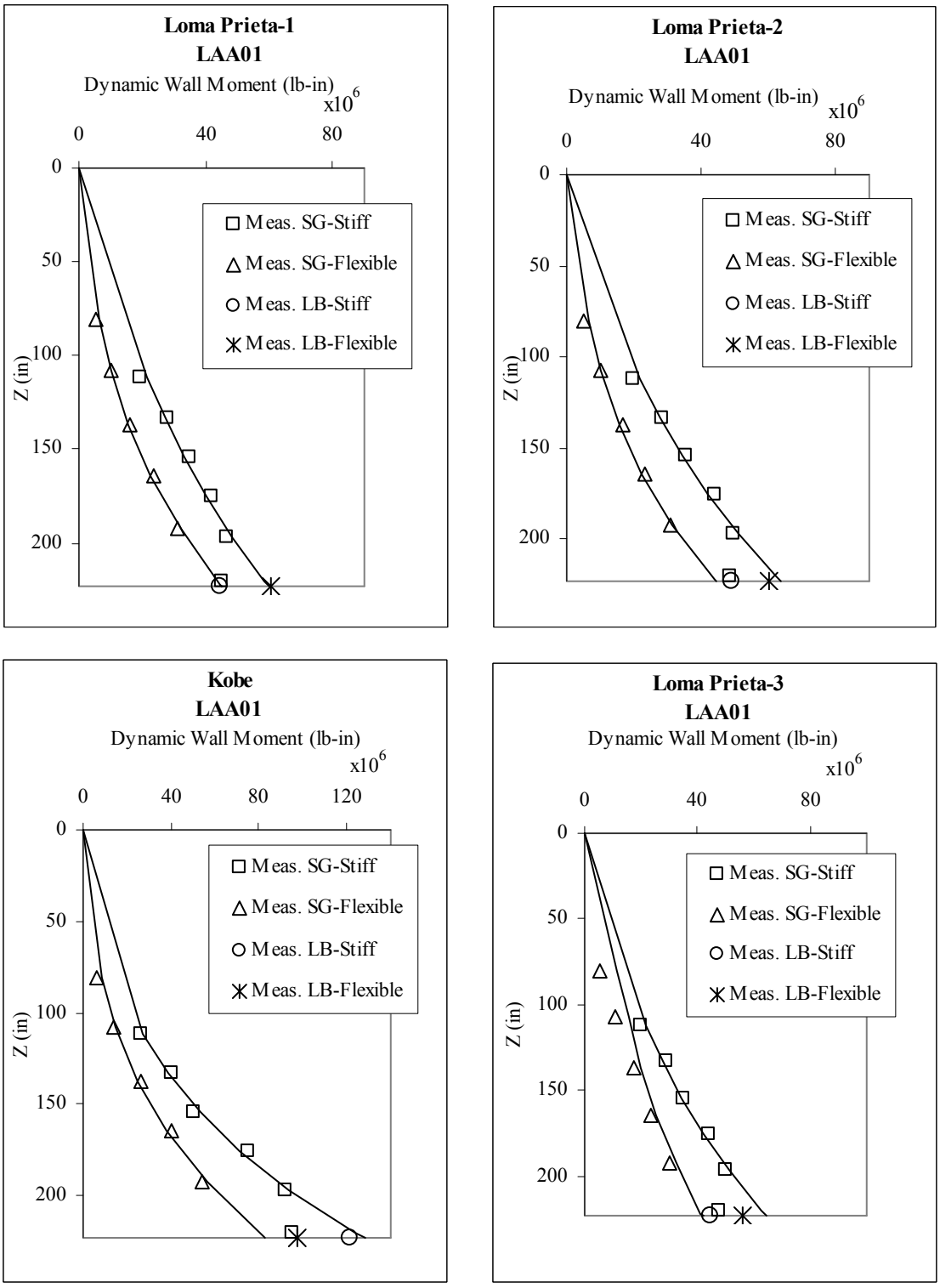

Fig. A.30 Maximum dynamic wall moment profiles measured by strain gages and force-sensing bolts on south stiff and north flexible walls for Loma Prieta-1, 2 and 3 and Kobe for LAA01.

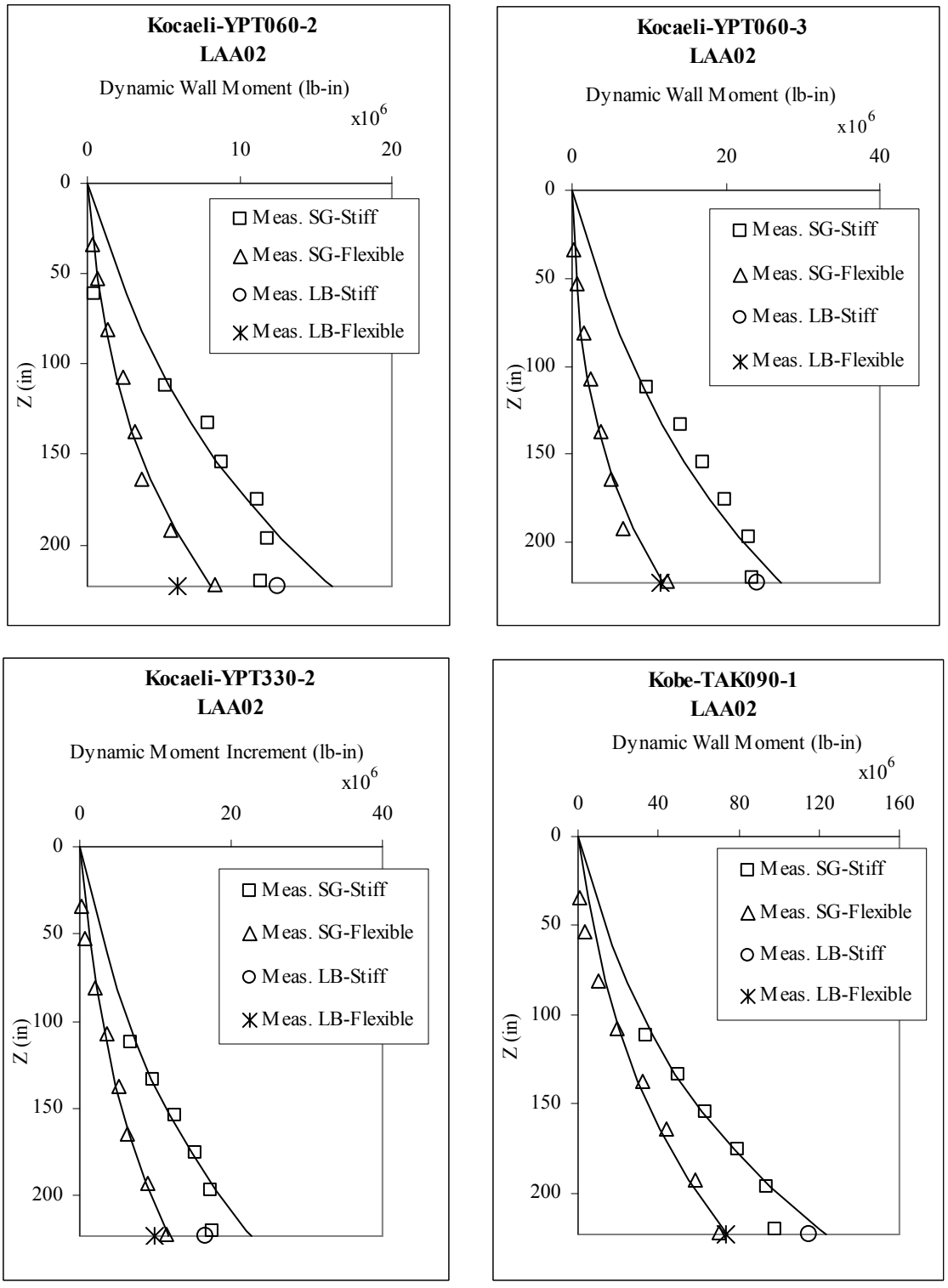

Fig. A.31 Maximum dynamic wall moment profiles measured by strain gages and force-sensing bolts on south stiff and north flexible walls for Kocaeli-YPT060-2 and 3, Kocaeli-YPT330-2 and Kobe-TAK090-1 for LAA02.

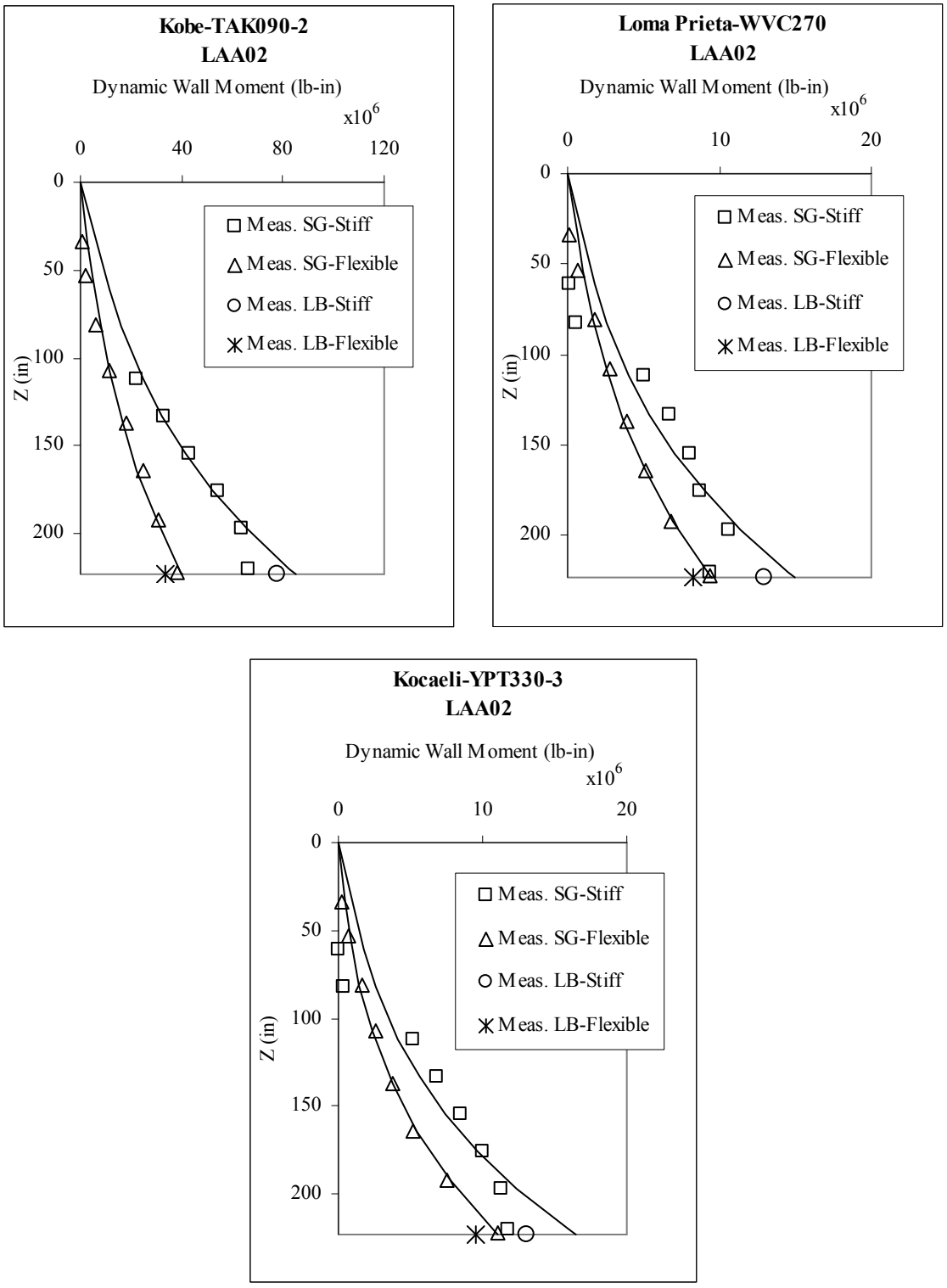

Fig. A.32 Maximum dynamic wall moment profiles measured by strain gages and force-sensing bolts on south stiff and north flexible walls for Kobe-TAK090-2, Loma Prieta-WVC270, and Kocaeli-YPT330-3 for LAA02.

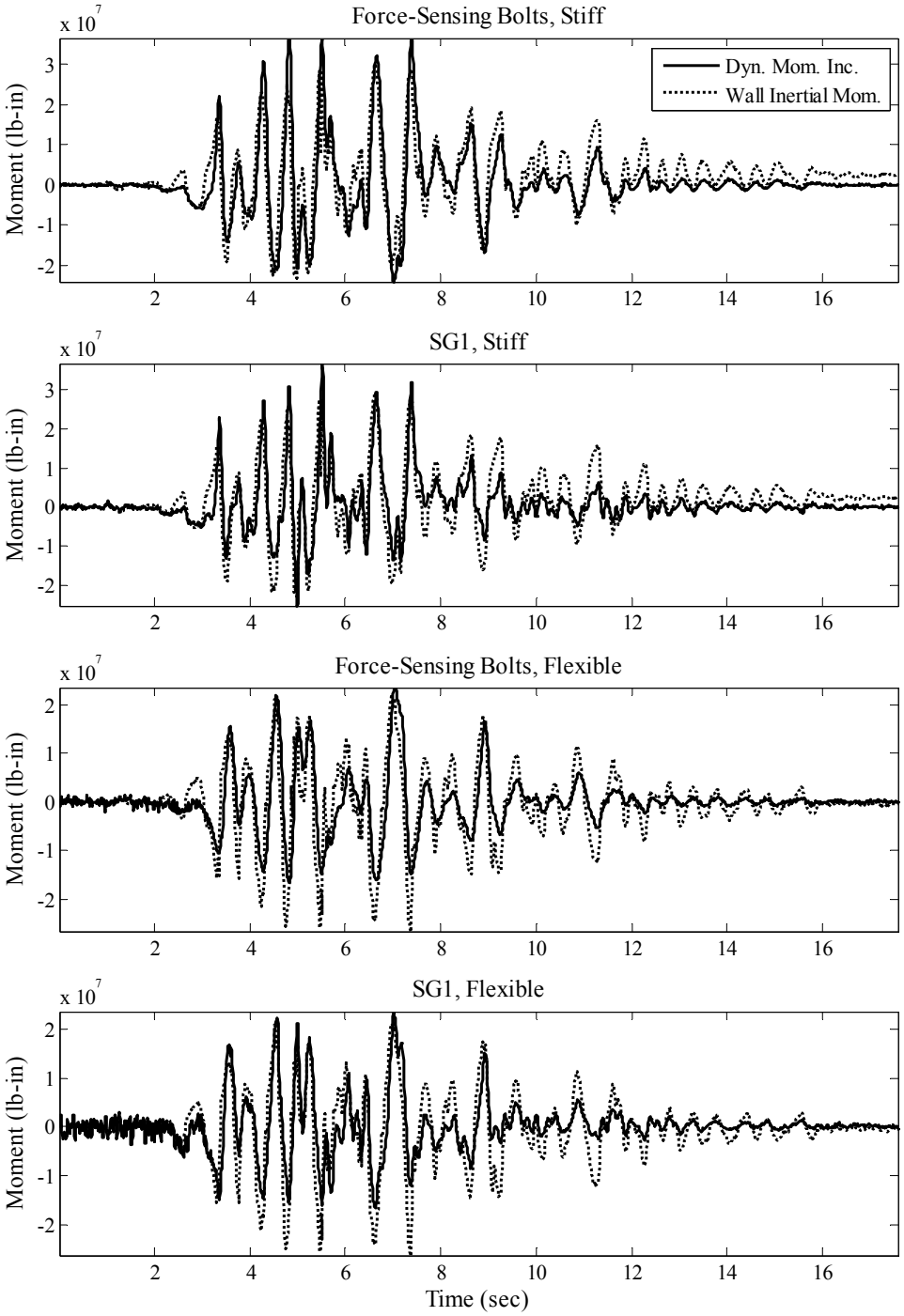

Fig. A.33 Dynamic wall moment time series interpreted from SG1 and force-sensing bolt data and corresponding wall inertial moment estimates on south stiff and north flexible walls for Loma Prieta-SC-1 for LAA02.

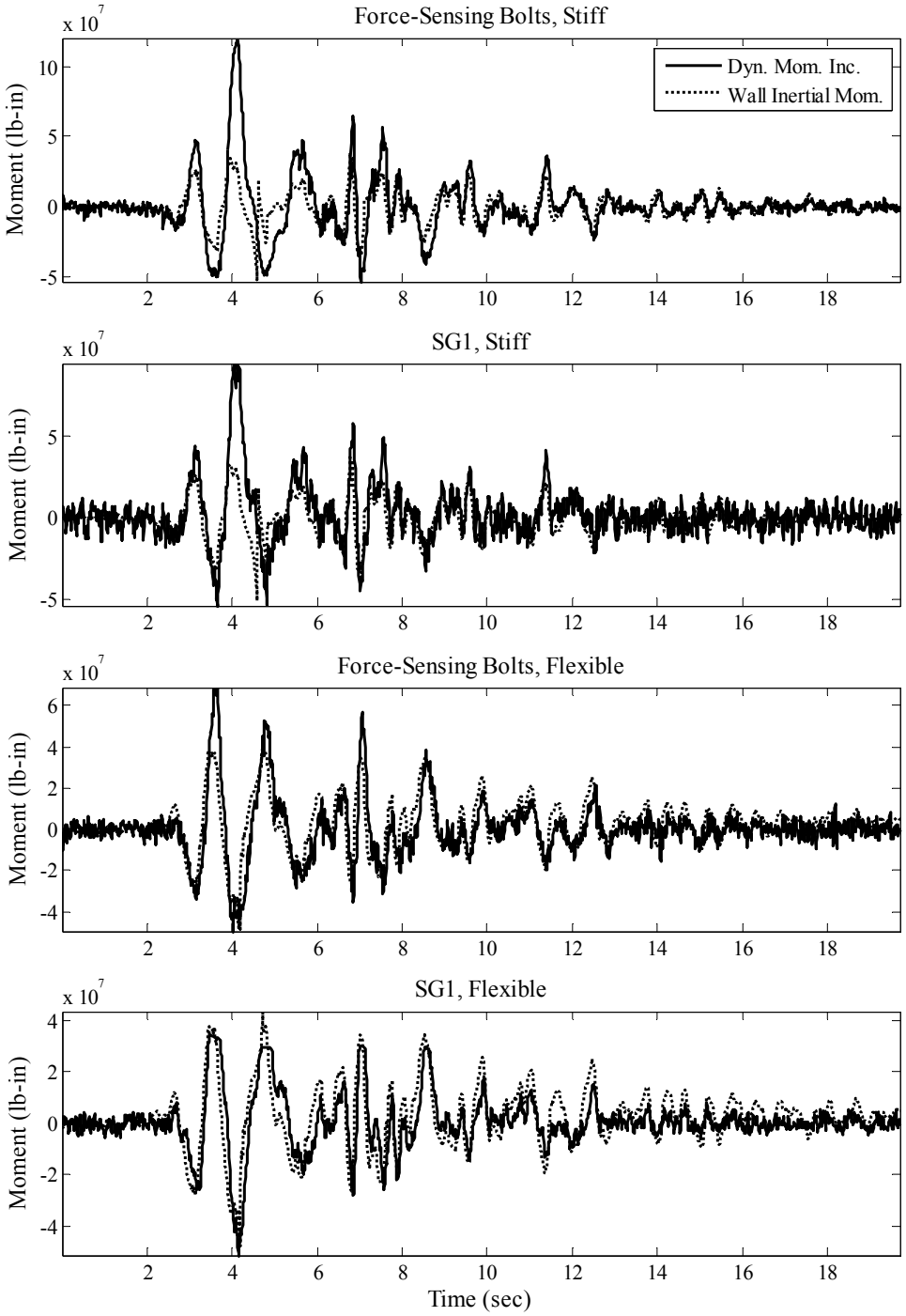

Fig. A.34 Dynamic wall moment time series interpreted from SG1 and force-sensing bolt data and corresponding wall inertial moment estimates on south stiff and north flexible walls for Kobe-PI-1 for LAA02.

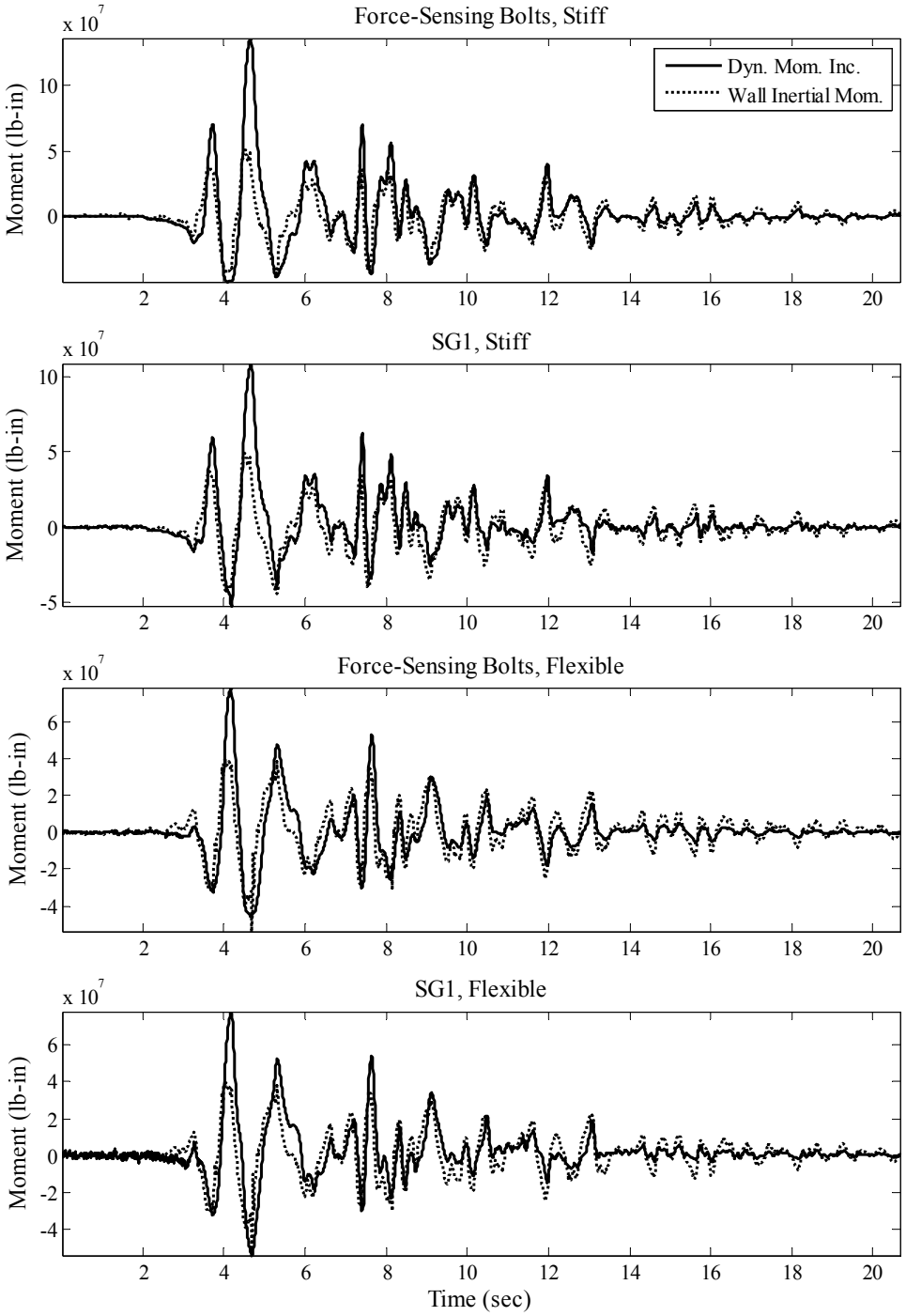

Fig. A.35 Dynamic wall moment time series interpreted from SG1 and force-sensing bolt data and corresponding wall inertial moment estimates on south stiff and north flexible walls for Kobe-PI-2 for LAA02.

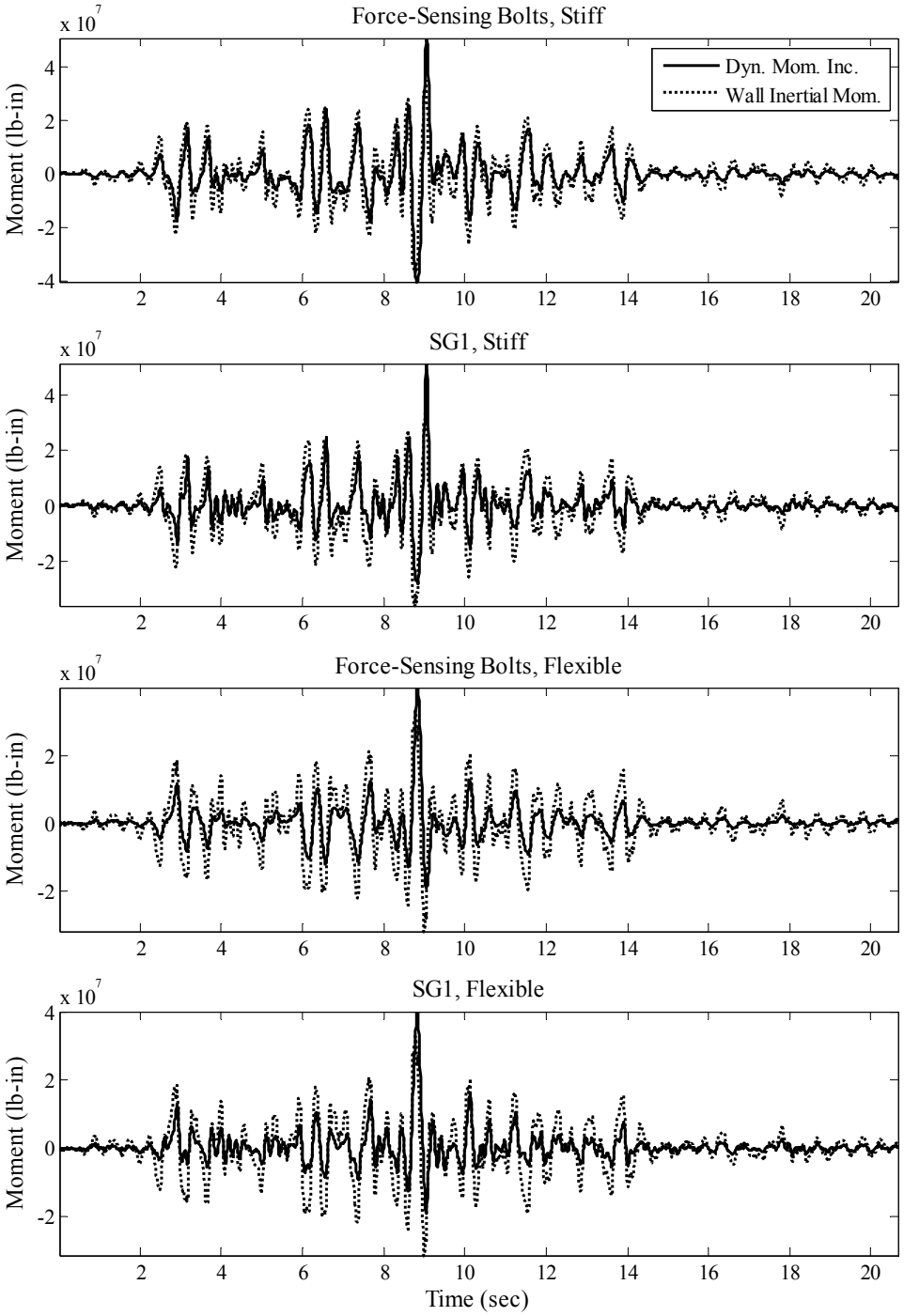

Fig. A.36 Dynamic wall moment time series interpreted from SG1 and force-sensing bolt data and corresponding wall inertial moment estimates on south stiff and north flexible walls for Loma Prieta-SC-2 for LAA02.

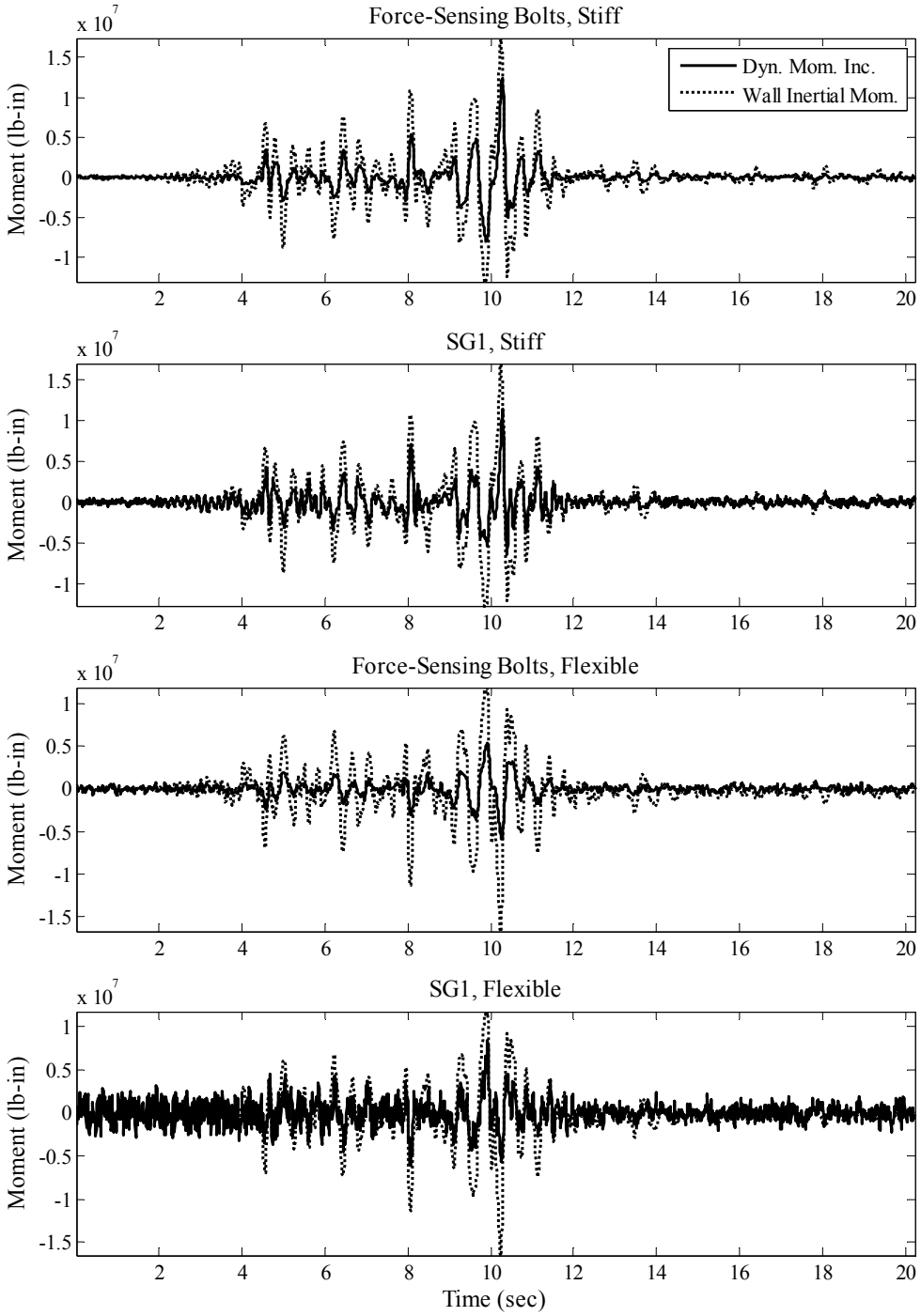

Fig. A.37 Dynamic wall moment time series interpreted from SG1 and force-sensing bolt data and corresponding wall inertial moment estimates on south stiff and north flexible walls for Kocaeli-YPT060-2 for LAA02.

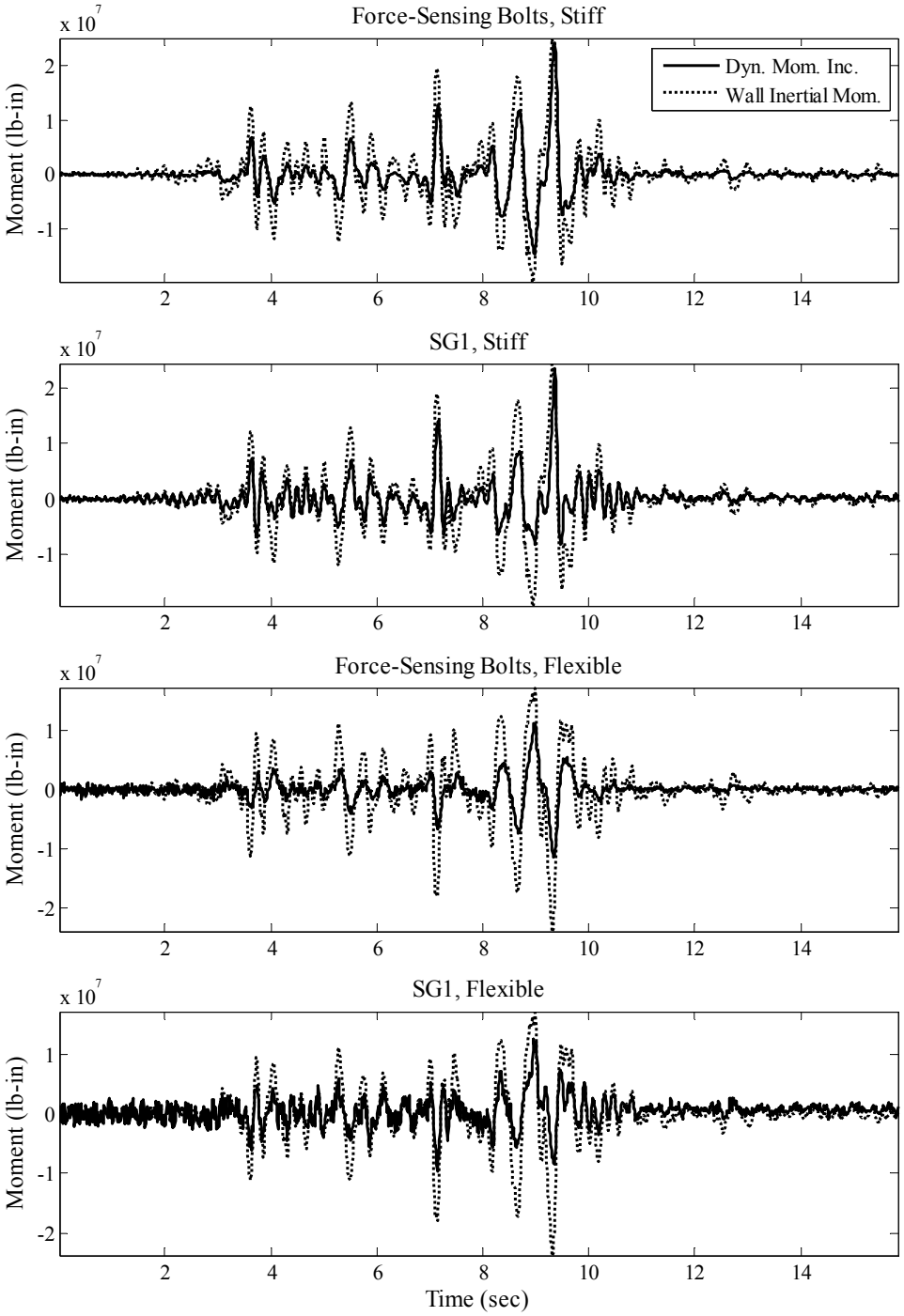

Fig. A.38 Dynamic wall moment time series interpreted from SG1 and force-sensing bolt data and corresponding wall inertial moment estimates on south stiff and north flexible walls for Kocaeli-YPT060-3 for LAA02.

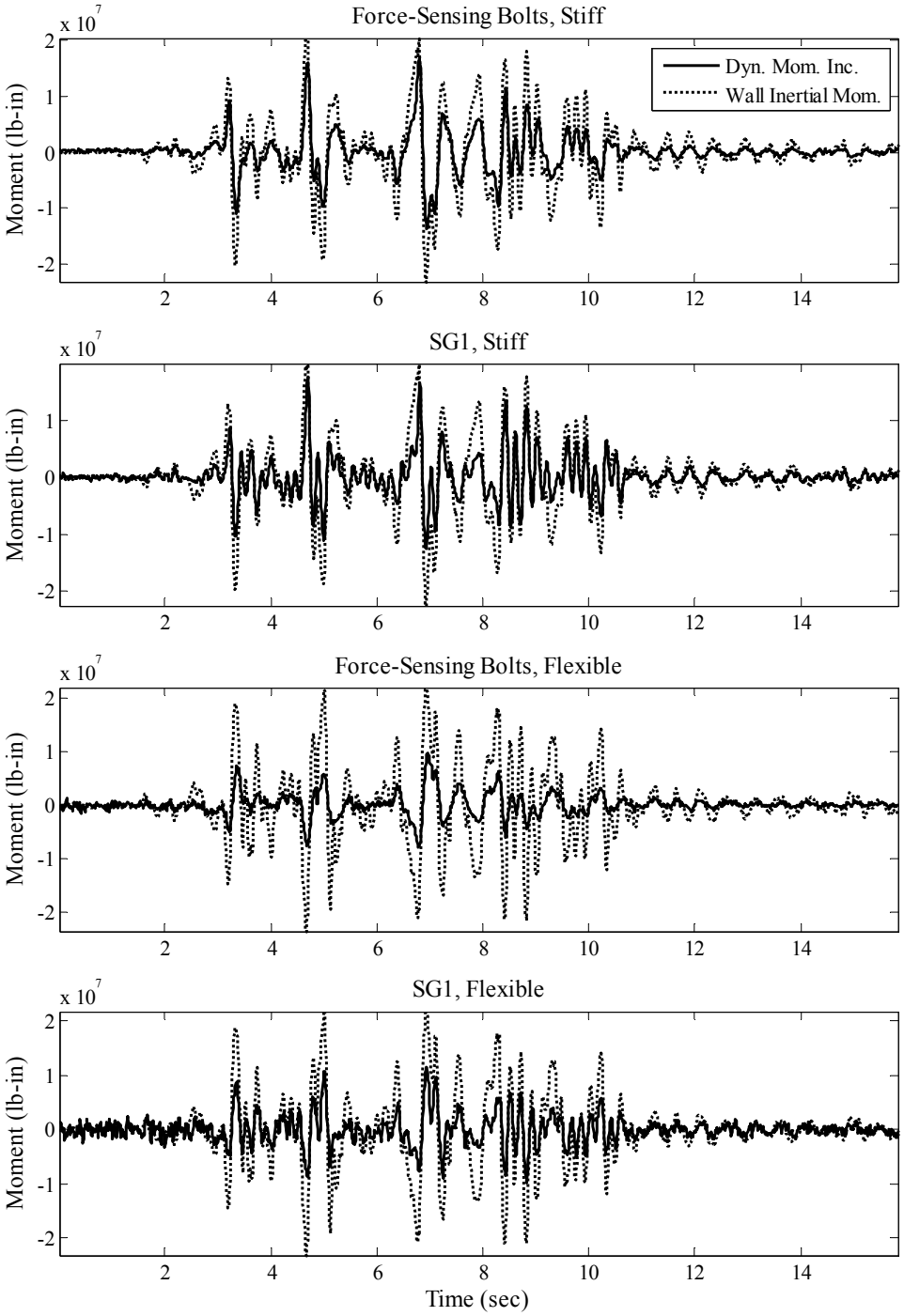

Fig. A.39 Dynamic wall moment time series interpreted from SG1 and force-sensing bolt data and corresponding wall inertial moment estimates on south stiff and north flexible walls for Kocaeli-YPT330-2 for LAA02.

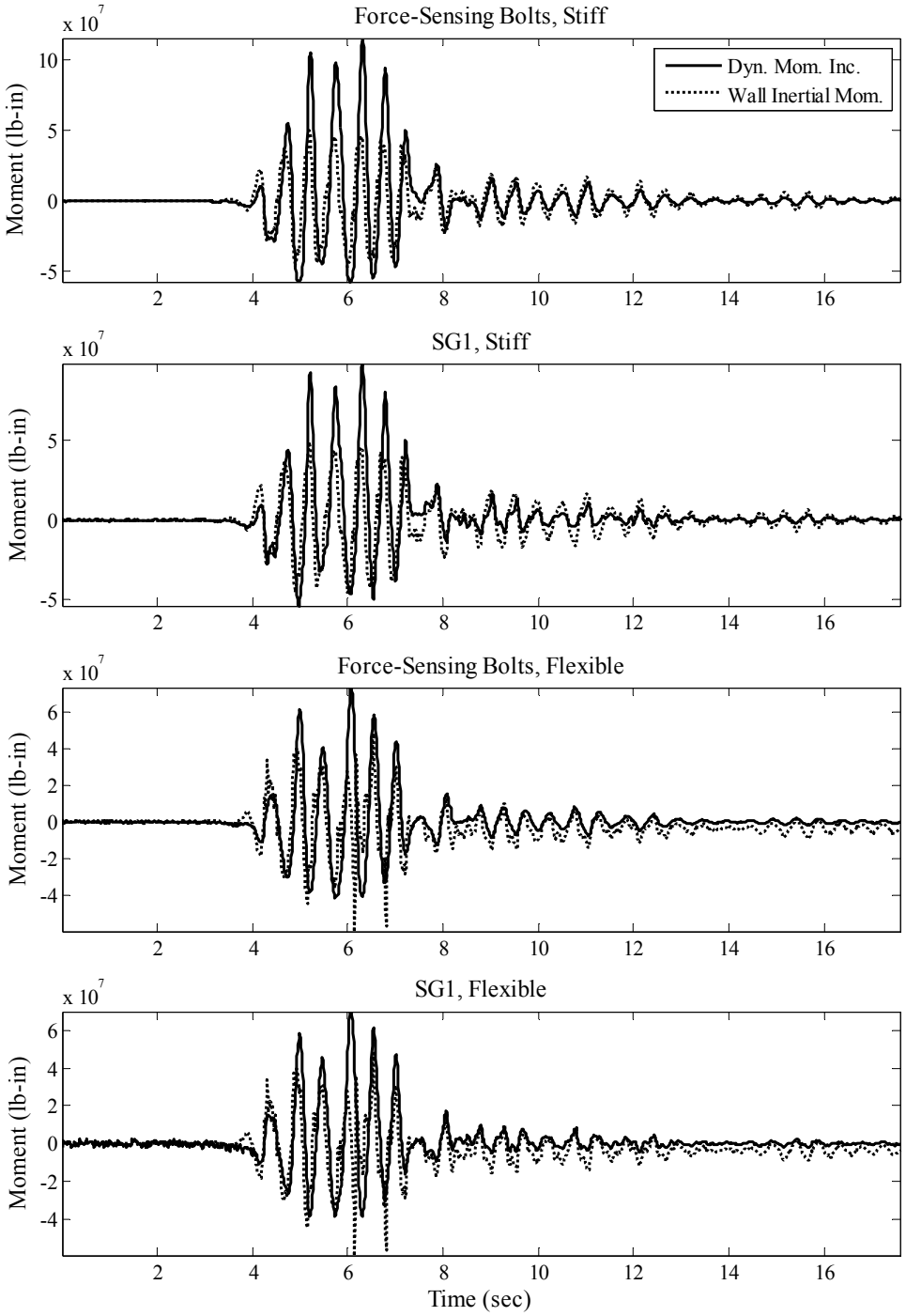

Fig. A.40 Dynamic wall moment time series interpreted from SG1 and force-sensing bolt data and corresponding wall inertial moment estimates on south stiff and north flexible walls for Kobe-TAK090-1 for LAA02.

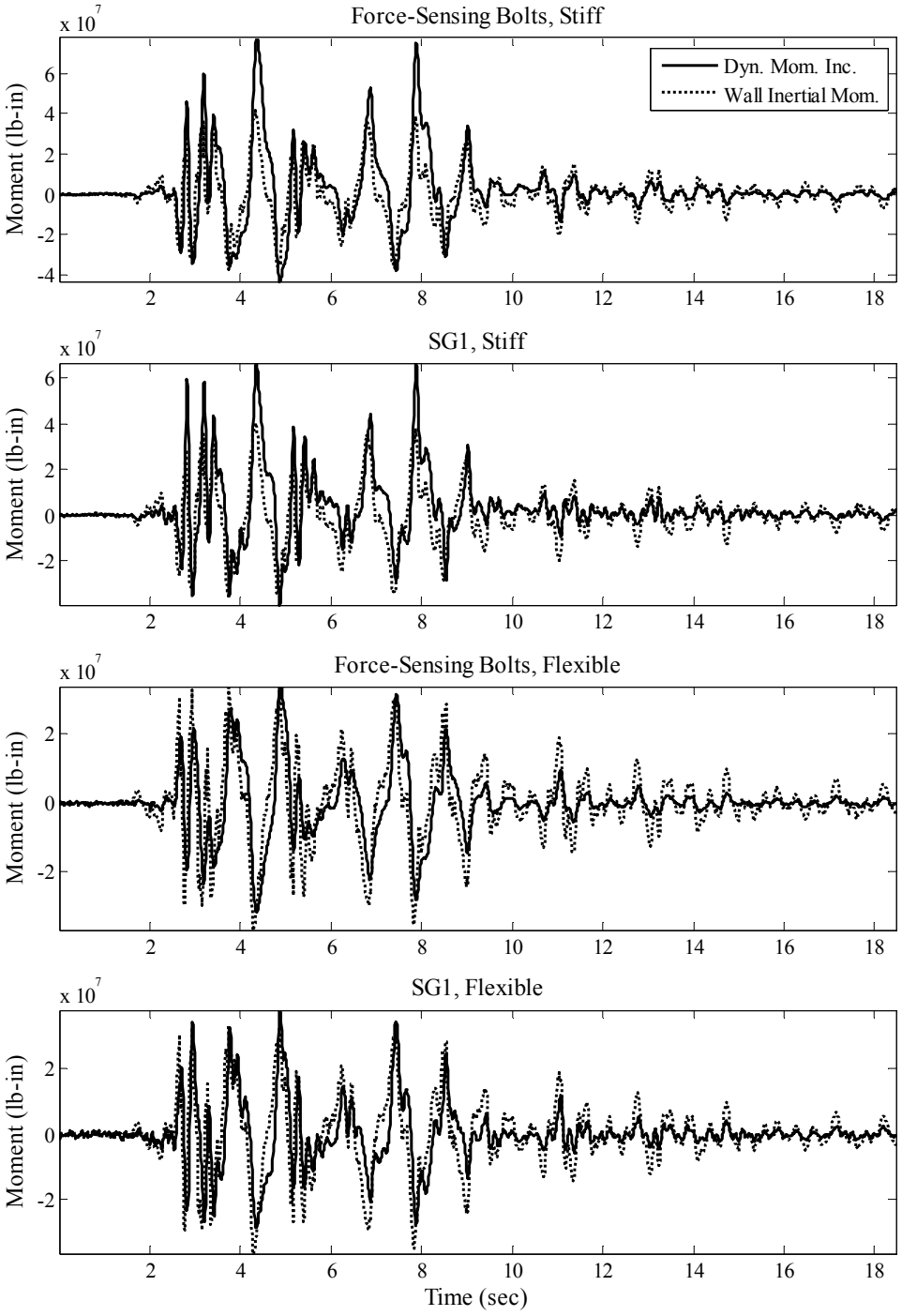

Fig. A.41 Dynamic wall moment time series interpreted from SG1 and force-sensing bolt data and corresponding wall inertial moment estimates on south stiff and north flexible walls for Kobe-TAK090-2 for LAA02.

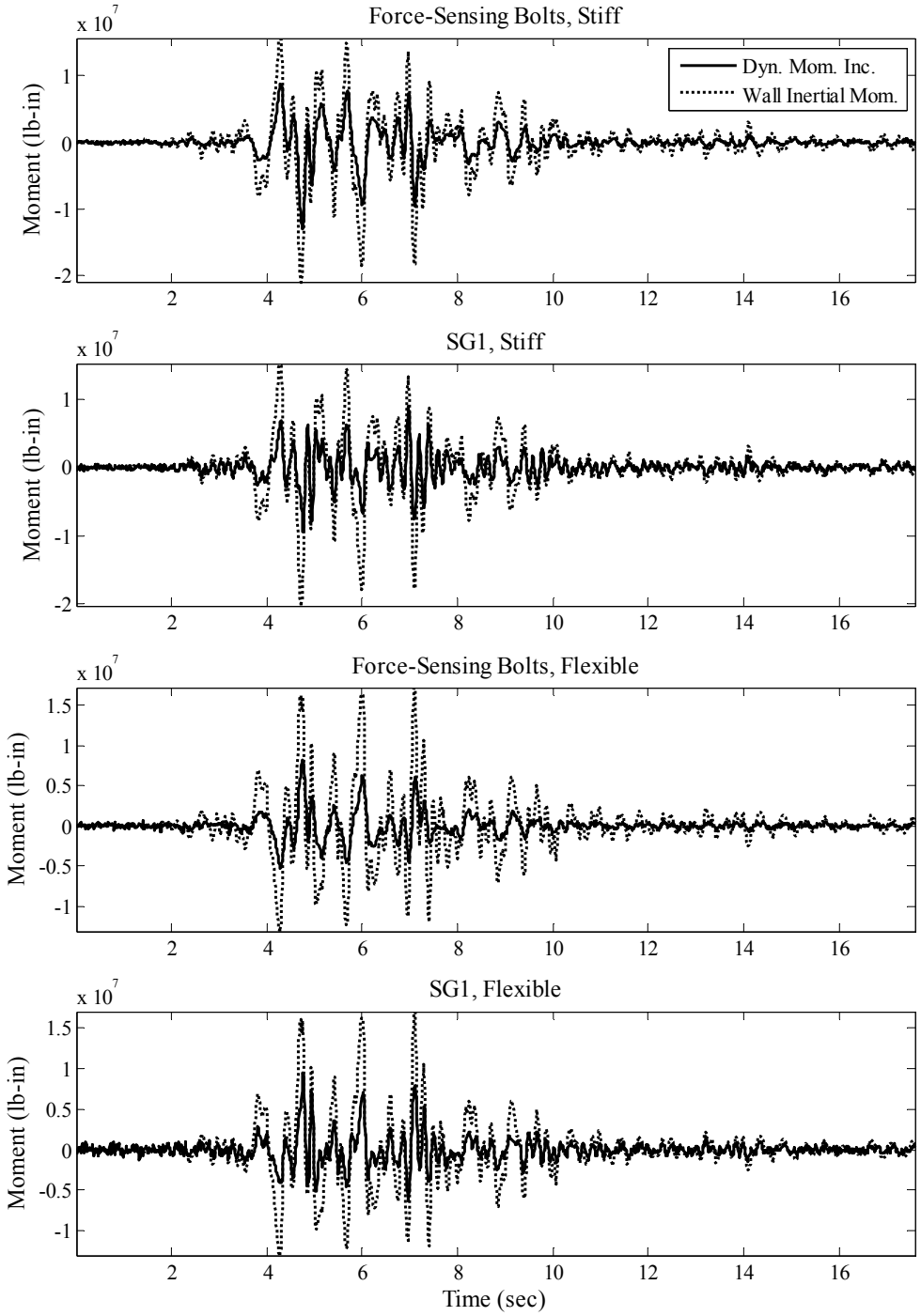

Fig. A.42 Dynamic wall moment time series interpreted from SG1 and force-sensing bolt data and corresponding wall inertial moment estimates on south stiff and north flexible walls for Loma Prieta-WVC270 for LAA02.

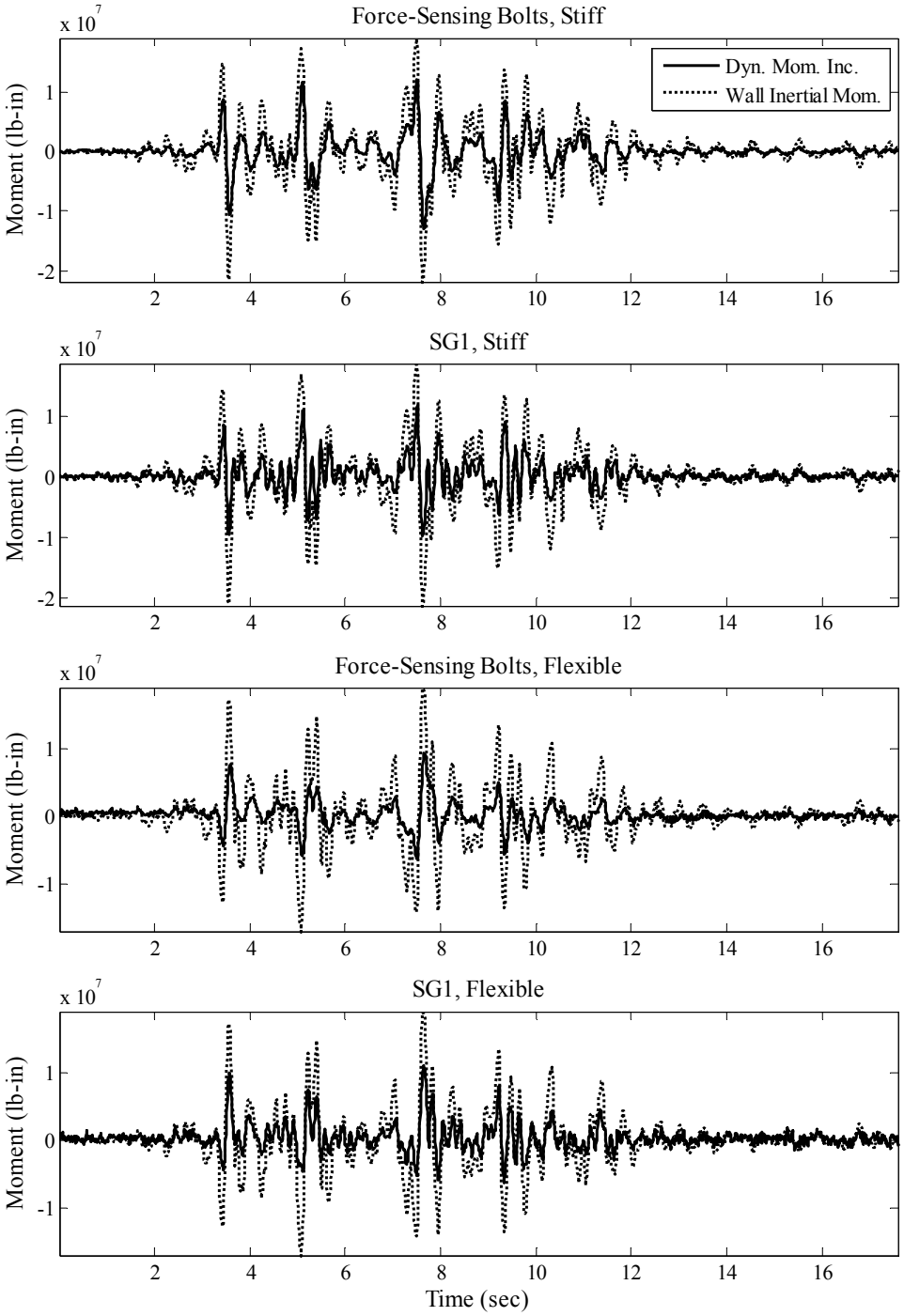

Fig. A.43 Dynamic wall moment time series interpreted from SG1 and force-sensing bolt data and corresponding wall inertial moment estimates on south stiff and north flexible walls for Kocaeli-YPT330-3 for LAA02.

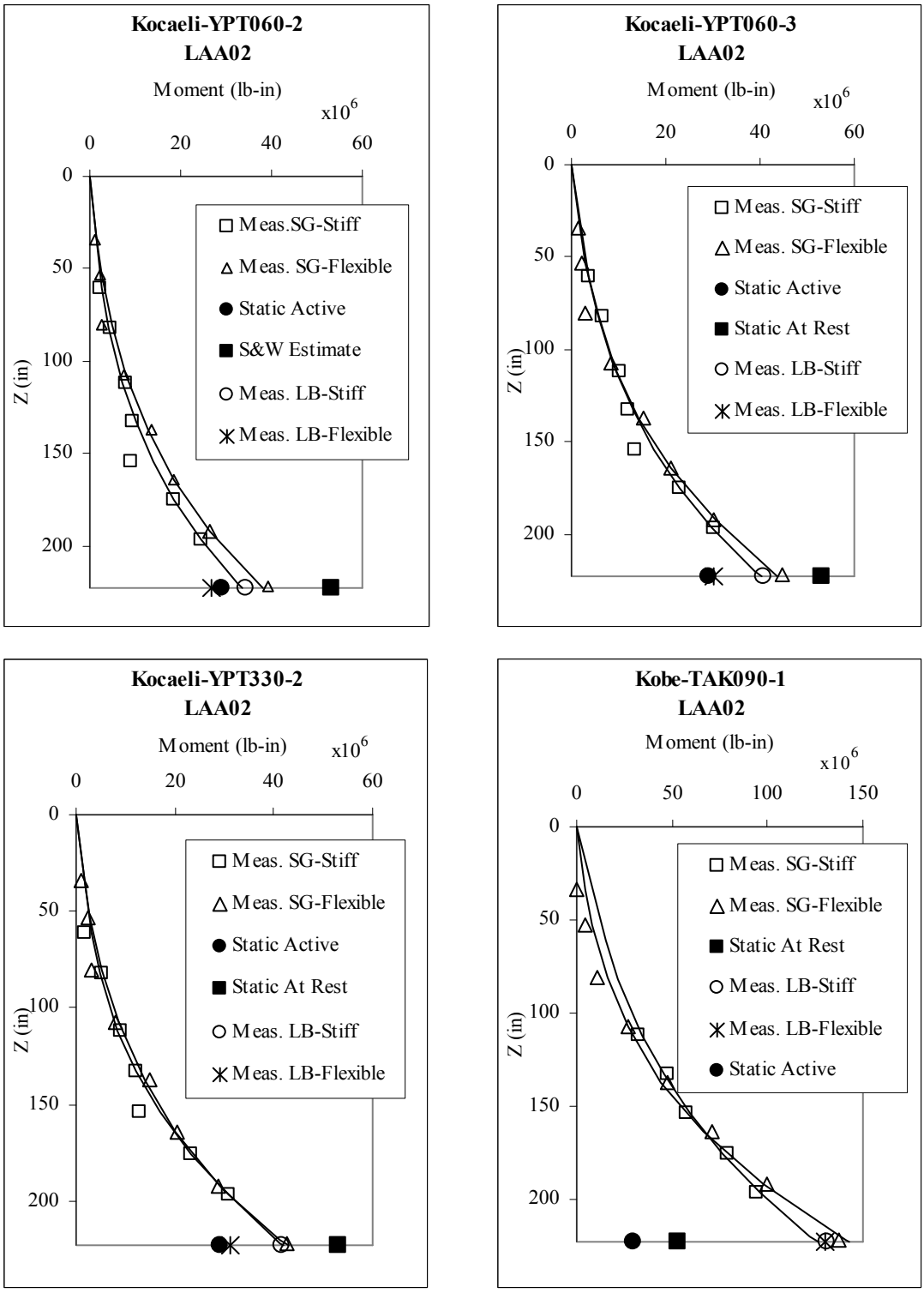

Fig. A.44 Maximum total earth pressure moment profiles interpreted from strain gage and force-sensing bolt measurements and static active and at-rest moment estimates on south stiff and north flexible walls for Kocaeli-YPT060-2 and 3, Kocaeli-YPT330-2 and Kobe-TAK090-1 for LAA02.

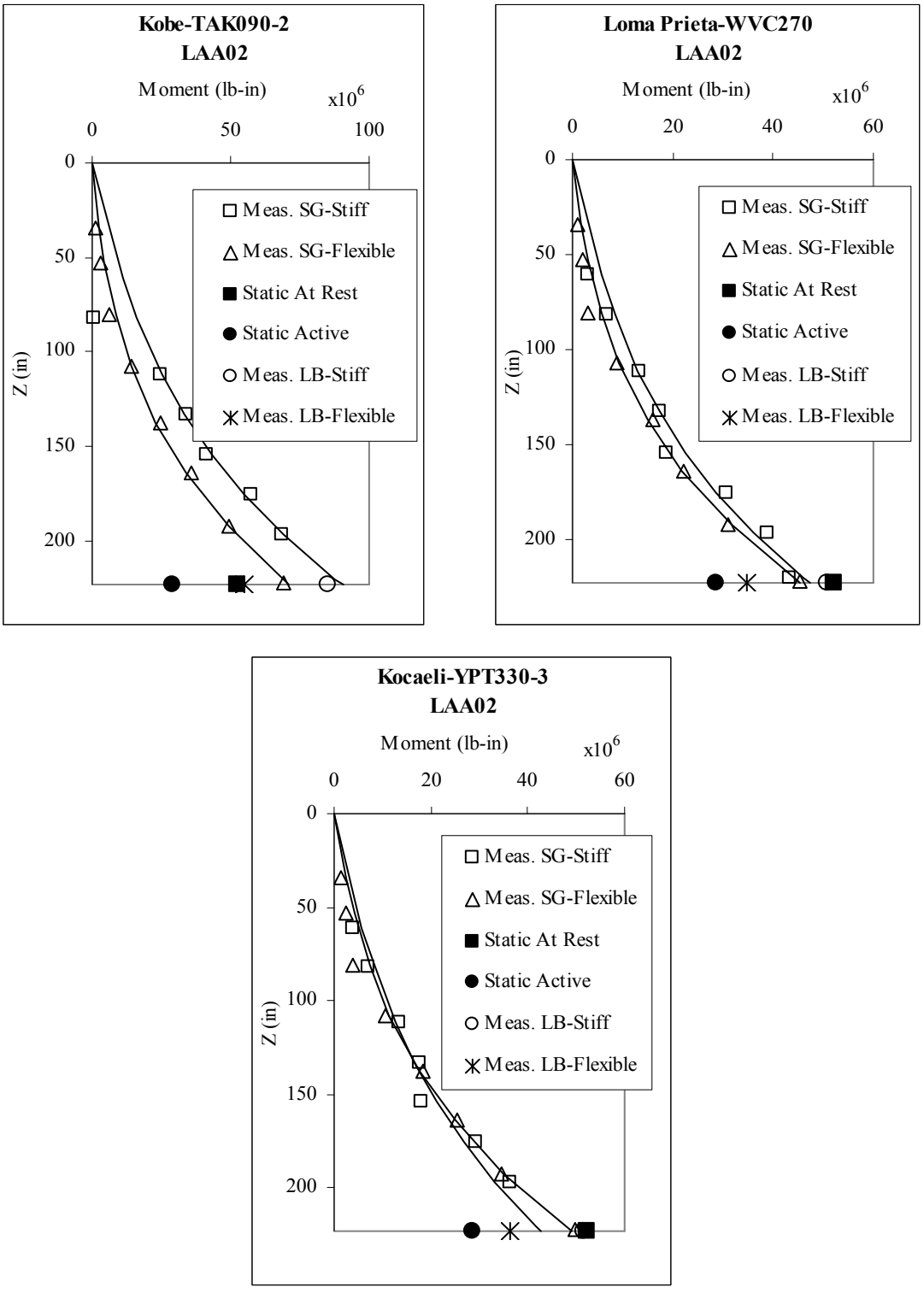

Fig. A.45 Maximum total earth pressure moment profiles interpreted from strain gage and force-sensing bolt measurements and static active and at-rest moment estimates on south stiff and north flexible walls for Kobe-TAK090-2, Loma Prieta-WVC270, and Kocaeli-YPT330-3 for LAA02.

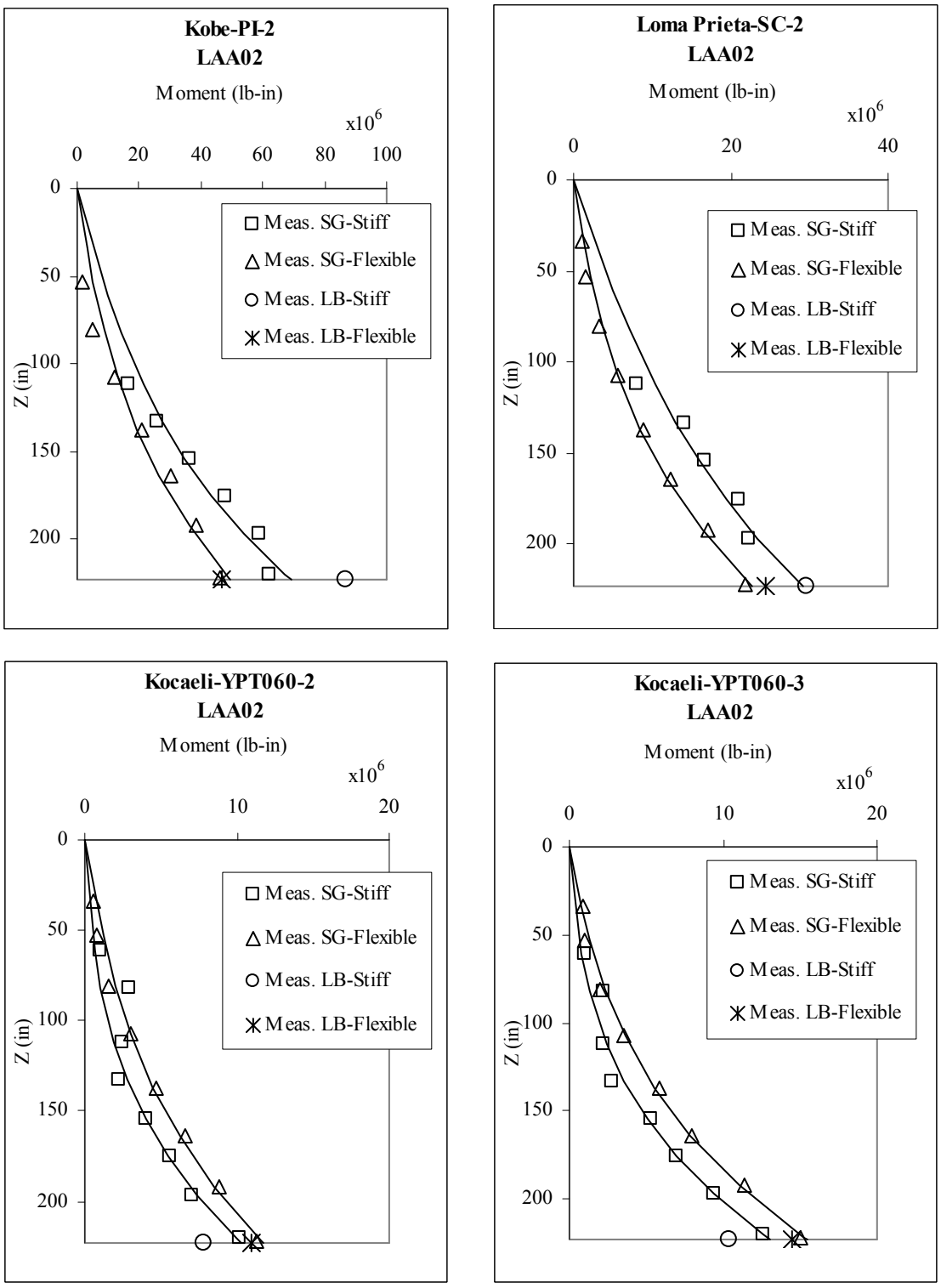

Fig. A.46 Maximum dynamic earth pressure moment profiles interpreted from strain gage and force-sensing bolt measurements on south stiff and north flexible walls for Kobe-PI-2, Loma Prieta-SC-2, and Kocaeli-YPT060-2 and 3 for LAA0.

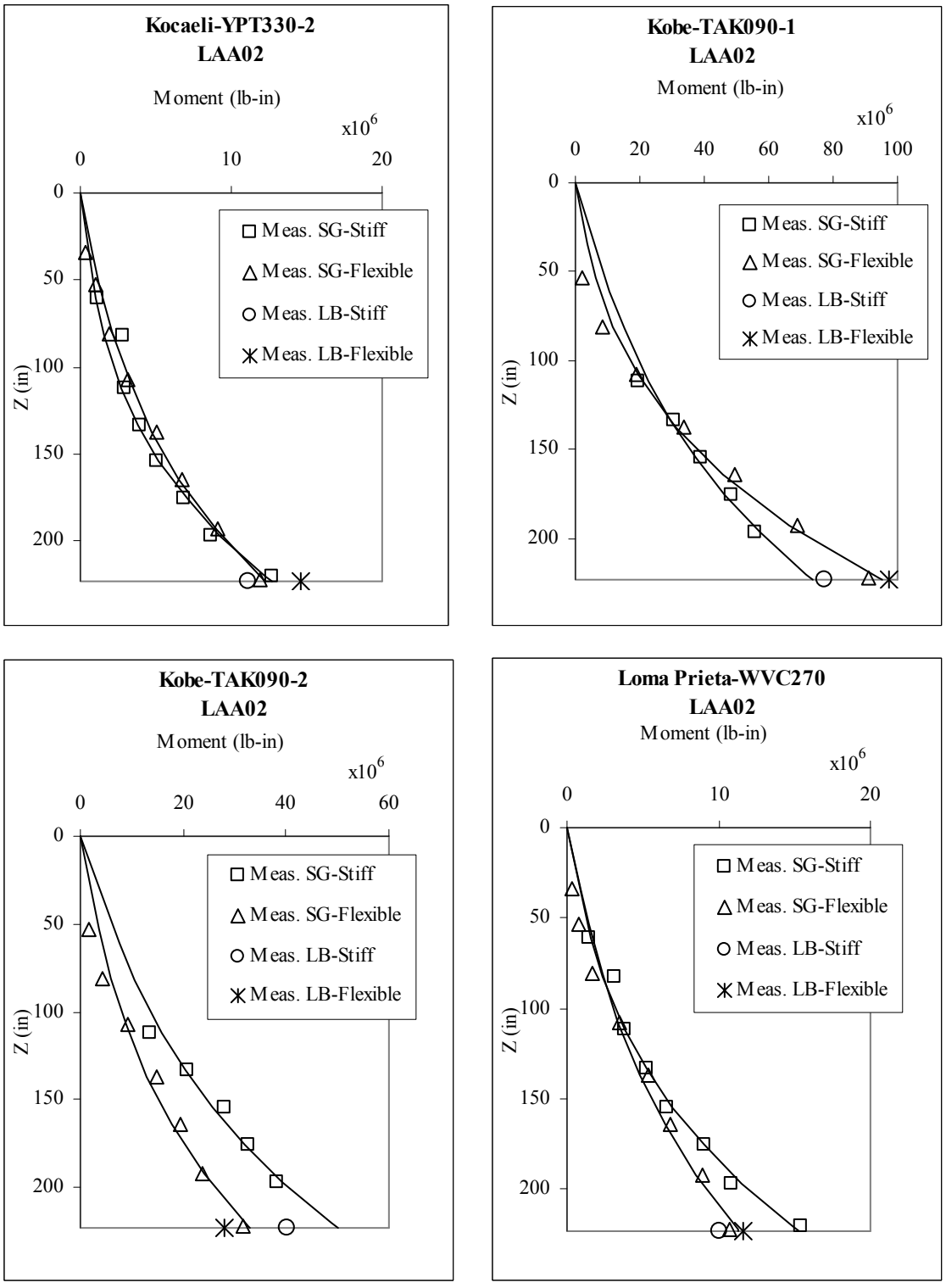

Fig. A.47 Maximum dynamic earth pressure moment profiles interpreted from strain gage and force-sensing bolt measurements on south stiff and north flexible walls for Kocaeli-YPT330-2, Kobe-TAK090-1 and 2, and Loma Prieta-WVC270 for LAA02.

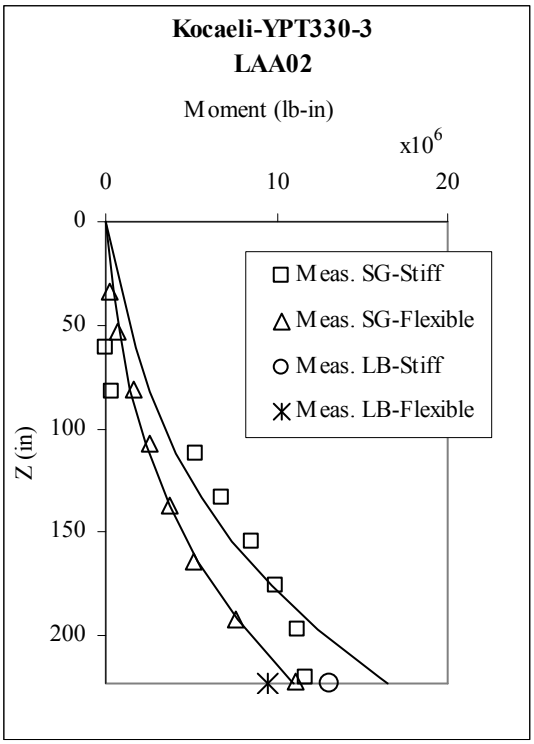

Fig. A.48 Maximum dynamic earth pressure moment profiles interpreted from strain gage and force-sensing bolt measurements on south stiff and north flexible walls for Kocaeli-YPT330-3 for LAA02.

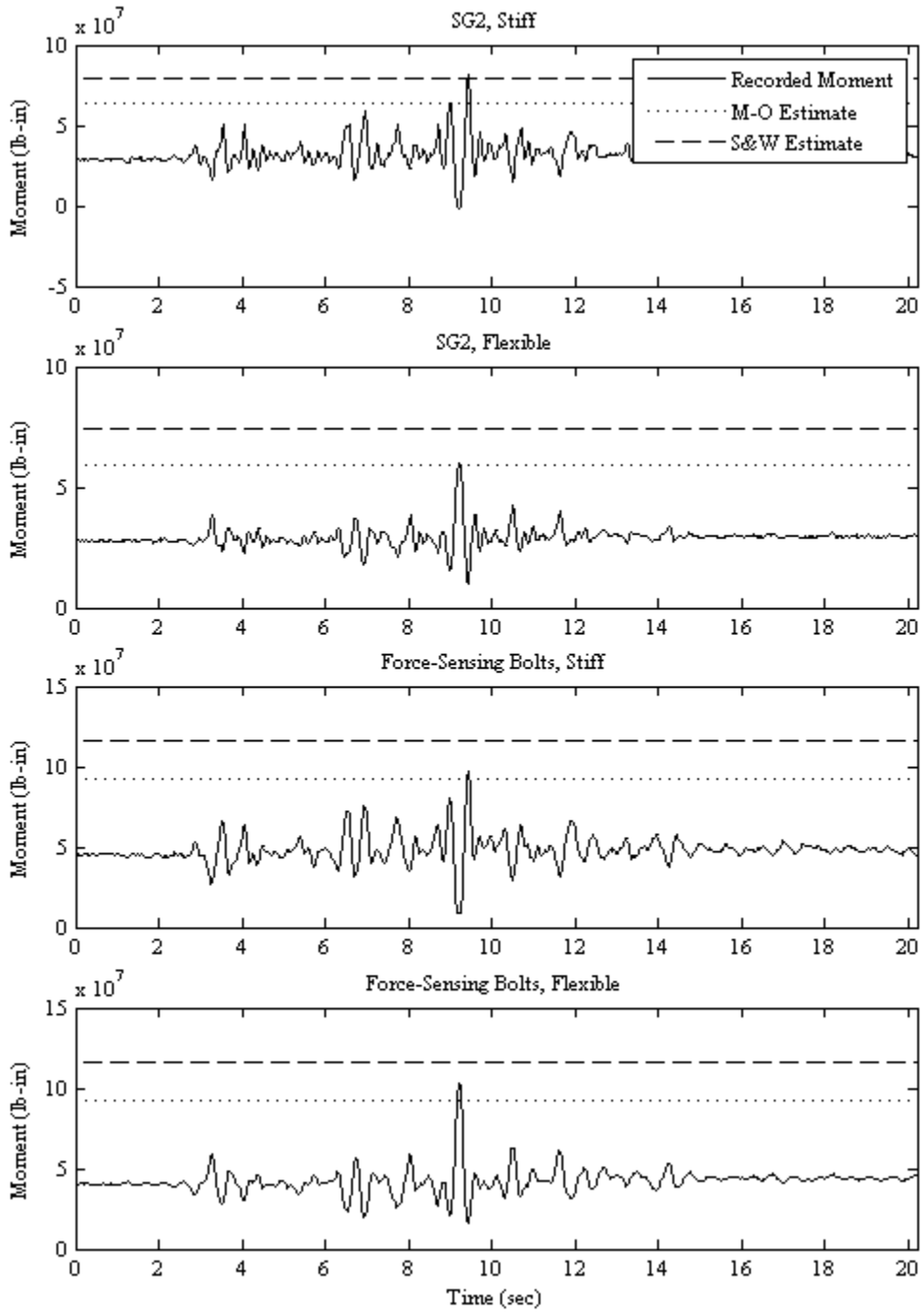

Fig. A.49 Comparison of total wall moment time series, recorded at SG2 on south stiff and north flexible walls and by force-sensing bolts, with M-O and Seed and Whitman (1970) moment estimates for Loma Prieta-2, LAA01.

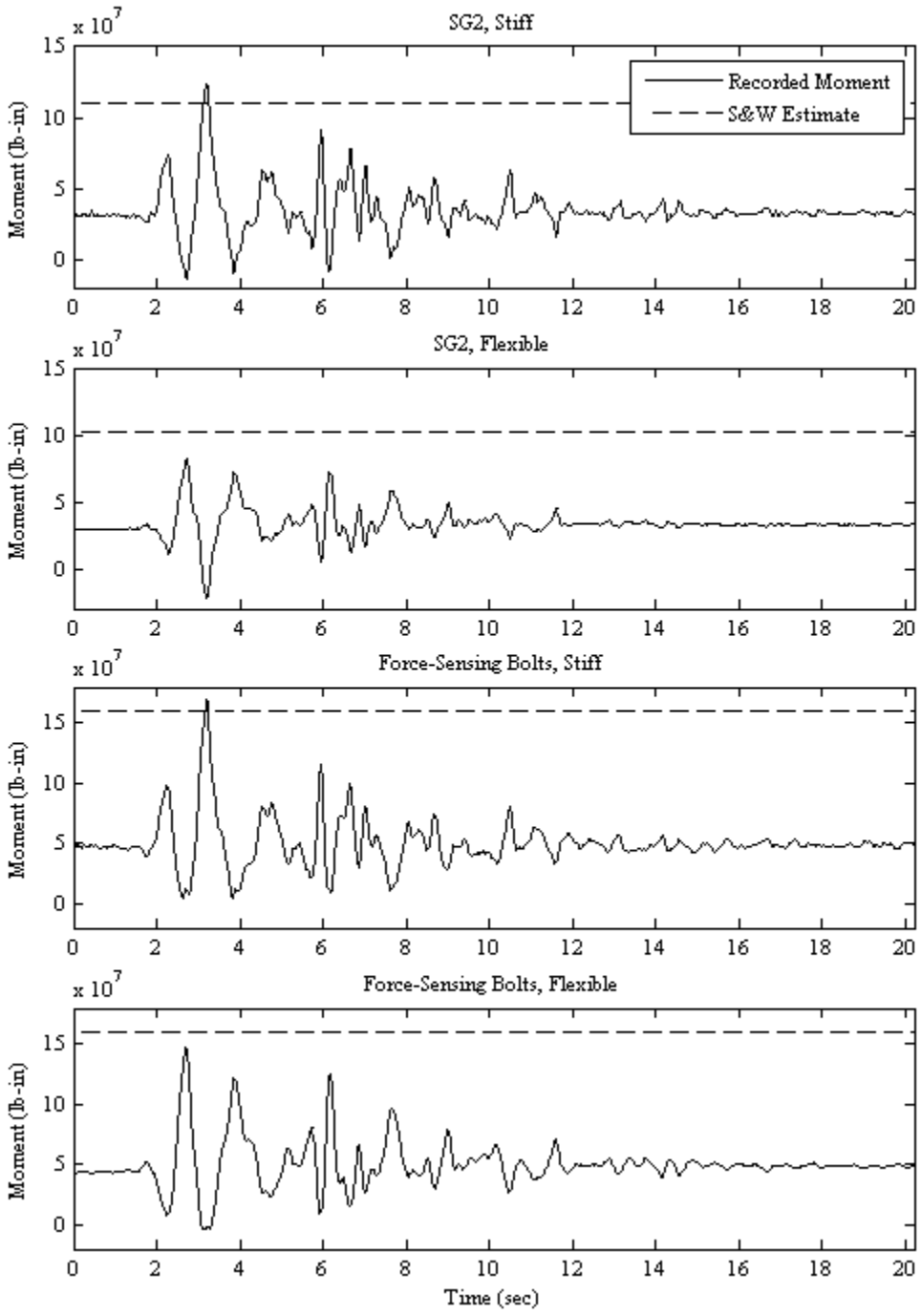

Fig. A.50 Comparison of total wall moment time series, recorded at SG2 on south stiff and north flexible walls and by force-sensing bolts, with M-O and Seed and Whitman (1970) moment estimates for Kobe, LAA01.

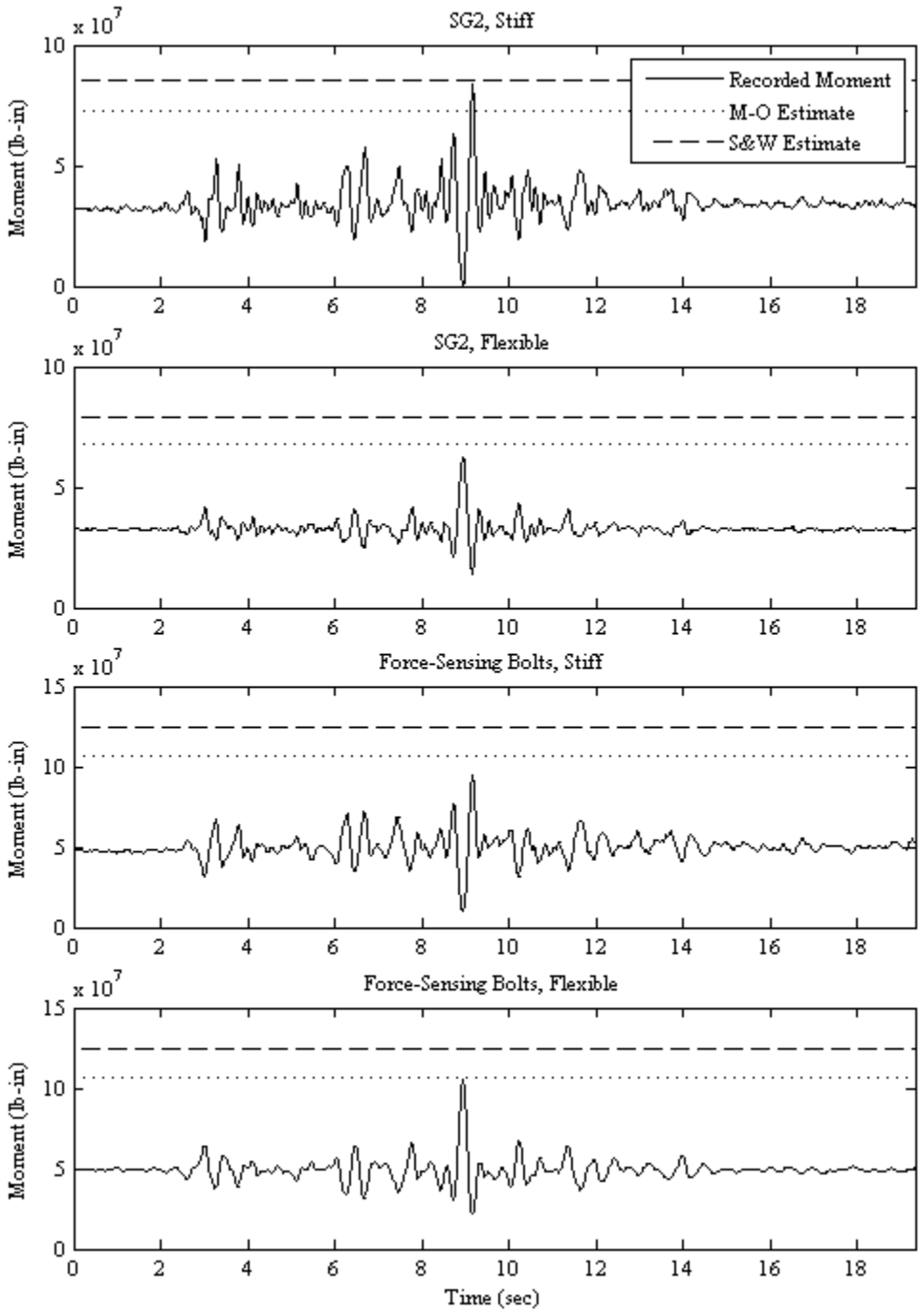

Fig. A.51 Comparison of total wall moment time series, recorded at SG2 on south stiff and north flexible walls and by force-sensing bolts, with M-O and Seed and Whitman (1970) moment estimates for Loma Prieta-3, LAA01.

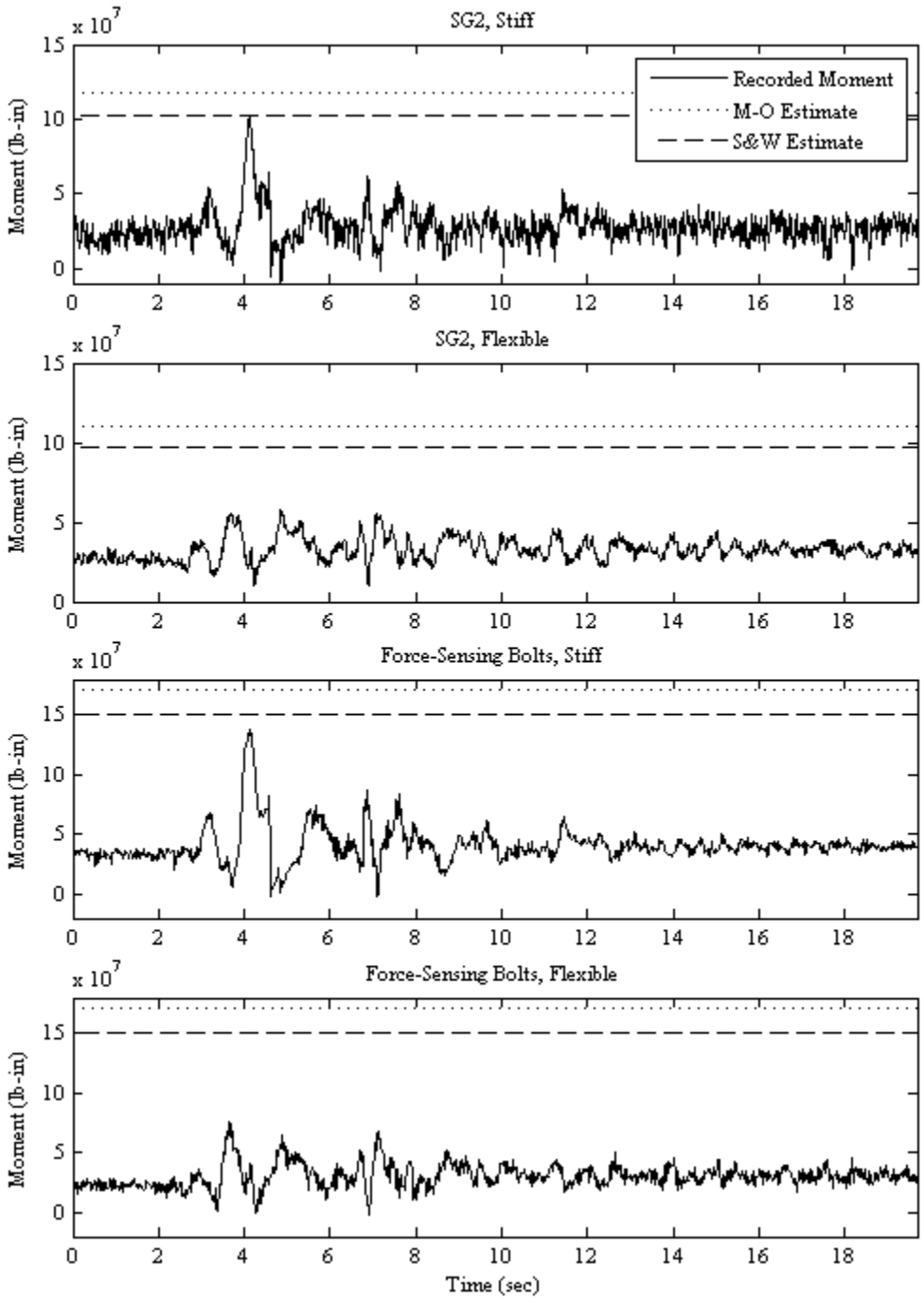

Fig. A.52 Comparison of total earth pressure moment time series, recorded at SG2 on south stiff and north flexible walls and by force-sensing bolts, with M-O and Seed and Whitman (1970) moment estimates for Kobe-PI-1, LAA02.

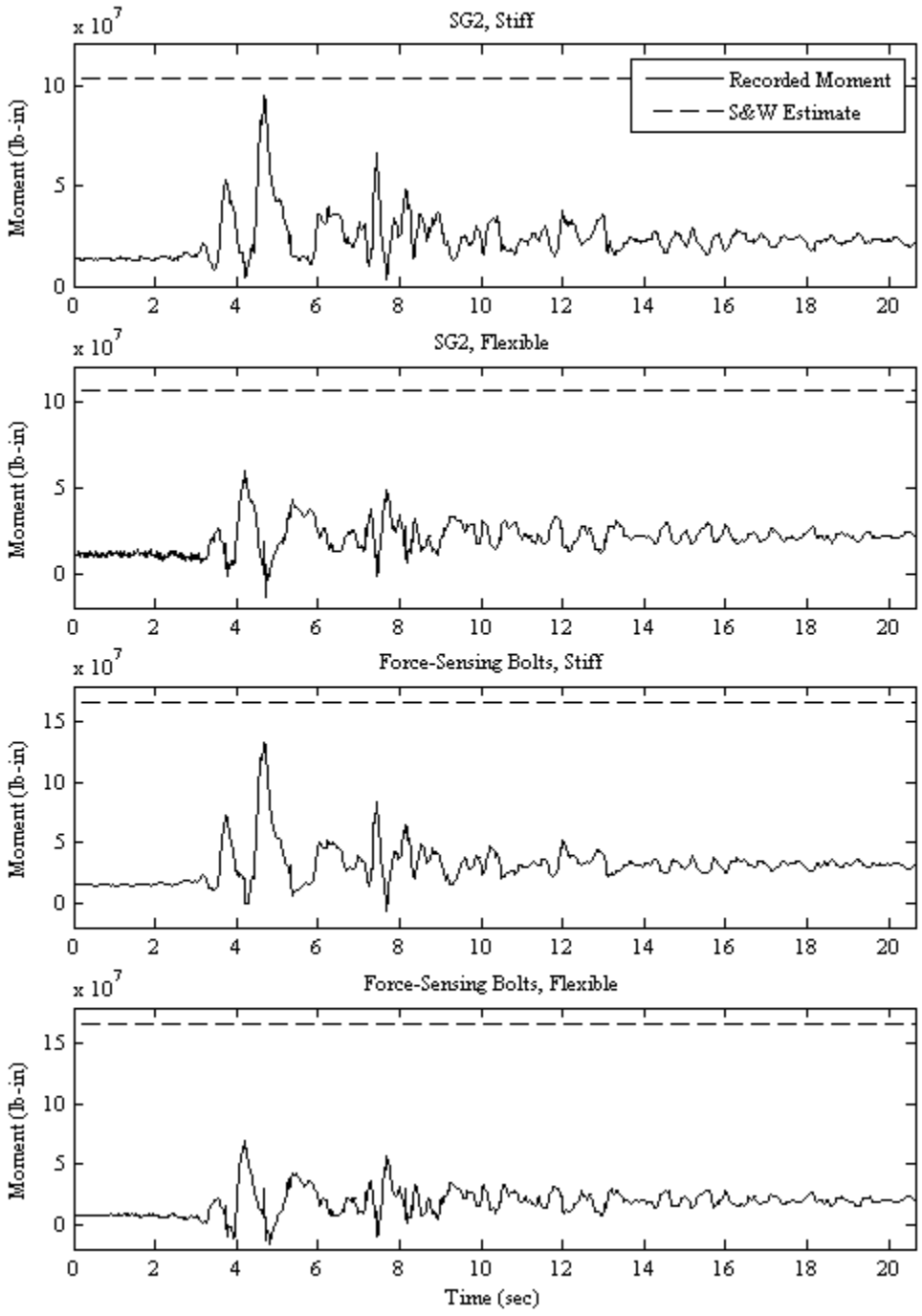

Fig. A.53 Comparison of total earth pressure moment time series, recorded at SG2 on south stiff and north flexible walls and by force-sensing bolts, with M-O and Seed and Whitman (1970) moment estimates for Kobe-PI-2, LAA02.

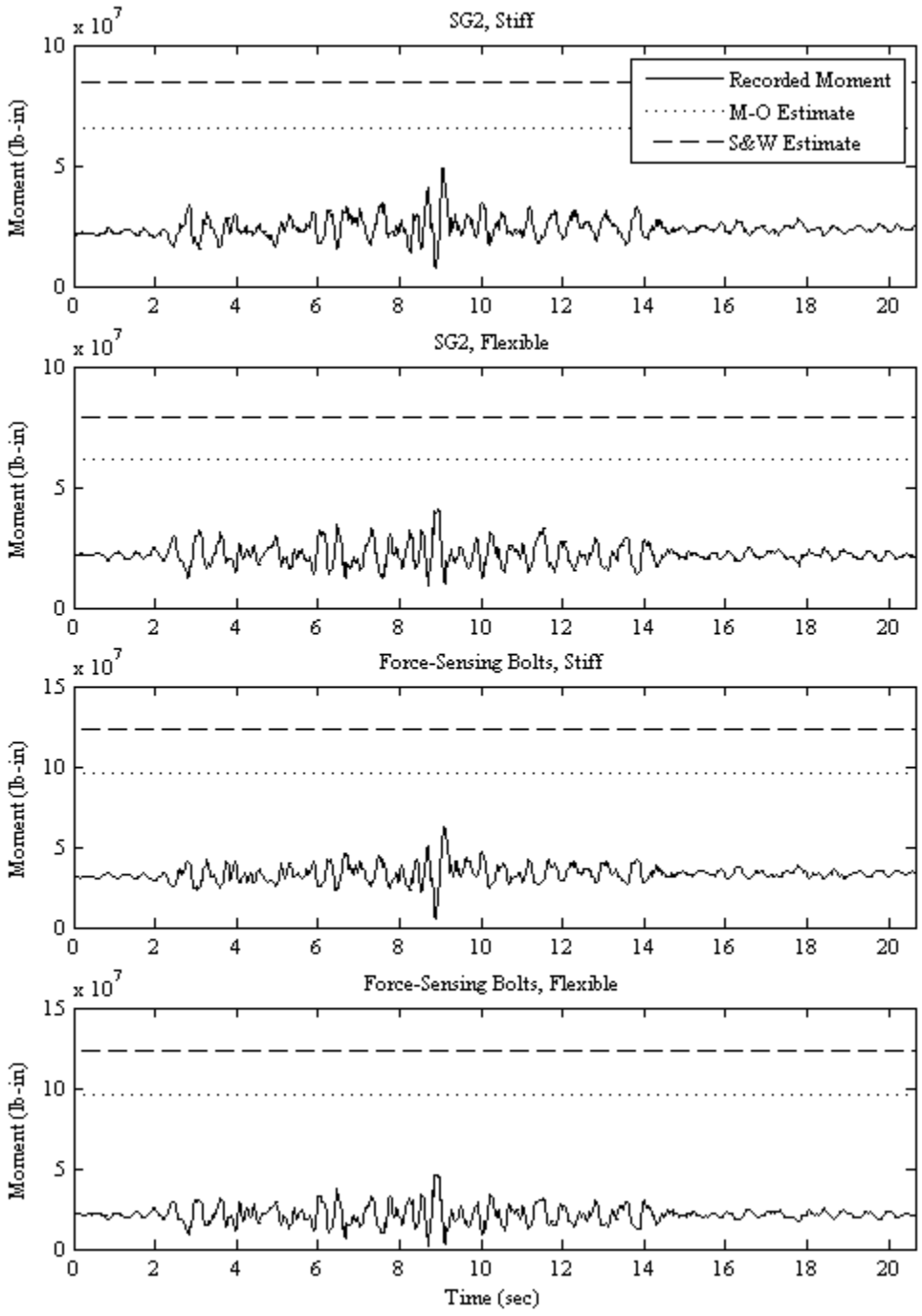

Fig. A.54 Comparison of total earth pressure moment time series, recorded at SG2 on south stiff and north flexible walls and by force-sensing bolts, with M-O and Seed and Whitman (1970) moment estimates for Loma Prieta-SC-2, LAA02.

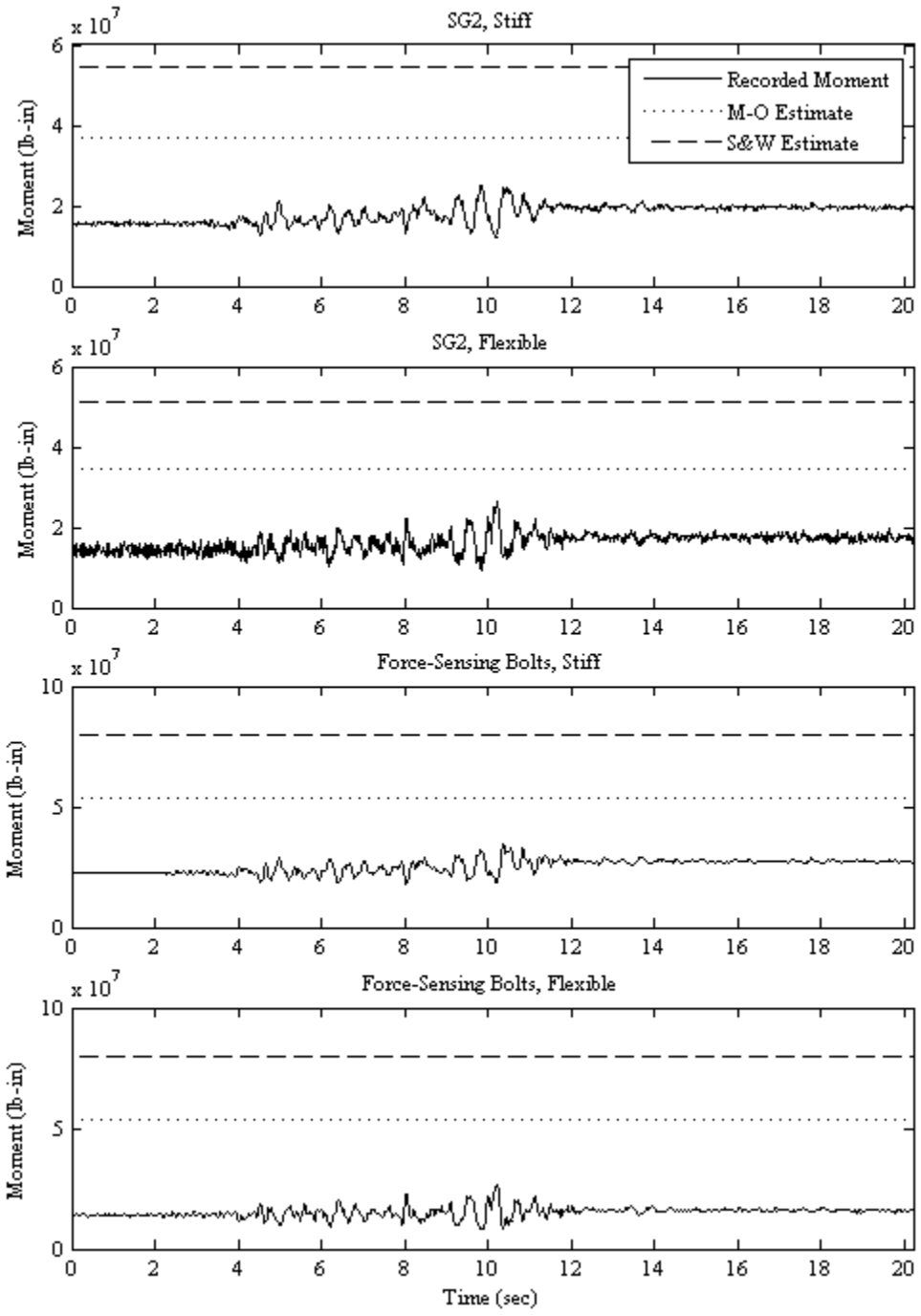

Fig. A.55 Comparison of total earth pressure moment time series, recorded at SG2 on south stiff and north flexible walls and by force-sensing bolts, with M-O and Seed and Whitman (1970) moment estimates for Kocaeli-YPT060-2, LAA02.

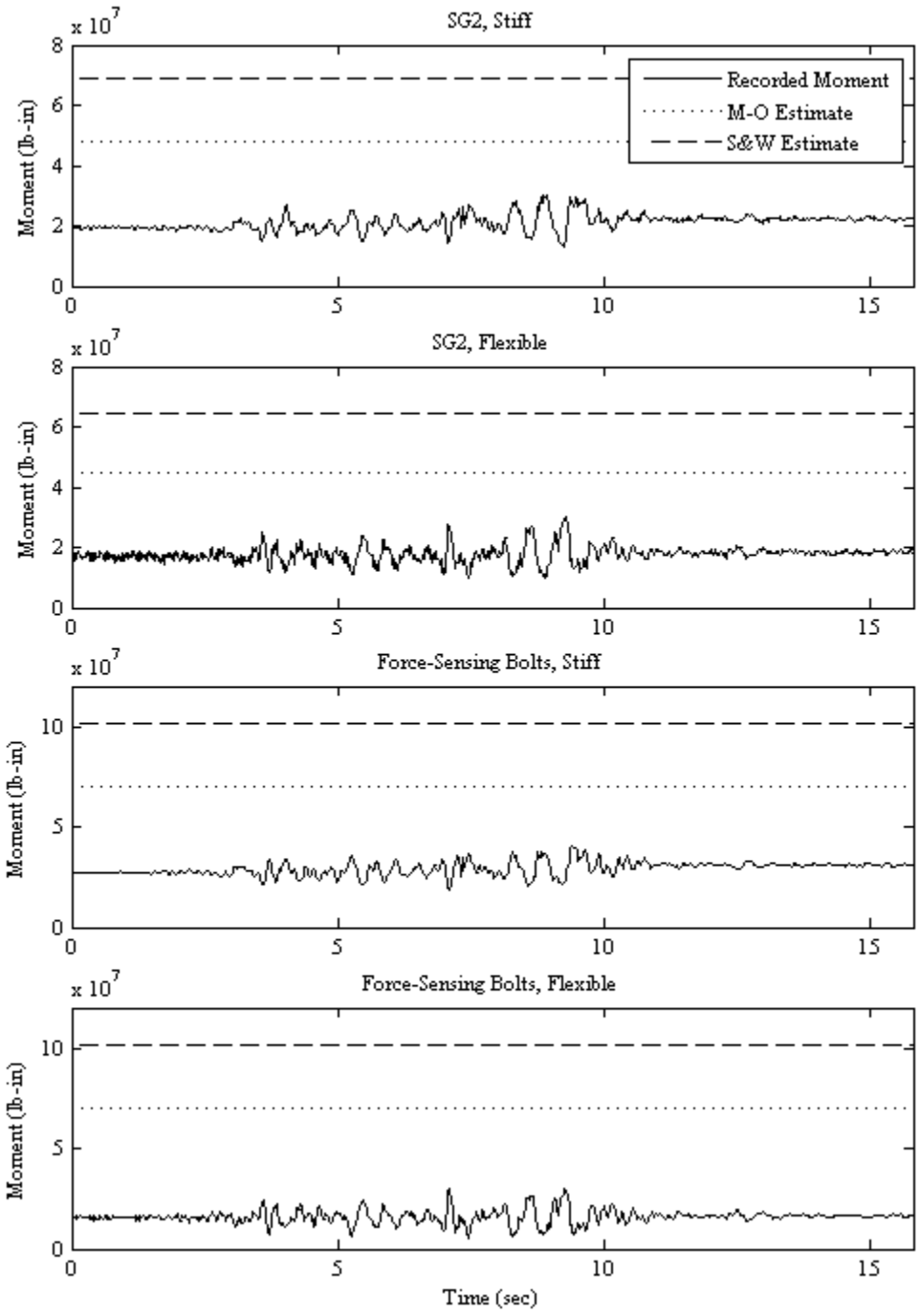

Fig. A.56 Comparison of total earth pressure moment time series, recorded at SG2 on south stiff and north flexible walls and by force-sensing bolts, with M-O and Seed and Whitman (1970) moment estimates for Kocaeli-YPT060-3, LAA02.

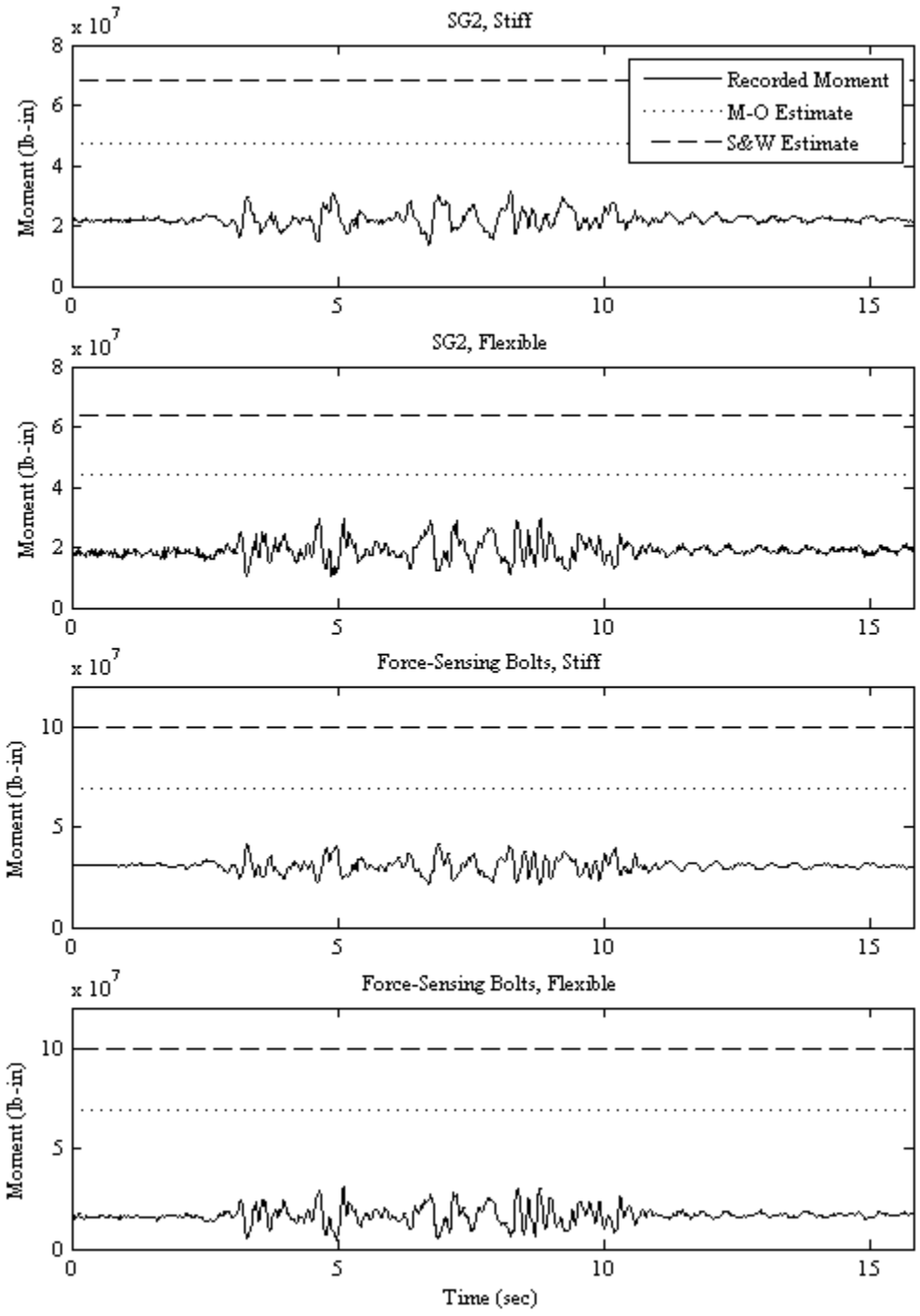

Fig. A.57 Comparison of total earth pressure moment time series, recorded at SG2 on south stiff and north flexible walls and by force-sensing bolts, with M-O and Seed and Whitman (1970) moment estimates for Kocaeli-YPT330-2, LAA02.

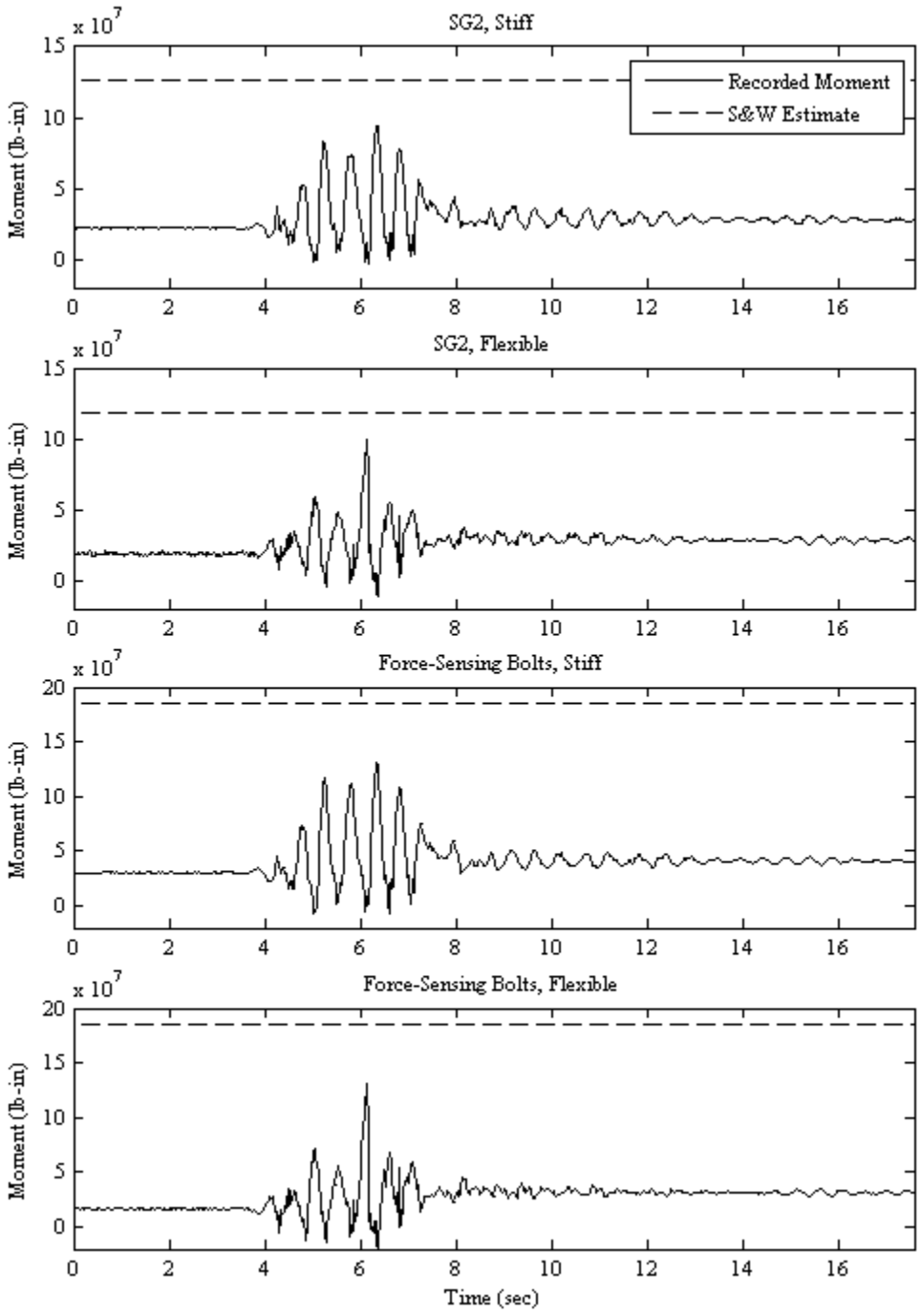

Fig. A.58 Comparison of total earth pressure moment time series, recorded at SG2 on south stiff and north flexible walls and by force-sensing bolts, with M-O and Seed and Whitman (1970) moment estimates for Kobe-TAK090-1, LAA02.

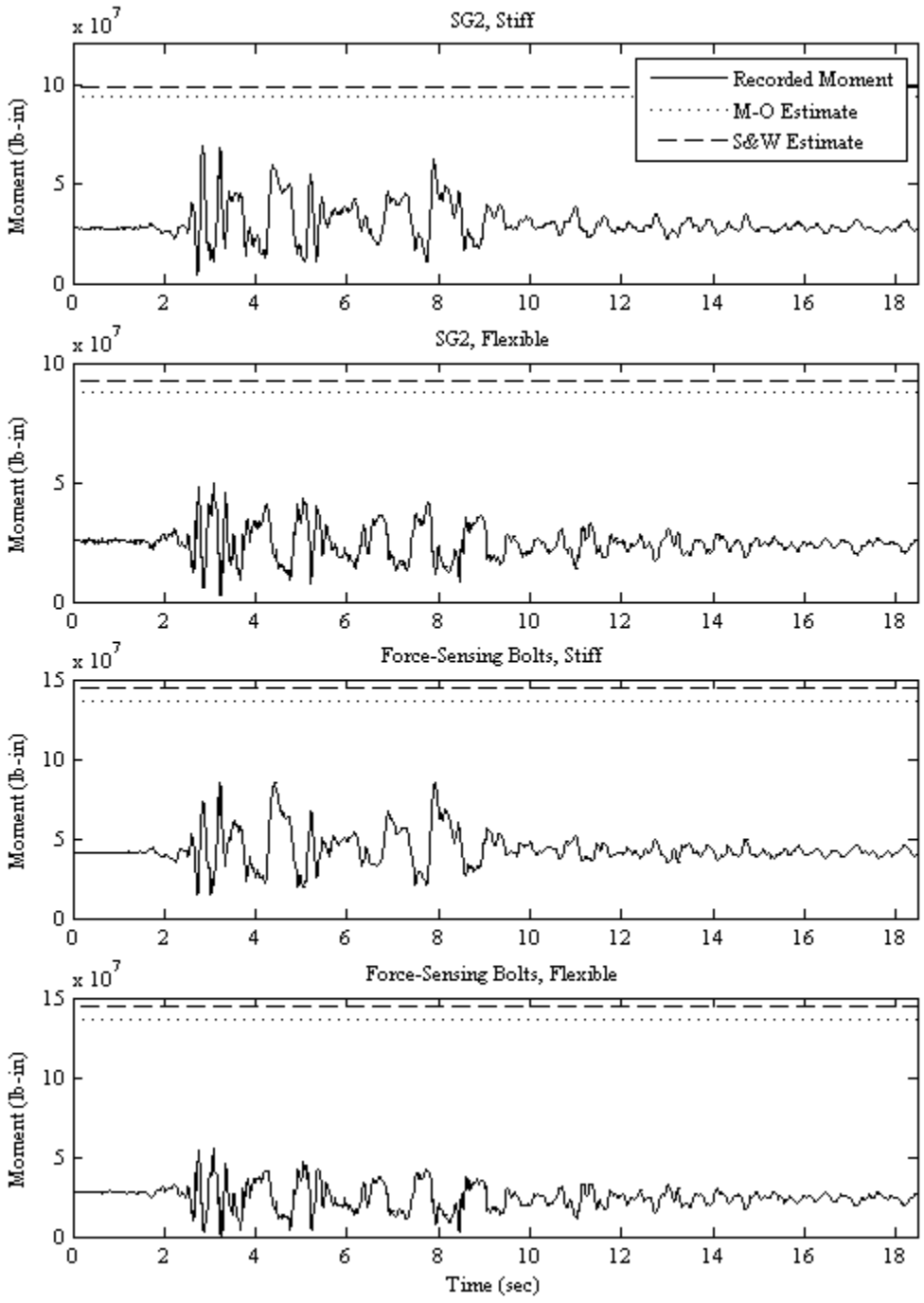

Fig. A.59 Comparison of total earth pressure moment time series, recorded at SG2 on south stiff and north flexible walls and by force-sensing bolts, with M-O and Seed and Whitman (1970) moment estimates for Kobe-TAK090-2, LAA02.

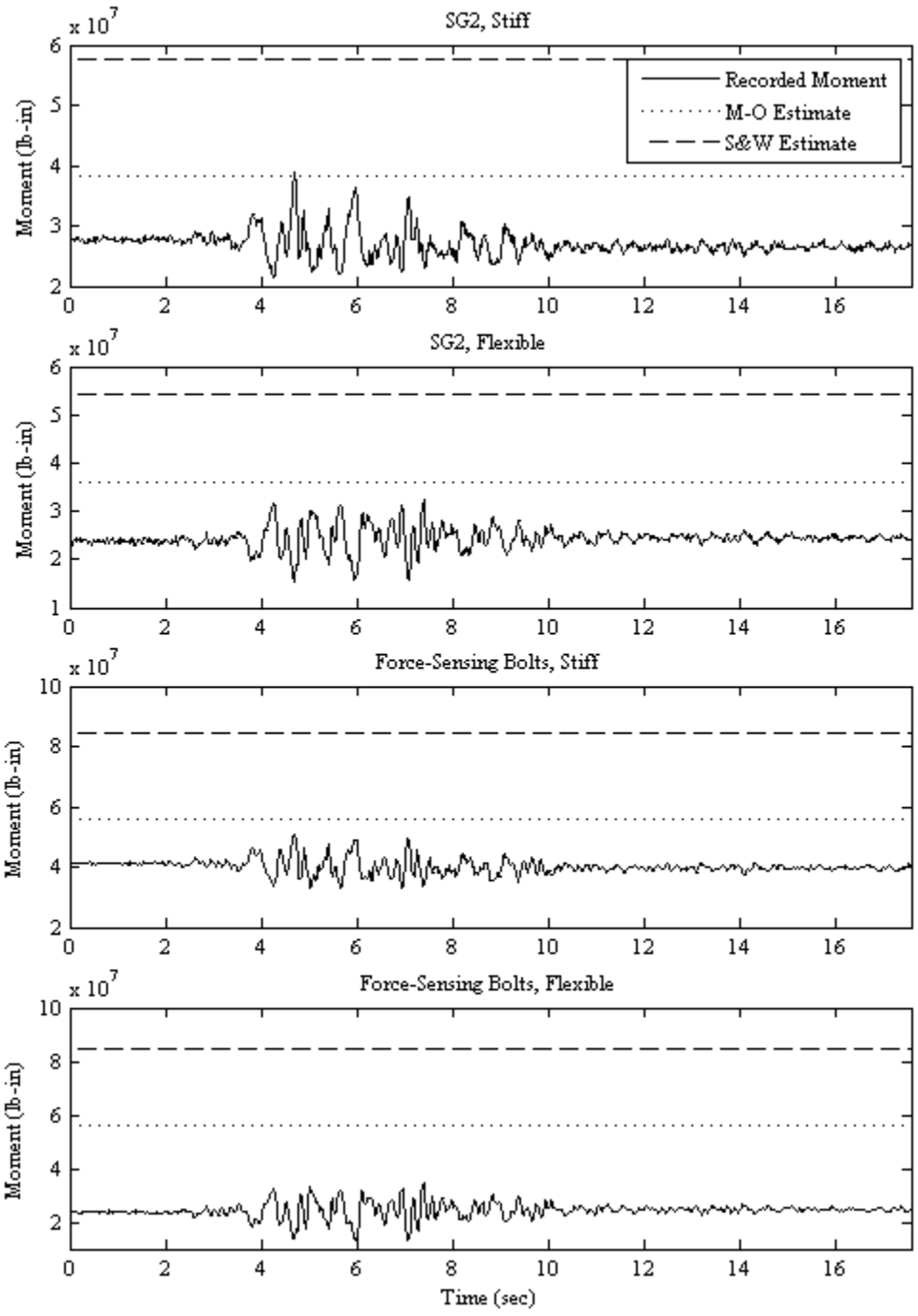

Fig. A.60 Comparison of total earth pressure moment time series, recorded at SG2 on south stiff and north flexible walls and by force-sensing bolts, with M-O and Seed and Whitman (1970) moment estimates for Loma Prieta-WVC270, LAA02.

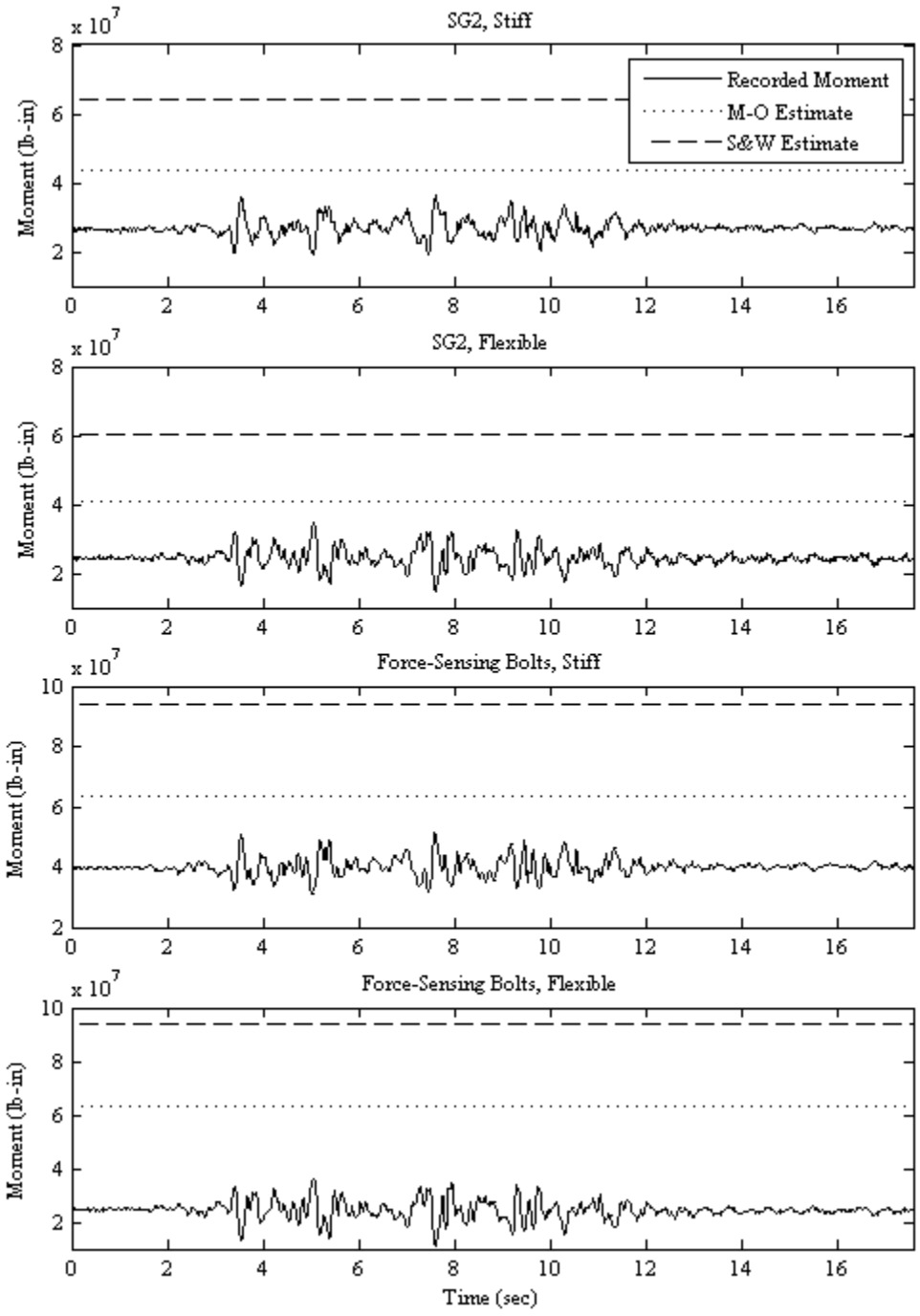

Fig. A.61 Comparison of total earth pressure moment time series, recorded at SG2 on south stiff and north flexible walls and by force-sensing bolts, with M-O and Seed and Whitman (1970) moment estimates for Kocaeli-YPT330-3, LAA02.

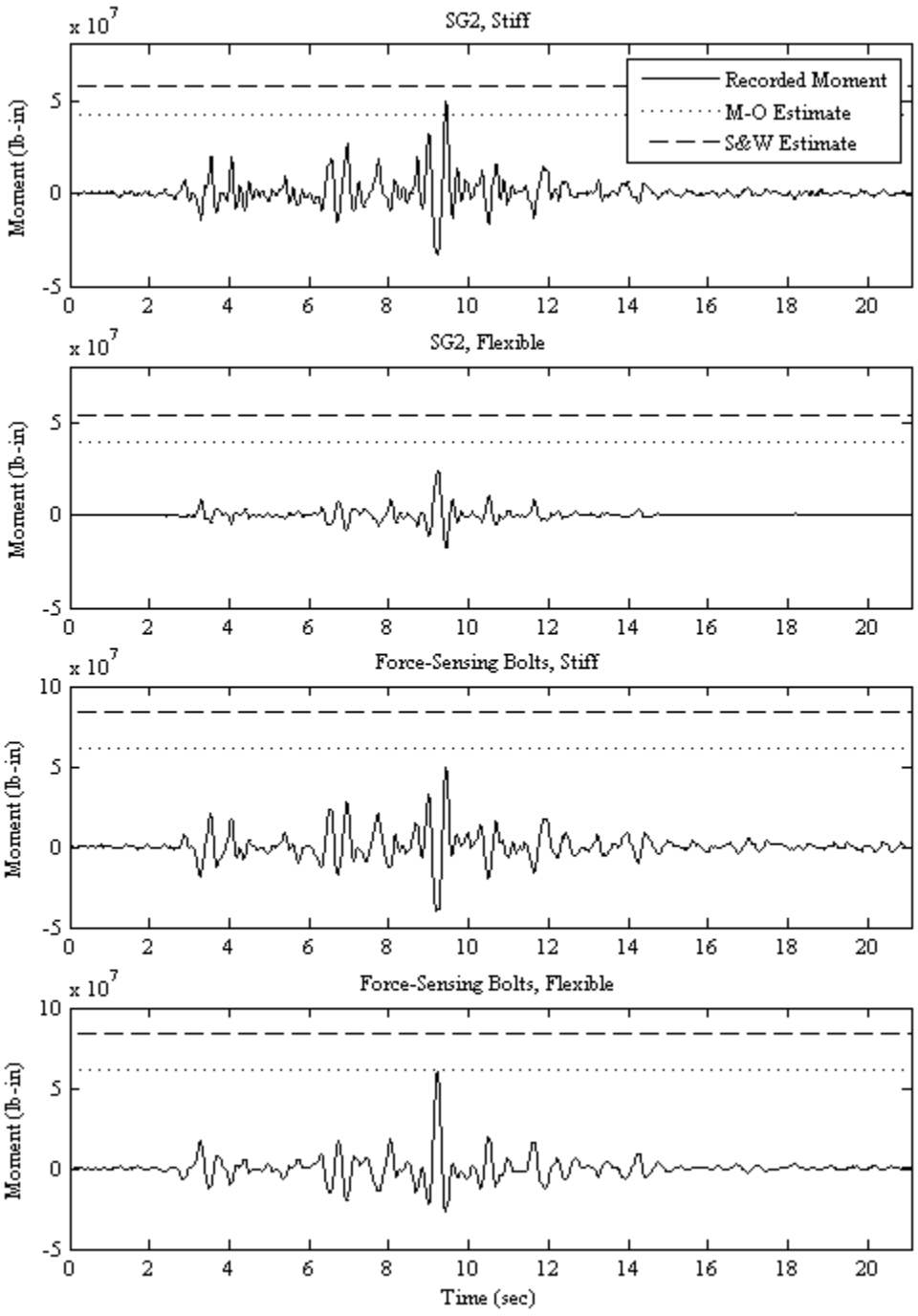

Fig. A.62 Comparison of dynamic wall moment time series, recorded at SG2 on south stiff and north flexible walls and by force-sensing bolts, with M-O and Seed and Whitman (1970) moment estimates for Loma Prieta-2, LAA01.

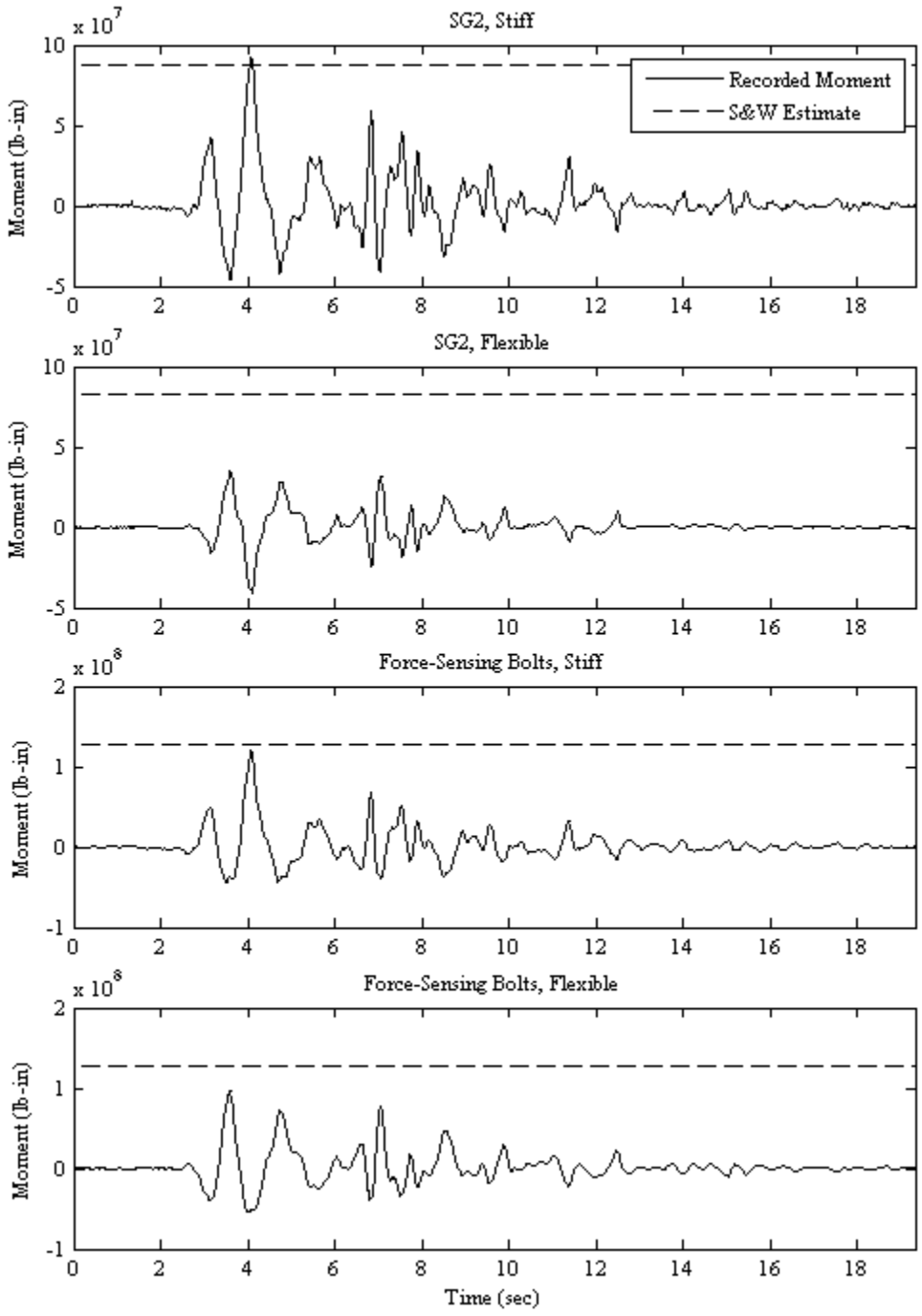

Fig. A.63 Comparison of dynamic wall moment time series, recorded at SG2 on south stiff and north flexible walls and by force-sensing bolts, with M-O and Seed and Whitman (1970) moment estimates for Kobe, LAA01.

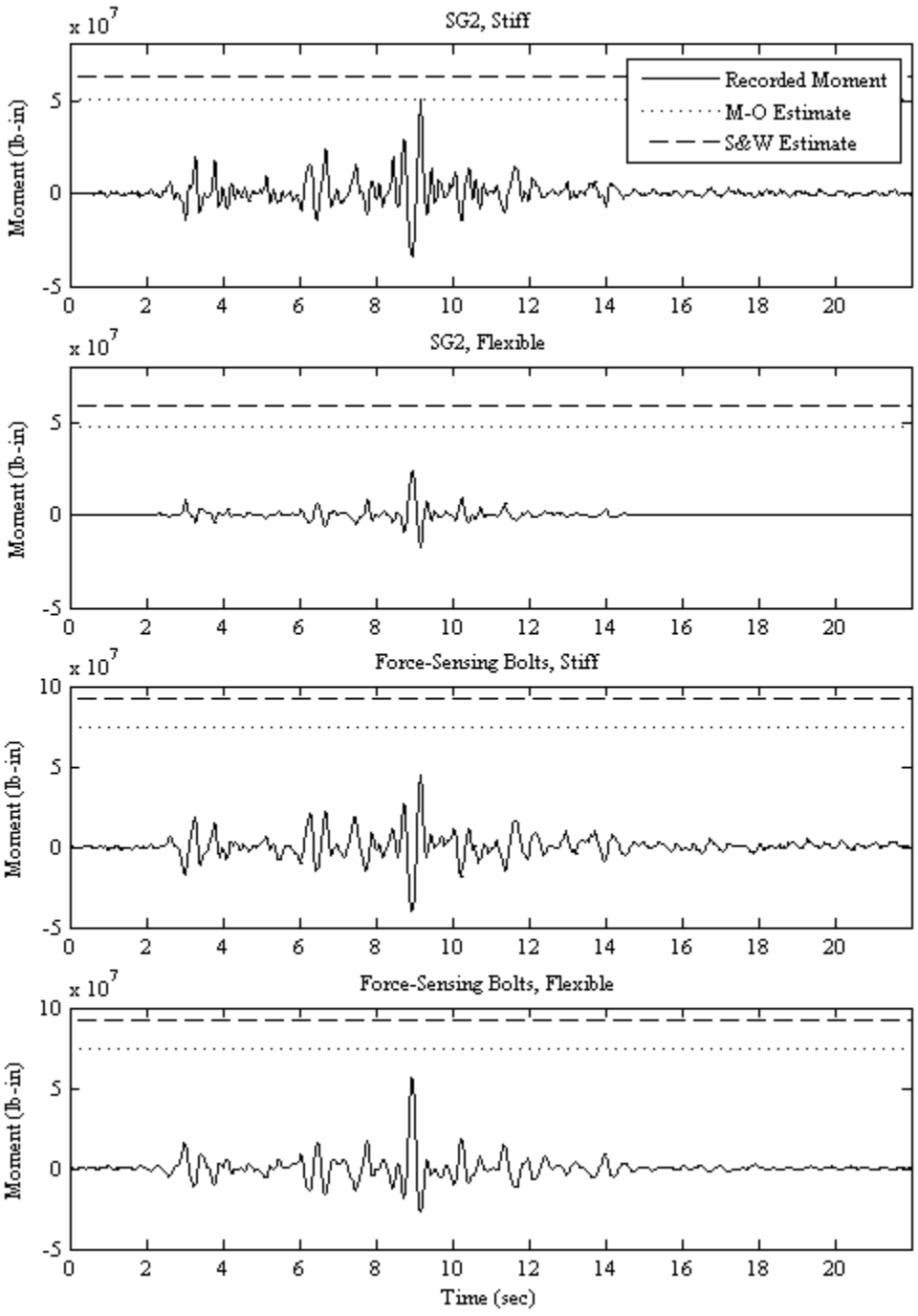

Fig. A.64 Comparison of dynamic wall moment time series, recorded at SG2 on south stiff and north flexible walls and by force-sensing bolts, with M-O and Seed and Whitman (1970) moment estimates for Loma Prieta-3, LAA01.

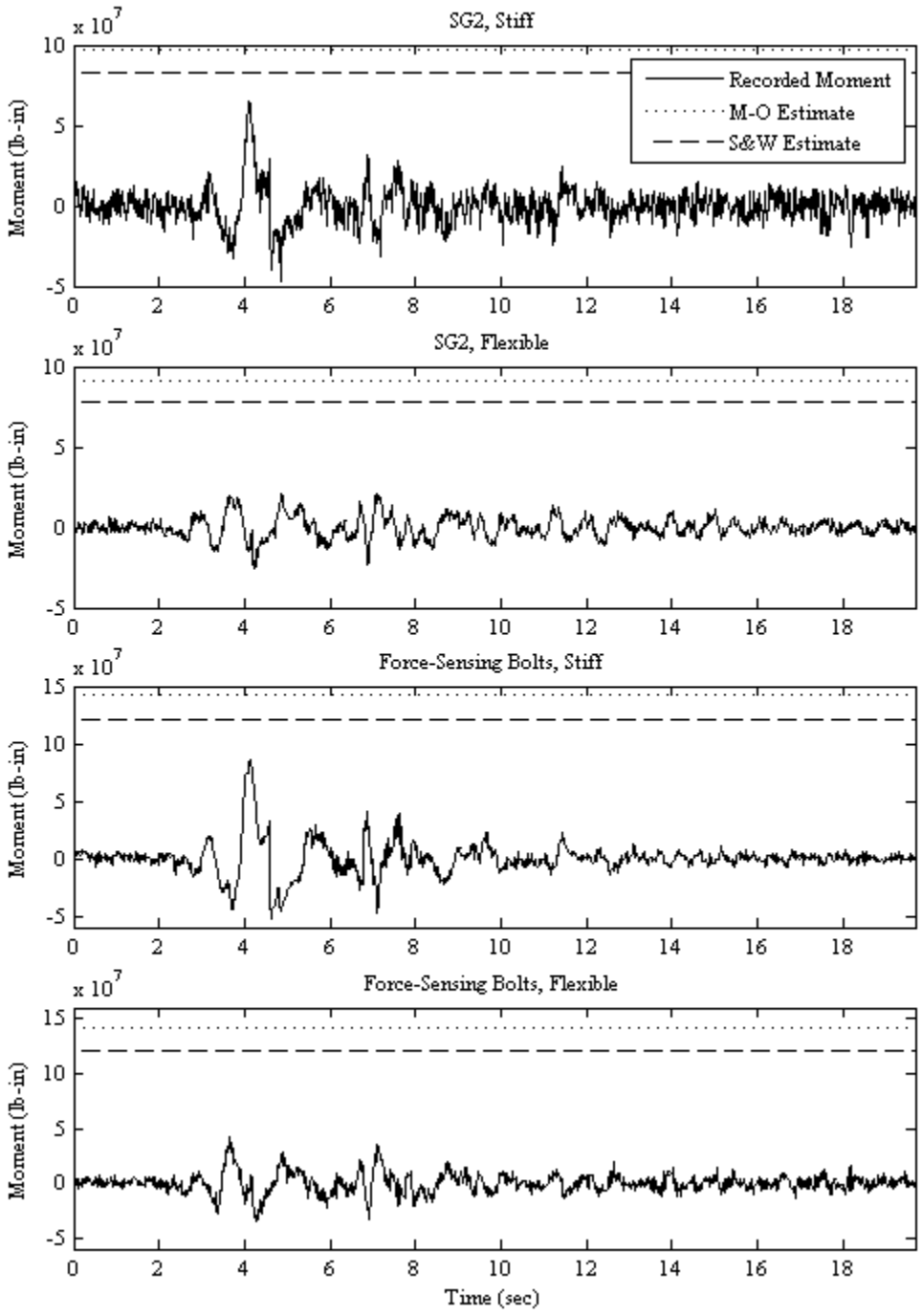

Fig. A.65 Comparison of dynamic earth pressure moment time series, recorded at SG2 on south stiff and north flexible walls and by force-sensing bolts, with M-O and Seed and Whitman (1970) moment estimates for Kobe-PI-1, LAA02.

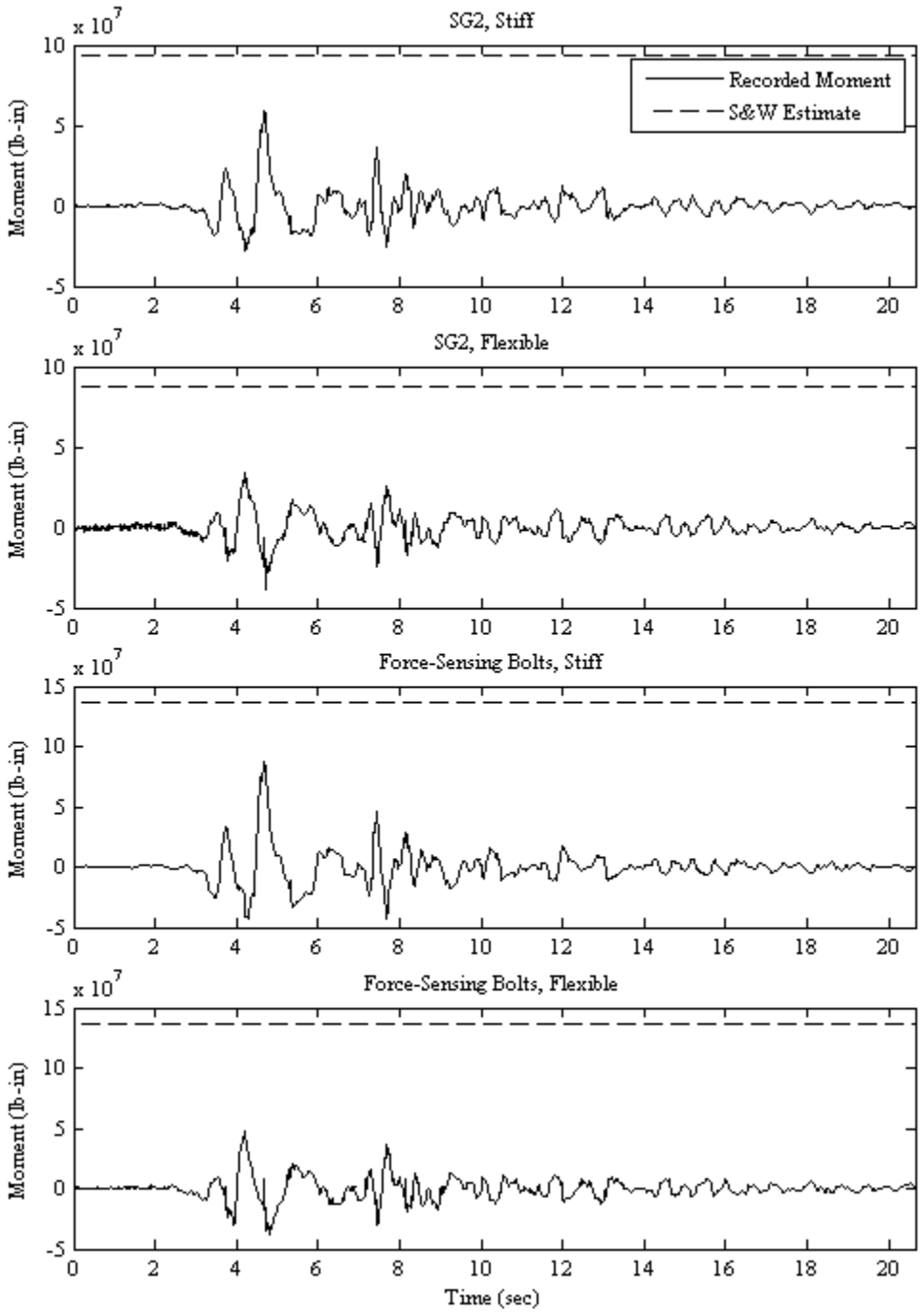

Fig. A.66 Comparison of dynamic earth pressure moment time series, recorded at SG2 on south stiff and north flexible walls and by force-sensing bolts, with M-O and Seed and Whitman (1970) moment estimates for Kobe-PI-2, LAA02.

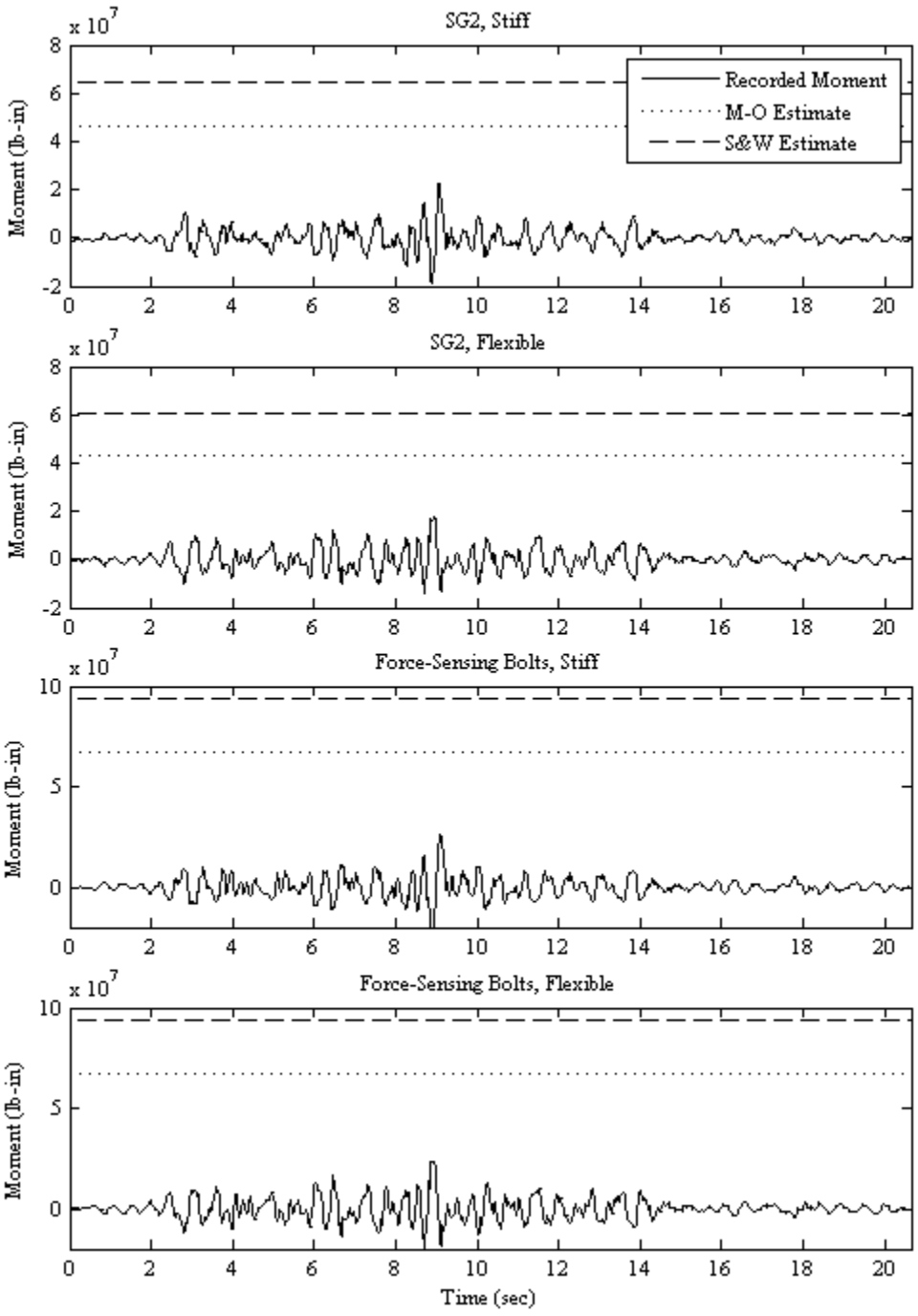

Fig. A.67 Comparison of dynamic earth pressure moment time series, recorded at SG2 on south stiff and north flexible walls and by force-sensing bolts, with M-O and Seed and Whitman (1970) moment estimates for Loma Prieta-SC-2, LAA02.

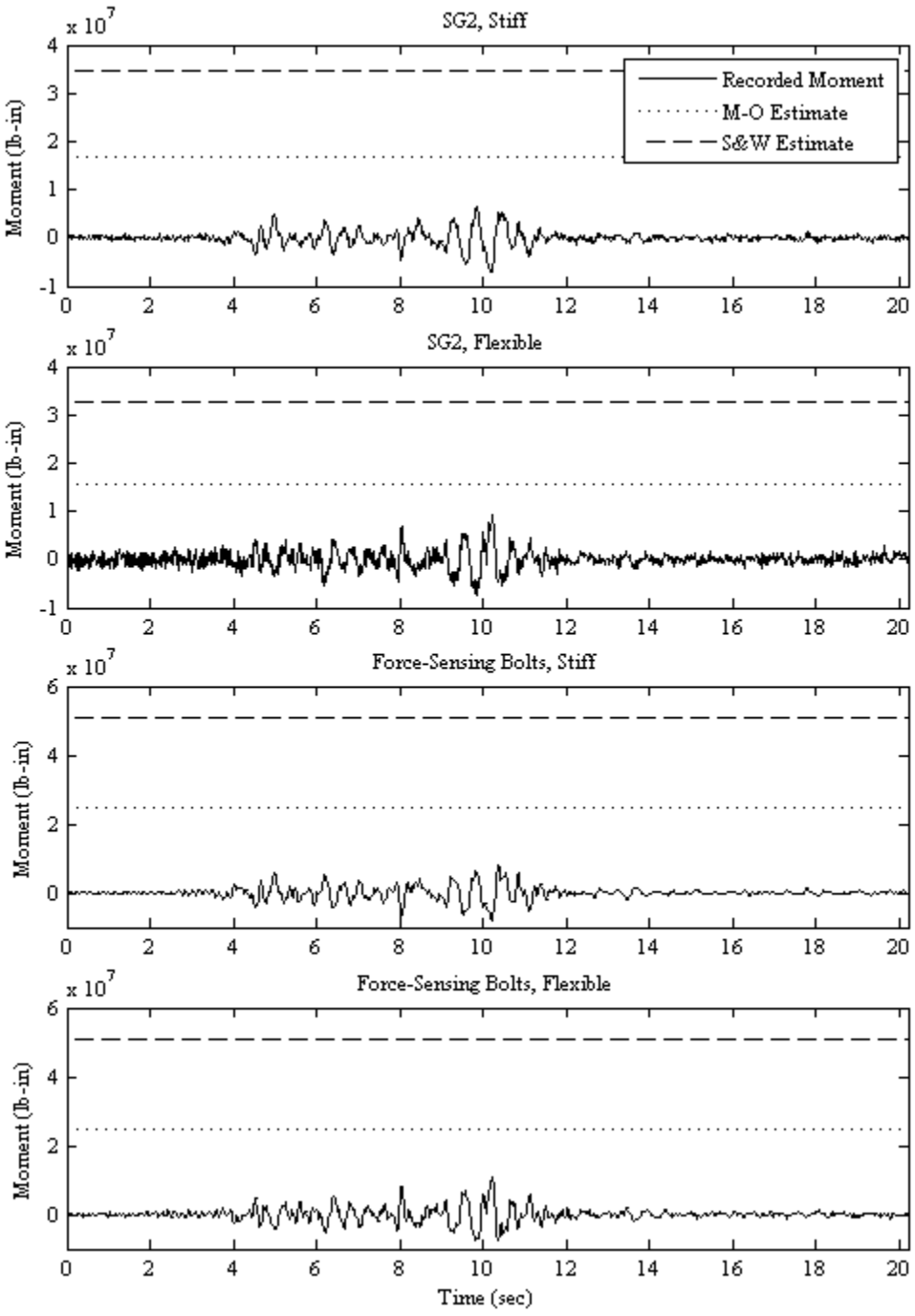

Fig. A.68 Comparison of dynamic earth pressure moment time series, recorded at SG2 on south stiff and north flexible walls and by force-sensing bolts, with M-O and Seed and Whitman (1970) moment estimates for Kocaeli-YPT060-2, LAA02.

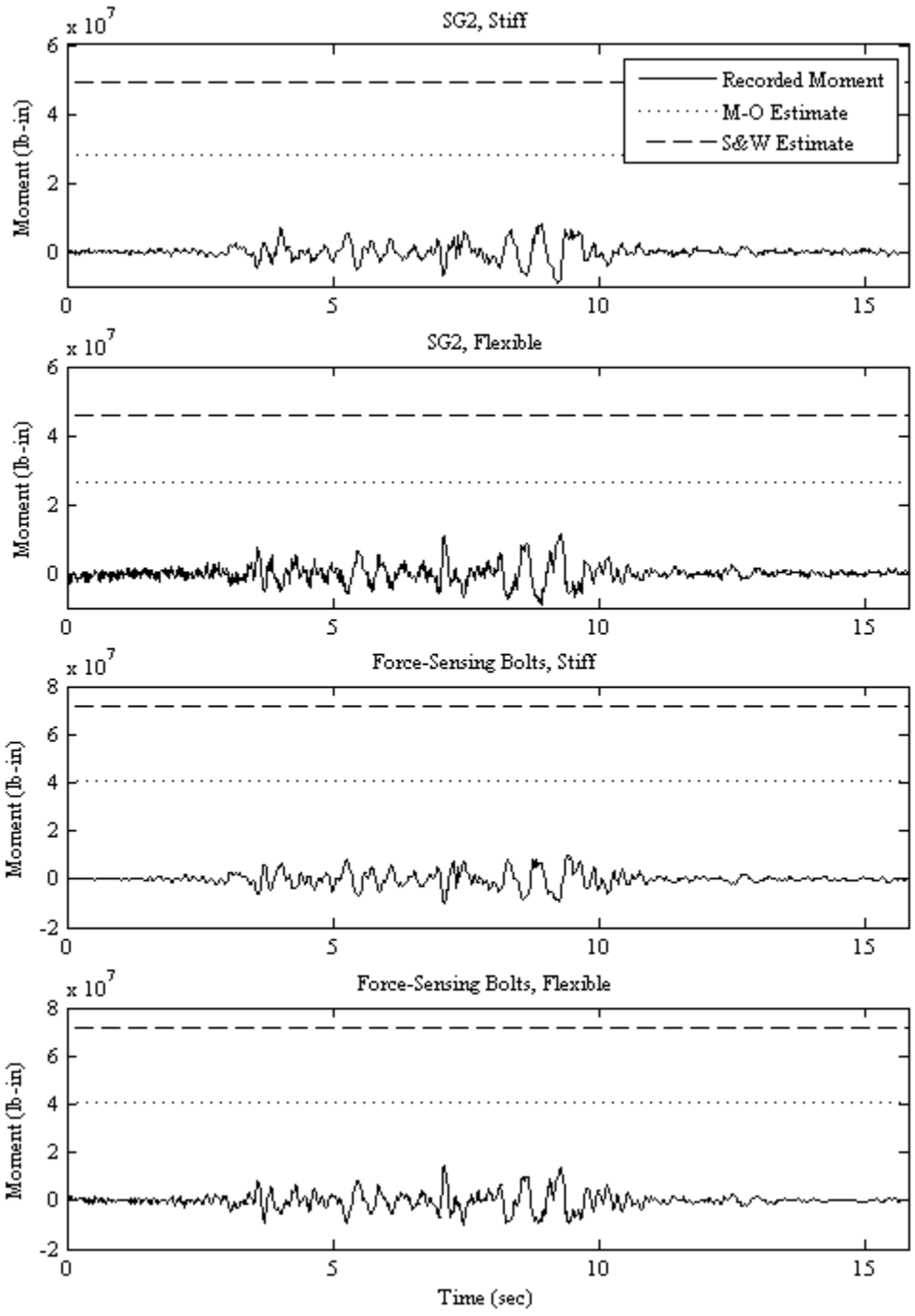

Fig. A.69 Comparison of dynamic earth pressure moment time series, recorded at SG2 on south stiff and north flexible walls and by force-sensing bolts, with M-O and Seed and Whitman (1970) moment estimates for Kocaeli-YPT060-3, LAA02.

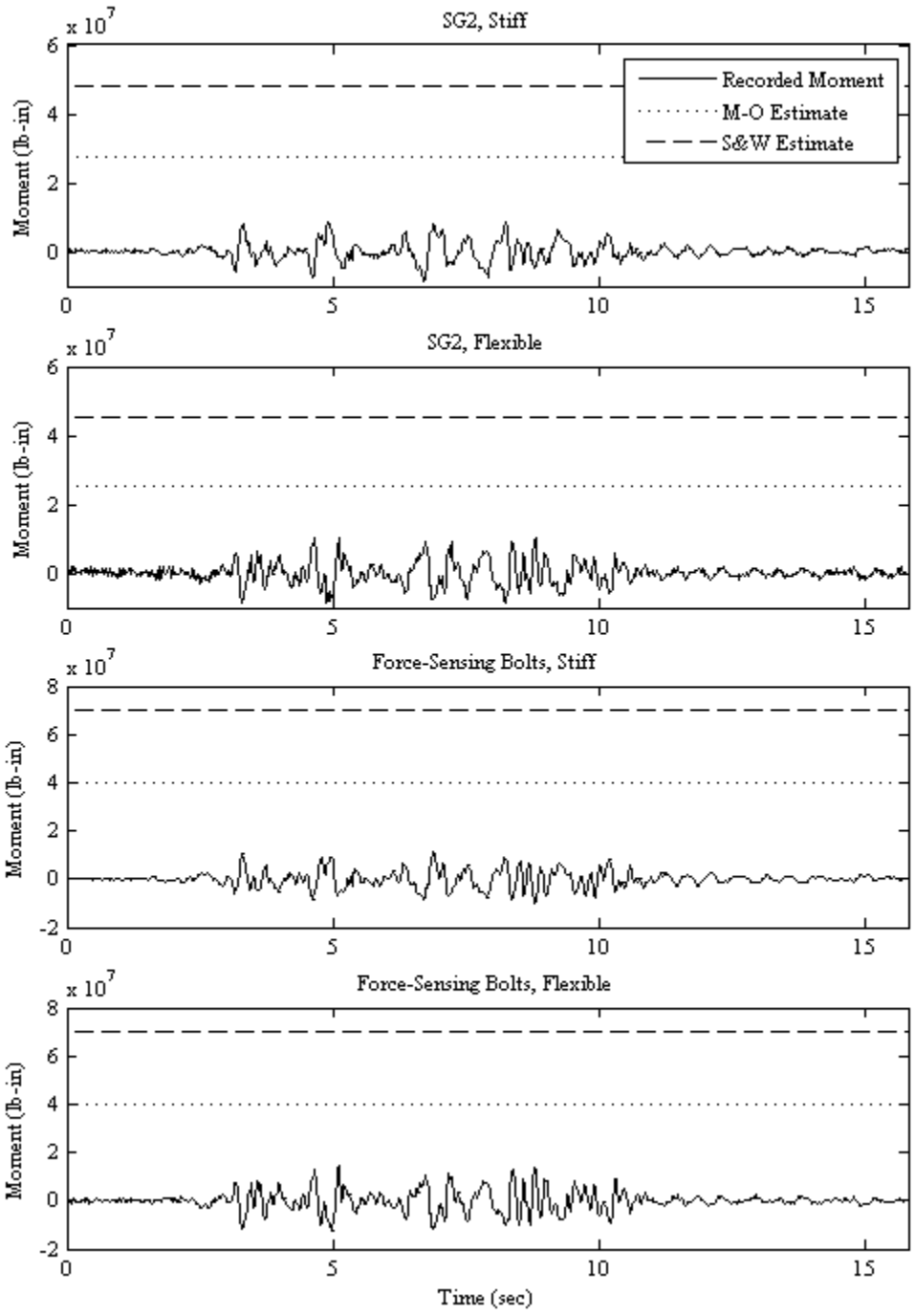

Fig. A.70 Comparison of dynamic earth pressure moment time series, recorded at SG2 on south stiff and north flexible walls and by force-sensing bolts, with M-O and Seed and Whitman (1970) moment estimates for Kocaeli-YPT330-2, LAA02.

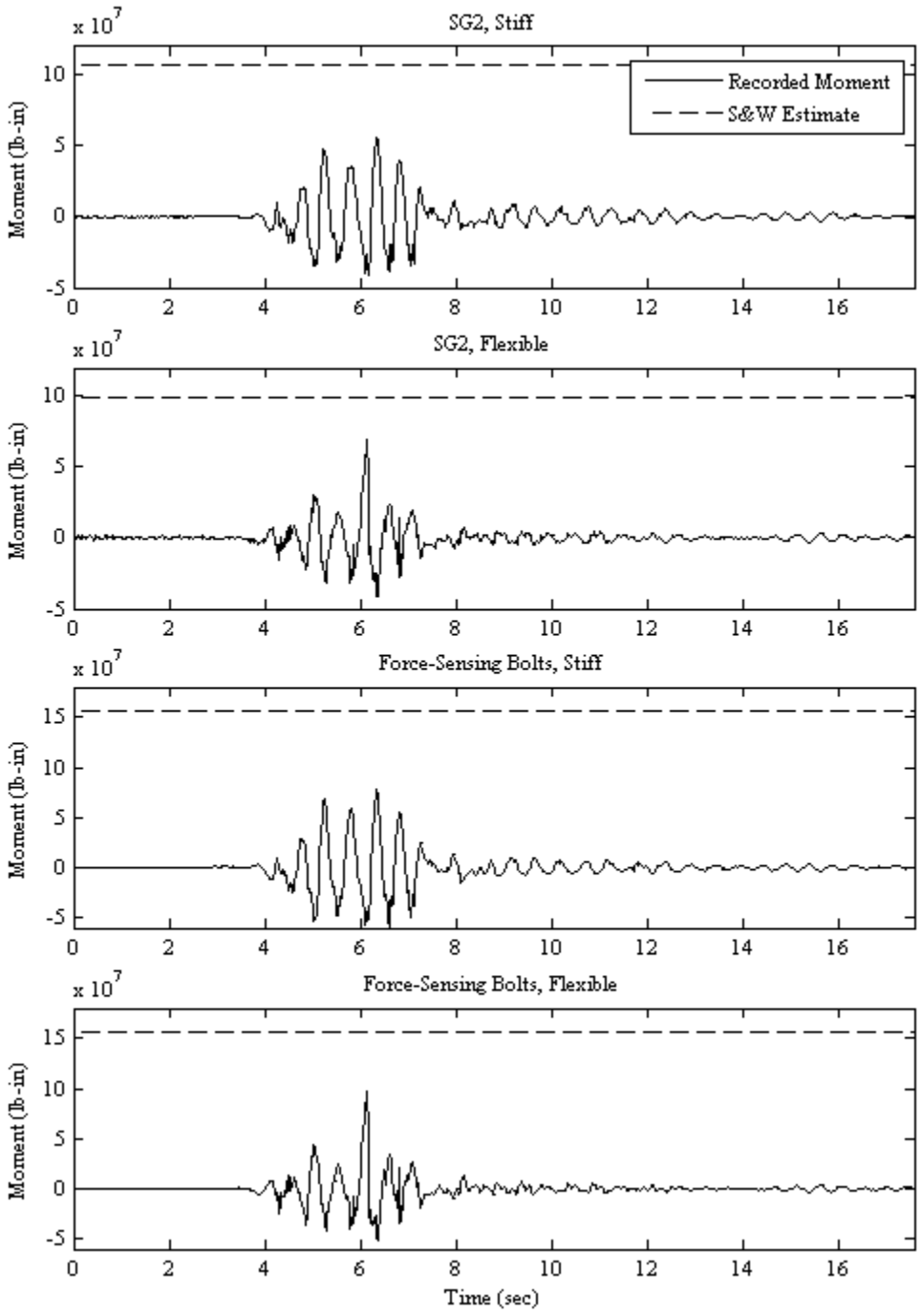

Fig. A.71 Comparison of dynamic earth pressure moment time series, recorded at SG2 on south stiff and north flexible walls and by force-sensing bolts, with M-O and Seed and Whitman (1970) moment estimates for Kobe-TAK090-1, LAA02.

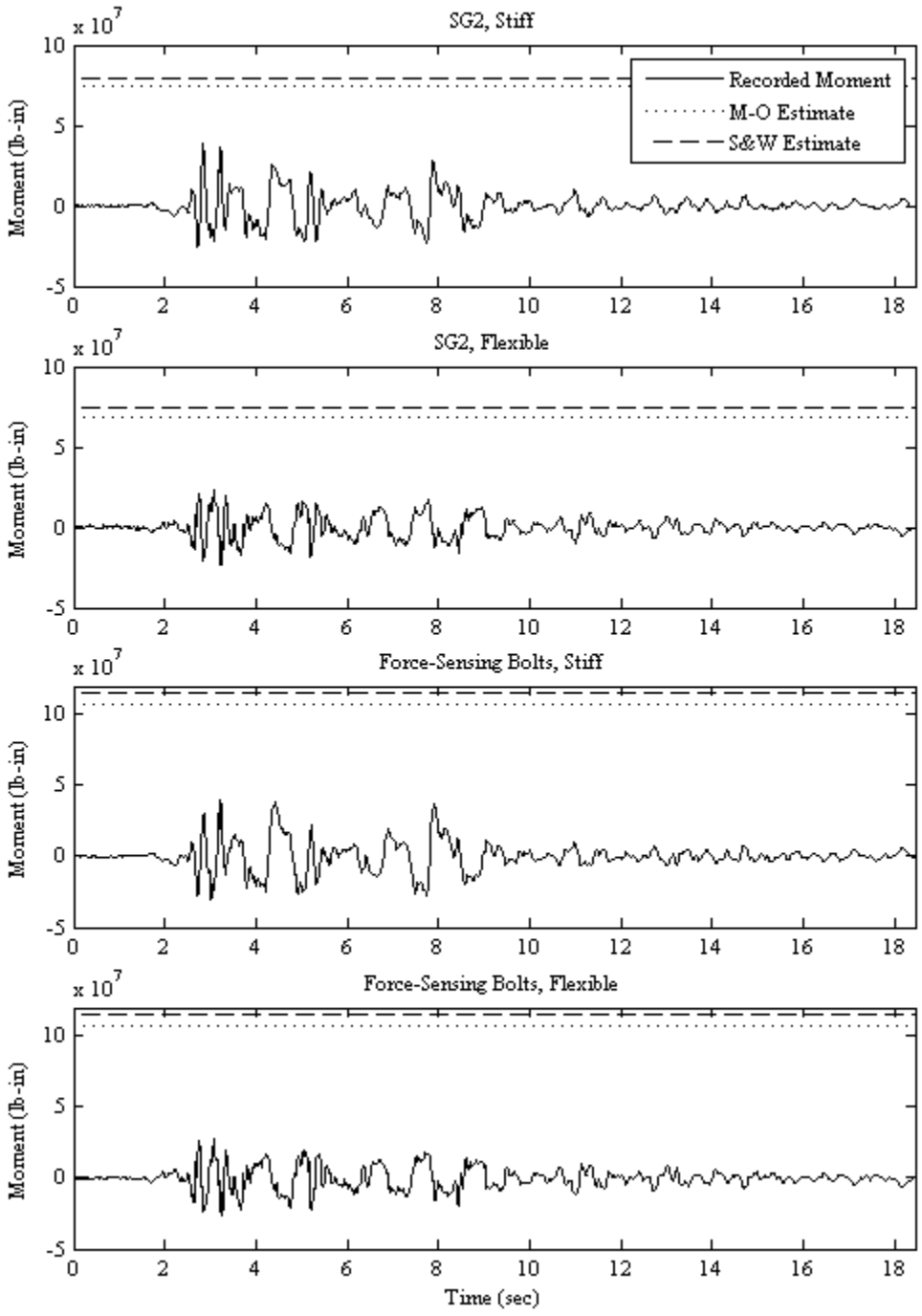

Fig. A.72 Comparison of dynamic earth pressure moment time series, recorded at SG2 on south stiff and north flexible walls and by force-sensing bolts, with M-O and Seed and Whitman (1970) moment estimates for Kobe-TAK090-2, LAA02.

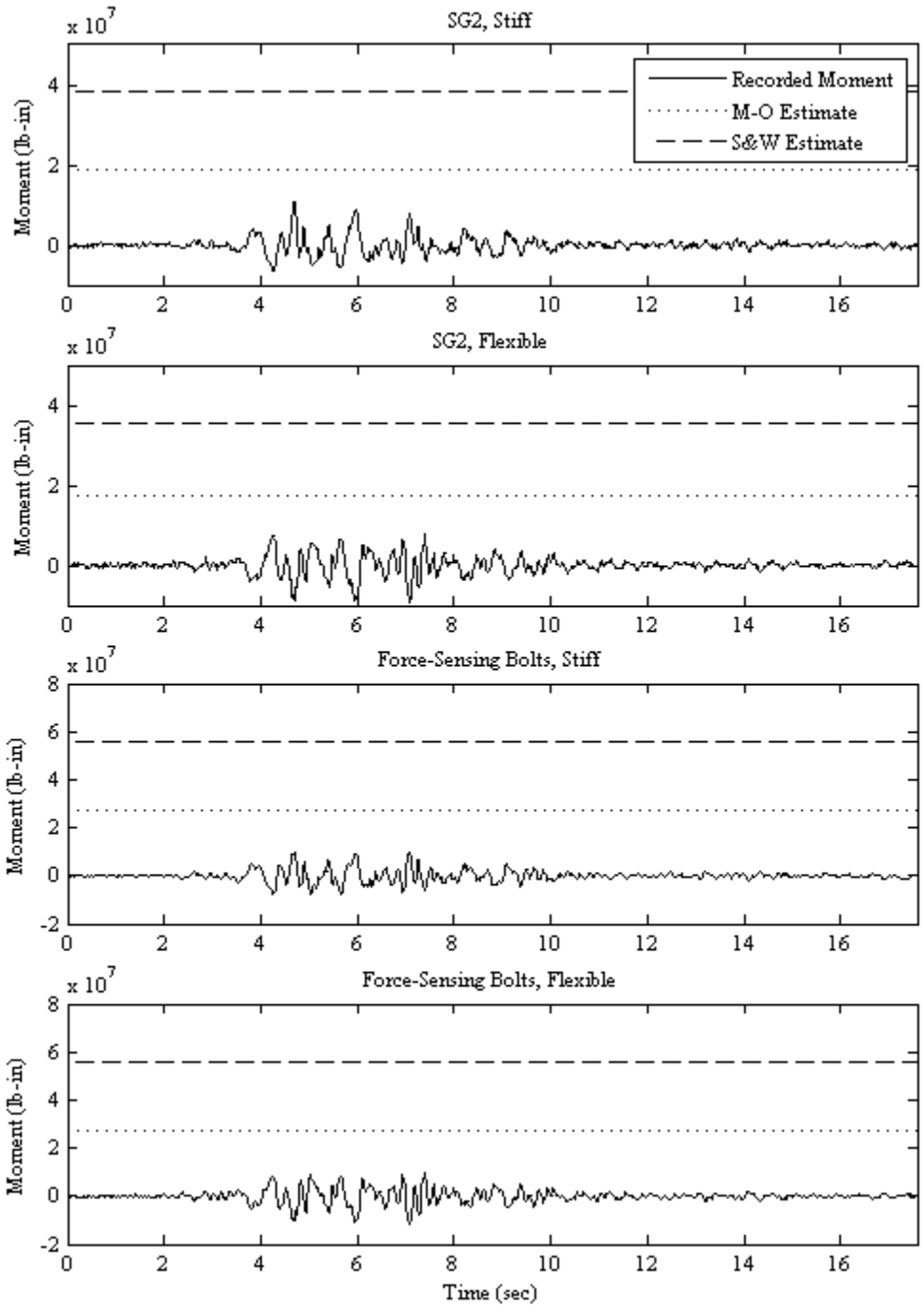

Fig. A.73 Comparison of dynamic earth pressure moment time series, recorded at SG2 on south stiff and north flexible walls and by force-sensing bolts, with M-O and Seed and Whitman (1970) moment estimates for Loma Prieta-WVC270, LAA02.

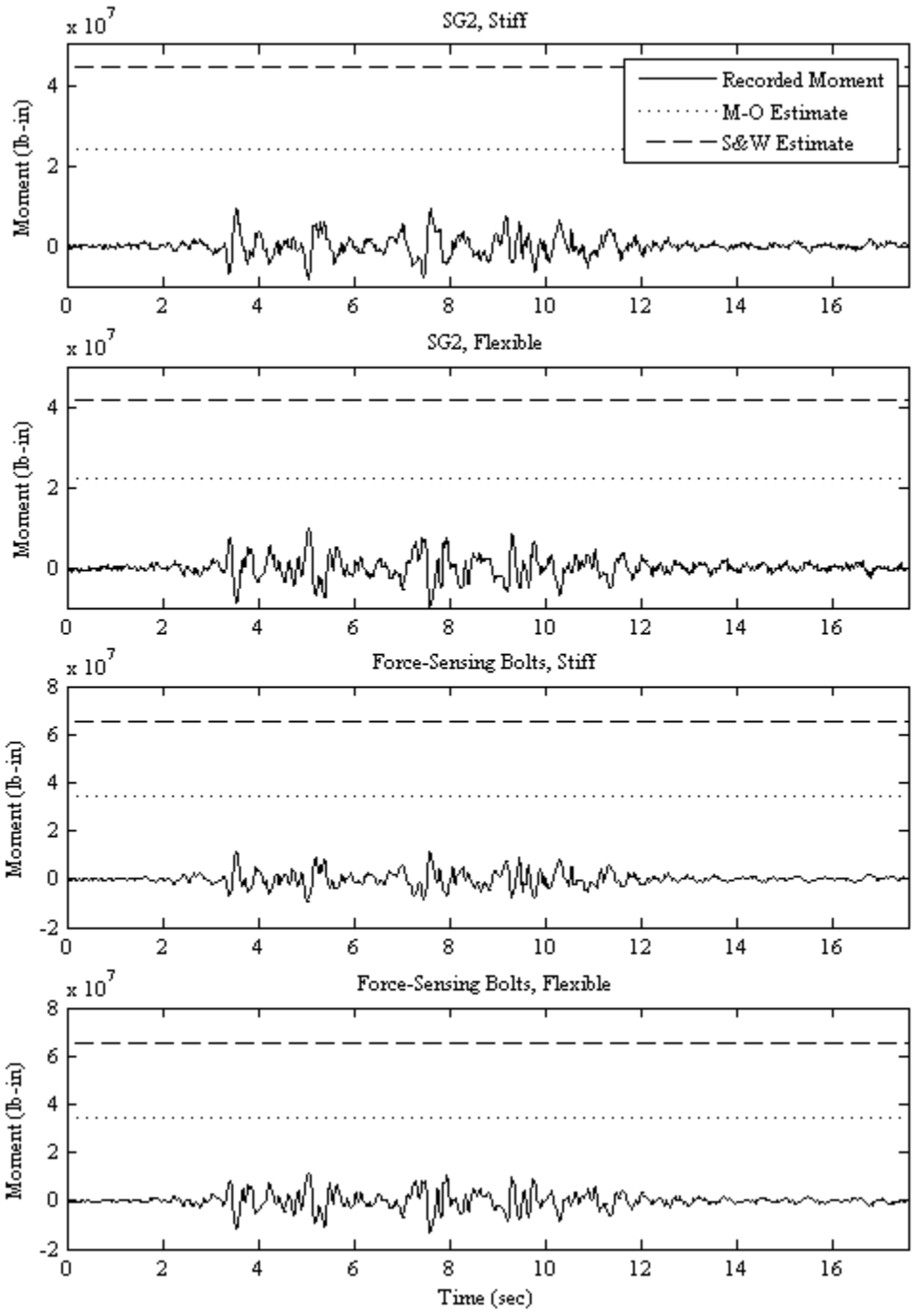

Fig. A.74 Comparison of dynamic earth pressure moment time series, recorded at SG2 on south stiff and north flexible walls and by force-sensing bolts, with M-O and Seed and Whitman (1970) moment estimates for Kocaeli-YPT330-3, LAA02.

Appendix B: Additional Tables

Table B.1 Maximum total moments measured and estimated at bases of south stiff and north flexible walls during Loma Prieta-1, 2, and 3, and Kobe shaking events for LAA01.

		Moment (lb-in)			
		Loma Prieta-1	**Loma Prieta-2**	**Kobe**	**Loma Prieta-3**
Strain Gages	**Stiff**	9.11E+07	9.69E+07	1.51E+08	9.93E+07
	Flexible	8.75E+07	9.11E+07	1.25E+07	9.45E+07
Force-Sensing Bolts	**Stiff**	9.00E+07	9.73E+07	1.70E+08	9.48E+07
	Flexible	9.89E+07	1.04E+08	1.47E+08	1.05E+08
M-O Method with a_{max}		9.33E+07	**9.28E+07**	INDET.	1.06E+08
M-O Method with 65% a_{max}		**6.13E+07**	**6.12E+07**	**9.18E+07**	**6.57E+07**
Seed and Whitman (1970) Method with a_{max}		1.16E+08	1.16E+08	1.60E+08	1.24E+08
Seed and Whitman (1970) Method with 65% a_{max}		**8.62E+07**	**8.61E+07**	**1.15E+08**	**9.16E+07**

Table B.2 Maximum total earth pressure moments measured and estimated at bases of south stiff and north flexible walls during Loma Prieta-SC-1 and 2, and Kobe-PI-1 and 2 shaking events for LAA02.

		Moment (lb-in)			
		Loma Prieta-SC-1	**Kobe-PI-1**	**Kobe-PI-2**	**Loma Prieta-SC-2**
Strain Gages	**Stiff**	5.80E+07	1.20E+08	1.09E+08	6.33E+07
	Flexible	5.44E+07	7.40E+07	8.62E+07	5.80E+07
Force-Sensing Bolts	**Stiff**	5.55E+07	1.38E+08	1.33E+08	6.20E+07
	Flexible	3.50E+07	7.63E+07	6.97E+07	4.69E+07
M-O Method with a_{max}		7.84E+07	1.72E+08	INDET.	9.63E+07
M-O Method with 65% a_{max}		**5.47E+07**	**7.84E+07**	**9.01E+07**	6.13E+07
Seed and Whitman (1970) Method with a_{max}		1.08E+08	1.51E+08	1.67E+08	1.23E+08
Seed and Whitman (1970) Method with 65% a_{max}		8.05E+07	**1.08E+08**	1.19E+08	9.05E+07

Table B.3 Maximum total earth pressure moments measured and estimated at bases of south stiff and north flexible walls during Kocaeli-YPT060-2 and 3, Kocaeli-YPT330-2 and Kobe-TAK090-1 shaking events for LAA02.

		Moment (lb-in)			
		Kocaeli-YPT060-2	**Kocaeli-YPT060-3**	**Kocaeli-YPT330-2**	**Kobe-TAK090-1**
Strain Gages	**Stiff**	3.36E+07	4.03E+07	4.29E+07	1.26E+08
	Flexible	3.80E+07	4.37E+07	4.18E+07	1.42E+08
Force-Sensing Bolts	**Stiff**	3.44E+07	4.09E+07	4.17E+07	1.31E+07
	Flexible	2.69E+07	3.01E+07	3.14E+07	1.30E+08
M-O Method with a_{max}		5.38E+07	7.03E+07	6.90E+07	INDET.
M-O Method with 65% a_{max}		4.34E+07	5.12E+07	5.06E+07	**1.07E+08**
Seed and Whitman (1970) Method with a_{max}		8.00E+07	1.01E+08	9.97E+07	1.85E+08
Seed and Whitman (1970) Method with 65% a_{max}		6.23E+07	7.60E+07	7.50E+07	1.30E+08

Table B.4 Maximum total earth pressure moments measured and estimated at bases of south stiff and north flexible walls during Kobe-TAK090-2, Loma Prieta-WVC270, and Loma Kocaeli-YPT330-3 shaking events for LAA02.

		Moment (lb-in)		
		Kobe-TAK090-2	**Loma Prieta-WVC270**	**Kocaeli-YPT330-3**
Strain Gages	**Stiff**	9.05E+07	4.75E+07	4.28E+07
	Flexible	7.13E+07	4.53E+07	4.91E+07
Force-Sensing Bolts	**Stiff**	8.54E+07	5.09E+07	5.17E+07
	Flexible	5.48E+07	3.48E+07	3.63E+07
M-O Method with a_{max}		1.37E+08	5.62E+07	6.35E+07
M-O Method with 65% a_{max}		**7.26E+07**	4.43E+07	4.78E+07
Seed and Whitman (1970) Method with a_{max}		1.44E+08	8.43E+07	9.40E+07
Seed and Whitman (1970) Method with 65% a_{max}		1.04E+08	6.49E+07	7.12E+07

Table B.5 Maximum dynamic moments measured and estimated at bases of south stiff and north flexible walls during Loma Prieta-1, 2, and 3, and Kobe shaking events for LAA01.

		Moment (lb-in)			
		Loma Prieta-1	**Loma Prieta-2**	**Kobe**	**Loma Prieta-3**
Strain Gages	**Stiff**	5.98E+07	6.38E+07	1.28E+08	6.45E+07
	Flexible	4.51E+07	4.43E+07	8.27E+07	4.25E+07
Force-Sensing Bolts	**Stiff**	4.45E+07	4.89E+07	1.21E+08	4.48E+07
	Flexible	6.08E+07	5.99E+07	9.74E+07	5.61E+07
M-O Method with a_{max}		6.20E+07	6.14E+07	INDET.	7.45E+07
M-O Method with 65% a_{max}		**3.00E+07**	**2.98E+07**	**6.04E+07**	**3.41E+07**
Seed and Whitman (1970) Method with a_{max}		8.44E+07	8.42E+07	1.28E+08	9.23E+07
Seed and Whitman (1970) Method with 65% a_{max}		5.49E+07	**5.47E+07**	**8.35E+07**	6.00E+07

Table B.6 Maximum dynamic earth pressure moments measured and estimated at bases of south stiff and north flexible walls during Loma Prieta-SC-1 and 2, and Kobe-PI-1 and 2 shaking events for LAA02.

		Moment (lb-in)			
		Loma Prieta-SC-1	**Kobe-PI-1**	**Kobe-PI-2**	**Loma Prieta-SC-2**
Strain Gages	**Stiff**	2.40E+07	6.77E+07	6.91E+07	2.92E+07
	Flexible	1.59E+07	3.44E+07	4.95E+07	2.27E+07
Force-Sensing Bolts	**Stiff**	2.26E+07	8.53E+07	8.67E+07	2.96E+07
	Flexible	1.79E+07	4.22E+07	4.69E+07	2.44E+07
M-O Method with a_{max}		4.90E+07	1.42E+08	INDET.	6.70E+07
M-O Method with 65% a_{max}		2.52E+07	**4.89E+07**	**6.07E+07**	3.21E+07
Seed and Whitman (1970) Method with a_{max}		7.85E+07	1.21E+08	1.37E+08	9.42E+07
Seed and Whitman (1970) Method with 65% a_{max}		5.10E+07	7.88E+07	8.92E+07	6.13E+07

Table B.7 Maximum dynamic earth pressure moments measured and estimated at bases of south stiff and north flexible walls during Kocaeli-YPT060-2 and 3, Kocaeli-YPT330-2 and Kobe-TAK090-1 shaking events for LAA02.

		Moment (lb-in)			
		Kocaeli-YPT060-2	Kocaeli-YPT060-3	Kocaeli-YPT330-2	Kobe-TAK090-1
Strain Gages	Stiff	1.03E+07	1.30E+07	1.27E+07	7.36E+07
	Flexible	1.17E+07	1.54E+07	1.22E+07	9.54E+07
Force-Sensing Bolts	Stiff	7.86E+06	1.04E+07	1.12E+07	7.74E+07
	Flexible	1.10E+07	1.45E+07	1.47E+07	9.75E+07
M-O Method with a_{max}		2.46E+07	4.11E+07	3.98E+07	INDET.
M-O Method with 65% a_{max}		1.42E+07	2.20E+07	2.14E+07	7.81E+07
Seed and Whitman (1970) Method with a_{max}		5.08E+07	7.19E+07	7.05E+07	1.56E+08
Seed and Whitman (1970) Method with 65% a_{max}		3.30E+07	4.67E+07	4.58E+07	1.01E+08

Table B.8 Maximum dynamic earth pressure moments measured and estimated at bases of south stiff and north flexible walls during Kobe-TAK090-2, Loma Prieta-WVC270, and Loma Kocaeli-YPT330-3 shaking events for LAA02.

		Moment (lb-in)		
		Kobe-TAK090-2	Loma Prieta-WVC270	Kocaeli-YPT330-3
Strain Gages	Stiff	5.02E+07	1.54E+07	1.15E+07
	Flexible	3.28E+07	1.13E+07	1.29E+07
Force-Sensing Bolts	Stiff	4.02E+07	1.00E+07	1.16E+07
	Flexible	2.81E+07	1.16E+07	1.33E+07
M-O Method with a_{max}		1.08E+08	2.75E+07	3.47E+07
M-O Method with 65% a_{max}		**4.36E+07**	1.56E+07	1.91E+07
Seed and Whitman (1970) Method with a_{max}		1.16E+08	5.56E+07	6.53E+07
Seed and Whitman (1970) Method with 65% a_{max}		7.51E+07	3.61E+07	4.24E+07

PEER REPORTS

PEER reports are available from the National Information Service for Earthquake Engineering (NISEE). To order PEER reports, please contact the Pacific Earthquake Engineering Research Center, 1301 South 46th Street, Richmond, California 94804-4698. Tel.: (510) 665-3405; Fax: (510) 665-3420.

PEER 2008/10 *Technical Manual for Strata.* Albert Kottke and Ellen M. Rathje. February 2009.

PEER 2008/08 *Toward Earthquake-Resistant Design of Concentrically Braced Steel Structures.* Patxi Uriz and Stephen A. Mahin. November 2008.

PEER 2008/07 *Using OpenSees for Performance-Based Evaluation of Bridges on Liquefiable Soils.* Stephen L. Kramer, Pedro Arduino, and HyungSuk Shin. November 2008.

PEER 2008/06 *Shaking Table Tests and Numerical Investigation of Self-Centering Reinforced Concrete Bridge Columns.* Hyung IL Jeong, Junichi Sakai, and Stephen A. Mahin. September 2008.

PEER 2008/05 *Performance-Based Earthquake Engineering Design Evaluation Procedure for Bridge Foundations Undergoing Liquefaction-Induced Lateral Ground Displacement.* Christian A. Ledezma and Jonathan D. Bray. August 2008.

PEER 2008/04 *Benchmarking of Nonlinear Geotechnical Ground Response Analysis Procedures.* Jonathan P. Stewart, Annie On-Lei Kwok, Yousseff M. A. Hashash, Neven Matasovic, Robert Pyke, Zhiliang Wang, and Zhaohui Yang. August 2008.

PEER 2008/03 *Guidelines for Nonlinear Analysis of Bridge Structures in California.* Ady Aviram, Kevin R. Mackie, and Božidar Stojadinović. August 2008.

PEER 2008/02 *Treatment of Uncertainties in Seismic-Risk Analysis of Transportation Systems.* Evangelos Stergiou and Anne S. Kiremidjian. July 2008.

PEER 2008/01 *Seismic Performance Objectives for Tall Buildings.* William T. Holmes, Charles Kircher, William Petak, and Nabih Youssef. August 2008.

PEER 2007/12 *An Assessment to Benchmark the Seismic Performance of a Code-Conforming Reinforced Concrete Moment-Frame Building.* Curt Haselton, Christine A. Goulet, Judith Mitrani-Reiser, James L. Beck, Gregory G. Deierlein, Keith A. Porter, Jonathan P. Stewart, and Ertugrul Taciroglu. August 2008.

PEER 2007/11 *Bar Buckling in Reinforced Concrete Bridge Columns.* Wayne A. Brown, Dawn E. Lehman, and John F. Stanton. February 2008.

PEER 2007/10 *Computational Modeling of Progressive Collapse in Reinforced Concrete Frame Structures.* Mohamed M. Talaat and Khalid M. Mosalam. May 2008.

PEER 2007/09 *Integrated Probabilistic Performance-Based Evaluation of Benchmark Reinforced Concrete Bridges.* Kevin R. Mackie, John-Michael Wong, and Božidar Stojadinović. January 2008.

PEER 2007/08 *Assessing Seismic Collapse Safety of Modern Reinforced Concrete Moment-Frame Buildings.* Curt B. Haselton and Gregory G. Deierlein. February 2008.

PEER 2007/07 *Performance Modeling Strategies for Modern Reinforced Concrete Bridge Columns.* Michael P. Berry and Marc O. Eberhard. April 2008.

PEER 2007/06 *Development of Improved Procedures for Seismic Design of Buried and Partially Buried Structures.* Linda Al Atik and Nicholas Sitar. June 2007.

PEER 2007/05 *Uncertainty and Correlation in Seismic Risk Assessment of Transportation Systems.* Renee G. Lee and Anne S. Kiremidjian. July 2007.

PEER 2007/04 *Numerical Models for Analysis and Performance-Based Design of Shallow Foundations Subjected to Seismic Loading.* Sivapalan Gajan, Tara C. Hutchinson, Bruce L. Kutter, Prishati Raychowdhury, José A. Ugalde, and Jonathan P. Stewart. May 2008.

PEER 2007/03 *Beam-Column Element Model Calibrated for Predicting Flexural Response Leading to Global Collapse of RC Frame Buildings.* Curt B. Haselton, Abbie B. Liel, Sarah Taylor Lange, and Gregory g. Deierlein. May 2008.

PEER 2007/02 *Campbell-Bozorgnia NGA Ground Motion Relations for the Geometric Mean Horizontal Component of Peak and Spectral Ground Motion Parameters.* Kenneth W. Campbell and Yousef Bozorgnia. May 2007.

PEER 2007/01 *Boore-Atkinson NGA Ground Motion Relations for the Geometric Mean Horizontal Component of Peak and Spectral Ground Motion Parameters.* David M. Boore and Gail M. Atkinson. May. May 2007.

PEER 2006/12 *Societal Implications of Performance-Based Earthquake Engineering.* Peter J. May. May 2007.

PEER 2006/11 *Probabilistic Seismic Demand Analysis Using Advanced Ground Motion Intensity Measures, Attenuation Relationships, and Near-Fault Effects.* Polsak Tothong and C. Allin Cornell. March 2007.

PEER 2006/10 *Application of the PEER PBEE Methodology to the I-880 Viaduct.* Sashi Kunnath. February 2007.

PEER 2006/09 *Quantifying Economic Losses from Travel Forgone Following a Large Metropolitan Earthquake.* James Moore, Sungbin Cho, Yue Yue Fan, and Stuart Werner. November 2006.

PEER 2006/08 *Vector-Valued Ground Motion Intensity Measures for Probabilistic Seismic Demand Analysis*. Jack W. Baker and C. Allin Cornell. October 2006.

PEER 2006/07 *Analytical Modeling of Reinforced Concrete Walls for Predicting Flexural and Coupled–Shear-Flexural Responses*. Kutay Orakcal, Leonardo M. Massone, and John W. Wallace. October 2006.

PEER 2006/06 *Nonlinear Analysis of a Soil-Drilled Pier System under Static and Dynamic Axial Loading.* Gang Wang and Nicholas Sitar. November 2006.

PEER 2006/05 *Advanced Seismic Assessment Guidelines.* Paolo Bazzurro, C. Allin Cornell, Charles Menun, Maziar Motahari, and Nicolas Luco. September 2006.

PEER 2006/04 *Probabilistic Seismic Evaluation of Reinforced Concrete Structural Components and Systems.* Tae Hyung Lee and Khalid M. Mosalam. August 2006.

PEER 2006/03 *Performance of Lifelines Subjected to Lateral Spreading.* Scott A. Ashford and Teerawut Juirnarongrit. July 2006.

PEER 2006/02 *Pacific Earthquake Engineering Research Center Highway Demonstration Project.* Anne Kiremidjian, James Moore, Yue Yue Fan, Nesrin Basoz, Ozgur Yazali, and Meredith Williams. April 2006.

PEER 2006/01 *Bracing Berkeley. A Guide to Seismic Safety on the UC Berkeley Campus.* Mary C. Comerio, Stephen Tobriner, and Ariane Fehrenkamp. January 2006.

PEER 2005/16 *Seismic Response and Reliability of Electrical Substation Equipment and Systems.* Junho Song, Armen Der Kiureghian, and Jerome L. Sackman. April 2006.

PEER 2005/15 *CPT-Based Probabilistic Assessment of Seismic Soil Liquefaction Initiation.* R. E. S. Moss, R. B. Seed, R. E. Kayen, J. P. Stewart, and A. Der Kiureghian. April 2006.

PEER 2005/14 *Workshop on Modeling of Nonlinear Cyclic Load-Deformation Behavior of Shallow Foundations.* Bruce L. Kutter, Geoffrey Martin, Tara Hutchinson, Chad Harden, Sivapalan Gajan, and Justin Phalen. March 2006.

PEER 2005/13 *Stochastic Characterization and Decision Bases under Time-Dependent Aftershock Risk in Performance-Based Earthquake Engineering.* Gee Liek Yeo and C. Allin Cornell. July 2005.

PEER 2005/12 *PEER Testbed Study on a Laboratory Building: Exercising Seismic Performance Assessment.* Mary C. Comerio, editor. November 2005.

PEER 2005/11 *Van Nuys Hotel Building Testbed Report: Exercising Seismic Performance Assessment.* Helmut Krawinkler, editor. October 2005.

PEER 2005/10 *First NEES/E-Defense Workshop on Collapse Simulation of Reinforced Concrete Building Structures.* September 2005.

PEER 2005/09 *Test Applications of Advanced Seismic Assessment Guidelines.* Joe Maffei, Karl Telleen, Danya Mohr, William Holmes, and Yuki Nakayama. August 2006.

PEER 2005/08 *Damage Accumulation in Lightly Confined Reinforced Concrete Bridge Columns.* R. Tyler Ranf, Jared M. Nelson, Zach Price, Marc O. Eberhard, and John F. Stanton. April 2006.

PEER 2005/07 *Experimental and Analytical Studies on the Seismic Response of Freestanding and Anchored Laboratory Equipment.* Dimitrios Konstantinidis and Nicos Makris. January 2005.

PEER 2005/06 *Global Collapse of Frame Structures under Seismic Excitations*. Luis F. Ibarra and Helmut Krawinkler. September 2005.

PEER 2005//05 *Performance Characterization of Bench- and Shelf-Mounted Equipment.* Samit Ray Chaudhuri and Tara C. Hutchinson. May 2006.

PEER 2005/04 *Numerical Modeling of the Nonlinear Cyclic Response of Shallow Foundations.* Chad Harden, Tara Hutchinson, Geoffrey R. Martin, and Bruce L. Kutter. August 2005.

PEER 2005/03 *A Taxonomy of Building Components for Performance-Based Earthquake Engineering.* Keith A. Porter. September 2005.

PEER 2005/02 *Fragility Basis for California Highway Overpass Bridge Seismic Decision Making*. Kevin R. Mackie and Božidar Stojadinović. June 2005.

PEER 2005/01 *Empirical Characterization of Site Conditions on Strong Ground Motion.* Jonathan P. Stewart, Yoojoong Choi, and Robert W. Graves. June 2005.

PEER 2004/09 *Electrical Substation Equipment Interaction: Experimental Rigid Conductor Studies.* Christopher Stearns and André Filiatrault. February 2005.

PEER 2004/08 *Seismic Qualification and Fragility Testing of Line Break 550-kV Disconnect Switches.* Shakhzod M. Takhirov, Gregory L. Fenves, and Eric Fujisaki. January 2005.

PEER 2004/07 *Ground Motions for Earthquake Simulator Qualification of Electrical Substation Equipment.* Shakhzod M. Takhirov, Gregory L. Fenves, Eric Fujisaki, and Don Clyde. January 2005.

PEER 2004/06 *Performance-Based Regulation and Regulatory Regimes.* Peter J. May and Chris Koski. September 2004.

PEER 2004/05 *Performance-Based Seismic Design Concepts and Implementation: Proceedings of an International Workshop.* Peter Fajfar and Helmut Krawinkler, editors. September 2004.

PEER 2004/04 *Seismic Performance of an Instrumented Tilt-up Wall Building.* James C. Anderson and Vitelmo V. Bertero. July 2004.

PEER 2004/03 *Evaluation and Application of Concrete Tilt-up Assessment Methodologies.* Timothy Graf and James O. Malley. October 2004.

PEER 2004/02 *Analytical Investigations of New Methods for Reducing Residual Displacements of Reinforced Concrete Bridge Columns.* Junichi Sakai and Stephen A. Mahin. August 2004.

PEER 2004/01 *Seismic Performance of Masonry Buildings and Design Implications.* Kerri Anne Taeko Tokoro, James C. Anderson, and Vitelmo V. Bertero. February 2004.

PEER 2003/18 *Performance Models for Flexural Damage in Reinforced Concrete Columns.* Michael Berry and Marc Eberhard. August 2003.

PEER 2003/17 *Predicting Earthquake Damage in Older Reinforced Concrete Beam-Column Joints.* Catherine Pagni and Laura Lowes. October 2004.

PEER 2003/16 *Seismic Demands for Performance-Based Design of Bridges.* Kevin Mackie and Božidar Stojadinović. August 2003.

PEER 2003/15 *Seismic Demands for Nondeteriorating Frame Structures and Their Dependence on Ground Motions.* Ricardo Antonio Medina and Helmut Krawinkler. May 2004.

PEER 2003/14 *Finite Element Reliability and Sensitivity Methods for Performance-Based Earthquake Engineering.* Terje Haukaas and Armen Der Kiureghian. April 2004.

PEER 2003/13 *Effects of Connection Hysteretic Degradation on the Seismic Behavior of Steel Moment-Resisting Frames.* Janise E. Rodgers and Stephen A. Mahin. March 2004.

PEER 2003/12 *Implementation Manual for the Seismic Protection of Laboratory Contents: Format and Case Studies.* William T. Holmes and Mary C. Comerio. October 2003.

PEER 2003/11 *Fifth U.S.-Japan Workshop on Performance-Based Earthquake Engineering Methodology for Reinforced Concrete Building Structures.* February 2004.

PEER 2003/10 *A Beam-Column Joint Model for Simulating the Earthquake Response of Reinforced Concrete Frames.* Laura N. Lowes, Nilanjan Mitra, and Arash Altoontash. February 2004.

PEER 2003/09 *Sequencing Repairs after an Earthquake: An Economic Approach.* Marco Casari and Simon J. Wilkie. April 2004.

PEER 2003/08 *A Technical Framework for Probability-Based Demand and Capacity Factor Design (DCFD) Seismic Formats.* Fatemeh Jalayer and C. Allin Cornell. November 2003.

PEER 2003/07 *Uncertainty Specification and Propagation for Loss Estimation Using FOSM Methods.* Jack W. Baker and C. Allin Cornell. September 2003.

PEER 2003/06 *Performance of Circular Reinforced Concrete Bridge Columns under Bidirectional Earthquake Loading.* Mahmoud M. Hachem, Stephen A. Mahin, and Jack P. Moehle. February 2003.

PEER 2003/05 *Response Assessment for Building-Specific Loss Estimation.* Eduardo Miranda and Shahram Taghavi. September 2003.

PEER 2003/04 *Experimental Assessment of Columns with Short Lap Splices Subjected to Cyclic Loads.* Murat Melek, John W. Wallace, and Joel Conte. April 2003.

PEER 2003/03 *Probabilistic Response Assessment for Building-Specific Loss Estimation.* Eduardo Miranda and Hesameddin Aslani. September 2003.

PEER 2003/02 *Software Framework for Collaborative Development of Nonlinear Dynamic Analysis Program.* Jun Peng and Kincho H. Law. September 2003.

PEER 2003/01 *Shake Table Tests and Analytical Studies on the Gravity Load Collapse of Reinforced Concrete Frames.* Kenneth John Elwood and Jack P. Moehle. November 2003.

PEER 2002/24 *Performance of Beam to Column Bridge Joints Subjected to a Large Velocity Pulse.* Natalie Gibson, André Filiatrault, and Scott A. Ashford. April 2002.

PEER 2002/23 *Effects of Large Velocity Pulses on Reinforced Concrete Bridge Columns.* Greg L. Orozco and Scott A. Ashford. April 2002.

PEER 2002/22 *Characterization of Large Velocity Pulses for Laboratory Testing.* Kenneth E. Cox and Scott A. Ashford. April 2002.

PEER 2002/21 *Fourth U.S.-Japan Workshop on Performance-Based Earthquake Engineering Methodology for Reinforced Concrete Building Structures*. December 2002.

PEER 2002/20 *Barriers to Adoption and Implementation of PBEE Innovations.* Peter J. May. August 2002.

PEER 2002/19 *Economic-Engineered Integrated Models for Earthquakes: Socioeconomic Impacts.* Peter Gordon, James E. Moore II, and Harry W. Richardson. July 2002.

PEER 2002/18 *Assessment of Reinforced Concrete Building Exterior Joints with Substandard Details.* Chris P. Pantelides, Jon Hansen, Justin Nadauld, and Lawrence D. Reaveley. May 2002.

PEER 2002/17 *Structural Characterization and Seismic Response Analysis of a Highway Overcrossing Equipped with Elastomeric Bearings and Fluid Dampers: A Case Study.* Nicos Makris and Jian Zhang. November 2002.

PEER 2002/16 *Estimation of Uncertainty in Geotechnical Properties for Performance-Based Earthquake Engineering.* Allen L. Jones, Steven L. Kramer, and Pedro Arduino. December 2002.

PEER 2002/15 *Seismic Behavior of Bridge Columns Subjected to Various Loading Patterns.* Asadollah Esmaeily-Gh. and Yan Xiao. December 2002.

PEER 2002/14 *Inelastic Seismic Response of Extended Pile Shaft Supported Bridge Structures.* T.C. Hutchinson, R.W. Boulanger, Y.H. Chai, and I.M. Idriss. December 2002.

PEER 2002/13 *Probabilistic Models and Fragility Estimates for Bridge Components and Systems.* Paolo Gardoni, Armen Der Kiureghian, and Khalid M. Mosalam. June 2002.

PEER 2002/12 *Effects of Fault Dip and Slip Rake on Near-Source Ground Motions: Why Chi-Chi Was a Relatively Mild M7.6 Earthquake.* Brad T. Aagaard, John F. Hall, and Thomas H. Heaton. December 2002.

PEER 2002/11 *Analytical and Experimental Study of Fiber-Reinforced Strip Isolators*. James M. Kelly and Shakhzod M. Takhirov. September 2002.

PEER 2002/10 *Centrifuge Modeling of Settlement and Lateral Spreading with Comparisons to Numerical Analyses***.** Sivapalan Gajan and Bruce L. Kutter. January 2003.

PEER 2002/09 *Documentation and Analysis of Field Case Histories of Seismic Compression during the 1994 Northridge, California, Earthquake.* Jonathan P. Stewart, Patrick M. Smith, Daniel H. Whang, and Jonathan D. Bray. October 2002.

PEER 2002/08 *Component Testing, Stability Analysis and Characterization of Buckling-Restrained Unbonded Braces™*. Cameron Black, Nicos Makris, and Ian Aiken. September 2002.

PEER 2002/07 *Seismic Performance of Pile-Wharf Connections*. Charles W. Roeder, Robert Graff, Jennifer Soderstrom, and Jun Han Yoo. December 2001.

PEER 2002/06 *The Use of Benefit-Cost Analysis for Evaluation of Performance-Based Earthquake Engineering Decisions*. Richard O. Zerbe and Anthony Falit-Baiamonte. September 2001.

PEER 2002/05 *Guidelines, Specifications, and Seismic Performance Characterization of Nonstructural Building Components and Equipment*. André Filiatrault, Constantin Christopoulos, and Christopher Stearns. September 2001.

PEER 2002/04 *Consortium of Organizations for Strong-Motion Observation Systems and the Pacific Earthquake Engineering Research Center Lifelines Program: Invited Workshop on Archiving and Web Dissemination of Geotechnical Data, 4–5 October 2001*. September 2002.

PEER 2002/03 *Investigation of Sensitivity of Building Loss Estimates to Major Uncertain Variables for the Van Nuys Testbed.* Keith A. Porter, James L. Beck, and Rustem V. Shaikhutdinov. August 2002.

PEER 2002/02 *The Third U.S.-Japan Workshop on Performance-Based Earthquake Engineering Methodology for Reinforced Concrete Building Structures*. July 2002.

PEER 2002/01 *Nonstructural Loss Estimation: The UC Berkeley Case Study.* Mary C. Comerio and John C. Stallmeyer. December 2001.

PEER 2001/16 *Statistics of SDF-System Estimate of Roof Displacement for Pushover Analysis of Buildings.* Anil K. Chopra, Rakesh K. Goel, and Chatpan Chintanapakdee. December 2001.

PEER 2001/15 *Damage to Bridges during the 2001 Nisqually Earthquake.* R. Tyler Ranf, Marc O. Eberhard, and Michael P. Berry. November 2001.

PEER 2001/14 *Rocking Response of Equipment Anchored to a Base Foundation.* Nicos Makris and Cameron J. Black. September 2001.

PEER 2001/13 *Modeling Soil Liquefaction Hazards for Performance-Based Earthquake Engineering.* Steven L. Kramer and Ahmed-W. Elgamal. February 2001.

PEER 2001/12 *Development of Geotechnical Capabilities in OpenSees.* Boris Jeremi . September 2001.

PEER 2001/11 *Analytical and Experimental Study of Fiber-Reinforced Elastomeric Isolators*. James M. Kelly and Shakhzod M. Takhirov. September 2001.

PEER 2001/10 *Amplification Factors for Spectral Acceleration in Active Regions.* Jonathan P. Stewart, Andrew H. Liu, Yoojoong Choi, and Mehmet B. Baturay. December 2001.

PEER 2001/09 *Ground Motion Evaluation Procedures for Performance-Based Design.* Jonathan P. Stewart, Shyh-Jeng Chiou, Jonathan D. Bray, Robert W. Graves, Paul G. Somerville, and Norman A. Abrahamson. September 2001.

PEER 2001/08 *Experimental and Computational Evaluation of Reinforced Concrete Bridge Beam-Column Connections for Seismic Performance*. Clay J. Naito, Jack P. Moehle, and Khalid M. Mosalam. November 2001.

PEER 2001/07 *The Rocking Spectrum and the Shortcomings of Design Guidelines*. Nicos Makris and Dimitrios Konstantinidis. August 2001.

PEER 2001/06 *Development of an Electrical Substation Equipment Performance Database for Evaluation of Equipment Fragilities*. Thalia Agnanos. April 1999.

PEER 2001/05 *Stiffness Analysis of Fiber-Reinforced Elastomeric Isolators.* Hsiang-Chuan Tsai and James M. Kelly. May 2001.

PEER 2001/04 *Organizational and Societal Considerations for Performance-Based Earthquake Engineering.* Peter J. May. April 2001.

PEER 2001/03 *A Modal Pushover Analysis Procedure to Estimate Seismic Demands for Buildings: Theory and Preliminary Evaluation.* Anil K. Chopra and Rakesh K. Goel. January 2001.

PEER 2001/02 *Seismic Response Analysis of Highway Overcrossings Including Soil-Structure Interaction.* Jian Zhang and Nicos Makris. March 2001.

PEER 2001/01 *Experimental Study of Large Seismic Steel Beam-to-Column Connections.* Egor P. Popov and Shakhzod M. Takhirov. November 2000.

PEER 2000/10 *The Second U.S.-Japan Workshop on Performance-Based Earthquake Engineering Methodology for Reinforced Concrete Building Structures.* March 2000.

PEER 2000/09 *Structural Engineering Reconnaissance of the August 17, 1999 Earthquake: Kocaeli (Izmit), Turkey*. Halil Sezen, Kenneth J. Elwood, Andrew S. Whittaker, Khalid Mosalam, John J. Wallace, and John F. Stanton. December 2000.

PEER 2000/08 *Behavior of Reinforced Concrete Bridge Columns Having Varying Aspect Ratios and Varying Lengths of Confinement.* Anthony J. Calderone, Dawn E. Lehman, and Jack P. Moehle. January 2001.

PEER 2000/07 *Cover-Plate and Flange-Plate Reinforced Steel Moment-Resisting Connections.* Taejin Kim, Andrew S. Whittaker, Amir S. Gilani, Vitelmo V. Bertero, and Shakhzod M. Takhirov. September 2000.

PEER 2000/06 *Seismic Evaluation and Analysis of 230-kV Disconnect Switches.* Amir S. J. Gilani, Andrew S. Whittaker, Gregory L. Fenves, Chun-Hao Chen, Henry Ho, and Eric Fujisaki. July 2000.

PEER 2000/05 *Performance-Based Evaluation of Exterior Reinforced Concrete Building Joints for Seismic Excitation.* Chandra Clyde, Chris P. Pantelides, and Lawrence D. Reaveley. July 2000.

PEER 2000/04 *An Evaluation of Seismic Energy Demand: An Attenuation Approach.* Chung-Che Chou and Chia-Ming Uang. July 1999.

PEER 2000/03 *Framing Earthquake Retrofitting Decisions: The Case of Hillside Homes in Los Angeles.* Detlof von Winterfeldt, Nels Roselund, and Alicia Kitsuse. March 2000.

PEER 2000/02 *U.S.-Japan Workshop on the Effects of Near-Field Earthquake Shaking.* Andrew Whittaker, ed. July 2000.

PEER 2000/01 *Further Studies on Seismic Interaction in Interconnected Electrical Substation Equipment.* Armen Der Kiureghian, Kee-Jeung Hong, and Jerome L. Sackman. November 1999.

PEER 1999/14 *Seismic Evaluation and Retrofit of 230-kV Porcelain Transformer Bushings*. Amir S. Gilani, Andrew S. Whittaker, Gregory L. Fenves, and Eric Fujisaki. December 1999.

PEER 1999/13 *Building Vulnerability Studies: Modeling and Evaluation of Tilt-up and Steel Reinforced Concrete Buildings.* John W. Wallace, Jonathan P. Stewart, and Andrew S. Whittaker, editors. December 1999.

PEER 1999/12 *Rehabilitation of Nonductile RC Frame Building Using Encasement Plates and Energy-Dissipating Devices.* Mehrdad Sasani, Vitelmo V. Bertero, James C. Anderson. December 1999.

PEER 1999/11 *Performance Evaluation Database for Concrete Bridge Components and Systems under Simulated Seismic Loads.* Yael D. Hose and Frieder Seible. November 1999.

PEER 1999/10 *U.S.-Japan Workshop on Performance-Based Earthquake Engineering Methodology for Reinforced Concrete Building Structures.* December 1999.

PEER 1999/09 *Performance Improvement of Long Period Building Structures Subjected to Severe Pulse-Type Ground Motions*. James C. Anderson, Vitelmo V. Bertero, and Raul Bertero. October 1999.

PEER 1999/08 *Envelopes for Seismic Response Vectors.* Charles Menun and Armen Der Kiureghian. July 1999.

PEER 1999/07 *Documentation of Strengths and Weaknesses of Current Computer Analysis Methods for Seismic Performance of Reinforced Concrete Members.* William F. Cofer. November 1999.

PEER 1999/06 *Rocking Response and Overturning of Anchored Equipment under Seismic Excitations.* Nicos Makris and Jian Zhang. November 1999.

PEER 1999/05 *Seismic Evaluation of 550 kV Porcelain Transformer Bushings.* Amir S. Gilani, Andrew S. Whittaker, Gregory L. Fenves, and Eric Fujisaki. October 1999.

PEER 1999/04 *Adoption and Enforcement of Earthquake Risk-Reduction Measures.* Peter J. May, Raymond J. Burby, T. Jens Feeley, and Robert Wood.

PEER 1999/03 *Task 3 Characterization of Site Response General Site Categories*. Adrian Rodriguez-Marek, Jonathan D. Bray, and Norman Abrahamson. February 1999.

PEER 1999/02 *Capacity-Demand-Diagram Methods for Estimating Seismic Deformation of Inelastic Structures: SDF Systems*. Anil K. Chopra and Rakesh Goel. April 1999.

PEER 1999/01 *Interaction in Interconnected Electrical Substation Equipment Subjected to Earthquake Ground Motions.* Armen Der Kiureghian, Jerome L. Sackman, and Kee-Jeung Hong. February 1999.

PEER 1998/08 *Behavior and Failure Analysis of a Multiple-Frame Highway Bridge in the 1994 Northridge Earthquake.* Gregory L. Fenves and Michael Ellery. December 1998.

PEER 1998/07 *Empirical Evaluation of Inertial Soil-Structure Interaction Effects.* Jonathan P. Stewart, Raymond B. Seed, and Gregory L. Fenves. November 1998.

PEER 1998/06 *Effect of Damping Mechanisms on the Response of Seismic Isolated Structures.* Nicos Makris and Shih-Po Chang. November 1998.

PEER 1998/05 *Rocking Response and Overturning of Equipment under Horizontal Pulse-Type Motions.* Nicos Makris and Yiannis Roussos. October 1998.

PEER 1998/04 *Pacific Earthquake Engineering Research Invitational Workshop Proceedings, May 14–15, 1998: Defining the Links between Planning, Policy Analysis, Economics and Earthquake Engineering.* Mary Comerio and Peter Gordon. September 1998.

PEER 1998/03 *Repair/Upgrade Procedures for Welded Beam to Column Connections.* James C. Anderson and Xiaojing Duan. May 1998.

PEER 1998/02 *Seismic Evaluation of 196 kV Porcelain Transformer Bushings.* Amir S. Gilani, Juan W. Chavez, Gregory L. Fenves, and Andrew S. Whittaker. May 1998.

PEER 1998/01 *Seismic Performance of Well-Confined Concrete Bridge Columns.* Dawn E. Lehman and Jack P. Moehle. December 2000.

ONLINE REPORTS

The following PEER reports are available by Internet only at http://peer.berkeley.edu/publications/peer_reports.html

PEER 2008/104 *Experimental and Analytical Study of the Seismic Performance of Retaining Structures.* Linda Al Atik and Nicholas Sitar. March 2009.

PEER 2008/103 *Experimental and Computational Evaluation of Current and Innovative In-Span Hinge Details in Reinforced Concrete Box-Girder Bridges. Part 1: Experimental Findings and Pre-Test Analysis.* Matias A. Hube and Khalid M. Mosalam. January 2009.

PEER 2008/102 *Modeling of Unreinforced Masonry Infill Walls Considering In-Plane and Out-of-Plane Interaction.* Stephen Kadysiewski and Khalid M. Mosalam. January 2009.

PEER 2008/101 *Seismic Performance Objectives for Tall Buildings.* William T. Holmes, Charles Kircher, William Petak, and Nabih Youssef. August 2008.

PEER 2007/101 *Generalized Hybrid Simulation Framework for Structural Systems Subjected to Seismic Loading.* Tarek Elkhoraibi and Khalid M. Mosalam. July 2007.

PEER 2007/100 *Seismic Evaluation of Reinforced Concrete Buildings Including Effects of Masonry Infill Walls.* Alidad Hashemi and Khalid M. Mosalam. July 2007.